eman ta zabal zazu

Universidad del País Vasco

Euskal Herriko Unibertsitatea

Spin-dependent and non-adiabatic phenomena related to the electron-phonon interaction in nanostructures with strong relativistic corrections

A thesis submitted to the University of the Basque Country to obtain the degree of Doctor in Physics by

Peio Garcia Goiricelaya

Supervised by Dr. Asier Eiguren Goienetxea
and Dr. Idoia Garcia de Gurtubay Galligo

February, 2020

(cc)2020 PEIO GARCIA GOIRICELAYA (cc by-nc-sa 4.0)

"Aut inveniam viam aut faciam"

Hannibal Barca

Zü eta ni, biak goxoki, dantzan dantzan, rock&rolling!

Contents

Introduction

This thesis focuses on the coupling between electrons and phonons. Phonons are the low-energy elementary excitations corresponding to the quanta of the collective vibrations of the atomic lattice in crystalline solids. The study of the electron-phonon interaction is contemporary to the concept of phonons themselves, dating back almost a century with the beginning of the quantum theory of solids. Thus, it represents one of the most extensively studied chapters of solid-state physics, well documented in a large number of books and reviews [1–4].

Despite being a classic subject, the coupling between electrons and phonons continues to attract a great interest, since it is present in a large variety of physical phenomena. It strongly influences the temperature dependence of the electronic heat capacity and the electrical mobility, conductivity and resisitivity of metals and semiconductors, as well as the thermalization or cooling of hot carriers and the thermoelectric effect. It also influences the optical properties of semiconductors and insulators, taking part in the temperature dependence of energy band gaps and phonon-assisted optical absorption of indirect-gap materials. Besides, it leads to characteristic band-splittings, so-called kink structures, in photoemission spectra and sharp frequency softenings, so-called Kohn anomalies, in inelastic neutron or light scattering spectra. Likewise, it plays a fundamental role in conventional, or phonon-mediated, superconductivity, since it provides the mechanism to attract electrons and the pairing in conventional superconductors.

The effective velocity, or equivalently the effective mass, the actual energy and the lifetime of electron states, as well as the frequency and the lifetime of phonon modes, are determined by many-body interactions [5]. These include the interaction of both electrons and phonons with other single-particle excitations – excited electrons or holes – as well as electron-hole pair excitations and other collective excitations – phonons, plasmons, magnons or excitons – and defects of solids. In order to illustrate the importance of the electron-phonon interaction, it is worth noting that at realistic temperatures of the order of a few hundred Kelvin, the phase space for electronic scattering is actually reduced to a narrow energy window of the order of ~ 10 meV close to the Fermi level in metals. This energy range coincides with the typical phonon frequencies while typical electronic transition ener-

gies are of the order of ~ 1 eV [6]. Thereby, low-energy dynamics of charge carriers, i.e. excited electrons and holes, is usually dominated by phonon-mediated electronic scattering, which therefore governs the transport and thermodynamical properties of solids [7].

Early studies of the electron-phonon interaction between the 1930s and 1950s [8–13] were motivated by the need to establish a quantum theory of transport in solids, based on semi-empirical – Fröhlich and Holstein – Hamiltonians [14, 15] along with the use of the Fermi gas model for electrons [16] and the Einstein [17] or Debye [18] models for phonons. These initial works were essential to understand the mathematical structure of the electron-phonon matrix elements and the role played by the electronic screening in the potential change induced by lattice displacements. It was during the late 1950s and the early 1960s that the modern formulation of the electron-phonon theory using a quantum field-theoretic approach started, as a result of the advent of Landau-Fermi liquid theory [19] together with the concept of quasi-particle and the development of many-body Green's function perturbation theory [5] together with the concept of self-energy, that relates the bare or non-interacting and dressed or interacting propagators via the Dyson's equation. The general and still today most complete formulation of the theory of the electron-phonon interaction was established during the 1960s and 1970s [20, 21].

This thesis is based on *ab initio* calculations of the electron-phonon interaction, whose first calculations were not performed until the late 1990s [22–26]. The reason for this delay is that the formulation and the practical implementation of the density functional theory (DFT) [27–29] took from the mids 1960s to the 1980s, while the development of the density functional perturbation theory (DFPT) [30–33] did not come until the lates 1980s and the early 1990s. Indeed, state-of-the-art first principles calculations of the electron-phonon interaction are based on approximated but useful expressions of the coupling [2] and have the electronic and lattice vibrational properties resulting from DFT and DFPT, respectively, as starting point [4]. The latter theoretical formalisms are founded on the adiabatic approximation [34], which assumes that electrons respond instantaneously to the lattice motion. This approach leads to a simplified physical picture of electrons moving in a rigid lattice, and phonons only including electrostatic screening on lattice vibrations. Nevertheless, the electron-phonon interaction is expected to affect both electron states and phonon modes defined within the adiabatic approximation, leading to a renormalization of their properties and a decrease of their lifetimes.

One of the main goal of this thesis is to analyze the impact of the electron-phonon interaction beyond the adiabatic approximation, i.e. non-adiabatic effects. Indeed, non-adiabatic electron-phonon corrections have been usually detected by comparing bare electron band structures and adiabatic phonon dispersion relations with, both theoretically calculated or experimentally

measured, electron and phonon spectral functions, respectively. The so-called spectral functions are physical magnitudes of great physical interest, since their momentum and energy dependent structure describes the probability density of electron states or phonon modes, and holds valuable information about the properties of quasi-particles [2, 5]. It is worth noting that while the non-adiabatic electron-phonon effects have been extensively studied on bare electrons, these effects have been mainly limited to the center of the Brillouin zone (BZ) in the case of adiabatic phonons [4]. On the other hand, renormalized electron band structures and phonon dispersion relations have been generally calculated using the standard Brillouin-Wigner and Rayleigh-Schrödinger pertubation theory approaches [5]. Although these results have been useful for quantitatively estimating several physical phenomena, they also lead to unphysical divergent results. In this sense, recent investigations have successfully rationalized photoemission kinks in terms of multiple and physically different renormalized electron bands arising from one bare band due to the electron-phonon interaction [35, 36]. These works combine first principles calculations with the analytic properties of Green's functions [37] for self-consistently solving the Dyson's equation in the whole complex energy plane, opening the door for a systematic evaluation of quasi-particles from *ab initio* techniques. Note that no proper examination of the electron-phonon renormalization of adiabatic phonons has been performed in these terms.

On the experimental side, angle-resolved photoemission spectroscopy (ARPES) [38] and inelastic neutron (INS) and/or x-ray (IXS) scattering, as well as Raman scattering, [39, 40] are the most common techniques for probing electron and phonon spectral functions, respectively. Most of these techniques analyze the surface-parallel component of the momentum, and hence, are only suitable for studying two-dimensional (2D) or quasi-2D materials, where the electron-phonon interaction is usually enhanced [41–46]. Therefore, low-dimensional surfaces and monolayers represent privileged targets for analyzing, both experimentally and theoretically, the non-adiabatic effects of the electron-phonon interaction on electrons and phonons, and thereby, testing the adequacy of many-body theories. In this respect, 2D systems composed of heavy elements have turned out to have an interesting added value. In these materials, the combination of the surface inherent inversion asymmetry and the heavy element inherent strong atomic spin-orbit coupling leads to the generation of strongly spin-split electron surface states with highly anisotropic spin-polarizations, even for non-magnetic materials [47–61]. Thus, understanding the low-energy coupled charge and spin dynamics in 2D systems with strong spin-orbit coupling is today of capital importance due to its appealing spintronic applications [62–67], and thus, has become a very active research front at the moment [68–70]. Nevertheless, the coexistence of spin-orbit and electron-phonon interactions has been only investigated considering instructive theoretical models based on

Fröhlich and Holstein Hamiltonians [71–74]. It has not been until very recently, and concurrently with this thesis, that the role of the spin-orbit coupling in the electron-phonon interaction has been treated beyond simple relativistic corrections [75–78].

This thesis is an attempt to take a step further in the research field of the electron-phonon interaction. On the one hand, we have centered on studying the role played by the electron spin and the spin-orbit coupling in the electron-phonon interaction of surfaces with strong relativistic corrections from first principles calculations. On the other hand, we have focused on the non-adiabatic electron-phonon renormalization not only of ground-state electrons but also of adiabatic phonons, beyond the widely used standard theoretical approximations in materials that represent a challenge for many-body theories. To this end, this thesis is organized as follows. Chapter 1 is devoted to present the state-of-the-art theoretical DFT and DFPT formalisms used for calculating the ground-state electronic properties and the lattice vibrational properties of solids from first principles. These are essential in order to undertake calculations of the electron-phonon interaction, whose Hamiltonian and practical expressions are derived in Chapter 2. Particular attention is paid to the proper theoretical framework for calculating electron and phonon quasi-particles and the interpolation techniques based on maximally localized Wannier functions that allow to perform accurate and converged calculations. In Chapter 3, we investigate the role played by the electron spin and the spin-orbit coupling in the electron-phonon interaction at the relativistic Tl/Si(111) surface from first principles calculations. To this end, we introduce the spin-dependent theoretical framework for both DFT and DFPT formalisms, as well as for the electron-phonon interaction. In Chapter 4, we analyze the emergence of a strong electron-phonon interaction and related spin-dependent effects beyond the adiabatic approximation on both bare electrons and adiabatic phonons in the MoS_2 monolayer as a function of electron-doping.

Chapter 1

Electrons and phonons from first principles

In this first chapter, we will introduce the theoretical formalism considered throughout this thesis for calculating the ground-state electronic properties and the lattice vibrational properties of solids from first principles. Starting from the intractable many-body problem of many interacting electrons and ions in Sec. 1.1, we will make use of the adiabatic approximation in Sec. 1.2 in order to split the total many-body problem into two different problems; one of electronic nature and the other one of ionic nature.

On the one hand, in Sec. 1.3, we will describe the basic theory for approximately solving the problem of many interacting electrons in solids. These theoretical methods are based on the Hohenberg-Kohn theorems and the Kohn-Sham approximation, which form the density functional theory (DFT). Practical ground-state electronic first principles calculations are implemented using the concept of periodic crystalline solids as well as the plane wave basis sets and the pseudopotential approximation. On the other hand, in Sec. 1.4, we will present the basic theory used for solving the problem of many interacting ions in solids. Starting from the optimally relaxed equilibrium geometry of the lattice, we will adopt the harmonic approximation in order to describe the lattice vibrational normal modes, i.e. the phonon modes. Practical lattice vibrational first principles calculations are implemented by means of the density linear response theory, or more efficiently by means of the density functional perturbation theory (DFPT).

1.1 The many-body problem

At the atomic level, a piece of matter can be seen as composed of N_{el} negatively charged electrons and N_{ion} positively charged ions interacting via the Coulomb interaction. In the framework of non-relativistic quantum mechanics and the absence of any time-varying external potential acting on the

interacting system, the corresponding many-body Hamiltonian is given by[1]:

$$\begin{aligned}\hat{H} =& \sum_{i}^{N_{\text{el}}} \frac{\hat{\mathbf{p}}_i^2}{2} + \sum_{I}^{N_{\text{ion}}} \frac{\hat{\mathbf{P}}_I^2}{2M_I} - \sum_{i}^{N_{\text{el}}} \sum_{I}^{N_{\text{ion}}} \frac{Z_I}{|\hat{\mathbf{r}}_i - \hat{\mathbf{R}}_I|} \\ &+ \frac{1}{2} \sum_{i \neq j}^{N_{\text{el}}} \frac{1}{|\hat{\mathbf{r}}_i - \hat{\mathbf{r}}_j|} + \frac{1}{2} \sum_{I \neq J}^{N_{\text{ion}}} \frac{Z_I Z_J}{|\hat{\mathbf{R}}_I - \hat{\mathbf{R}}_J|} \\ \hat{H} =& \hat{T}_{\text{el}} + \hat{T}_{\text{ion}} + \hat{V}_{\text{el-ion}} + \hat{V}_{\text{el}} + \hat{V}_{\text{ion}},\end{aligned} \tag{1.1}$$

where electrons are denoted by lowercase subscripts (i and j), ions are denoted by uppercase subscripts (I and J), and Z_I and M_I are the charge and mass of the I-th ion, respectively. $\hat{\mathbf{r}}_i$ and $\hat{\mathbf{p}}_i = -i\hat{\boldsymbol{\nabla}}_i$ are the position and momentum operators of the i-th electron, respectively. $\hat{\mathbf{R}}_I$ and $\hat{\mathbf{P}}_I = -i\hat{\boldsymbol{\nabla}}_I$ are the position and momentum operators of the I-th ion, respectively. The first two terms on the right-hand side in Eq. 1.1 represent the electronic ($\hat{T}_{\text{el}}$) and ionic ($\hat{T}_{\text{ion}}$) kinetic energy operators, respectively, and the final three terms are the electron-ion ($\hat{V}_{\text{el-ion}}$), electron-electron ($\hat{V}_{\text{el}}$) and ion-ion ($\hat{V}_{\text{ion}}$) Coulomb interaction operators, respectively.

Since $\hat{H}$ does not depend on time, the formal way to solve the many-body problem is via the time-independent Schrödinger equation [79]: $\hat{H}\,|\Psi\rangle = E\,|\Psi\rangle$, where $|\Psi\rangle$ are the eigenstates of the many-body system with energy eigenvalues E. The many-body wave function depends on the position of all the particles in the system as, $\langle \mathbf{r}|\Psi\rangle = \Psi(\{\mathbf{r}_i\}, \{\mathbf{R}_I\})$, where $\{\mathbf{r}_i\}$ and $\{\mathbf{R}_I\}$ represent the set of electronic and ionic coordinates, respectively.

As it can be seen, the many-body problem is already well defined and fully established in terms of fundamental physics. Nevertheless, analytical solutions for realistic many-body systems are almost never accessible, being limited to the two-body hydrogen-like problem. A direct numerical treatment is not even possible, since obtaining the solutions requires an unattainable amount of memory storage that scales with the number of spatial degrees of freedom, $3(N_{\text{el}}+N_{\text{ion}}) \sim N_{\text{A}}$, with N_{A} the Avogrado number[2]. Therefore, appropriate approximations are needed in order to simplify the many-body problem.

1.2 The adiabatic approximation

The first approach adopted for simplifying the many-body problem (Sec. 1.1) can be intuitively understood by looking to the different dynamics of electrons and ions in solids. The typical electronic velocities ($\sim 10^8$cm/s) are of the order of 10^3 times larger than the typical ionic velocities ($\sim 10^5$cm/s) [6].

[1] Atomic units (a.u.) are adopted: $m_e = e = \hbar = 4\pi\epsilon_0 = 1$.

[2] Avogadro number: $N_{\text{A}} = 6.02214076 \times 10^{23}$ particles/mol

Thus, electrons can be assumed to respond instantaneously to the ionic motion, and equivalently, ions can be assumed to be static in space with an effective infinite mass ($M_I \to \infty$) with respect to the electronic motion.

This approach is the so-called adiabatic or Born-Oppenheimer approximation [34] and has a dramatic simplifying effect on the many-body Hamiltonian (Eq. 1.1). Within this approach, $\hat{T}_{\text{ion}}$ can be neglected and $\hat{V}_{\text{ion}}$ can be replaced by the classical pairwise Coulomb interaction between static ions $E_{\text{ion}}(\{\mathbf{R}_I\})$, which does not affect the dynamics of electrons. As a result, an electronic Hamiltonian depending parametrically on the ionic configuration $\{\mathbf{R}_I\}$ can be written: $\hat{H}_{\text{el}} = \hat{T}_{\text{el}} + \hat{V}_{\text{el}} + \hat{V}_{\text{el-ion}}(\{\mathbf{R}_I\})$. The corresponding electronic Schrödinger equation is defined as:

$$\hat{H}_{\text{el}}\Psi^{\alpha}_{\text{el}}(\{\mathbf{r}_i\},\{\mathbf{R}_I\}) = E^{\alpha}_{\text{el}}(\{\mathbf{R}_I\})\Psi^{\alpha}_{\text{el}}(\{\mathbf{r}_i\},\{\mathbf{R}_I\}), \tag{1.2}$$

where $|\Psi^{\alpha}_{\text{el}}\rangle$ is the electronic eigenstate with energy eigenvalue E^{α}_{el} and α is the quantum number accounting for the electronic degrees of freedom. On the other hand, the total many-body eigenstates $|\Psi\rangle$ are considered as the product of the electronic and ionic eigenstates:

$$\Psi^{\alpha\beta}(\{\mathbf{r}_i\},\{\mathbf{R}_I\}) = \Psi^{\alpha}_{\text{el}}(\{\mathbf{r}_i\},\{\mathbf{R}_I\}) \otimes \Psi^{\beta}_{\text{ion}}(\{\mathbf{R}_I\}), \tag{1.3}$$

where $|\Psi^{\beta}_{\text{ion}}\rangle$ is the ionic eigenstate and β is the quantum number accounting for the ionic degrees of freedom. Operating the total many-body Hamiltonian in Eq. 1.1 with the defined total many-body eigenstate in Eq. 1.3 and then projecting the resulting state into the electronic eigenstate:

$$\begin{aligned}\langle\Psi^{\alpha}_{\text{el}}|\hat{H}|\Psi^{\alpha'\beta}\rangle &= \langle\Psi^{\alpha}_{\text{el}}|\hat{T}_{\text{ion}} + E_{\text{ion}}(\{\mathbf{R}_I\}) + \hat{H}_{\text{el}}|\Psi^{\alpha'\beta}\rangle \\ &= \Big(\big[\hat{T}_{\text{ion}} + E_{\text{ion}}(\{\mathbf{R}_I\}) + E^{\alpha}_{\text{el}}(\{\mathbf{R}_I\})\big]\delta_{\alpha\alpha'} + \Delta\hat{H}^{\alpha\alpha'}\Big)\Psi^{\beta}_{\text{ion}}(\{\mathbf{R}_I\}),\end{aligned} \tag{1.4}$$

where $\delta_{\alpha\alpha'}$ is the Kronecker delta and $\Delta\hat{H}^{\alpha\alpha'}$ is the so-called non-adiabatic interaction term describing the coupling of the electrons with the ionic motion. The latter is given by [1, 2, 80]:

$$\begin{aligned}\Delta\hat{H}^{\alpha\alpha'} = &\sum_{I}^{N_{\text{ion}}} \frac{1}{M_I}\int\{\mathrm{d}\mathbf{r}_i\}\big(\Psi^{\alpha}_{\text{el}}(\{\mathbf{r}_i\},\{\mathbf{R}_I\})\big)^{*}\hat{\mathbf{P}}_I\Psi^{\alpha'}_{\text{el}}(\{\mathbf{r}_i\},\{\mathbf{R}_I\})\hat{\mathbf{P}}_I \\ &+ \sum_{I}^{N_{\text{ion}}} \frac{1}{2M_I}\int\{\mathrm{d}\mathbf{r}_i\}\big(\Psi^{\alpha}_{\text{el}}(\{\mathbf{r}_i\},\{\mathbf{R}_I\})\big)^{*}\hat{\mathbf{P}}^2_I\Psi^{\alpha'}_{\text{el}}(\{\mathbf{r}_i\},\{\mathbf{R}_I\}).\end{aligned} \tag{1.5}$$

Since electrons are assumed to be insensitive to the ionic movement within the adiabatic approximation, $\Delta\hat{H}^{\alpha\alpha'} = 0$. In addition, electrons are always considered in their ground state with respect to any ionic configuration. Thereby, the index α in Eq. 1.4 can be dropped ($\alpha = 0$). Hence, a fully ionic Schrödinger equation comes out:

$$\hat{H}_{\text{ion}}\Psi^{\beta}_{\text{ion}}(\{\mathbf{R}_I\}) = E^{0\beta}\Psi^{\beta}_{\text{ion}}(\{\mathbf{R}_I\}) = E^{\beta}\Psi^{\beta}_{\text{ion}}(\{\mathbf{R}_I\}), \tag{1.6}$$

where the ionic Hamiltonian $\hat{H}_{\text{ion}}$ is defined in terms of the ground-state electronic energy $E^0_{\text{el}}(\{\mathbf{R}_I\})$: $\hat{H}_{\text{ion}} = \hat{T}_{\text{ion}} + E_{\text{ion}}(\{\mathbf{R}_I\}) + E^0_{\text{el}}(\{\mathbf{R}_I\})$.

Therefore, the adiabatic approximation is a basic but extraordinarily valuable tool that allows to separate the total many-body problem into an electronic part, as in Eq. 1.2, and a ionic part, as in Eq. 1.6, and solve it. This approach has historically been widely used as the starting point for dealing with the interacting system of many electrons and ions, and has become a very useful procedure for many purposes as lattice vibrational first principles calculations [6, 80]. However, in some cases the coupling between electrons and the ionic motion can not be neglected. This foces to go beyond the adiabatic approximation in order to describe several physical properties, as for instance, the electrical resistivity in metals, or even superconductivity [1, 2].

1.3 Ground-state electronic structure

As soon as the adiabatic approximation is assumed, we focus on solving the electronic Schrödinger equation in Eq. 1.2, whose ground-state energy is also mandatory for solving the ionic Schrödinger equation in Eq. 1.6. As already stated in Sec. 1.2, the electronic problem depends parametrically on the ionic configuration $\{\mathbf{R}_I\}$ through the electron-ion Coulomb interaction. In this respect, the adiabatically fixed ionic background can be seen as a static external one-body potential acting equivalently and independently on each electron. The electron-ion Coulomb interaction operator $\hat{V}_{\text{el-ion}}$ can be rewritten in terms of the external potential operator $\hat{V}_{\text{ext}}$ as follows:

$$\hat{V}_{\text{el-ion}} = \sum_{i}^{N_{\text{el}}} \hat{V}_{\text{ext}}(\mathbf{r}_i, \{\mathbf{R}_I\}) = -\sum_{i}^{N_{\text{el}}} \sum_{I}^{N_{\text{ion}}} \frac{Z_I}{|\hat{\mathbf{r}}_i - \mathbf{R}_I|}. \tag{1.7}$$

It is worth noting that if the electronic potential was simply formed by the electron-ion Coulomb interaction, the system would be formed by N_{el} non-interacting electrons moving in the one-body external potential, which is already a solvable problem [6]. Nevertheless, the many-body electron-electron Coulomb interaction operator $\hat{V}_{\text{el}}$ depends on the position of all the electrons (Eq. 1.1), avoiding the electronic Hamiltonian to be split into a set of solvable one-body Hamiltonians. Thereby, the dimensionality of the electronic system is still large and equal to $3N_{\text{el}}$ electronic spatial variables, apart from depending parametrically on the ionic positions[3].

[3] All the electronic properties resulting from the solution of the electronic problem depend parametrically on the ionic coordinates $\{\mathbf{R}_I\}$. For the sake of clarity, the explicit notation of this dependence is omitted in the rest of Sec. 1.3.

1.3.1 Density functional theory

In this context, the density functional theory (DFT) has turned out to be one of the most widely used and successful methods for simplifying and solving the electronic problem in Eq. 1.2 [29, 81]. This "exact" quantum many-body theory is based on two fundamental mathematical theorems firstly proved in 1964 by Hohenberg and Kohn [27].

Briefly said, following the work of Thomas and Fermi in 1927 [82], Hohenberg and Kohn formulated the many-body electronic problem in terms of the electron density $n(\mathbf{r})$. They demonstrated that all the properties of the electronic system are completely and uniquely determined given only the ground-state electron density $n_0(\mathbf{r})$. With this perspective, they defined the energy of the electronic system in its lowest-energy state as a functional in terms of the electron density:

$$E_{\text{el}} \equiv E_{\text{el}}[n] = F[n] + \int V_{\text{ext}}(\mathbf{r}) n(\mathbf{r}) \mathrm{d}\mathbf{r}, \tag{1.8}$$

where $F[n]$ is a purely electronic universal functional of $n(\mathbf{r})$, and thus, independent of the external potential acting on the electrons. They proved that the exact ground-state energy of the electronic system is the global minimum value of the energy functional in Eq. 1.8. In addition, the electron density that minimizes this functional is that of the exact ground state[4].

Undoubtedly, reformulating the electronic problem in terms of the electron density is a masterful move, since the dimensionality of the problem is dramatically reduced to only three spatial variables. However, while the Hohenberg-Kohn theorems provide a general theoretical result, no practical methodology is given for calculating the ground-state electron density, since the exact dependence of $F[n]$ with respect to $n(\mathbf{r})$ is unknown.

Connecting to this, Kohn and Sham proposed in 1965 an elegant approach for overcoming this issue [28]. This consists in mapping the system of many interacting electrons moving in the external potential onto an auxiliary system made of as many non-interacting electrons moving in an effective potential, i.e. the electronic screened external potential, on the condition that both systems have the same ground-state electron density. In addition, the unknown functional $F[n]$ is introduced in the following form:

$$F[n] = T_{\text{el}}[n] + E_{\text{H}}[n] + E_{\text{xc}}[n], \tag{1.9}$$

where $T_{\text{el}}[n]$, $E_{\text{H}}[n]$ and $E_{\text{xc}}[n]$ represent the electronic kinetic energy, the Hartree energy and the exchange-correlation energy functionals, respectively. Within the Kohn-Sham representation of non-interacting electrons,

[4] $E_{\text{el}}^0 \equiv E_{\text{el}}[n_0] < E_{\text{el}}[n] \; \forall \; n(\mathbf{r}) \neq n_0(\mathbf{r})$. Detailed statements and demonstrations of the Hohenberg-Kohn theorems and their corollaries are also available in Refs.[29, 81].

the electronic kinetic energy is equal to the sum of the kinetic energies of each of the electrons:

$$T_{\mathrm{el}}[n] = -\frac{1}{2}\sum_{i}^{N_{\mathrm{el}}}\langle\psi_i|\hat{\boldsymbol{\nabla}}_i^2|\psi_i\rangle \equiv -\frac{1}{2}\sum_{i}^{N_{\mathrm{el}}}\int \mathrm{d}\mathbf{r}\big(\psi_i(\mathbf{r})\big)^*\hat{\boldsymbol{\nabla}}_i^2\psi_i(\mathbf{r}), \tag{1.10}$$

where $|\psi_i\rangle$ is the Kohn-Sham single-particle state of the i-th electron. The many-body electron-electron interaction is defined by the Hartree and exchange-correlation energies. The Hartree energy represents the classical Coulomb self-interaction of the electron density [83], defined as:

$$E_{\mathrm{H}}[n] = \frac{1}{2}\iint \frac{n(\mathbf{r})n(\mathbf{r}')}{|\mathbf{r}-\mathbf{r}'|}\mathrm{d}\mathbf{r}\mathrm{d}\mathbf{r}'. \tag{1.11}$$

The exchange-correlation energy accounts for all the quantum many-body effects missing in the Hartree energy. Namely, the exchange energy [84] accounts for the anti-symmetric property of the many-body electronic wave function [85] with respect to particle exchange, since electrons are defined as indistinguishable fermions. The correlation energy [86] accounts for the interaction effects beyond the independent single-electron picture within the Hartree-Fock approximation. Unfortunately, the exact expression of the exchange-correlation energy functional is unknown, and therefore, appropriate approximations must be made. Indeed, the great success of DFT relies on the ability of accounting for these energy terms, albeit approximately. In this thesis, the local density approximation (LDA) [87, 88] and the generalized gradient approximation (GGA) [89, 90] have been used for approximating $E_{\mathrm{xc}}[n]$. The reader is refered to Refs. [29, 81], or to Appendix A, for a detailed description of these approximations.

Following the Hohenberg-Kohn theorems [27], the electron density minimizing the electronic energy functional in Eq. 1.8 is the ground-state one. Thereby, we minimize this functional using Lagrange multipliers under the restriction that the Kohn-Sham states are orthonormal, i.e. $\langle\psi_i|\psi_j\rangle = \delta_{ij}$:

$$\frac{\delta}{\delta\psi_i^*(\mathbf{r})}\left[F[n] + \int V_{\mathrm{ext}}(\mathbf{r})n(\mathbf{r})\mathrm{d}\mathbf{r} - \sum_{j}^{N_{\mathrm{el}}}\varepsilon_j\left(\int \big|\psi_j(\mathbf{r}')\big|^2\mathrm{d}\mathbf{r}' - 1\right)\right] = 0. \tag{1.12}$$

Derivations of Eq. 1.12 using the definition of $F[n]$ in Eq. 1.9 together with Eqs. 1.10 and 1.11, as well as the derivation chain rule, lead to the Kohn-Sham single-electron Schrödinger equation:

$$\hat{H}_{\mathrm{KS}}\psi_i(\mathbf{r}) = \left(-\frac{\hat{\boldsymbol{\nabla}}^2}{2} + \hat{V}_{\mathrm{KS}}(\mathbf{r})\right)\psi_i(\mathbf{r}) = \varepsilon_i\psi_i(\mathbf{r}), \tag{1.13}$$

whose solution is the Kohn-Sham eigenstate $\psi_i(\mathbf{r})$ with energy ε_i for each i-th electron. The Kohn-Sham Hamiltonian $\hat{H}_{\mathrm{KS}}$ holds for the Kohn-Sham system of non-interacting electrons subject to the Kohn-Sham potential $V_{\mathrm{KS}}(\mathbf{r})$,

whose form is:

$$
\begin{aligned}
V_{\mathrm{KS}}(\mathbf{r}) &= V_{\mathrm{ext}}(\mathbf{r}) + \frac{\delta E_{\mathrm{H}}[n]}{\delta n(\mathbf{r})} + \frac{\delta E_{\mathrm{xc}}[n]}{\delta n(\mathbf{r})} = V_{\mathrm{ext}}(\mathbf{r}) + V_{\mathrm{H}}(\mathbf{r}) + V_{\mathrm{xc}}(\mathbf{r}) \\
V_{\mathrm{KS}}(\mathbf{r}) &= -\sum_{I}^{N_{\mathrm{ion}}} \frac{Z_I}{|\mathbf{r} - \mathbf{R}_I|} + \int \mathrm{d}\mathbf{r}' \, \frac{n(\mathbf{r}')}{|\mathbf{r} - \mathbf{r}'|} + \frac{\delta E_{\mathrm{xc}}[n]}{\delta n(\mathbf{r})},
\end{aligned}
\tag{1.14}
$$

with $V_{\mathrm{H}}(\mathbf{r})$ and $V_{\mathrm{xc}}(\mathbf{r})$ the Hartree and exchange-correlation potentials, respectively. Note that the Kohn-Sham potential is the one-body effective counterpart of the many-body electronic potential. It operates independently and equivalently on each non-interacting electron of the Kohn-Sham system at any spatial position $\mathbf{r}$. Finally, the electron density distribution is given in terms of the Kohn-Sham wave functions as follows:

$$
n(\mathbf{r}) = \sum_{i}^{N_{\mathrm{el}}} \left|\psi_i(\mathbf{r})\right|^2. \tag{1.15}
$$

Thus, the DFT formalism allows us to reformulate the difficult many-body electronic Schrödinger equation in Eq. 1.2 as a set of N_{el} solvable one-body Schrödinger equations (Eq. 1.13). Note that we have managed to derive the latter equation, as well as the Kohn-Sham potential in Eq. 1.14, independently of any approximation of the exchange-correlation energy functional. In fact, if the exact form of $E_{\mathrm{xc}}[n]$ was known, the exact ground-state electron density and energy of the interacting electronic system could be obtained. This is why DFT is considered an "exact" quantum many-body theory [29, 81].

In practice, once an approximate form of the exchange-correlation energy functional is chosen, Eqs. 1.13−1.15 compose the set of the so-called Kohn-Sham equations that has to be solved self-consistently through an efficient numerical iterative procedure [29, 81, 91]. Indeed, the Kohn-Sham potential depends on the electron density, which is determined by the Kohn-Sham states. In turn, the latter are solutions of the Kohn-Sham Schrödinger equation, that, at the same time, is defined by the Kohn-Sham potential. Figure 1.1 illustrates schematically the self-consistent loop for solving the set of Kohn-Sham equations. The strategy is to start any new cycle assuming the electron density of the previous iteration, the old density $n_{\mathrm{old}}(\mathbf{r})$, or an initial guess for the first iteration that can be created by the superposition of atomic charge densities. The Kohn-Sham potential corresponding to this old density is then constructed via Eq. 1.14. Next, the Kohn-Sham Schrödinger equations in Eq. 1.13 are solved in order to obtain the new Kohn-Sham states and energies. Then, the corresponding new electron density $n_{\mathrm{new}}(\mathbf{r})$ is calculated by means of Eq. 1.15. Finally, this new density is used as the starting point for the next cycle iteration, repeated in the

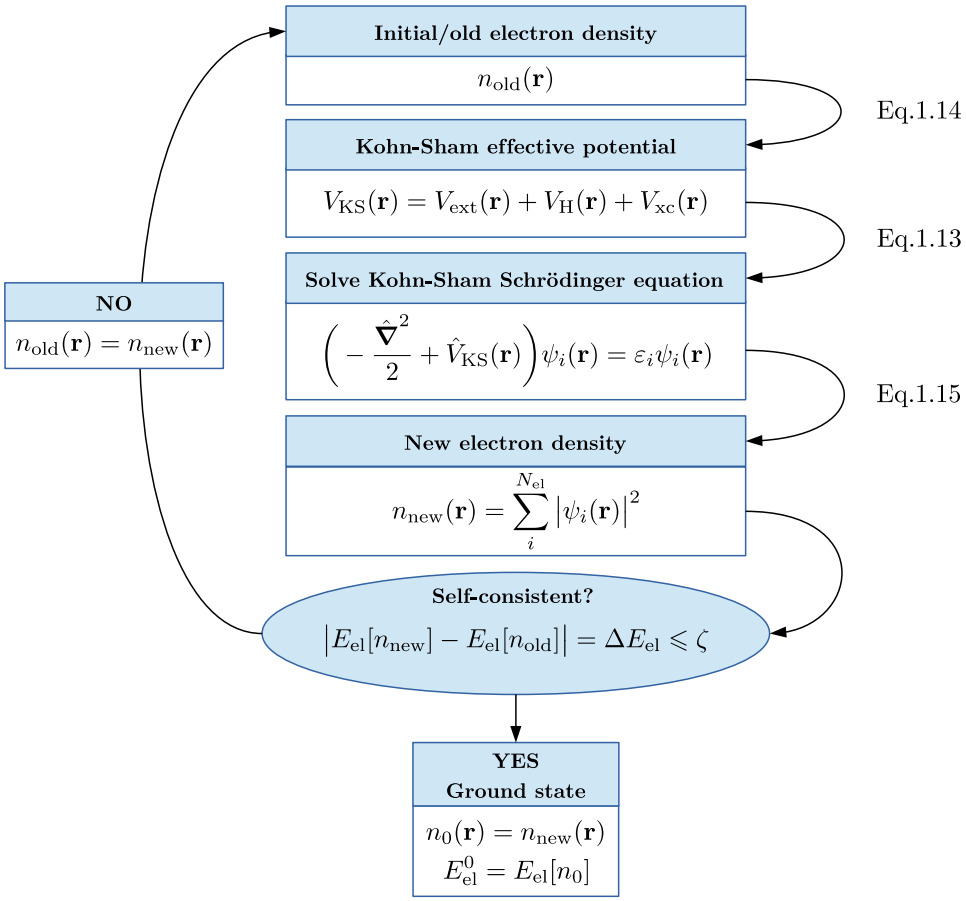

Figure 1.1. Schematic representation of the self-consistent loop for solving the set of Kohn-Sham equations in Eqs. 1.13−1.15.

same way[5]. The self-consistent loop cycles until the change in the electronic energy ΔE_{el} is smaller than a chosen convergence threshold ζ, usually less than 10^{-4} a.u. $\approx 10^{-3}$ eV. Once this condition is fulfilled, the electronic ground state is achieved and all the related properties of interest can be calculated.

1.3.2 Periodicity of the crystal

The calculation of the ground-state electronic structure, as well as the lattice vibrational structure in Sec. 1.4, can be additionally simplified by conveniently defining the problem within a tractable region of the space exploiting the periodicity of crystals.

[5]For stability, the calculated electron density is often mixed with the electron density of the previous iteration in order to get a new density for the next iteration [29, 81].

Indeed, an ideal crystalline solid is built by the periodic repetition of its primitive unit cell (u.c.), which corresponds to the irreducible region of the solid with respect to the translational symmetry. The unit cell is spatially delimited by the set of primitive real lattice vectors $\{\mathbf{a}_1, \mathbf{a}_2, \mathbf{a}_3\}$ and is defined by the basis that describes the ionic arrangement within it. Thus, the volume of the unit cell is defined as $V_{\text{u.c.}} = \left|\mathbf{a}_1 \cdot (\mathbf{a}_2 \times \mathbf{a}_3)\right|$. The real or direct Bravais lattice is generated by all the possible translations of the unit cell given by the real primitive lattice vectors [6].

The crystal periodicity imposes the same periodic conditions upon the Kohn-Sham potential felt by the electrons:

$$V_{\text{KS}}(\mathbf{r}) = V_{\text{KS}}(\mathbf{r} + \mathbf{T}), \tag{1.16}$$

where $\mathbf{T} = \sum_{i=1}^{3} l_i \mathbf{a}_i$ is a Bravais lattice vector with $l_i \in \mathbb{Z}$ and $\mathbf{r}$ is the vector of the real space defined within the unit cell. Bloch's theorem [92] states that the eigenstates of the Kohn-Sham Hamiltonian in Eq. 1.13 can be chosen to have the form of a plane wave times a crystal periodic function[6]:

$$\psi_{\mathbf{k}n}(\mathbf{r}) = e^{i\mathbf{k}\cdot(\mathbf{r})} u_{\mathbf{k}n}(\mathbf{r}), \tag{1.17}$$

where $u_{\mathbf{k}n}(\mathbf{r}) = u_{\mathbf{k}n}(\mathbf{r} + \mathbf{T})$ is the lattice-periodic part of the Kohn-Sham wave functions $\psi_{\mathbf{k}n}(\mathbf{r})$. These two previous definitions lead also to the additional relation: $\psi_{\mathbf{k}n}(\mathbf{r}+\mathbf{T}) = e^{i\mathbf{k}\cdot\mathbf{T}}\psi_{\mathbf{k}n}(\mathbf{r})$. Note that, within this definition, the electronic quantum number i is substituted by a band index n and a wave vector $\mathbf{k}$. The wave vector $\mathbf{k}$ is commonly known as the crystal momentum. It is defined within the first Brillouin zone (1BZ), which is the Wigner-Seitz primitive cell of the reciprocal lattice. By imposing Born-von Karman boundary conditions on the Kohn-Sham wave functions, it is demonstrated that the momentum $\mathbf{k}$ is real and restricted to the following allowed values [6]:

$$\mathbf{k} = \sum_{i=1}^{3} \frac{m_i}{N_i} \mathbf{b}_i. \tag{1.18}$$

where $\{\mathbf{b}_1, \mathbf{b}_2, \mathbf{b}_3\}$ is the set of primitive reciprocal lattice vectors fulfilling the condition: $\mathbf{a}_i \cdot \mathbf{b}_j = 2\pi\delta_{ij}$, with $m_i \in \mathbb{N}$ and $|m_i| < N_i$, being N_i the number of unit cells along the crystal direction i. The number $N_{\mathbf{k}}$ of allowed $\mathbf{k}$-points is exactly the same as the total number of unit cells in the supercell crystal: $N_{\mathbf{k}} = \prod_{i=1}^{3} N_i$. In what follows, the electron band structure of a solid will describe the dispersion of the Kohn-Sham energies $\varepsilon_{\mathbf{k}n}$ as a function of the momentum $\mathbf{k}$ for each band n.

1.3.3 Plane wave basis sets

Related to the periodicity of the crystal, plane waves are an interesting basis set to describe wave functions to take advantage of, since they are

[6] The reader is referred to Refs.[6, 81] for different proofs of the theorem.

per se spatially periodic functions. Indeed, plane waves are solutions of the Schrödinger equation for a free particle, and hence, they physically describe totally delocalized states. In Dirac's notation, a plane wave with momentum $\mathbf{k}$ is denoted by the state $|\mathbf{k}\rangle$ and has a kinetic energy equal to $|\mathbf{k}^2|/2$. Its normalized wave function[7] is defined as:

$$\langle \mathbf{r}|\mathbf{k}\rangle = \frac{1}{\sqrt{V}} e^{i\mathbf{k}\cdot\mathbf{r}} \tag{1.19}$$

where $V = N_{\mathbf{k}} V_{\text{u.c.}}$ is the volume of the supercell crystal. Since the lattice-periodic parts of the Kohn-Sham states have the same periodicity of the crystal (Eq. 1.16), it is a good idea to expand them, as well as the Kohn-Sham states through Eq. 1.17, in terms of an initially complete set of plane waves:

$$|u_{\mathbf{k}n}\rangle = \sum_{\mathbf{G}} c_{\mathbf{k}+\mathbf{G}n} \,|\mathbf{G}\rangle\,; \quad |\psi_{\mathbf{k}n}\rangle = \sum_{\mathbf{G}} c_{\mathbf{k}+\mathbf{G}n} \,|\mathbf{k}+\mathbf{G}\rangle\,, \tag{1.20}$$

where $c_{\mathbf{k}+\mathbf{G}n} = \langle \mathbf{G}|\psi_{\mathbf{k}n}\rangle$ are the expansion coefficients of the plane wave basis. The infinite summation in Eq. 1.20 is over the reciprocal lattice vectors $\mathbf{G} = \sum_{i=1}^{3} l_i \mathbf{b}_i$ with $l_i \in \mathbb{Z}$ and fulfilling the relation[8]: $e^{i\mathbf{G}\cdot\mathbf{T}} = 1$.

In crystals, electrons tend to lose their localized atomic character becoming more delocalized. Therefore, a finite number of coefficients in Eq. 1.20 is enough to accurately describe the Kohn-Sham states [81]. Thus, the sum over $\mathbf{G}$ vectors can be truncated to include only plane waves with kinetic energy values less than a given cutoff energy, E_{cut}, with typical values in the range of $20 - 100$ Ry [93, 94]:

$$|\psi_{\mathbf{k}n}\rangle = \sum_{\frac{|\mathbf{k}+\mathbf{G}|^2}{2E_{\text{cut}}} \leqslant 1} c_{\mathbf{k}+\mathbf{G}n} \,|\mathbf{k}+\mathbf{G}\rangle\,. \tag{1.21}$$

In practice, the Kohn-Sham Schrödinger equation in Eq. 1.13 is solved in a discrete and unbiased Monkhorst-Pack grid [95] of $\mathbf{k}$-points that samples the 1BZ. By expanding the Kohn-Sham states on the plane wave basis as in Eq. 1.21, we can reformulate the Kohn-Sham Schrödinger equation as a matrix set of eigenvalue equations for the expansion coefficients, defined as:

$$\sum_{\mathbf{G}'} \left(\frac{|\mathbf{k}+\mathbf{G}|^2}{2} \delta_{\mathbf{G}\mathbf{G}'} + V_{\text{KS}}(\mathbf{G}-\mathbf{G}') \right) c_{\mathbf{k}+\mathbf{G}'n} = \varepsilon_{\mathbf{k}n} c_{\mathbf{k}+\mathbf{G}n}, \tag{1.22}$$

where $V_{\text{KS}}(\mathbf{G}-\mathbf{G}')$ is the Fourier transform of the Kohn-Sham potential:

$$V_{\text{KS}}(\mathbf{G}-\mathbf{G}') = \big\langle \mathbf{k}+\mathbf{G}\big|V_{\text{KS}}\big|\mathbf{k}+\mathbf{G}'\big\rangle = \frac{1}{V}\int V_{\text{KS}}(\mathbf{r}) e^{-i(\mathbf{G}-\mathbf{G}')\cdot\mathbf{r}} \mathrm{d}\mathbf{r}. \tag{1.23}$$

[7] Plane waves are also a set of orhonormal functions: $\langle \mathbf{k}'|\mathbf{k}\rangle = \frac{1}{V}\int_V \mathrm{d}\mathbf{r}\; e^{i(\mathbf{k}-\mathbf{k}')\cdot\mathbf{r}} = \delta_{\mathbf{k}'\mathbf{k}}$.

[8] This is a well-known property of periodic functions. See Refs.[6, 81].

The matrix of Eq. 1.22 has $N_{\mathbf{G}} \times N_{\mathbf{G}}$ dimensions, where $N_{\mathbf{G}}$ is the number of reciprocal lattice vectors $\mathbf{G}$ used in the plane wave basis expansion in Eq. 1.21. This can be typically of the order of $\sim 10^5$ elements, and therefore, it must be diagonalized by efficient computational algorithms. In this thesis, all the self-consistent first principles DFT calculations (Fig. 1.1) have been performed using the QUANTUM ESPRESSO *ab initio* package [93, 94] implemented with the LAPACK mathematical libraries [96].

The diagonalization of Eq. 1.22 yields the Kohn-Sham energies $\varepsilon_{\mathbf{k}n}$ and the coefficients $c_{\mathbf{k}+\mathbf{G}n}$. Thereby, the Kohn-Sham states are built by means of Eq. 1.21 and the electron density in Eq. 1.15 is actually computed as:

$$n(\mathbf{r}) = \frac{1}{N_{\mathbf{k}}} \sum_{\mathbf{k}}^{1\mathrm{BZ}} \sum_{n} f(\varepsilon_{\mathbf{k}n}) \left|\psi_{\mathbf{k}n}(\mathbf{r})\right|^2, \tag{1.24}$$

where $f(\varepsilon_{\mathbf{k}n})$ is the Fermi-Dirac occupation factor of the Kohn-Sham state $|\psi_{\mathbf{k}n}\rangle$ with energy $\varepsilon_{\mathbf{k}n}$:

$$f(\varepsilon_{\mathbf{k}n}) = \frac{1}{1 + \exp[(\varepsilon_{\mathbf{k}n} - \varepsilon_{\mathrm{F}})/(k_{\mathrm{B}}T)]}, \tag{1.25}$$

with k_{B} the Boltzmann's constant and T the temperature. ε_{F} represents the Fermi energy, i.e. the energy of the occupied Kohn-Sham state with highest energy at zero temperature ($T = 0$ K). In this context, the Fermi surface (FS) is defined as the surface in the reciprocal space formed by the $\mathbf{k}$-points within the 1BZ that satisfy $\varepsilon_{\mathbf{k}n} = \varepsilon_{\mathrm{F}}$. Thus, the Fermi surface is also defined as the surface of the reciprocal space separating the occupied and non-occupied Kohn-Sham states.

Another useful magnitude that is worth introducing here is the density of states (DOS), which gives the number of Kohn-Sham states with energy ε per unit cell:

$$N(\varepsilon) = \frac{1}{N_{\mathbf{k}}} \sum_{\mathbf{k}}^{1\mathrm{BZ}} \sum_{n} \delta(\varepsilon - \varepsilon_{\mathbf{k}n}). \tag{1.26}$$

Likewise, for the following, it is also important to particularly introduce the specific DOS at the Fermi level, which we denostes as $N_{\mathrm{F}} = N(\varepsilon_{\mathrm{F}})$.

1.3.4 The pseudopotential approximation

Despite all the approaches introduced so far, there are still some practical impediments for solving the electronic problem. On the one hand, the total number of electrons present in the unit cell of a periodic crystal is usually large and increases getting larger with heavier atoms. On the other hand, electrons close to the atomic nuclei exhibit highly localized and rapidly oscillating wave functions, which require, albeit finite, a large amount of plane waves to adequately describe them, increasing thereby the computational cost.

In this context, one can take advantage of the different dynamical character of atomic core and valence electrons, and treat them separately. Indeed, the highly localized core electrons are tightly bound to the atomic nuclei at deep binding energy scales ($\gtrsim 10$ eV) and turn out to be rather unaffected by the valence electrons in most favorable cases. Conversely, the latter exhibit highly delocalized wave functions and strongly interact with the medium in which atoms are placed, being the responsible for most of the electronic and chemical properties of solids. As a result, the core electrons can be considered as frozen together with the atomic nuclei, whose pseudopotentials model the interaction between the valence electrons and the ions, i.e. the external potential in Eq. 1.7. This approach is the so-called pseudopotential approximation [81, 91]. It has a double computational benefit, since it allows us to deal with few delocalized valence electrons, whose wave functions are well described within a basis of a few plane waves.

The pseudopotential of any given atom is generated from the pseudo-wavefunctions of the set of chosen valence electrons. The latter are arbitrarily constructed in such a way that they match the self-consistently calculated all-electron atomic wave functions[9] beyond a chosen core radius. Inside the core radius, the pseudo-wavefunctions are smoothed out, removing the nodes of the functions and getting rid of the rapidly oscillatory part close to the nucleus. In this thesis, all the self-consistent first principles DFT calculations have been performed with norm-conserving pseudopotentials [97]. The reader is referred to Refs. [81, 91], or to Appendix B, for a detailed description of the generation of this kind of pseudopotentials.

1.4 Lattice vibrational structure

Within the adiabatic approximation (Sec. 1.2), once the ground-state electronic energy is self-consistently calculated from first principles (Sec. 1.3), the ionic Schrödinger equation in Eq. 1.6 is already accessible. In this context, the ground-state electronic energy acts as an effective potential on ions and, together with the Coulomb interaction between ions, forms the ionic potential energy [33, 98–100]:

$$U(\{\mathbf{R}_I\}) = E^0_{\mathrm{el}}(\{\mathbf{R}_I\}) + E_{\mathrm{ion}}(\{\mathbf{R}_I\}). \tag{1.27}$$

where the ionic coordinates $\{\mathbf{R}_I\}$ are not fixed parameters anymore, but represent the $3N_{\mathrm{ion}}$ spatial variables of the ionic system. Note that despite the decoupling of the electronic and ionic problems in the adiabatic picture, the ionic problem is actually defined by the ground-state electronic properties for a given ionic configuration $\{\mathbf{R}_I\}$.

[9] Within the DFT formalism, this is an "exact" quantum many-body problem subject to the approximation of the exchange-correlation energy functional.

1.4.1 Lattice equilibrium geometry optimization

Before studying the dynamical properties of solids, it is important to make sure that the lattice is in its equilibrium geometry. By treating ions as classical particles, the equilibrium condition is fulfilled when all the forces acting on each ion vanish:

$$\mathbf{F}_I = -\frac{\partial U(\{\mathbf{R}_I\})}{\partial \mathbf{R}_I}\bigg|_{\mathbf{R}_I=\mathbf{R}_I^0} = 0, \tag{1.28}$$

where $\mathbf{F}_I$ is the force acting on the I-th ion and $\{\mathbf{R}_I^0\}$ is the set of ionic coordinates at equilibrium. Since the ionic potential energy in Eq. 1.27 depends on the ground-state electronic energy, which in turn depends on the ionic configuration $\{\mathbf{R}_I\}$, calculating the set of ionic forces $\{\mathbf{F}_I\}$ at any ionic configuration by means of a finite difference method would require $3N_{\text{ion}}+1$ self-consistent first principles DFT calculations. However, for typical studied materials, this is extremely time demanding.

Fortunately, the Hellmann-Feynman theorem [101, 102] helps us to overcome this issue. It states that the first derivative of the eigenvalues of a Hamiltonian $\hat{H}_\lambda$ depending on a parameter λ is given by the expectation value of the derivative of the Hamiltonian:

$$\frac{\partial E_\lambda}{\partial \lambda} = \left\langle \Psi_\lambda \middle| \frac{\partial \hat{H}_\lambda}{\partial \lambda} \middle| \Psi_\lambda \right\rangle, \tag{1.29}$$

where Ψ_λ is the eigenstate of $\hat{H}_\lambda$ with eigenvalue E_λ, $\hat{H}_\lambda |\Psi_\lambda\rangle = E_\lambda |\Psi_\lambda\rangle$. By using this relation, the force acting on the I-th ion for the ionic configuration $\{\mathbf{R}_I\}$ can be expressed as follows [33, 98–100]:

$$\begin{aligned}
\mathbf{F}_I &= -\frac{\partial U(\{\mathbf{R}_I\})}{\partial \mathbf{R}_I} = -\frac{\partial E_{\text{el}}^0(\{\mathbf{R}_I\})}{\partial \mathbf{R}_I} - \frac{\partial E_{\text{ion}}(\{\mathbf{R}_I\})}{\partial \mathbf{R}_I} \\
&= -\left\langle \Psi_{\text{el}}^0 \middle| \frac{\partial \hat{H}_{\text{el}}}{\partial \mathbf{R}_I} \middle| \Psi_{\text{el}}^0 \right\rangle - \frac{\partial E_{\text{ion}}(\{\mathbf{R}_I\})}{\partial \mathbf{R}_I} \\
&= -\int \mathrm{d}\mathbf{r}\; n_0(\mathbf{r}, \{\mathbf{R}_I\}) \frac{\partial V_{\text{ext}}(\mathbf{r}, \{\mathbf{R}_I\})}{\partial \mathbf{R}_I} - \frac{\partial E_{\text{ion}}(\{\mathbf{R}_I\})}{\partial \mathbf{R}_I},
\end{aligned} \tag{1.30}$$

where $n_0(\mathbf{r}, \{\mathbf{R}_I\})$, $|\Psi_{\text{el}}^0\rangle$ and $E_{\text{el}}^0(\{\mathbf{R}_I\})$ are the ground-state electron density, eigenstate and eigenvalue of the electronic Hamiltonian $\hat{H}_{\text{el}}$ (Eq. 1.2). Since the latter depends explicitly on the ionic coordinates only through the external potential $V_{\text{ext}}(\mathbf{r}, \{\mathbf{R}_I\})$ (Eq. 1.7), only this term has been retained in the last step of Eq. 1.30. As a result, the set of ionic forces can be directly obtained by means of the ground-state electron density, whose knowledge requires a unique self-consistent first principles DFT calculation rather than $3N_{\text{ion}} + 1$ cycles.

In practice, for finding the optimal equilibrium geometry of the lattice, a reasonable initial guess is made for the ionic positions. Then, the electron

density and the electronic energy are self-consistently calculated solving the scheme of Fig. 1.1, from which the ionic forces are then obtained by means of Eq. 1.30. Afterwards, one gradually relaxes the ionic geometry by means of different iterative methods [103] performing at each step the pertinent self-consistent first principles DFT calculation. This is done systematically until all the ionic force components are smaller than a specified threshold, usually less than 10^{-3} a.u. ~ 10 meV/Å.

1.4.2 The harmonic approximation

Once the crystal is in its equilibrium geometry, i.e. the ions are in their equilibrium configuration $\{\mathbf{R}_I^0\}$, the instantaneous position $\mathbf{R}_I$ of the I-th ion vibrating around its equilibrium lattice site can be written as [33, 98–100]:

$$\mathbf{R}_I = \mathbf{R}_I^0 + \mathbf{u}_I = \mathbf{T}_l + \boldsymbol{\tau}_s + \mathbf{u}_{ls}, \tag{1.31}$$

where $\mathbf{T}_l$ is the Bravais lattice vector of the l-th unit cell, $\boldsymbol{\tau}_s$ is the equilibrium position of the s-th atom within the unit cell and $\mathbf{u}_{ls}$ is the out-of-equilibrium displacement of the $I = \{l, s\}$-th ion.

As the ionic displacements are small compared to the interatomic distances, we may expand the ionic potential energy on a Taylor series in powers of the ionic displacements about the equilibrium position coordinates. We also apply the so-called harmonic approximation, which consists in retaining the terms of the expansion up to second order:

$$U(\{\mathbf{R}_I\}) = U(\{\mathbf{R}_I^0\}) - \sum_{ls\alpha} F_{ls}^{\alpha} u_{ls}^{\alpha} + \frac{1}{2} \sum_{\substack{ls\alpha \\ l's'\alpha'}} u_{ls}^{\alpha} \left. \frac{\partial^2 U(\{\mathbf{R}_I\})}{\partial u_{ls}^{\alpha} \partial u_{l's'}^{\alpha'}} \right|_{u=0} u_{l's'}^{\alpha'}, \tag{1.32}$$

where $\alpha = \{x, y, z\}$ denotes the cartesian directions. At equilibrium, the forces acting on ions are zero (Eq. 1.28). Therefore, the ionic potential energy within the harmonic approximation is given by:

$$U(\{\mathbf{R}_I\}) = U_0 + \frac{1}{2} \sum_{\substack{ls\alpha \\ l's'\alpha'}} u_{ls}^{\alpha} C_{ss'}^{\alpha\alpha'}(l, l') u_{l's'}^{\alpha'}, \tag{1.33}$$

where the constant $U_0 = U(\{\mathbf{R}_I^0\})$ and $C_{ss'}^{\alpha\alpha'}(l, l')$ represents the matrix of interatomic force constants [33, 98–100]. The latter is equal to the second derivative of the ionic potential energy with respect to the ionic displacements, or equivalently, its negative gives the force acting on the $I = \{l, s\}$-th ion in the α direction per unit of displacement of the $J = \{l', s'\}$-th ion along the α' direction:

$$C_{ss'}^{\alpha\alpha'}(l, l') = \left. \frac{\partial^2 U(\{\mathbf{R}_I\})}{\partial u_{ls}^{\alpha} \partial u_{l's'}^{\alpha'}} \right|_{u=0} \equiv -\frac{\partial F_{ls}^{\alpha}}{\partial u_{l's'}^{\alpha'}}. \tag{1.34}$$

The force acting on the $I = \{l, s\}$-th ion should be slightly retarded with respect to the other ionic displacements due to the electronic screening, i.e. the response of electrons [104, 105]. Still, since the electronic response to the ionic motion is assumed instantaneous within the adiabatic approximation, the interatomic force constants are considered static, $C_{ss'}^{\alpha\alpha'}(l, l', t - t') = C_{ss'}^{\alpha\alpha'}(l, l')\delta(t - t')$. Moreover, due to the translational invariance of the crystal lattice (Sec. 1.3.2), the interatomic force constant matrix depends on l and l' only through the difference $\mathbf{T}_l - \mathbf{T}_{l'}$, and therefore, $C_{ss'}^{\alpha\alpha'}(l, l') = C_{ss'}^{\alpha\alpha'}(l - l')$.

Classical theory of the harmonic vibrating lattice

In this context, by means of the Newton's second law and treating the ions as classical particles, one can derive the equation of motion of the individual $I = \{l, s\}$-th ion:

$$-\sum_{l's'\alpha'} C_{ss'}^{\alpha\alpha'}(l - l')u_{l's'}^{\alpha'} = F_{ls}^{\alpha} = M_s \ddot{u}_{ls}^{\alpha}. \tag{1.35}$$

Looking for solutions in the form of propagating plane waves [6, 33, 105], the ionic displacement is defined as: $u_{ls}^{\alpha} = (\epsilon_{\mathbf{q}s}^{\alpha}/\sqrt{M_s})e^{i(\mathbf{q}\cdot\mathbf{T}_l - \omega t)}$, where ω and $\epsilon_{\mathbf{q}s}^{\alpha}$ are the frequency and the mass-scaled displacement amplitude of the s-th ion in the l-th unit cell along the direction α, respectively, for a lattice distortion of momentum $\mathbf{q}$. Making the pertinent substitution in Eq. 1.35, we obtain the secular eigenvalue equation for the vibrating lattice:

$$\sum_{s'\alpha'} D_{ss'}^{\alpha\alpha'}(\mathbf{q})\epsilon_{\mathbf{q}\nu}^{s'\alpha'} = \omega_{\mathbf{q}\nu}^2 \epsilon_{\mathbf{q}\nu}^{s\alpha}, \tag{1.36}$$

which is equivalent to diagonalize the so-called dynamical matrix $D_{ss'}^{\alpha\alpha'}(\mathbf{q})$. The latter is related to the Fourier transform of the interatomic force constant matrix $C_{ss'}^{\alpha\alpha'}(\mathbf{q})$ as follows:

$$D_{ss'}^{\alpha\alpha'}(\mathbf{q}) = \frac{C_{ss'}^{\alpha\alpha'}(\mathbf{q})}{\sqrt{M_s M_{s'}}} = \sum_{l'} e^{-i\mathbf{q}\cdot(\mathbf{T}_l - \mathbf{T}_{l'})} \frac{C_{ss'}^{\alpha\alpha'}(l - l')}{\sqrt{M_s M_{s'}}}. \tag{1.37}$$

In Eq. 1.36, $\omega_{\mathbf{q}\nu}$ and $\epsilon_{\mathbf{q}\nu}^{s\alpha}$ are the frequency (eigenvalue) and polarization vector (eigenvector), respectively, of the lattice vibrational normal mode, i.e. the phonon mode, with branch index ν at momentum $\mathbf{q}$. Since the dynamical matrix is fully Hermitian, $D_{ss'}^{\alpha\alpha'}(\mathbf{q}) = \left[D_{s's}^{\alpha'\alpha}(\mathbf{q})\right]^*$, the phonon eigenvalues are real numbers and the phonon eigenvectors are orthonormal for each wave vector $\mathbf{q}$:

$$\sum_{\nu} \left(\epsilon_{\mathbf{q}\nu}^{s\alpha}\right)^* \epsilon_{\mathbf{q}\nu}^{s'\alpha'} = \delta_{ss'}\delta_{\alpha\alpha'}; \quad \sum_{s\alpha} \left(\epsilon_{\mathbf{q}\nu}^{s\alpha}\right)^* \epsilon_{\mathbf{q}\nu'}^{s\alpha} = \delta_{\nu\nu'}. \tag{1.38}$$

In this thesis, we focus on non-magnetic materials with time-reversal symmetry, and hence, the following relations are also fulfilled:

$$\omega^2_{\mathbf{q}\nu} = \omega^2_{-\mathbf{q}\nu}; \quad \epsilon^{s\alpha}_{\mathbf{q}\nu} = \epsilon^{s\alpha}_{-\mathbf{q}\nu}. \tag{1.39}$$

Physically, phonons as above are the vibrational normal modes of the lattice within the adiabatic and harmonic approximations. They represent well-defined and infinitely long-lived collective oscillations of coupled ions vibrating with the same frequency and with a fixed relative amplitude and phase. For each momentum $\mathbf{q}$, we have $3N^{\text{u.c.}}_{\text{ion}}$ phonon modes, where $N^{\text{u.c.}}_{\text{ion}}$ is the number of ions per unit cell of the crystal. In crystals, there are always three low frequency branches of acoustic character, i.e. phonon branches describing vibrations with frequencies that vanish linearly with $\mathbf{q}$ in the long-wavelength limit ($\mathbf{q} \to 0$). The other $3(N^{\text{u.c.}}_{\text{ion}} - 1)$ phonon modes are of optical character, i.e. phonon branches with finite frequencies at $\mathbf{q} = 0$. This makes a total of $3N_{\text{ion}} = 3N_{\mathbf{q}}N^{\text{u.c.}}_{\text{ion}}$ phonon modes in the supercell crystal, which is equal to the number of ionic degrees of freedom. In what follows, the phonon dispersion relation of a solid will describe the dispersion of the frequencies $\omega_{\mathbf{q}\nu}$ as a function of the momentum $\mathbf{q}$ for each branch ν.

Quantum theory of the vibrating lattice

So far, lattice vibrations have been evaluated using classical mechanics. Nevertheless, the classical theory is not adequate to explain several behaviors. For instance, the classical law of Dulong and Petit, which states that the contribution of the vibrating lattice to the specific heat is independent of the temperature, fails loudly at low temperatures and quantum mechanics is required to account for it [6]. Consequently, and for practical purposes, it is convenient to turn to the quantum theory. Plugging the ionic harmonic potential definition at equilibrium in Eq. 1.33 into the ionic Hamiltonian in Eq. 1.6, and explicitly expressing the ionic kinetic operator in terms of the ionic cartesians coordinates, the ionic harmonic Hamiltonian is written as:

$$\hat{H}_{\text{ion}} = U_0 + \sum_{ls\alpha} \frac{(\hat{P}^{\alpha}_{ls})^2}{2M_s} + \frac{1}{2} \sum_{\substack{ls\alpha \\ l's'\alpha'}} \hat{u}^{\alpha}_{ls} C^{\alpha\alpha'}_{ss'}(l - l') \hat{u}^{\alpha'}_{l's'}, \tag{1.40}$$

where the commutation relations in real space are well-established as [6, 106]:

$$[\hat{\mathbf{P}}_{ls}, \hat{\mathbf{P}}_{l's'}] = [\hat{\mathbf{u}}_{ls}, \hat{\mathbf{u}}_{l's'}] = 0; \quad [\hat{u}^{\alpha}_{ls}, \hat{P}^{\alpha'}_{l's'}] = i\delta_{\alpha\alpha'}\delta_{ss'}\delta_{ll'}, \tag{1.41}$$

If we now substitute in Eq. 1.40 the real ionic displacements and momenta operators with their Fourier transforms, defined respectively as:

$$u^{\alpha}_{ls} = \frac{1}{\sqrt{N_{\mathbf{q}}}} \sum_{\mathbf{q}}^{1\text{BZ}} e^{i\mathbf{q}\cdot\mathbf{T}_l} u^{\alpha}_{s}(\mathbf{q}); \quad P^{\alpha}_{ls} = \frac{1}{\sqrt{N_{\mathbf{q}}}} \sum_{\mathbf{q}}^{1\text{BZ}} e^{i\mathbf{q}\cdot\mathbf{T}_l} P^{\alpha}_{s}(\mathbf{q}), \tag{1.42}$$

and making use of the identity $\sum_l e^{i(\mathbf{q}+\mathbf{q}')\cdot\mathbf{T}_l} = N_{\mathbf{q}}\delta_{-\mathbf{q}\mathbf{q}'}$, we obtain the expression of the ionic harmonic Hamiltonian in the reciprocal space:

$$\hat{H}_{\text{ion}} = U_0 + \sum_{\mathbf{q}}^{1\text{BZ}} \left(\sum_{s\alpha} \frac{\hat{P}_s^{\alpha}(-\mathbf{q})\hat{P}_s^{\alpha}(\mathbf{q})}{2M_s} + \frac{1}{2} \sum_{\substack{s\alpha \\ s'\alpha'}} \hat{u}_s^{\alpha}(-\mathbf{q}) C_{ss'}^{\alpha\alpha'}(\mathbf{q}) \hat{u}_{s'}^{\alpha'}(\mathbf{q}) \right). \quad (1.43)$$

Following the definition of the canonical commutation relations in the real space in Eq. 1.41, it is straightforward to show that the ionic displacement and momentum operators in the reciprocal space satisfy the following canonical commutation relations:

$$\begin{aligned} [\hat{\mathbf{P}}_s(\mathbf{q}), \hat{\mathbf{P}}_{s'}(\mathbf{q}')] &= [\hat{\mathbf{u}}_s(\mathbf{q}), \hat{\mathbf{u}}_{s'}(\mathbf{q}')] = 0 \\ [\hat{u}_s^{\alpha}(\mathbf{q}), \hat{P}_{s'}^{\alpha'}(\mathbf{q}')] &= i\delta_{\mathbf{q},-\mathbf{q}}\delta_{\alpha\alpha'}\delta_{ss'} \end{aligned} \quad (1.44)$$

In second quantization, both the reciprocal ionic displacements and momenta operators can be expanded in terms of the creation and destruction/annihilation operators of each phonon mode $|\mathbf{q}, \nu\rangle$, $\hat{a}_{\mathbf{q}\nu}^{\dagger}$ and $\hat{a}_{\mathbf{q}\nu}$ respectively, as follows:

$$\begin{aligned} \hat{u}_s^{\alpha}(\mathbf{q}) &= \sum_{\nu} \frac{1}{\sqrt{2M_s\omega_{\mathbf{q}\nu}}} \epsilon_{\mathbf{q}\nu}^{s\alpha} (\hat{a}_{\mathbf{q}\nu} + \hat{a}_{-\mathbf{q}\nu}^{\dagger}) \\ \hat{P}_s^{\alpha}(\mathbf{q}) &= -i \sum_{\nu} \sqrt{\frac{M_s\omega_{\mathbf{q}\nu}}{2}} \epsilon_{\mathbf{q}\nu}^{s\alpha} (\hat{a}_{\mathbf{q}\nu} - \hat{a}_{-\mathbf{q}\nu}^{\dagger}). \end{aligned} \quad (1.45)$$

The operators $\hat{a}_{\mathbf{q}\nu}^{\dagger}$ and $\hat{a}_{\mathbf{q}\nu}$ are equivalent to the standard non-Hermitian ladder operators of a simple quantum harmonic oscillator and satisfy the following commutation relations [6, 106]:

$$[\hat{a}_{\mathbf{q}\nu}, \hat{a}_{\mathbf{q}'\nu'}^{\dagger}] = \delta_{\mathbf{q}\mathbf{q}'}\delta_{\nu\nu'}; \quad [\hat{a}_{\mathbf{q}\nu}, \hat{a}_{\mathbf{q}'\nu'}] = [\hat{a}_{\mathbf{q}\nu}^{\dagger}, \hat{a}_{\mathbf{q}'\nu'}^{\dagger}] = 0. \quad (1.46)$$

Plugging Eq. 1.45 into Eq. 1.43 and using the relations in Eqs. 1.36-1.39, the ionic harmonic Hamiltonian in second quantization can be written as the sum of the Hamiltonians of $3N_{\text{ion}}$ independent quantum harmonic oscillators:

$$\hat{H}_{\text{ion}} = U_0 + \sum_{\mathbf{q}}^{1\text{BZ}} \sum_{\nu} \omega_{\mathbf{q}\nu} \left(\hat{a}_{\mathbf{q}\nu}^{\dagger} \hat{a}_{\mathbf{q}\nu} + \frac{1}{2} \right). \quad (1.47)$$

The corresponding ionic eigenstate is equal to the product of the eigenstates of the $3N_{\text{ion}}$ independent quantum harmonic oscillators:

$$|\Psi_{\text{ion}}^{\beta}\rangle = \prod_{\mathbf{q}\nu} |n_{\mathbf{q}\nu}\rangle = \prod_{\mathbf{q}\nu} \frac{(\hat{a}_{\mathbf{q}\nu}^{\dagger})^{n_{\mathbf{q}\nu}}}{\sqrt{n_{\mathbf{q}\nu}!}} |0\rangle, \quad (1.48)$$

where $|0\rangle$ is the state of no phonons and $n_{\mathbf{q}\nu}$ denotes the number of phonon modes $|\mathbf{q},\nu\rangle$. The energy eigenvalue E^β of this ionic eigenstate is equal to:

$$E^\beta = \langle \Psi^\beta_{\text{ion}} | \hat{H}_{\text{ion}} | \Psi^\beta_{\text{ion}} \rangle = U_0 + \sum_{\mathbf{q}}^{\text{1BZ}} \sum_{\nu} \omega_{\mathbf{q}\nu} \left(n_{\mathbf{q}\nu} + \frac{1}{2} \right) \tag{1.49}$$

At this point, note that the ionic Schrödinger equation in Eq. 1.6 has been solved within the harmonic approximation, and therefore, the total many-body problem is solved within the adiabatic and harmonic approximations. Since phonons are bosons, in thermal equilibrium, the lattice dynamics of a solid can formally be considered as a gas of independent phonons obeying the Bose-Einstein statistics, i.e. with an occupation number:

$$\langle n_{\mathbf{q}\nu} \rangle = n_{\text{B}}(\omega_{\mathbf{q}\nu}) = \frac{1}{\exp\left[\omega_{\mathbf{q}\nu}/(k_{\text{B}}T)\right] - 1}. \tag{1.50}$$

Finally, it is worth introducing here the useful magnitude of the phonon density of states (phDOS), which, similar to DOS for electrons in Eq. 1.26, gives the number of phonon modes with frequency ω per unit cell:

$$F(\omega) = \frac{1}{N_{\mathbf{q}}} \sum_{\mathbf{q}}^{\text{1BZ}} \sum_{\nu} \delta(\omega - \omega_{\mathbf{q}\nu}) \tag{1.51}$$

1.4.3 Density linear response theory

As seen from Eq. 1.36, the phonon modes at a momentum $\mathbf{q}$ are obtained by diagonalizing the corresponding dynamical matrix, which is determined by the Fourier transform of the interatomic force constant matrix (Eq. 1.37). In turn, the latter is formally defined as the negative first-order derivative of the ionic forces $\{\mathbf{F}_I\}$, with respect to the ionic displacements (Eq. 1.34). The most direct way to calculate the interatomic force constants is from finite differences within a supercell, in which the desired $\mathbf{q}$ is defined as a reciprocal lattice vector. This procedure is known as the frozen-phonon method. Despite of its wide use in literature because of its simple implementation within DFT [107–113], this method may involve the treatment of supercells that may become impractically large when evaluating the dynamical matrix in the long-wavelength limit ($\mathbf{q} \to 0$).

Alternatively, from Eq. 1.34, the interatomic force constants can be also obtained by differentiating the Hellmann-Feynman forces in Eq. 1.30:

$$\begin{aligned} C^{\alpha\alpha'}_{ss'}(l,l') = &\int \frac{\partial n(\mathbf{r})}{\partial u^\alpha_{ls}}\bigg|_{u=0} \frac{\partial V_{\text{ext}}(\mathbf{r})}{\partial u^{\alpha'}_{l's'}}\bigg|_{u=0} \mathrm{d}\mathbf{r} \\ &+ \int n(\mathbf{r}) \frac{\partial^2 V_{\text{ext}}(\mathbf{r})}{\partial u^\alpha_{ls} \partial u^{\alpha'}_{l's'}}\bigg|_{u=0} \mathrm{d}\mathbf{r} + \frac{\partial^2 E_{\text{ion}}}{\partial u^\alpha_{ls} \partial u^{\alpha'}_{l's'}}\bigg|_{u=0}, \end{aligned} \tag{1.52}$$

where $n(\mathbf{r}) = n_0(\mathbf{r}, \{\mathbf{R}_I^0\})$, $V_{\text{ext}}(\mathbf{r}) = V_{\text{ext}}(\mathbf{r}, \{\mathbf{R}_I^0\})$ and $E_{\text{ion}} = E_{\text{ion}}(\{\mathbf{R}_I^0\})$ for the sake of clarity in the notation. The calculation in Eq. 1.52 requires the knowledge of the ground-state electron density as well as its first-order derivatives with respect to the ionic displacements[10] $\partial n(\mathbf{r})/\partial u_{ls}^{\alpha}$. The ground-state electron density is already directly accessible from the self-consistent DFT calculation of the relaxed crystal. On the other hand, the first-order derivative of the electron density can be calculated making use of the linear response theory [114–116], where, in addition, the responses to perturbations of different momenta are decoupled. Thus, one can evaluate directly the dynamical matrix at any arbitrary momentum $\mathbf{q}$ avoiding the use of supercells and limiting calculations to the unit cell. Substituting Eq. 1.52 in Eq. 1.37:

$$D_{ss'}^{\alpha\alpha'}(\mathbf{q}) = \frac{1}{\sqrt{M_s M_{s'}}} \left[\int \left(\frac{\partial n(\mathbf{r})}{\partial u_s^{\alpha}(\mathbf{q})} \right)^* \frac{\partial V_{\text{ext}}(\mathbf{r})}{\partial u_{s'}^{\alpha'}(\mathbf{q})} \mathrm{d}\mathbf{r} + \int n(\mathbf{r}) \frac{\partial^2 V_{\text{ext}}(\mathbf{r})}{\left(\partial u_s^{\alpha}(\mathbf{q})\right)^* \partial u_{s'}^{\alpha'}(\mathbf{q})} \mathrm{d}\mathbf{r} + \frac{\partial^2 E_{\text{ion}}}{\left(\partial u_s^{\alpha}(\mathbf{q})\right)^* \partial u_{s'}^{\alpha'}(\mathbf{q})} \right]_{u=0}. \tag{1.53}$$

Within this theory, the first-order derivatives of the electron density and the external potential are related by:

$$\frac{\partial n(\mathbf{r})}{\partial u_s^{\alpha}(\mathbf{q})} = \int \chi_{\mathbf{q}}(\mathbf{r}, \mathbf{r}') \frac{\partial V_{\text{ext}}(\mathbf{r}')}{\partial u_s^{\alpha}(\mathbf{q})} \mathrm{d}\mathbf{r}', \tag{1.54}$$

where $\chi_{\mathbf{q}}(\mathbf{r}, \mathbf{r}')$ is the static, i.e. frequency-independent, density-response function[11] of the system of interacting electrons to any external perturbation of momentum $\mathbf{q}$. Substituting Eq. 1.54 in Eq. 1.53, it is straightforward to show that the dynamical matrix can be rewritten as follows:

$$D_{ss'}^{\alpha\alpha'}(\mathbf{q}) = \frac{1}{\sqrt{M_s M_{s'}}} \left[\iint \left(\frac{\partial V_{\text{ext}}(\mathbf{r}')}{\partial u_s^{\alpha}(\mathbf{q})} \right)^* \left(\chi_{\mathbf{q}}(\mathbf{r}, \mathbf{r}')\right)^* \frac{\partial V_{\text{ext}}(\mathbf{r})}{\partial u_{s'}^{\alpha'}(\mathbf{q})} \mathrm{d}\mathbf{r}\mathrm{d}\mathbf{r}' + \int n(\mathbf{r}) \frac{\partial^2 V_{\text{ext}}(\mathbf{r})}{\left(\partial u_s^{\alpha}(\mathbf{q})\right)^* \partial u_{s'}^{\alpha'}(\mathbf{q})} \mathrm{d}\mathbf{r} + \frac{\partial^2 E_{\text{ion}}}{\left(\partial u_s^{\alpha}(\mathbf{q})\right)^* \partial u_{s'}^{\alpha'}(\mathbf{q})} \right]_{u=0}. \tag{1.55}$$

Within this formalism, the central problem is to calculate the interacting density-response function. The problem can be also formulated in the Kohn-Sham picture of non-interacting electrons. Within this approach, any external perturbation is self-consistently screened by an electronic potential

[10] Note that, both, the adiabatic definition of the interatomic force constant matrix in Eq. 1.52, and the dynamical matrix in Eq. 1.53, are defined by the static response of the electron density to the ionic motion. Therefore, they already incorporate the static effects of the electron-phonon interaction, which is an unequivocal signal that the ground-state electronic properties govern the lattice vibrational structure of the crystal [99, 100].

[11] In literature, the density-response function is also called susceptibility or polarizability.

set up by the density-response resulting from the Hartree and exchange-correlation energy terms (Eq. 1.14), leading to a change in the effective potential. Thereby, the first-order derivatives of the Kohn-Sham potential and the external potential are related by [115, 116]:

$$\begin{aligned}\frac{\partial V_{\mathrm{KS}}(\mathbf{r})}{\partial u_s^\alpha(\mathbf{q})} &= \int \big(\epsilon_{\mathbf{q}}(\mathbf{r},\mathbf{r}')\big)^{-1}\frac{\partial V_{\mathrm{ext}}(\mathbf{r}')}{\partial u_s^\alpha(\mathbf{q})}\mathrm{d}\mathbf{r}' \\ &= \frac{\partial V_{\mathrm{ext}}(\mathbf{r})}{\partial u_s^\alpha(\mathbf{q})} + \int K(\mathbf{r},\mathbf{r}')\frac{\partial n(\mathbf{r}')}{\partial u_s^\alpha(\mathbf{q})}\mathrm{d}\mathbf{r}',\end{aligned} \tag{1.56}$$

where $\epsilon_{\mathbf{q}}(\mathbf{r},\mathbf{r}')$ is the dielectric function and $K(\mathbf{r},\mathbf{r}')$ is the Hartree and exchange-correlation kernel, which is defined as:

$$K(\mathbf{r},\mathbf{r}') = \frac{\delta V_{\mathrm{H}}(\mathbf{r})}{\delta n(\mathbf{r}')} + \frac{\delta V_{\mathrm{xc}}(\mathbf{r})}{\delta n(\mathbf{r}')} = \frac{1}{|\mathbf{r}-\mathbf{r}'|} + \frac{\delta V_{\mathrm{xc}}(\mathbf{r})}{\delta n(\mathbf{r}')}. \tag{1.57}$$

Combining Eqs. 1.54 and 1.56, one obtains the expression relating the inverse of the dielectric function and the interacting density-response function:

$$\big(\epsilon_{\mathbf{q}}(\mathbf{r},\mathbf{r}')\big)^{-1} = \delta(\mathbf{r}-\mathbf{r}') + \int K(\mathbf{r},\mathbf{r}'')\chi(\mathbf{r}'',\mathbf{r}')\mathrm{d}\mathbf{r}'' \tag{1.58}$$

The relation between the first-order derivatives of the self-consistent screened Kohn-Sham effective potential and the density reads:

$$\begin{aligned}\frac{\partial n(\mathbf{r})}{\partial u_s^\alpha(\mathbf{q})} &= \int \chi_{\mathbf{q}}^0(\mathbf{r},\mathbf{r}')\frac{\partial V_{\mathrm{KS}}(\mathbf{r}')}{\partial u_s^\alpha(\mathbf{q})}\mathrm{d}\mathbf{r}' \\ &= \int \chi_{\mathbf{q}}^0(\mathbf{r},\mathbf{r}')\left(\frac{\partial V_{\mathrm{ext}}(\mathbf{r}')}{\partial u_s^\alpha(\mathbf{q})} + K(\mathbf{r},\mathbf{r}')\frac{\partial n(\mathbf{r}')}{\partial u_s^\alpha(\mathbf{q})}\right)\mathrm{d}\mathbf{r}',\end{aligned} \tag{1.59}$$

where $\chi_{\mathbf{q}}^0(\mathbf{r},\mathbf{r}') = \chi_{\mathbf{q}}^0(\mathbf{r},\mathbf{r}',\omega=0)$ is the static, i.e. frequency-independent, density-response function of the system of non-interacting electrons to any external perturbation of momentum $\mathbf{q}$. Within DFT, the non-interacting density-response function is easily derived from standard first-order time-independent perturbation theory in terms of the Kohn-Sham single-electron states [81]:

$$\begin{aligned}\chi_{\mathbf{q}}^0(\mathbf{r},\mathbf{r}',\omega) = \frac{1}{N_{\mathbf{k}}}\sum_{\mathbf{k}}^{1\mathrm{BZ}}\sum_{mn}\frac{f(\varepsilon_{\mathbf{k}n}) - f(\varepsilon_{\mathbf{k}+\mathbf{q}m})}{\varepsilon_{\mathbf{k}n} - \varepsilon_{\mathbf{k}+\mathbf{q}m} + \omega + i\eta}\times \\ \big(\psi_{\mathbf{k}n}(\mathbf{r})\big)^*\psi_{\mathbf{k}+\mathbf{q}m}(\mathbf{r})\big(\psi_{\mathbf{k}+\mathbf{q}m}(\mathbf{r}')\big)^*\psi_{\mathbf{k}n}(\mathbf{r}'),\end{aligned} \tag{1.60}$$

where η is a positive real infinitesimal. Substituting Eq. 1.59 in Eq. 1.53 and using the relation in Eq. 1.56, we obtain an additional expression for the

dynamical matrix in which $\chi^0_{\mathbf{q}}(\mathbf{r},\mathbf{r}')$ appears explicitly:

$$D^{\alpha\alpha'}_{ss'}(\mathbf{q}) = \frac{1}{\sqrt{M_s M_{s'}}}\Bigg[\iint\left(\frac{\partial V_{\mathrm{KS}}(\mathbf{r}')}{\partial u^{\alpha}_{s}(\mathbf{q})}\right)^{*}\left(\chi^0_{\mathbf{q}}(\mathbf{r},\mathbf{r}')\right)^{*}\frac{\partial V_{\mathrm{KS}}(\mathbf{r})}{\partial u^{\alpha'}_{s'}(\mathbf{q})}\mathrm{d}\mathbf{r}\mathrm{d}\mathbf{r}' - \iint\left(\frac{\partial n(\mathbf{r})}{\partial u^{\alpha}_{s}(\mathbf{q})}\right)^{*}K(\mathbf{r},\mathbf{r}')\frac{\partial n(\mathbf{r}')}{\partial u^{\alpha'}_{s'}(\mathbf{q})}\mathrm{d}\mathbf{r}\mathrm{d}\mathbf{r}' + \int n(\mathbf{r})\frac{\partial^2 V_{\mathrm{ext}}(\mathbf{r})}{\left(\partial u^{\alpha}_{s}(\mathbf{q})\right)^{*}\partial u^{\alpha'}_{s'}(\mathbf{q})}\mathrm{d}\mathbf{r} + \frac{\partial^2 E_{\mathrm{ion}}}{\left(\partial u^{\alpha}_{s}(\mathbf{q})\right)^{*}\partial u^{\alpha'}_{s'}(\mathbf{q})}\Bigg]_{u=0}. \tag{1.61}$$

From the first term on the right-hand side of Eq. 1.61, it is clear that the adiabatic dynamical matrix in Eq. 1 is valid as long as a electronic static-screening of lattice vibrations is similar to the response function at typical phonon frequencies, i.e. $\chi^0_{\mathbf{q}}(\mathbf{r},\mathbf{r}',\omega) \approx \chi^0_{\mathbf{q}}(\mathbf{r},\mathbf{r}')$. In other words, adiabatic phonons are valid as long as the phonon-mediated electronic transition energies between occupied and empty states are much greater than the vibrational frequencies themselves, i.e. $|\varepsilon_{\mathbf{k}n} - \varepsilon_{\mathbf{k}+\mathbf{q}m}| \gg \omega$ in Eq. 1.60.

By combining Eq. 1.54 and 1.59, we obtain an explicit expression for calculating the interacting density-response function in terms of the Hartree and exchange-correlation kernel and the non-interacting density-response function:

$$\chi_{\mathbf{q}}(\mathbf{r},\mathbf{r}') = \chi^0_{\mathbf{q}}(\mathbf{r},\mathbf{r}') + \iint \chi^0_{\mathbf{q}}(\mathbf{r},\mathbf{r}'')K(\mathbf{r}'',\mathbf{r}''')\chi_{\mathbf{q}}(\mathbf{r}''',\mathbf{r}')\mathrm{d}\mathbf{r}''\mathrm{d}\mathbf{r}''', \tag{1.62}$$

or equivalently:

$$\left[\chi_{\mathbf{q}}(\mathbf{r},\mathbf{r}')\right]^{-1} = \left[\chi^0_{\mathbf{q}}(\mathbf{r},\mathbf{r}')\right]^{-1} - K(\mathbf{r},\mathbf{r}'). \tag{1.63}$$

In the same way, combining Eq. 1.56 and 1.59, we obtain an explicit expression for calculating the dielectric function in terms of the Hartree and exchange-correlation kernel and the non-interacting density-response function:

$$\epsilon_{\mathbf{q}}(\mathbf{r},\mathbf{r}') = \delta(\mathbf{r},\mathbf{r}') - \int K(\mathbf{r},\mathbf{r}'')\chi^0_{\mathbf{q}}(\mathbf{r}'',\mathbf{r}')\mathrm{d}\mathbf{r}''. \tag{1.64}$$

Thus, in order to find $\chi_{\mathbf{q}}(\mathbf{r},\mathbf{r}')$ and $\epsilon_{\mathbf{q}}(\mathbf{r},\mathbf{r}')$, one can calculate $\chi^0_{\mathbf{q}}(\mathbf{r},\mathbf{r}')$ by means of Eq. 1.60 and afterwards solve the matrix equations in Eq. 1.62 and Eq. 1.64, respectively. This method is historically known within the microscopic theory of lattice dynamics as the dielectric approach [100, 115–117] and has been successfully applied in several simple metals [118–121]. The great advantage of this procedure is that all the information needed for computing the dynamical matrix comes already from a single self-consistent first principles DFT calculation. Still, the calculation of the interacting density-response function and the dielectric function is typically highly expensive and time consuming, since it requires the inversion of large matrices

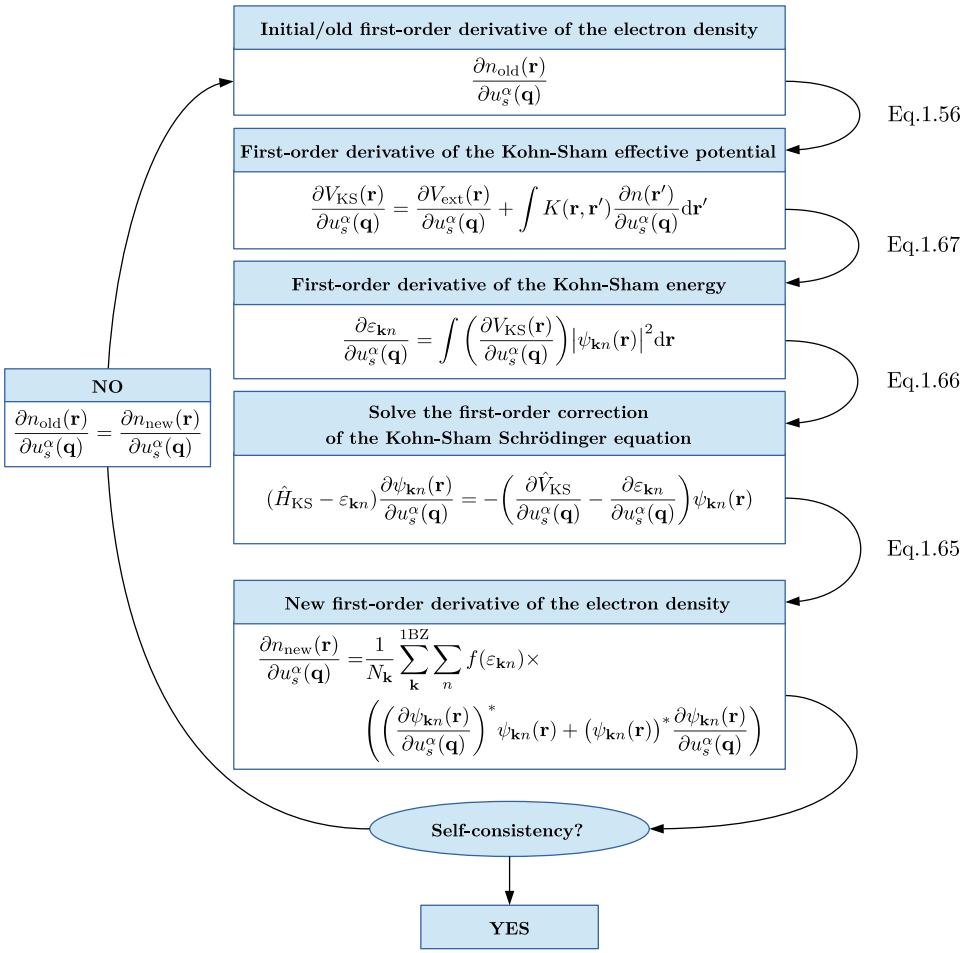

Figure 1.2. Schematic representation of the self-consistent loop for solving the set of Sternheimer equations in Eqs. 1.56 and 1.65-1.67.

in Eq. 1.63 for each momentum $\mathbf{q}$, as well as the convergence of the non-interacting density-response function in Eq. 1.60, which involves an expensive sum over unoccupied bands within the 1BZ.

1.4.4 Density functional perturbation theory

An alternative method to overcome these drawbacks is the density functional perturbation theory (DFPT) [30–33, 122, 123]. Within this formalism, one actually only needs the knowledge of the occupied Kohn-Sham electronic structure in order to self-consistently solve the set of the so-called Sternheimer equations. In this way, despite of evaluating perturbed quantities, the computational cost of determining the density-response to a single perturbation is of the same order as that needed to calculate the unperturbed ground-state density.

Regarding Eq. 1.24, the first-order derivative of the electron density with respect to the ionic displacements can be written in terms of the Kohn-Sham wave functions and their first-order derivatives as follows:

$$\frac{\partial n(\mathbf{r})}{\partial u_s^\alpha(\mathbf{q})} = \frac{1}{N_\mathbf{k}} \sum_{\mathbf{k}}^{1\mathrm{BZ}} \sum_n f(\varepsilon_{\mathbf{k}n}) \times \left(\left(\frac{\partial \psi_{\mathbf{k}n}(\mathbf{r})}{\partial u_s^\alpha(\mathbf{q})} \right)^* \psi_{\mathbf{k}n}(\mathbf{r}) + \left(\psi_{\mathbf{k}n}(\mathbf{r})\right)^* \frac{\partial \psi_{\mathbf{k}n}(\mathbf{r})}{\partial u_s^\alpha(\mathbf{q})} \right). \tag{1.65}$$

Within perturbation theory [106], the first-order derivatives of the Kohn-Sham wave functions are determined by the first-order correction of the Kohn-Sham Schrödinger equation in Eq. 1.13:

$$(\hat{H}_{\mathrm{KS}} - \varepsilon_{\mathbf{k}n}) \frac{\partial \psi_{\mathbf{k}n}(\mathbf{r})}{\partial u_s^\alpha(\mathbf{q})} = -\left(\frac{\partial \hat{V}_{\mathrm{KS}}}{\partial u_s^\alpha(\mathbf{q})} - \frac{\partial \varepsilon_{\mathbf{k}n}}{\partial u_s^\alpha(\mathbf{q})} \right) \psi_{\mathbf{k}n}(\mathbf{r}), \tag{1.66}$$

where the first-order derivative of the Kohn-Sham energy reads:

$$\frac{\partial \varepsilon_{\mathbf{k}n}}{\partial u_s^\alpha(\mathbf{q})} = \left\langle \psi_{\mathbf{k}n} \middle| \frac{\partial \hat{V}_{\mathrm{KS}}}{\partial u_s^\alpha(\mathbf{q})} \middle| \psi_{\mathbf{k}n} \right\rangle = \int \left(\frac{\partial V_{\mathrm{KS}}(\mathbf{r})}{\partial u_s^\alpha(\mathbf{q})} \right) \left| \psi_{\mathbf{k}n}(\mathbf{r}) \right|^2 \mathrm{d}\mathbf{r}, \tag{1.67}$$

and the first-order derivative of the Kohn-Sham potential is obtained by means of Eq. 1.56, which actually depends on the first-order derivative of the electron density.

Eqs. 1.65-1.67, together with Eq. 1.56, compose the set of Sternheimer equations for the perturbed Kohn-Sham system. The latter has to be solved self-consistently through an efficient numerical iterative procedure [30–33, 122–124] in order to calculate the first-order derivatives of the electron density, or equivalently those of the Kohn-Sham potential, with respect to the ionic displacements. Figure 1.2 illustrates schematically the self-consistent loop for solving the set of Sternheimer equations, in clear analogy with the self-consistent loop for solving the set of Kohn-Sham equations in Fig. 1.1 for the unperturbed case.

Chapter 2

Electron-phonon interaction from first principles

The theoretical formalism presented in Chapter 1 is insufficient for describing several physical phenomena observed in experiments. In particular, the coupling between electrons and phonons, i.e. the electron-phonon interaction, plays a crucial role in the charge transport and the thermodynamical properties of solids, among which superconductivity stands out [2].

In this chapter, we introduce the theoretical formalism used throughout this thesis for calculating several physical properties related to the electron-phonon interaction in solids from first principles. Indeed, the electron-phonon Hamiltonian appears as the natural first step when going beyond the adiabatic approximation in Sec. 2.1, and is derived from the ground-state electronic structure given by DFT and the lattice vibrational structure given by DFPT. By means of many-body perturbation theory based on Green's functions together with some additional approximations, in Sec. 2.2 we derive practical first principles expressions for calculating the electron and phonon self-energies due to the electron-phonon interaction. The effects of the electron-phonon interaction on electrons and phonons are discussed in Sec. 2.3 and 2.4, respectively. The concepts of electron and phonon quasiparticles, as well as the electron and phonon spectral functions, are also introduced. Section 2.5 is devoted to deduce from the electron and phonon self-energies all the relevant physical properties of the electron-phonon interaction that have been studied throughout this thesis. We also present the semi-empirical McMillan-Allen-Dynes formula for estimating the superconducting critical temperature of metals. Finally, in Sec. 2.6, we introduce an interpolation technique based on maximally localized Wannier functions for efficiently perform first principles calculations of the electron-phonon interaction.

2.1 Beyond the adiabatic approximation

Within the adiabatic approximation (Sec. 1.2), the non-adiabatic interaction term $\Delta\hat{H}^{\alpha\alpha'}$ has been neglected when solving the total many-body Schrödinger equation (Eq. 1.4). However, this procedure is not always totally justified [2, 5]. From Eq. 1.5, we see that $\Delta\hat{H}^{\alpha\alpha'}$ physically describes the coupling between electrons and the ionic motion, i.e. the so-called electron-phonon interaction. The right-hand side of Eq. 1.5 is composed of a first term dealing with the first-order derivatives of the electronic wave function with respect to the ionic positions and a second term dealing with the second-order derivatives. Henceforth, we limit to the first-order derivatives, which contribute at linear order in the ionic displacements, and therefore, are the important part of the electron-phonon interaction [2].

Within DFT, the ground-state system of many interacting electrons is replaced by the Kohn-Sham system of non-interacting electrons (Sec. 1.3.1). In this context, the linear-order electronic-phonon interaction in Eq. 1.5 can be easily rewritten within the second quantization formalism making use of the usual fermionic creation and annihilation operators, $\hat{c}^{\dagger}_{\mathbf{k}n}$ and $\hat{c}_{\mathbf{k}n}$, respectively, of the Kohn-Sham single-electron states [2, 5]. Thereby, the electron-phonon Hamiltonian is given by:

$$\hat{H}_{\mathrm{ep}} = \sum_{ls\alpha} \frac{1}{M_s} \sum_{\mathbf{k}\mathbf{k}'}^{1\mathrm{BZ}} \sum_{nn'} \langle \psi_{\mathbf{k}'n'} | \hat{P}^{\alpha}_{ls} | \psi_{\mathbf{k}n} \rangle \, \hat{c}^{\dagger}_{\mathbf{k}'n'} \hat{c}_{\mathbf{k}n} \hat{P}^{\alpha}_{ls}. \tag{2.1}$$

In order to get a non-vanishing contribution in Eq. 2.1, we need to explicitly take into account that the Kohn-Sham electron states are perturbed when the ions are displaced from their equilibrium positions. Within standard time-independent perturbation theory, the perturbed Kohn-Sham states are linearly expanded as: $|\psi_{\mathbf{k}n}\rangle + |\Delta\psi_{\mathbf{k}n}\rangle$, with $|\psi_{\mathbf{k}n}\rangle$ the unperturbed Kohn-Sham states and $|\Delta\psi_{\mathbf{k}n}\rangle$ the corresponding first-order corrections given by [106]:

$$|\Delta\psi_{\mathbf{k}n}\rangle = \sum_{\mathbf{k}''\neq\mathbf{k}}^{1\mathrm{BZ}} \sum_{n''\neq n} \frac{\langle \psi_{\mathbf{k}''n''} | \Delta\hat{V}_{\mathrm{KS}} | \psi_{\mathbf{k}n} \rangle}{\varepsilon_{\mathbf{k}n} - \varepsilon_{\mathbf{k}''n''}} \, |\psi_{\mathbf{k}''n''}\rangle \,, \tag{2.2}$$

where $\Delta\hat{V}_{\mathrm{KS}}$ is the first-order correction to the Kohn-Sham potential in terms of the ionic displacements with respect to their equilibrium positions:

$$\Delta V_{\mathrm{KS}} = \sum_{ls\alpha} \frac{\partial V_{\mathrm{KS}}}{\partial u^{\alpha}_{ls}} u^{\alpha}_{ls}. \tag{2.3}$$

It is worth noting that a static, i.e. frequency-independent, definition has been adopted for the change in the Kohn-Sham potential when accounting for the first-order change in the Kohn-Sham states in Eq. 2.2. This is

indeed a reminiscence of the adiabatic approximation, where only electrostatic fields are assumed. In fact, a proper definition of the electron-phonon interaction should include a dynamic, i.e. frequency-dependent, change in the Kohn-Sham potential by means of a treatment within time-dependent perturbation theory. Nevertheless, this is computationally not practical for first-principles calculations, and hence, a frequency-independent formalism is followed for the derivation of the coupling functions. Recalling that the momentum operator reads as: $P_{ls}^{\alpha} = -i(\partial/\partial\hat{u}_{ls}^{\alpha})$ and using Eqs. 2.2 and 2.3, it is straightforward to see that the matrix element in Eq. 2.1 can be rewritten as follows:

$$\langle\psi_{\mathbf{k}'n'}|\hat{P}_{ls}^{\alpha}|\psi_{\mathbf{k}n}\rangle = -i\left\langle\psi_{\mathbf{k}'n'}\left|\frac{\partial}{\partial\hat{u}_{ls}^{\alpha}}\right|\Delta\psi_{\mathbf{k}n}\right\rangle = -i\frac{\left\langle\psi_{\mathbf{k}'n'}\left|\frac{\partial\hat{V}_{\mathrm{KS}}}{\partial u_{ls}^{\alpha}}\right|\Delta\psi_{\mathbf{k}n}\right\rangle}{\varepsilon_{\mathbf{k}n}-\varepsilon_{\mathbf{k}'n'}}. \quad (2.4)$$

Plugging Eq. 2.4 into Eq. 2.1 and using the Fourier transform of the ionic momentum operator in terms of the bosonic ladder operators for each phonon mode $|\mathbf{q}\nu\rangle$ in Eq. 1.45 [6], we arrive to a Fröhlich-like reformulation of the electron-phonon Hamiltonian as follows [2, 5]:

$$\hat{H}_{\mathrm{ep}} = \frac{1}{\sqrt{N_{\mathbf{q}}}}\sum_{\mathbf{kq}}^{1\mathrm{BZ}}\sum_{mn\nu} g_{mn}^{\nu}(\mathbf{k},\mathbf{q})\hat{c}_{\mathbf{k}+\mathbf{q}m}^{\dagger}\hat{c}_{\mathbf{k}n}(\hat{a}_{\mathbf{q}\nu}+\hat{a}_{-\mathbf{q}\nu}^{\dagger}). \quad (2.5)$$

In this form, it is easy to see that the electron-phonon Hamiltonian describes the emission or absorption of phonon modes by the relaxation or excitation, respectively, of electron-hole pairs. The self-consistent static-screened electron-phonon matrix element in Eq. 2.5 is given by [2]:

$$g_{mn}^{\nu}(\mathbf{k},\mathbf{q}) = \sum_{s\alpha}\frac{\epsilon_{\mathbf{q}\nu}^{s\alpha}}{\sqrt{2M_s\omega_{\mathbf{q}\nu}}}g_{mn}^{s\alpha}(\mathbf{k},\mathbf{q}), \quad (2.6)$$

where the self-consistent static-screened potential-change matrix element is defined as [2]:

$$g_{mn}^{s\alpha}(\mathbf{k},\mathbf{q}) = \sum_{l} e^{i\mathbf{q}\cdot\mathbf{T}_l}\left\langle\psi_{\mathbf{k}+\mathbf{q}m}\left|\frac{\partial\hat{V}_{\mathrm{KS}}}{\partial u_{ls}^{\alpha}}\right|\psi_{\mathbf{k}n}\right\rangle = \left\langle\psi_{\mathbf{k}+\mathbf{q}m}\left|\frac{\partial\hat{V}_{\mathrm{KS}}}{\partial u_{s}^{\alpha}(\mathbf{q})}\right|\psi_{\mathbf{k}n}\right\rangle. \quad (2.7)$$

The electron-phonon matrix element in Eq. 2.6 gives the probability amplitude for effectively scattering an electron from the Kohn-Sham state $|\psi_{\mathbf{k}n}\rangle$ to the Kohn-Sham state $|\psi_{\mathbf{k}+\mathbf{q}m}\rangle$ via the absorption of a phonon mode $|\mathbf{q}\nu\rangle$ and the emission of a phonon mode $|-\mathbf{q}\nu\rangle$, as shown in Figs. 2.1(a) and (b), respectively. This magnitude has physical dimensions of energy. The potential change matrix element in Eq. 2.7 describes the strength of the effective coupling between the Kohn-Sham electron states $|\psi_{\mathbf{k}n}\rangle$ and $|\psi_{\mathbf{k}+\mathbf{q}m}\rangle$ via the change in the Kohn-Sham potential due to the ionic displacement

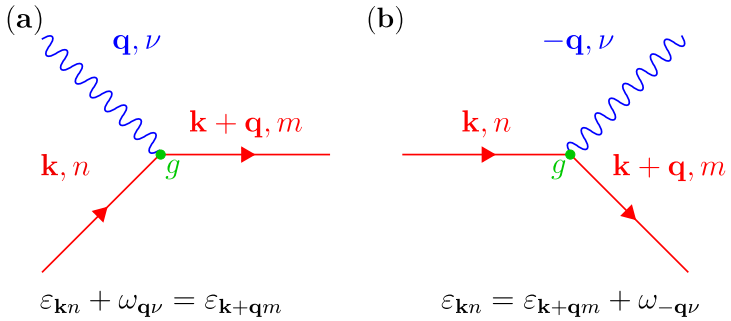

Figure 2.1. Diagrams that represent the vertex interactions of $\hat{H}_{\text{ep}}$ in Eq. 2.5. The time evolution is depicted from left to right. Straight red and wavy blue lines represent electrons and phonons, respectively. The green dot represents the electron-phonon matrix element $g = g^{\nu}_{mn}(\mathbf{k}, \mathbf{q})$ in Eq. 2.6. In the phonon absorption diagram (a) energy conservation requires $\varepsilon_{\mathbf{k}n} + \omega_{\mathbf{q}\nu} = \varepsilon_{\mathbf{k}+\mathbf{q}m}$, while in the phonon emission diagram (b) $\varepsilon_{\mathbf{k}n} = \varepsilon_{\mathbf{k}+\mathbf{q}m} + \omega_{-\mathbf{q}\nu}$. Momentum conservation is also satisfied for each case.

$u^{\alpha}_{s}(\mathbf{q})$ for a lattice distortion of momentum $\mathbf{q}$. This magnitude has physical dimensions of energy per length.

All the ingredients needed for calculating the electron-phonon matrix elements in Eq. 2.6, and therefore, for constructing the electron-phonon Hamiltonian $\hat{H}_{\text{ep}}$ in Eq. 2.5, are directly available from state-of-the-art self-consistent first principles calculations based on DFT (Sec. 1.3.1) and DFPT (Sec. 1.4.4). Although the matrix elements are not directly probed magnitudes from experiment, they are essential for the definition of all the measurable physical properties related to the electron-phonon interaction.

2.2 From a many-body formalism to practical expressions

The electron-phonon interaction affects both the electronic and lattice vibrational structures of the system, which in turn modify the electron-phonon interaction itself [2]. The effects due to the electron-phonon interaction are self-consistently taken into account by means of many-body perturbation theory based on Green's functions [5]. Within this formalism, the poles of the resulting functions define the so-called elementary excitations or quasiparticles of the system [5], i.e. dressed particles with renormalized energies and finite lifetimes due to many-body interactions. In this regard, the interacting particle Green's function is obtained from the non-interacting particle Green's function[1] and the so-called particle self-energy via the Dyson's equa-

[1] In literature, the interacting particle Green's function is also known as the dressed or perturbed particle Green's function. The non-interacting particle Green's function is also known as the bare or unperturbed particle Green's function.

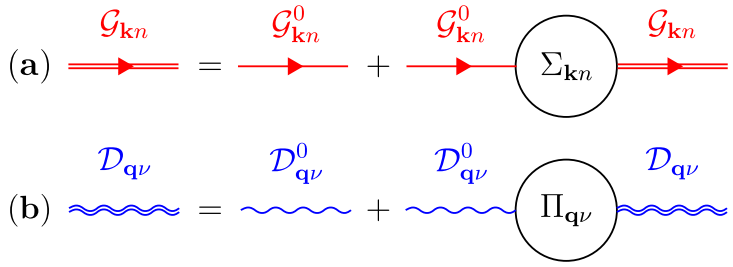

Figure 2.2. Diagrammatic representation of the Dyson's equation for (a) electrons in Eq. 2.8 and (b) phonons in Eq. 2.9. The double straight red and wavy blue lines represent the interacting electron and phonon Green's functions, $\mathcal{G}_{\mathbf{k}n}$ and $\mathcal{D}_{\mathbf{q}\nu}$, respectively. The single straight red and wavy blue lines represent the non-interacting electron and phonon Green's functions, $\mathcal{G}^0_{\mathbf{k}n}$ and $\mathcal{D}^0_{\mathbf{q}\nu}$, respectively.

tion [2, 5]. The self-energy is the key magnitude in the many-body Green's function perturbation theory. It encodes all the information of the many-body effects on the particle absent in the non-interacting Green's function. For electrons, the Dyson's equation reads as:

$$\mathcal{G}_{\mathbf{k}n}(\omega) = \mathcal{G}^0_{\mathbf{k}n}(\omega) + \mathcal{G}^0_{\mathbf{k}n}(\omega)\Sigma_{\mathbf{k}n}(\omega)\mathcal{G}_{\mathbf{k}n}(\omega), \tag{2.8}$$

or equivalently: $\left(\mathcal{G}_{\mathbf{k}n}(\omega)\right)^{-1} = \left(\mathcal{G}^0_{\mathbf{k}n}(\omega)\right)^{-1} - \Sigma_{\mathbf{k}n}(\omega)$, where $\mathcal{G}_{\mathbf{k}n}(\omega)$ and $\mathcal{G}^0_{\mathbf{k}n}(\omega)$ are the interacting and non-interacting electron Green's functions, respectively, and $\Sigma_{\mathbf{k}n}(\omega)$ is the electron self-energy. In the same way, for phonons, the Dyson's equation reads as:

$$\mathcal{D}_{\mathbf{q}\nu}(\omega) = \mathcal{D}^0_{\mathbf{q}\nu}(\omega) + \mathcal{D}^0_{\mathbf{q}\nu}(\omega)\Pi_{\mathbf{q}\nu}(\omega)\mathcal{D}_{\mathbf{q}\nu}(\omega), \tag{2.9}$$

or equivalently: $\left(\mathcal{D}_{\mathbf{q}\nu}(\omega)\right)^{-1} = \left(\mathcal{D}^0_{\mathbf{q}\nu}(\omega)\right)^{-1} - \Pi_{\mathbf{q}\nu}(\omega)$, where $\mathcal{D}_{\mathbf{q}\nu}(\omega)$ and $\mathcal{D}^0_{\mathbf{q}\nu}(\omega)$ are the interacting and non-interacting phonon Green's functions, respectively, and $\Pi_{\mathbf{q}\nu}(\omega)$ is the phonon self-energy. The diagrammatic representations of Eqs. 2.8 and 2.9 are shown in Figs. 2.2(a) and (b), respectively.

Throughout this work, only the diagonal elements, $n = n'$ in Eq. 2.8 and $\nu = \nu'$ in Eq. 2.9, have been retained for the evaluation of the electron and phonon self-energy matrices, respectively, and hence for the interacting electron and phonon Green's function matrices, respectively. We therefore neglect off-diagonal terms, $n \neq n'$ in Eq. 2.8 and $\nu \neq \nu'$ in Eq. 2.9, which is equivalent to disregarding any coupling and any hybridization between different non-interacting electronic bands or different non-interacting phonon branches. In this way, the interacting electrons maintain the orbital character of the non-interacting electrons, as well as the interacting phonons maintain the polarization of the non-interacting phonon mode, but both with renormalized properties. This is a rather common procedure in the

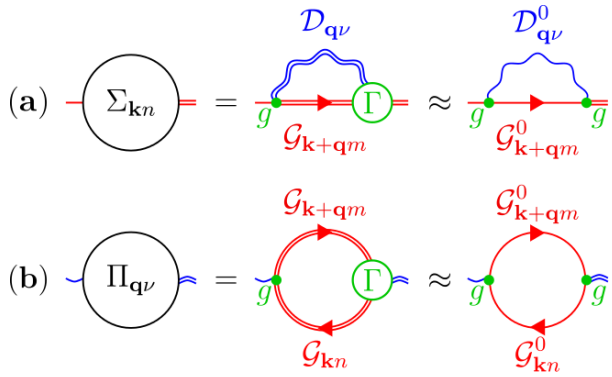

Figure 2.3. Diagrammatic representation of (a) the electron self-energy and (b) the phonon self-energy using Feynman rules [5, 21]. They are shown in their exact form, and within the Migdal's approximation ($\Gamma \approx g$) [125] together with the substitution of the interacting Green's functions by their non-interacting counterparts, $\mathcal{G}_{\mathbf{k}n}(\omega) \approx \mathcal{G}^0_{\mathbf{k}n}(\omega)$ and $\mathcal{D}_{\mathbf{k}n}(\omega) \approx \mathcal{D}^0_{\mathbf{k}n}(\omega)$, respectively. The green dot represents the electron-phonon coupling first-order vertex function, equivalent to the electron-phonon matrix element $g = g^{\nu}_{mn}(\mathbf{k}, \mathbf{q})$ in Eq. 2.6. In turn, the open green circle represents the electron-phonon full vertex function $\Gamma = \Gamma^{\nu}_{mn}(\mathbf{k}, \mathbf{q}, \omega, \omega')$, which accounts for the infinite number of Feynman diagrams.

literature [4] and a safe approximation as demonstrated in practical calculations.

In the absence of many-body interactions, the electronic system is in its ground state, which is obtained by means of self-consistent first principles DFT calculations. The well-known temperature-dependent expression of the so-called retarded Green's function for a non-interacting electron in the Kohn-Sham state $|\psi_{\mathbf{k}n}\rangle$ is defined as the simple pole at the infinitely long-lived Kohn-Sham energy $\varepsilon_{\mathbf{k}n}$ [2, 5, 21]:

$$\mathcal{G}^0_{\mathbf{k}n}(\omega) = \lim_{\eta \to 0^+} \frac{f(\varepsilon_{\mathbf{k}n})}{\omega - \varepsilon_{\mathbf{k}n} - i\eta} + \frac{1 - f(\varepsilon_{\mathbf{k}n})}{\omega - \varepsilon_{\mathbf{k}n} + i\eta}, \tag{2.10}$$

where η is a positive real infinitesimal. Similarly, the lattice vibrational structure is obtained by means of self-consistent first principles DFPT calculations. The well-known temperature-dependent expression of the retarded non-interacting Green's function for a phonon mode $|\mathbf{q}\nu\rangle$ is defined in terms of the infinitely long-lived adiabatic phonon frequency $\omega_{\mathbf{q}\nu}$ [2, 5, 21]:

$$\mathcal{D}^0_{\mathbf{q}\nu}(\omega) = \lim_{\eta \to 0^+} 2\omega_{\mathbf{q}\nu} \left(\frac{1 + n_{\mathrm{B}}(\omega_{\mathbf{q}\nu})}{\omega^2 - (\omega_{\mathbf{q}\nu} - i\eta)^2} - \frac{n_{\mathrm{B}}(\omega_{\mathbf{q}\nu})}{\omega^2 - (\omega_{\mathbf{q}\nu} + i\eta)^2} \right), \tag{2.11}$$

Plugging Eq. 2.10 and Eq. 2.11 into Eq. 2.8 and Eq. 2.9, respectively, and taking $\eta = 0$, the interacting electron and phonon Green's functions are defined as:

$$\mathcal{G}_{\mathbf{k}n}(\omega) = \frac{1}{\omega - \varepsilon_{\mathbf{k}n} - \Sigma_{\mathbf{k}n}(\omega)}, \tag{2.12}$$

and:

$$\mathcal{D}_{\mathbf{q}\nu}(\omega) = \frac{2\omega_{\mathbf{q}\nu}}{\omega^2 - \omega_{\mathbf{q}\nu}^2 - 2\omega_{\mathbf{q}\nu}\Pi_{\mathbf{q}\nu}(\omega)}, \tag{2.13}$$

respectively. Regarding the electron and phonon self-energies, their expressions can be derived by examining their diagrammatic representations in Figs. 2.3(a) and (b), respectively, following the standard Feynman rules [5, 21]. The electron and phonon self-energies are formally written as [5]:

$$\begin{aligned}\Sigma_{\mathbf{k}n}(\omega) = \frac{i}{N_{\mathbf{q}}}\sum_{\mathbf{q}}^{1\mathrm{BZ}}\sum_{m\nu}\int\frac{\mathrm{d}\omega'}{2\pi}\left(g_{mn}^{\nu}(\mathbf{k},\mathbf{q},\omega)\right)^{*}\mathcal{G}_{\mathbf{k}+\mathbf{q}m}(\omega+\omega') \\ \times\,\mathcal{D}_{\mathbf{q}\nu}(\omega')\Gamma_{mn}^{\nu}(\mathbf{k},\mathbf{q},\omega,\omega'),\end{aligned} \tag{2.14}$$

and:

$$\begin{aligned}\Pi_{\mathbf{q}\nu}(\omega) = -\frac{i}{N_{\mathbf{k}}}\sum_{\mathbf{k}}^{1\mathrm{BZ}}\sum_{mn}\int\frac{\mathrm{d}\omega'}{2\pi}\left(g_{mn}^{*\nu}(\mathbf{k},\mathbf{q},\omega)\right)^{*}\mathcal{G}_{\mathbf{k}+\mathbf{q}m}(\omega+\omega') \\ \times\,\mathcal{G}_{\mathbf{k}n}(\omega')\Gamma_{mn}^{\nu}(\mathbf{k},\mathbf{q},\omega,\omega'),\end{aligned} \tag{2.15}$$

respectively, where $\Gamma_{mn}^{\nu}(\mathbf{k},\mathbf{q},\omega,\omega')$ is the electron-phonon full vertex function, containing the infinite series of Feynman diagrams. In what follows, $\Sigma_{\mathbf{k}n}(\omega)$ will refer to the electron self-energy function and $\Pi_{\mathbf{q}\nu}(\omega)$ to the phonon self-energy function.

The latter function can be separated into the sum of the lowest first-order vertex diagram, which is described by the linear electron-phonon matrix element $g_{mn}^{\nu}(\mathbf{k},\mathbf{q})$ in Eq. 2.6 containing a single-phonon process (Fig. 2.1), and the additional vertex correction term that comprises all the infinite higher-order vertex diagrams containing multi-phonon processes [2, 5]. Migdal argued that the corrections induced by the higher-order vertex terms in $\Gamma_{mn}^{\nu}(\mathbf{k},\mathbf{q},\omega,\omega')$ are small, of the order of $1/\sqrt{M_I}$ for normal metals [125]. Therefore, a widely used approximation in Eqs. 2.14 and 2.15 is to neglect higher-order vertex corrections and directly substitute $\Gamma_{mn}^{\nu}(\mathbf{k},\mathbf{q},\omega,\omega')$ by $g_{mn}^{\nu}(\mathbf{k},\mathbf{q})$. Besides, for practical reasons, it is common to substitute the interacting electron and phonon Green's functions by their non-interacting counterparts. These approaches lead then to the following expressions for the electron and phonon self-energies [2, 4, 5]:

$$\Sigma_{\mathbf{k}n}(\omega) = \frac{i}{N_{\mathbf{q}}}\sum_{\mathbf{q}}^{1\mathrm{BZ}}\sum_{m\nu}\left|g_{mn}^{\nu}(\mathbf{k},\mathbf{q})\right|^2\int\frac{\mathrm{d}\omega'}{2\pi}\mathcal{G}_{\mathbf{k}+\mathbf{q}m}^{0}(\omega+\omega')\mathcal{D}_{\mathbf{q}\nu}^{0}(\omega'), \tag{2.16}$$

and:

$$\Pi_{\mathbf{q}\nu}(\omega) = -\frac{i}{N_{\mathbf{k}}}\sum_{\mathbf{k}}^{1\mathrm{BZ}}\sum_{mn}\left|g_{mn}^{\nu}(\mathbf{k},\mathbf{q})\right|^2\int\frac{\mathrm{d}\omega'}{2\pi}\mathcal{G}_{\mathbf{k}+\mathbf{q}n}^{0}(\omega+\omega')\mathcal{G}_{\mathbf{k}m}^{0}(\omega'). \tag{2.17}$$

In order to find practical expressions for the electron and phonon self-energies, we can use Eqs. 2.10 and 2.11 in Eqs. 2.16 and 2.17, respectively, and performed the corresponding integrations in the complex plane [21]. Thereby, we find the extensively used temperature-dependent practical expressions for the so-called retarded electron and phonon self-energies due to the electron-phonon interaction [2, 4, 5]:

$$\Sigma_{\mathbf{k}n}(\omega) = \lim_{\eta\to 0^+} \frac{1}{N_{\mathbf{q}}} \sum_{\mathbf{q}}^{1\mathrm{BZ}} \sum_{m\nu} \left|g^{\nu}_{mn}(\mathbf{k},\mathbf{q})\right|^2 \times \left(\frac{1 - f(\varepsilon_{\mathbf{k}+\mathbf{q}m}) + n_{\mathrm{B}}(\omega_{\mathbf{q}\nu})}{\omega - \varepsilon_{\mathbf{k}+\mathbf{q}m} - \omega_{\mathbf{q}\nu} + i\eta} + \frac{f(\varepsilon_{\mathbf{k}+\mathbf{q}m}) + n_{\mathrm{B}}(\omega_{\mathbf{q}\nu})}{\omega - \varepsilon_{\mathbf{k}+\mathbf{q}m} + \omega_{\mathbf{q}\nu} + i\eta} \right), \tag{2.18}$$

and:

$$\Pi_{\mathbf{q}\nu}(\omega) = \lim_{\eta\to 0^+} \frac{1}{N_{\mathbf{k}}} \sum_{\mathbf{k}}^{1\mathrm{BZ}} \sum_{mn} \left|g^{\nu}_{mn}(\mathbf{k},\mathbf{q})\right|^2 \left(\frac{f(\varepsilon_{\mathbf{k}n}) - f(\varepsilon_{\mathbf{k}+\mathbf{q}m})}{\varepsilon_{\mathbf{k}n} - \varepsilon_{\mathbf{k}+\mathbf{q}m} + \omega + i\eta} \right). \tag{2.19}$$

In Eqs. 2.18 and 2.19, the sign in the imaginary infinitesimal on the denominators indicates that these functions are actually retarded, i.e. they have all poles below the real axis. In addition, the retarded electron and phonon self-energies have to satisfy causality, and therefore, their real and imaginary parts are related by Kramers-Kronig relations [2, 5]:

$$\begin{aligned} \mathrm{Re}\Sigma_{\mathbf{k}n}(\omega) &= -\frac{1}{\pi} \int_{-\infty}^{\infty} \frac{\mathrm{Im}\Sigma_{\mathbf{k}n}(\omega')}{\omega - \omega'} \mathrm{d}\omega' \\ \mathrm{Im}\Sigma_{\mathbf{k}n}(\omega) &= \frac{1}{\pi} \int_{-\infty}^{\infty} \frac{\mathrm{Re}\Sigma_{\mathbf{k}n}(\omega')}{\omega - \omega'} \mathrm{d}\omega'. \end{aligned} \tag{2.20}$$

and:

$$\begin{aligned} \mathrm{Re}\Pi_{\mathbf{q}\nu}(\omega) &= -\frac{1}{\pi} \int_{-\infty}^{\infty} \frac{\mathrm{Im}\Pi_{\mathbf{q}\nu}(\omega')}{\omega - \omega'} \mathrm{d}\omega' \\ \mathrm{Im}\Pi_{\mathbf{q}\nu}(\omega) &= \frac{1}{\pi} \int_{-\infty}^{\infty} \frac{\mathrm{Re}\Pi_{\mathbf{q}\nu}(\omega')}{\omega - \omega'} \mathrm{d}\omega'. \end{aligned} \tag{2.21}$$

Before concluding with this section, it is important to note that the non-interacting phonon modes are calculated by diagonalizing the dynamical matrix in Eq. 1.53, which already accounts for the static response of the electron density to the ionic motion, i.e. the static effects of the electron-phonon interaction. The importance of this detail is better understood from examining the double integral in the first term on the right-hand side of the additional expression of the dynamical matrix in Eq. 1.61, where we substitute $\chi^0_{\mathbf{q}}(\mathbf{r},\mathbf{r}')$ by the expression in Eq. 1.60, obtaining:

$$d^{\alpha\alpha'}_{ss'}(\mathbf{q}) = \frac{1}{N_{\mathbf{k}}} \sum_{\mathbf{k}}^{1\mathrm{BZ}} \sum_{mn} \left(\frac{g^{s\alpha}_{mn}(\mathbf{k},\mathbf{q})}{\sqrt{M_s}} \right)^* \frac{g^{s'\alpha'}_{mn}(\mathbf{k},\mathbf{q})}{\sqrt{M_{s'}}} \frac{f(\varepsilon_{\mathbf{k}n}) - f(\varepsilon_{\mathbf{k}+\mathbf{q}m})}{\varepsilon_{\mathbf{k}n} - \varepsilon_{\mathbf{k}+\mathbf{q}m}}. \tag{2.22}$$

Rewriting the equation above in the phonon-mode representation, i.e. the representation in which the dynamical matrix is diagonal and equal to the square of the phonon frequencies, by means of a unitary transformation:

$$\begin{aligned} d_{\nu\nu}(\mathbf{q}) &= \sum_{ss'}\sum_{\alpha\alpha'} \left(\epsilon_{\mathbf{q}\nu}^{s\alpha}\right)^* d_{ss'}^{\alpha\alpha'}(\mathbf{q}) \epsilon_{\mathbf{q}\nu}^{s'\alpha'} \\ &= \frac{2\omega_{\mathbf{q}\nu}}{N_{\mathbf{k}}} \sum_{\mathbf{k}}^{1\mathrm{BZ}} \sum_{mn} \left|g_{mn}^{\nu}(\mathbf{k},\mathbf{q})\right|^2 \left(\frac{f(\varepsilon_{\mathbf{k}n}) - f(\varepsilon_{\mathbf{k}+\mathbf{q}m})}{\varepsilon_{\mathbf{k}n} - \varepsilon_{\mathbf{k}+\mathbf{q}m}}\right) = 2\omega_{\mathbf{q}\nu}\Pi_{\mathbf{q}\nu}(0), \end{aligned} \tag{2.23}$$

we show that the first term on the right-hand side of Eq. 1.61 is directly related to the frequency-independent term of the retarded phonon self-energy in Eq. 2.19. Therefore, the latter is already included in the adiabatic description of the dynamical matrix and the phonon modes resulting from self-consistent first principles DFPT calculations that form our non-interacting phonon description (Eq. 2.11). Thus, the actual expression of the retarded phonon self-energy that correctly takes into account the effects of the electron-phonon interaction on phonons beyond the adiabatic approximation, i.e. non-adiabatic effects, is given by [4]:

$$\begin{aligned} \tilde{\Pi}_{\mathbf{q}\nu}(\omega) = \Pi_{\mathbf{q}\nu}(\omega) - \Pi_{\mathbf{q}\nu}(0) = \lim_{\eta\to 0^+} \frac{1}{N_{\mathbf{k}}} \sum_{\mathbf{k}}^{1\mathrm{BZ}} \sum_{mn} \left|g_{mn}^{\nu}(\mathbf{k},\mathbf{q})\right|^2 \times \\ \left(\frac{f(\varepsilon_{\mathbf{k}n}) - f(\varepsilon_{\mathbf{k}+\mathbf{q}m})}{\varepsilon_{\mathbf{k}n} - \varepsilon_{\mathbf{k}+\mathbf{q}m} + \omega + i\eta} - \frac{f(\varepsilon_{\mathbf{k}n}) - f(\varepsilon_{\mathbf{k}+\mathbf{q}m})}{\varepsilon_{\mathbf{k}n} - \varepsilon_{\mathbf{k}+\mathbf{q}m}}\right). \end{aligned} \tag{2.24}$$

2.3 Effects of the electron-phonon interaction on electrons

Once the retarded electron self-energy is calculated from first principles, we have immediate access to the retarded interacting electron Green's function by means of Eq. 2.12. The poles of the interacting electron Green's function determine the electron quasi-particle structure of the system, allowing to study the renormalization of the non-interacting electronic structure induced by the electron-phonon interaction. Furthermore, the spectral representation of the interacting Green's function, i.e. the electron spectral function, is an extremely useful physical magnitude, since it is experimentally accessible by means of ARPES [38].

2.3.1 Electron quasi-particles

The electron quasi-particle structure is conformed by the poles of the interacting electron Green's function in Eq. 2.12. Thus, the electron quasi-particle poles are the solutions of the following equation:

$$\omega = \varepsilon_{\mathbf{k}n} + \Sigma_{\mathbf{k}n}(\omega) = \varepsilon_{\mathbf{k}n} + \mathrm{Re}\Sigma_{\mathbf{k}n}(\omega) + i\mathrm{Im}\Sigma_{\mathbf{k}n}(\omega), \tag{2.25}$$

where it is clear that the real and imaginary parts of the electron self-energy contain all the necessary information to compute the energy renormalization and lifetime, respectively, of an electron in the Kohn-Sham state $|\psi_{\mathbf{k}n}\rangle$ with energy $\varepsilon_{\mathbf{k}n}$ propagating in a many-body system.

Although ω has been so far considered as purely real, the electron Dyson's equation in Eq. 2.25 must be self-consistently solved within the whole complex energy plane z. This is so because of the complex definition of the electron self-energy, and consequently, the energy argument and the electron quasi-particle pole itself, whose renormalized energy $E_{\mathbf{k}n}$ and linewidth $\Gamma_{\mathbf{k}n}$ can be compactly expressed as an ordinary complex number $z_{\mathbf{k}n} = E_{\mathbf{k}n} - i\Gamma_{\mathbf{k}n}$. The energies $E_{\mathbf{k}n}$ yield the band structure corrected by the electron-phonon interaction, while the linewidth $\Gamma_{\mathbf{k}n}$ is connected with the electron quasi-particle lifetime as $\tau_{\mathbf{k}n} = 1/(2\Gamma_{\mathbf{k}n})$. In order to correctly extend Eq. 2.25 into the complex energy plane, the electron self-energy needs to be considered as a complex function of complex energy, i.e. $\Sigma_{\mathbf{k}n}(z)$. Nevertheless, simply replacing real excitation energies by their complex counterparts ($\omega \to z$) usually leads to discontinuous functions across the real axis [5]. In fact, one needs to resort to the analytic continuation of these functions in order to recover mathematically meaningful expressions [21, 114, 126]. In this sense, Refs. [35, 36] proposed a scheme for solving the electron Dyson's equation within the complex plane, by first replacing $\omega \to z$ in the electron self-energy for the upper half complex plane, and then, by analytically continuing $\Sigma_{\mathbf{k}n}(z)$ from the upper to the lower half complex plane.

The electron Dyson's equation in Eq. 2.25 can be rewritten using the complex definition of the electron quasi-particle pole as a system of two coupled non-linear equations defined in the whole complex plane [35, 36]:

$$\begin{aligned} E_{\mathbf{k}n} &= \varepsilon_{\mathbf{k}n} + \mathrm{Re}\Sigma_{\mathbf{k}n}(E_{\mathbf{k}n} - i\Gamma_{\mathbf{k}n}) \\ \Gamma_{\mathbf{k}n} &= -\mathrm{Im}\Sigma_{\mathbf{k}n}(E_{\mathbf{k}n} - i\Gamma_{\mathbf{k}n}), \end{aligned} \tag{2.26}$$

where it appears obvious that the electron quasi-particle linewidth has a crucial impact on its renormalized energy, and vice versa. It is also worth noting that the equation system in Eq. 2.26 may lead to several solutions, due to the non-linear character of the self-energy function [35, 36]. In this way, one can define the first-order Laurent series expansion of the interacting electron Green's function in the vicinity of the different electron quasi-particle (qp) poles as follows:

$$\mathcal{G}^{\mathrm{qp}}_{\mathbf{k}n}(z) = \sum_j \frac{\mathbb{Z}^{(j)}_{\mathbf{k}n}}{z - z^{(j)}_{\mathbf{k}n}} = \sum_j \frac{\mathbb{Z}^{(j)}_{\mathbf{k}n}}{z - E^{(j)}_{\mathbf{k}n} + i\Gamma^{(j)}_{\mathbf{k}n}}, \tag{2.27}$$

where the index j accounts for the possibility of several electron quasi-particle states, i.e. a multiple-electron quasi-particle picture, starting from a non-interacting Kohn-Sham single-electron state $|\psi_{\mathbf{k}n}\rangle$. In Eq. 2.27, $\mathbb{Z}^{(j)}_{\mathbf{k}n}$

represents the dimensionless complex renormalization factor of the j-th electron quasi-particle state. Physically, it is related to the spectral weight of the electron quasi-particle pole. Mathematically, it is defined as the complex residue of the analytical continuation of the interacting electron Green's function $\mathcal{G}_{\mathbf{k}n}(z)$ evaluated at the complex pole $z_{\mathbf{k}n}^{(j)}$ [35, 36]. Since the electron quasi-particle pole is a first-order pole in Eq. 2.26, the renormalization factor can be directly obtained by applying the well-known simple-pole residue formula as follows:

$$\mathbb{Z}_{\mathbf{k}n}^{(j)} = \mathrm{Res}\big(\mathcal{G}_{\mathbf{k}n}(z), z_{\mathbf{k}n}^{(j)}\big) = \frac{1}{1 - \Sigma'_{\mathbf{k}n}(z_{\mathbf{k}n}^{(j)})}. \tag{2.28}$$

The most standard treatment used in literature for solving the electron Dyson's equation is to simply ignore the complex nature of the energy plane by neglecting the interplay between the electron quasi-particle energy and linewidth in Eq. 2.25 [4]. Thereby, one avoids any analytical continuation of the electron self-energy and arrives to a non-lineal equation equivalent to the Brillouin-Wigner (BW) perturbation theory method [5]. Within the above procedure, the approximate electron quasi-particle energy $E_{\mathbf{k}n}^{\mathrm{BW}}$ is obtained by self-consistently solving the real part of the electron Dyson's equation in Eq. 2.26 along the real axis and the approximate linewidth $\Gamma_{\mathbf{k}n}^{\mathrm{BW}}$ is obtained by directly evaluating the imaginary part of the electron self-energy at $E_{\mathbf{k}n}^{\mathrm{BW}}$:

$$\begin{aligned} E_{\mathbf{k}n}^{\mathrm{BW}} &= \varepsilon_{\mathbf{k}n} + \mathrm{Re}\Sigma_{\mathbf{k}n}(E_{\mathbf{k}n}^{\mathrm{BW}}) \\ \Gamma_{\mathbf{k}n}^{\mathrm{BW}} &= -\mathrm{Im}\Sigma_{\mathbf{k}n}(E_{\mathbf{k}n}^{\mathrm{BW}}). \end{aligned} \tag{2.29}$$

Note that one can also recover the most basic and non-selfconsistent Rayleigh-Schrödinger (RS) perturbation theory method [5] by replacing $E_{\mathbf{k}n}^{\mathrm{BW}} \to \varepsilon_{\mathbf{k}n}$ in the argument of the electron self-energy function in Eq. 2.29.

A popular procedure for improving the Brillouin-Wigner perturbation theory results (Eq. 2.29) is the so-called quasi-particle expansion, in which the improved approximate electron quasi-particle linewidth is defined as [4, 38]:

$$\Gamma_{\mathbf{k}n}^{\mathrm{BW}} = -\mathbb{Z}_{\mathbf{k}n}^{\mathrm{BW}} \mathrm{Im}\Sigma_{\mathbf{k}n}(E_{\mathbf{k}n}^{\mathrm{BW}}) \tag{2.30}$$

where $\mathbb{Z}_{\mathbf{k}n}^{\mathrm{BW}}$ is the real renormalization factor of the approximate electron quasi-particle state. It is defined as in Eq. 2.28 but this time only considering the derivative of the real part of the electron self-energy evaluated at $E_{\mathbf{k}n}^{\mathrm{BW}}$:

$$\mathbb{Z}_{\mathbf{k}n}^{\mathrm{BW}} = \frac{1}{1 - \mathrm{Re}\Sigma'_{\mathbf{k}n}(E_{\mathbf{k}n}^{\mathrm{BW}})}. \tag{2.31}$$

It is worth noting that there is no justification for the general use of these standard procedures, since the real and imaginary parts of the electron self-energy are usually of the same order of magnitude.

Indeed, the standard schemes are only acceptable in the limit close to the Fermi level at zero temperature, where the imaginary part of the electron self-energy, and hence, the imaginary part of the electron quasi-particle pole, vanishes (Appendix C). In this limit, Eqs. 2.26 and 2.29 are therefore equivalent. The momentum-derivative of the real part of the electron Dyson's equation accounts for the distortion of the band structure due to the electron-phonon interaction, showing that the electron quasi-particle band velocity decreases as [2]:

$$\boldsymbol{\nabla}_{\mathbf{k}} E_{\mathbf{k}n} = \boldsymbol{\nabla}_{\mathbf{k}} \varepsilon_{\mathbf{k}n} + \boldsymbol{\nabla}_{\mathbf{k}} \mathrm{Re}\Sigma_{\mathbf{k}n}(E_{\mathbf{k}n}) \rightarrow \mathbf{V}_{\mathbf{k}n} = \frac{\mathbf{v}_{\mathbf{k}n}}{1+\lambda_{\mathbf{k}n}}, \tag{2.32}$$

where $\mathbf{V}_{\mathbf{k}n} = \boldsymbol{\nabla}_{\mathbf{k}} E_{\mathbf{k}n}$ and $\mathbf{v}_{\mathbf{k}n} = \boldsymbol{\nabla}_{\mathbf{k}} \varepsilon_{\mathbf{k}n}$ are the effective band velocities of the electron quasi-particle and the non-interacting electron, respectively. This can be also interpreted as an enhancement of the electron quasi-particle band mass due to the electron-phonon interaction, given by [2]:

$$M^*_{\mathbf{k}n} = m^*_{\mathbf{k}n}(1+\lambda_{\mathbf{k}n}), \tag{2.33}$$

where $M^*_{\mathbf{k}n}$ and $m^*_{\mathbf{k}n}$ are the effective band masses of the electron quasi-particle and the non-interacting electron, respectively.

The dimensionless magnitude $\lambda_{\mathbf{k}n}$ is the so-called mass enhancement parameter or state-dependent electron-phonon coupling strength, and accounts for the distortion of the non-interacting Kohn-Sham electron state $|\psi_{\mathbf{k}n}\rangle$ close to the Fermi level due to the electron-phonon interaction. It is given by [2]:

$$\lambda_{\mathbf{k}n} = -\frac{\partial \mathrm{Re}\Sigma_{\mathbf{k}n}(\omega)}{\partial \omega}\bigg|_{\omega=\varepsilon_{\mathbf{k}n}=0} \tag{2.34}$$

2.3.2 The electron spectral function

The so-called electron spectral function physically describes the probability distribution of electrons with energy ω at momentum $\mathbf{k}$ in a many-body system. This magnitude is precisely of high physical interest, since it is directly probed by a variety of experimental ARPES techniques [38]. The electron spectral function for an electron state with band index n is related to the corresponding interacting electron Green's function as follows [2, 5]:

$$\begin{aligned} A_{\mathbf{k}n}(\omega) &= -\frac{1}{\pi}\mathrm{Im}\mathcal{G}_{\mathbf{k}n}(\omega) = -\frac{1}{\pi}\mathrm{Im}\left[\frac{1}{\omega-\varepsilon_{\mathbf{k}n}-\Sigma_{\mathbf{k}n}(\omega)}\right] \\ &= -\frac{1}{\pi}\frac{\mathrm{Im}\Sigma_{\mathbf{k}n}(\omega)}{\left[\omega-\varepsilon_{\mathbf{k}n}-\mathrm{Re}\Sigma_{\mathbf{k}n}(\omega)\right]^2+\left[\mathrm{Im}\Sigma_{\mathbf{k}n}(\omega)\right]^2}. \end{aligned} \tag{2.35}$$

$A_{\mathbf{k}n}(\omega)$ obeys the following sum rule that guarantees the conservation of the number of charge carriers [2, 5]:

$$\int_{-\infty}^{\infty} \mathrm{d}\omega A_{\mathbf{k}n}(\omega) = 1. \tag{2.36}$$

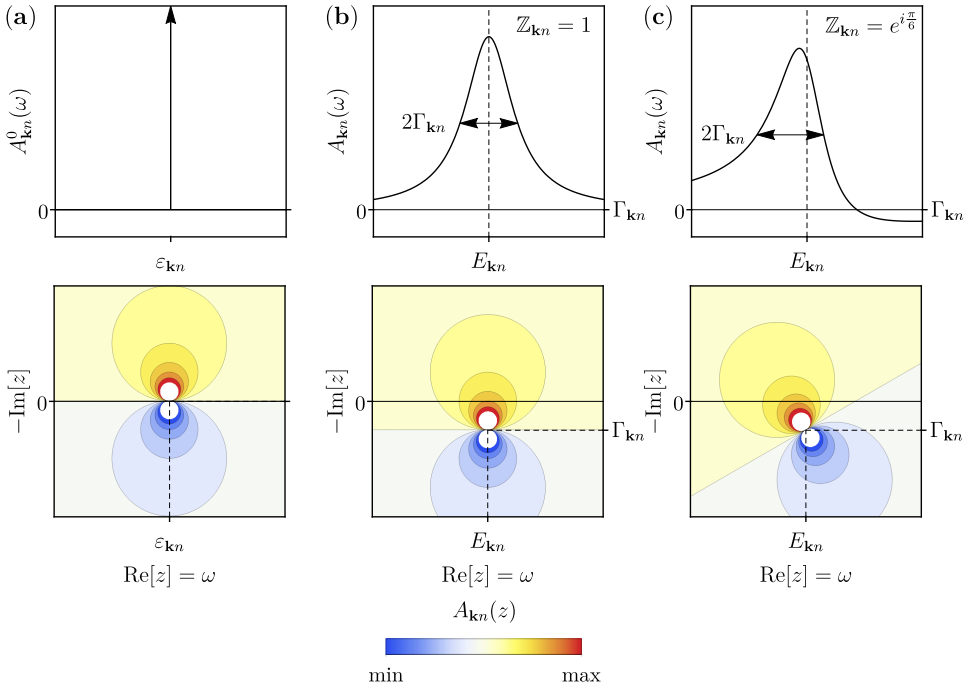

Figure 2.4. Representation of the electron spectral function for (a) the non-interacting case in which the electron has the Kohn-Sham energy $\varepsilon_{\mathbf{k}n}$, and (b) and (c) considering the case in which the electron quasi-particle has acquired a renormalized energy $E_{\mathbf{k}n}$ and a linewidth $\Gamma_{\mathbf{k}n}$, with a purely real and complex quasi-particle strength, $\mathbb{Z}_{\mathbf{k}n} = 1$ and $\mathbb{Z}_{\mathbf{k}n} = e^{i\pi/6}$, respectively. Top panels represent $A_{\mathbf{k}n}(\omega)$ in the real energy axis. Bottom panels show the contour map in the complex energy plane of $A_{\mathbf{k}n}(z)$, where quasi-particle poles are located by dashed black lines at $z_{\mathbf{k}n} = \varepsilon_{\mathbf{k}n}$ in panel (a), and $z_{\mathbf{k}n} = E_{\mathbf{k}n} - i\Gamma_{\mathbf{k}n}$ in panels (b) and (c). The cuts at $\mathrm{Im}[z] = 0$ represented by horizontal solid black lines correspond to the spectra shown in top panels. The color code scale represents the height of the spectral line.

As an aid for later physical interpretations, it is useful to briefly explore how the main features of the electron spectral function evolves from the non-interacting case in the absence of any interaction, i.e. $\Sigma_{\mathbf{k}n}(\omega) = 0$, to the interacting case in the presence of many-body interactions, i.e. $\Sigma_{\mathbf{k}n}(\omega) \neq 0$. In this respect, let us start from the spectral representation of a non-interacting electron in the Kohn-Sham state $|\psi_{\mathbf{k}n}\rangle$ with energy $\varepsilon_{\mathbf{k}n}$, related to the temperature-independent expression of the non-interacting electron Green's function as follows [2, 5]:

$$A^0_{\mathbf{k}n}(\omega) = -\frac{1}{\pi}\mathrm{Im}\mathcal{G}^0_{\mathbf{k}n}(\omega) = \lim_{\eta\to 0^+} -\frac{1}{\pi}\mathrm{Im}\left[\frac{1}{\omega - \varepsilon_{\mathbf{k}n} + i\eta}\right] = \delta(\omega - \varepsilon_{\mathbf{k}n}), \quad (2.37)$$

leading to a Dirac delta function at $\varepsilon_{\mathbf{k}n}$ that trivially fulfills the sum rule in Eq. 2.36. The top panel in Fig. 2.4(a) represents the non-interacting electron

spectral function $A^0_{\mathbf{k}n}(\omega)$ in Eq. 2.37, while the bottom panel represents the corresponding contour map in the complex energy of its analytic continuation $A^0_{\mathbf{k}n}(z)$. Let us now analyze the spectral representation of the interacting electron. As in Eq. 2.27, the interacting electron Green's function can be expanded up to first-order in terms of a multiple-electron quasi-particle picture, whose corresponding spectral function is given by [36]:

$$\begin{aligned} A^{\mathrm{qp}}_{\mathbf{k}n}(\omega) =& -\frac{1}{\pi}\mathrm{Im}\mathcal{G}^{\mathrm{qp}}_{\mathbf{k}n}(z) = -\frac{1}{\pi}\sum_j \mathrm{Im}\left[\frac{\mathbb{Z}^{(j)}_{\mathbf{k}n}}{\omega - E^{(j)}_{\mathbf{k}n} + i\Gamma^{(j)}_{\mathbf{k}n}}\right] \\ =& \frac{1}{\pi}\sum_j \frac{\Gamma^{(j)}_{\mathbf{k}n}\mathrm{Re}\mathbb{Z}^{(j)}_{\mathbf{k}n}}{\left(\omega - E^{(j)}_{\mathbf{k}n}\right)^2 + \left(\Gamma^{(j)}_{\mathbf{k}n}\right)^2} - \frac{\left(\omega - E^{(j)}_{\mathbf{k}n}\right)\mathrm{Im}\mathbb{Z}^{(j)}_{\mathbf{k}n}}{\left(\omega - E^{(j)}_{\mathbf{k}n}\right)^2 + \left(\Gamma^{(j)}_{\mathbf{k}n}\right)^2}, \end{aligned} \tag{2.38}$$

which is a sum of weighted even Lorentzian functions and odd Dawson functions centered at the energies $E^{(j)}_{\mathbf{k}n}$ for each j-th electron quasi-particle state. Taking into account that the electron quasi-particle spectral function in Eq. 2.38 must obey the sum rule in Eq. 2.36, the following relation can be trivially derived:

$$\int_{-\infty}^{\infty} \mathrm{d}\omega A^{\mathrm{qp}}_{\mathbf{k}n}(\omega) = \sum_j \mathrm{Re}\mathbb{Z}^{(j)}_{\mathbf{k}n} \leqslant 1. \tag{2.39}$$

which shows that the total spectral weight coming from electron quasi-particle states is equal to the sum of the real parts of the renormalization factors, being smaller than or equal to unity. As a simple illustration, we only consider the spectral representation of a single-electron quasi-particle state with renormalized energy $E_{\mathbf{k}n}$ and finite linewidth $\Gamma_{\mathbf{k}n}$. The top panels of Figs. 2.4(b) and (c) represent the electron quasi-particle spectral function $A^{\mathrm{qp}}_{\mathbf{k}n}(\omega)$ in Eq. 2.38 for the cases in which the electron quasi-particle renormalization factor is purely real and complex, respectively. The bottom panels of Figs. 2.4(b) and (c) represent the contour maps in the complex energy plane of the corresponding analytical continuations of $A^{\mathrm{qp}}_{\mathbf{k}n}(z)$, respectively.

Unlike the non-interacting case, in which the pole is at $\varepsilon_{\mathbf{k}n}$ in the real axis, in the interacting case the electron quasi-particle pole is located in the lower half complex plane at $z_{\mathbf{k}n} = E_{\mathbf{k}n} - i\Gamma_{\mathbf{k}n}$. This makes the non-interacting Dirac delta spectral representation broaden and acquire a peaked line shape in the interacting case. In the ideal interacting case, the electron quasi-particle renormalization factor is purely real and the complex pole is perpendicularly orientated with respect to the real energy axis. This leads to a perfectly symmetric Lorentzian spectral function in the real axis, whose peak is located at the electron quasi-particle energy $E_{\mathbf{k}n}$ with a full-width at half-maximum of $2\Gamma_{\mathbf{k}n}$. In the more general case where the electron quasi-particle renormalization factor has a finite imaginary part, the pole is rotated a finite angle within the complex plane from the previous ideal orientation.

This has the direct effect of distorting the previous ideal Lorentzian spectral function into an asymmetric spectral peak shape, whose maximum is shifted from the electron quasi-particle energy, $E_{\mathbf{k}n}$.

Actual interacting electron spectra are by far more complicated than the previous simple examples. Indeed, many-body interactions make the spectral structures to extend over a wide energy range with quite irregular shapes. Even in the simple Einstein model (Appendix C), the electron quasi-particle renormalization factors acquire finite imaginary components, which lead to the appearance of asymmetric spectral peaks instead of perfect Lorentzians.

2.4 Effects of the electron-phonon interaction on phonons

Once the retarded phonon self-energy is calculated from first principles by means of Eq. 2.24, we have immediately access to the retarded interacting phonon Green's function by means of Eq. 2.13. On the one hand, the poles of the interacting phonon Green's function determine the phonon quasi-particle branch structure of the system, allowing to study the renormalization of the lattice vibrational structure induced by the electron-phonon interaction. On the other hand, the spectral representation of the interacting phonon Green's function, i.e. the phonon spectral function, is an extremely useful physical magnitude, since it is experimentally accessible by means of INS/IXS and Raman scattering [39, 40].

2.4.1 Phonon quasi-particles

The phonon quasi-particle structure is conformed by the poles of the interacting phonon Green's function in Eq. 2.13, substituting $\Pi_{\mathbf{q}\nu}(\omega)$ in Eq. 2.19 by $\tilde{\Pi}_{\mathbf{q}\nu}(\omega)$ in Eq. 2.24. Thus, the phonon quasi-particle structure are the solutions of the following equation:

$$\omega^2 = \omega^2_{\mathbf{q}\nu} + 2\omega_{\mathbf{q}\nu}\tilde{\Pi}_{\mathbf{q}\nu}(\omega) = \omega^2_{\mathbf{q}\nu} + 2\omega_{\mathbf{q}\nu}\mathrm{Re}\tilde{\Pi}_{\mathbf{q}\nu}(\omega) + i2\omega_{\mathbf{q}\nu}\mathrm{Im}\tilde{\Pi}_{\mathbf{q}\nu}(\omega), \quad (2.40)$$

where it is also clear that the real and imaginary parts of the phonon self-energy contain all the information on the frequency renormalization and the lifetime, respectively, of a non-interacting adiabatic phonon mode $|\mathbf{q}\nu\rangle$ propagating in a many-body system.

As we have done for electrons, the phonon Dyson's equation in Eq. 2.40 must be self-consistently solved within the whole complex frequency plane z, due to the complex definition of both, the phonon self-energy and its frequency argument, and due to the complex character of the phonon quasi-particle pole itself, whose renormalized frequency $\Omega_{\mathbf{q}\nu}$ and linewidth $\gamma_{\mathbf{q}\nu}$ can be expressed as $z_{\mathbf{q}\nu} = \Omega_{\mathbf{q}\nu} - i\gamma_{\mathbf{q}\nu}$. The frequencies $\Omega_{\mathbf{q}\nu}$ represent the

corrected phonon dispersion relation by the non-adiabatic electron-phonon coupling, while the linewidth $\gamma_{\mathbf{q}\nu}$ is connected to the phonon quasi-particle lifetime by $\tau_{\mathbf{q}\nu} = 1/(2\gamma_{\mathbf{q}\nu})$. Therefore, as for electrons, the analytical continuation of the non-adiabatic phonon self-energy, $\tilde{\Pi}_{\mathbf{q}\nu}(z)$, is in principle mandatory for properly solving the phonon Dyson's equation.

The phonon Dyson's equation in Eq. 2.40 can be rewritten using the complex definition of the phonon quasi-particle pole as a system of two coupled non-linear equations defined in the whole frequency complex plane [4]:

$$\begin{aligned} \Omega^2_{\mathbf{q}\nu} &= \omega^2_{\mathbf{q}\nu} + \gamma^2_{\mathbf{q}\nu} + 2\omega_{\mathbf{q}\nu}\mathrm{Re}\tilde{\Pi}_{\mathbf{q}\nu}\big(\Omega_{\mathbf{q}\nu} - i\gamma_{\mathbf{q}\nu}\big) \\ \gamma_{\mathbf{q}\nu} &= -\frac{\omega_{\mathbf{q}\nu}}{\Omega_{\mathbf{q}\nu}}\mathrm{Im}\tilde{\Pi}_{\mathbf{q}\nu}\big(\Omega_{\mathbf{q}\nu} - i\gamma_{\mathbf{q}\nu}\big), \end{aligned} \tag{2.41}$$

where it is also evident the crucial impact of the phonon quasi-particle linewidth on its renormalized frequency and vice versa. Also for phonons, the non-linear character of the phonon Dyson's equation system in Eq. 2.41 may lead to additional several solutions. Thus, one can define the first-order Laurent series expansion of the interacting phonon Greens function in the vicinity of the different electron quasi-particle (qp) poles as follows [127]:

$$\begin{aligned} \mathcal{D}^{\mathrm{qp}}_{\mathbf{q}\nu}(z) &= \sum_j \frac{\mathbb{Z}^{(j)}_{\mathbf{q}\nu}}{z - z^{(j)}_{\mathbf{q}\nu}} - \frac{\mathbb{Z}^{(j)}_{\mathbf{q}\nu}}{z + z^{(j)}_{\mathbf{q}\nu}} = \sum_j \frac{2z^{(j)}_{\mathbf{q}\nu}\mathbb{Z}^{(j)}_{\mathbf{q}\nu}}{z^2 - \left(z^{(j)}_{\mathbf{q}\nu}\right)^2} \\ &= \sum_j \frac{2\left(\Omega^{(j)}_{\mathbf{q}\nu} - i\gamma^{(j)}_{\mathbf{q}\nu}\right)\mathbb{Z}^{(j)}_{\mathbf{q}\nu}}{z^2 - \left(\Omega^{(j)}_{\mathbf{q}\nu} - i\gamma^{(j)}_{\mathbf{q}\nu}\right)^2}, \end{aligned} \tag{2.42}$$

where the index j accounts for the possibility of several phonon quasi-particle modes, i.e. a multiple-phonon quasi-particle picture, starting from an adiabatic single-phonon mode $|\mathbf{q}\nu\rangle$. In Eq. 2.42 $\mathbb{Z}^{(j)}_{\mathbf{q}\nu}$ represents the dimensionless complex renormalization factor of the j-th phonon quasi-particle mode. Similar to electrons, it physically describes the spectral weight of the phonon quasi-particle pole. Mathematically, it is defined as the complex residue of the analytical continuation of the interacting phonon Green's function evaluated at the complex pole:

$$\mathbb{Z}^{(j)}_{\mathbf{q}\nu} = \mathrm{Res}\Big(\mathcal{D}_{\mathbf{q}\nu}(z), z^{(j)}_{\mathbf{q}\nu}\Big) = \frac{1}{z^{(j)}_{\mathbf{q}\nu}/\omega_{\mathbf{q}\nu} - \tilde{\Pi}'_{\mathbf{q}\nu}\Big(z^{(j)}_{\mathbf{q}\nu}\Big)}. \tag{2.43}$$

The standard treatment for solving the phonon Dyson's equation is to simply ignore the complex nature of the frequency plane by neglecting the interplay between the phonon quasi-particle frequency and linewidth in Eq. 2.40 [4]. Thereby, one avoids any analytical continuation of the phonon self-energy and arrives to a non-lineal equation equivalent to the Brillouin-Wigner (BW) perturbation theory [5]. Within the above procedure, the

approximate renormalized phonon quasi-particle frequency $\Omega^{\mathrm{BW}}_{\mathbf{q}\nu}$ is obtained by self-consistently solving the real part of the phonon Dyson's equation in Eq. 2.41 only along the real axis and the approximate linewidth $\gamma^{\mathrm{BW}}_{\mathbf{q}\nu}$ is obtained by directly evaluating the imaginary part of the phonon self-energy at $\Omega^{\mathrm{BW}}_{\mathbf{q}\nu}$:

$$\begin{aligned}\left(\Omega^{\mathrm{BW}}_{\mathbf{q}\nu}\right)^2 &= \omega^2_{\mathbf{q}\nu} + 2\omega_{\mathbf{q}\nu}\mathrm{Re}\tilde{\Pi}_{\mathbf{q}\nu}(\Omega^{\mathrm{BW}}_{\mathbf{q}\nu}) \\ \gamma^{\mathrm{BW}}_{\mathbf{q}\nu} &= -\frac{\omega_{\mathbf{q}\nu}}{\Omega^{\mathrm{BW}}_{\mathbf{q}\nu}}\mathrm{Im}\tilde{\Pi}_{\mathbf{q}\nu}(\Omega^{\mathrm{BW}}_{\mathbf{q}\nu}).\end{aligned} \tag{2.44}$$

However, the most standard treatment used in literature for the case of phonons is still the non-selfconsistent Rayleigh-Schrödinger (RS) perturbation theory method, where $\Omega^{\mathrm{BW}}_{\mathbf{q}\nu}$ is replaced by $\omega_{\mathbf{q}\nu}$ in the argument of the phonon self-energy in Eq. 2.44.

2.4.2 The phonon spectral function

Similar to electrons, the so-called phonon spectral function physically describes the probability distribution of phonons with frequency ω at momentum $\mathbf{q}$ in a many-body system. This magnitude is precisely of high physical interest, since it is directly probed by a variety of experimental techniques, among which the INS/IXS and Raman scattering [39, 40]. The phonon spectral function for a phonon mode with branch index ν is related to the corresponding interacting phonon Green's function as follows [2, 5]:

$$\begin{aligned}B_{\mathbf{q}\nu}(\omega) &= -\frac{1}{\pi}\mathrm{Im}\mathcal{D}_{\mathbf{q}\nu}(\omega) = -\frac{1}{\pi}\mathrm{Im}\left[\frac{2\omega_{\mathbf{q}\nu}}{\omega^2 - \omega^2_{\mathbf{q}\nu} - 2\omega_{\mathbf{q}\nu}\tilde{\Pi}_{\mathbf{q}\nu}(\omega)}\right] \\ &= -\frac{1}{\pi}\frac{4\omega^2_{\mathbf{q}\nu}\mathrm{Im}\tilde{\Pi}_{\mathbf{q}\nu}(\omega)}{\left(\omega^2 - \omega^2_{\mathbf{q}\nu} - 2\omega_{\mathbf{q}\nu}\mathrm{Re}\tilde{\Pi}_{\mathbf{q}\nu}(\omega)\right)^2 + 4\omega^2_{\mathbf{q}\nu}\left(\mathrm{Im}\tilde{\Pi}_{\mathbf{q}\nu}(\omega)\right)^2},\end{aligned} \tag{2.45}$$

which fulfills the following sum-rule that guarantees the conservation of the number of emitted or absorbed phonon modes [127]:

$$\int_0^\infty \mathrm{d}\omega B_{\mathbf{q}\nu}(\omega) = 1 \tag{2.46}$$

In the absence of the non-adiabatic electron-phonon interaction, i.e. $\tilde{\Pi}_{\mathbf{q}\nu}(\omega) = 0$, the spectral representation of the phonon mode $|\mathbf{q}\nu\rangle$ is related to the temperature-independent expression of the non-interacting phonon Green's function in Eq. 2.11 as follows [2, 5]:

$$B^0_{\mathbf{q}\nu}(\omega) = -\frac{1}{\pi}\mathrm{Im}\mathcal{D}^0_{\mathbf{q}\nu}(\omega) = \lim_{\eta\to 0} -\frac{1}{\pi}\mathrm{Im}\left[\frac{2\omega_{\mathbf{q}\nu}}{\omega^2 - (\omega_{\mathbf{q}\nu} - i\eta)^2}\right] = \delta(\omega \pm \omega_{\mathbf{q}\nu}), \tag{2.47}$$

leading to a Dirac delta function at $\pm\omega_{\mathbf{q}\nu}$ (Fig. 2.4(a)), which trivially fulfills the sum rule in Eq. 2.46. On the other hand, as in Eq. 2.42, the Green's

function for an interacting phonon, i.e. $\tilde{\Pi}_{\mathbf{q}\nu}(\omega) \neq 0$, can be expanded up to first-order in terms of a multiple-phonon quasi-particle picture, whose corresponding spectral representation is given by [127]:

$$\begin{aligned} B^{\mathrm{qp}}_{\mathbf{q}\nu}(\omega) &= -\frac{1}{\pi}\mathrm{Im}\mathcal{D}^{\mathrm{qp}}_{\mathbf{q}\nu}(\omega) = -\frac{1}{\pi}\sum_j \mathrm{Im}\left[\frac{2z^{(j)}_{\mathbf{q}\nu}\mathbb{Z}^{(j)}_{\mathbf{q}\nu}}{\omega^2 - \left(z^{(j)}_{\mathbf{q}\nu}\right)^2}\right] \\ &= \frac{1}{\pi}\sum_j \frac{\left(\Omega^{(j)}_{\mathbf{q}\nu} \pm \omega\right)\mathrm{Im}\mathbb{Z}^{(j)}_{\mathbf{q}\nu} + \gamma^{(j)}_{\mathbf{q}\nu}\mathrm{Re}\mathbb{Z}^{(j)}_{\mathbf{q}\nu}}{\left(\Omega^{(j)}_{\mathbf{q}\nu} \pm \omega\right)^2 + \left(\gamma^{(j)}_{\mathbf{q}\nu}\right)^2}, \end{aligned} \tag{2.48}$$

which is a sum of weighted even Lorentzian functions and odd Dawson functions centered at the frequencies $\pm\Omega^{(j)}_{\mathbf{q}\nu}$ for each j-th phonon quasi-particle mode. In addition, $B^{\mathrm{qp}}_{\mathbf{q}\nu}(\omega)$ is an even function [127], i.e. $B^{\mathrm{qp}}_{\mathbf{q}\nu}(\omega) = B^{\mathrm{qp}}_{\mathbf{q}\nu}(-\omega)$, and therefore:

$$\int_0^\infty B^{\mathrm{qp}}_{\mathbf{q}\nu}(\omega)\mathrm{d}\omega = \frac{1}{2}\int_{-\infty}^\infty B^{\mathrm{qp}}_{\mathbf{q}\nu}(\omega)\mathrm{d}\omega. \tag{2.49}$$

Taking into account that the phonon quasi-particle spectral function in Eq. 2.48 must obey the sum rule in Eq. 2.46, the following relation can be trivially derived:

$$\int_0^\infty B^{\mathrm{qp}}_{\mathbf{q}\nu}(\omega)\mathrm{d}\omega = \sum_j \mathrm{Re}\mathbb{Z}^{(j)}_{\mathbf{q}\nu} \leqslant 1, \tag{2.50}$$

which shows that the total spectral weight coming from phonon quasi-particle modes is equal to the sum of the real parts of the renormalization factors, which should be smaller than or equal to unity. Similarly to electrons, the imaginary character of $\mathbb{Z}^{(j)}_{\mathbf{q}\nu}$ in Eq. 2.48 leads to the appearance of asymmetric peaks in the phonon quasi-particle spectral function.

The most standard procedure used in literature for rationalizing both, experimentally and theoretically, the phonon spectral function in terms of quasi-particle modes is to completely neglect the imaginary part of the renormalization factors, i.e. to interpret the spectrum using full-symmetric Lorentzian functions (Fig. 2.4(b)). As seen for electrons, this can give wrong estimations of the renormalized phonon quasi-particle frequencies and linewidths, since the actual phonon spectral functions are by far more complicated (Fig. 2.4(c)).

2.5 Relevant physical properties of the electron-phonon interaction

In this section, all the additional relevant physical properties related to the electron-phonon interaction studied throughout this thesis are derived from the retarded electron and phonon self-energies in Eqs. 2.18 and 2.24.

2.5.1 The Eliashberg spectral function and the electron-phonon coupling strength

On the one hand, in order to get a more direct formulation of the state-dependent electron-phonon coupling strength or mass enhancement parameter defined in Eq. 2.34, one can start from the explicit expression of the imaginary part of the electron self-energy in Eq. 2.18 that can be obtained by using of the following mathematical property:

$$\lim_{\eta\to 0^+}\frac{1}{a+i\eta}=\mathcal{P}\left(\frac{1}{a}\right)-i\pi\delta(a). \tag{2.51}$$

Applying Eq. 2.51 to Eq. 2.18, the imaginary part of the electron self-energy is directly expressed as follows:

$$\begin{aligned}\mathrm{Im}\Sigma_{\mathbf{k}n}(\omega)=-\frac{\pi}{N_{\mathbf{q}}}\sum_{\mathbf{q}}^{1\mathrm{BZ}}\sum_{m\nu}\left|g^{\nu}_{mn}(\mathbf{k},\mathbf{q})\right|^2\times\\ \Big[\big(1-f(\varepsilon_{\mathbf{k}+\mathbf{q}m})+n_{\mathrm{B}}(\omega_{\mathbf{q}\nu})\big)\delta(\omega-\varepsilon_{\mathbf{k}+\mathbf{q}m}-\omega_{\mathbf{q}\nu})+\\ \big(f(\varepsilon_{\mathbf{k}+\mathbf{q}m})+n_{\mathrm{B}}(\omega_{\mathbf{q}\nu})\big)\delta(\omega-\varepsilon_{\mathbf{k}+\mathbf{q}m}+\omega_{\mathbf{q}\nu})\Big].\end{aligned} \tag{2.52}$$

Since the state-dependent electron-phonon coupling strength in Eq. 2.34 has been physically defined as a property close to the Fermi level ($\omega=\varepsilon_{\mathbf{k}n}\to\varepsilon_{\mathrm{F}}$) at zero temperature, i.e. $n_{\mathrm{B}}(\omega_{\mathbf{q}\nu})=0$, we can rewrite the imaginary part of the electron self-energy in Eq. 2.52 as follows:

$$\begin{aligned}\mathrm{Im}\Sigma_{\mathbf{k}n}(\omega)=-\pi\int_0^{\infty}\mathrm{d}\omega'\big[\alpha^2F^{-}_{\mathbf{k}n}(\omega')\big(1-f(\omega-\omega')\big)+\\ \alpha^2F^{+}_{\mathbf{k}n}(\omega')f(\omega+\omega')\big],\end{aligned} \tag{2.53}$$

where the so-called state-dependent Eliashberg spectral functions $\alpha^2F^{\pm}_{\mathbf{k}n}(\omega)$ are properly defined as follows [43]:

$$\alpha^2F^{\pm}_{\mathbf{k}n}(\omega)=\frac{1}{N_{\mathbf{q}}}\sum_{\mathbf{q}}^{1\mathrm{BZ}}\delta(\omega-\omega_{\mathbf{q}\nu})\sum_{m\nu}\left|g^{\nu}_{mn}(\mathbf{k},\mathbf{q})\right|^2\delta(\varepsilon_{\mathbf{k}n}-\varepsilon_{\mathbf{k}+\mathbf{q}m}\pm\omega). \tag{2.54}$$

These functions can be interpreted as the probability of scattering at zero temperature an electron (-) or a hole (+) from the Kohn-Sham state $|\psi_{\mathbf{k}n}\rangle$ with energy $\varepsilon_{\mathbf{k}n}$ to all the other energetically allowed states via the emission of a phonon of frequency ω, or equivalently as the phDOS in Eq. 1.51 weighted by the electron-phonon interaction. One can recover the expression of the real part of the electron self-energy in terms of the Eliashberg functions by plugging Eq. 2.53 into the Kramers-Kronig relations in Eq. 2.20:

$$\mathrm{Re}\Sigma_{\mathbf{k}n}(\omega) = \int_{-\infty}^{\infty} \mathrm{d}\omega'' \int_{0}^{\infty} \mathrm{d}\omega' \Bigg[\alpha^2 F^{-}_{\mathbf{k}n}(\omega') \frac{1 - f(\omega'' - \omega')}{\omega - \omega''} + \alpha^2 F^{+}_{\mathbf{k}n}(\omega') \frac{f(\omega'' + \omega')}{\omega - \omega''} \Bigg]. \tag{2.55}$$

The differences between $\alpha^2 F^{\pm}_{\mathbf{k}n}(\omega)$ are usually small, since the scale of the electron energies scale is typically much larger than that of the phonon frequencies. One can therefore assume that: $\alpha^2 F^{+}_{\mathbf{k}n}(\omega) \approx \alpha^2 F^{-}_{\mathbf{k}n}(\omega)$, and the real part of the electron self-energy can be rewritten as [2]:

$$\mathrm{Re}\Sigma_{\mathbf{k}n}(\omega) = -\int_{-\infty}^{\infty} \mathrm{d}\omega'' \int_{0}^{\infty} \mathrm{d}\omega' \big(\alpha^2 F^{+}_{\mathbf{k}n}(\omega') + \alpha^2 F^{-}_{\mathbf{k}n}(\omega') \big) \frac{\omega' f(\omega'' + \omega)}{\omega''^2 - \omega'^2}. \tag{2.56}$$

Plugging Eq. 2.56 into Eq. 2.34 and having that $\partial f(\omega'' + \omega)/\partial\omega|_{\omega=0} = \delta(\omega'')$ at zero temperature, the state-dependent electron-phonon coupling strength is given by:

$$\lambda_{\mathbf{k}n} = \int_{0}^{\infty} \mathrm{d}\omega \frac{\alpha^2 F^{+}_{\mathbf{k}n}(\omega) + \alpha^2 F^{-}_{\mathbf{k}n}(\omega)}{\omega}, \tag{2.57}$$

which, using the state-dependent Eliashberg functions in Eq. 2.54, can be also written as:

$$\lambda_{\mathbf{k}n} = \frac{1}{N_{\mathbf{q}}} \sum_{\mathbf{q}}^{1\mathrm{BZ}} \sum_{m\nu} \frac{\big| g^{\nu}_{mn}(\mathbf{k}, \mathbf{q}) \big|^2}{\omega_{\mathbf{q}\nu}} \delta(\varepsilon_{\mathbf{k}n} - \varepsilon_{\mathbf{k}+\mathbf{q}m} \pm \omega_{\mathbf{q}\nu}). \tag{2.58}$$

Likewise, the electron-phonon coupling strength can be averaged over the Fermi surface as:

$$\lambda = \frac{1}{N_{\mathrm{F}}} \frac{1}{N_{\mathbf{k}}} \sum_{\mathbf{k}}^{1\mathrm{BZ}} \sum_{n} \lambda_{\mathbf{k}n} \delta(\varepsilon_{\mathbf{k}n} - \varepsilon_{\mathrm{F}}) = \int_{0}^{\infty} \mathrm{d}\omega \frac{\alpha^2 F^{+}(\omega) + \alpha^2 F^{-}(\omega)}{\omega}, \tag{2.59}$$

where the FS-averaged Eliashberg spectral functions are defined as:

$$\alpha^2 F^{\pm}(\omega) = \frac{1}{N_{\mathrm{F}}} \frac{1}{N_{\mathbf{k}}} \sum_{\mathbf{k}}^{1\mathrm{BZ}} \sum_{n} \alpha^2 F^{\pm}_{\mathbf{k}n}(\omega) \delta(\varepsilon_{\mathbf{k}n} - \varepsilon_{\mathrm{F}}) \tag{2.60}$$

The expression of the electron-phonon coupling strength can be also rationalized starting from the imaginary part of the phonon self-energy. The explicit expression for the latter is deduced by applying the mathematical relation in Eq. 2.51 to the retarded phonon self-energy in Eq. 2.24:

$$\mathrm{Im}\tilde{\Pi}_{\mathbf{q}\nu}(\omega) = -\frac{\pi}{N_{\mathbf{k}}} \sum_{\mathbf{k}}^{1\mathrm{BZ}} \sum_{mn} \big| g^{\nu}_{mn}(\mathbf{k}, \mathbf{q}) \big|^2 \big(f(\varepsilon_{\mathbf{k}n}) - f(\varepsilon_{\mathbf{k}+\mathbf{q}m}) \big) \times \delta(\varepsilon_{\mathbf{k}n} - \varepsilon_{\mathbf{k}+\mathbf{q}m} + \omega). \tag{2.61}$$

As mentioned in Sec. 2.4.1, the most standard procedure for studying the effects of the electron-phonon interaction on phonons is the Rayleigh-Schrödinger perturbation theory. Within this approach, the phonon quasi-particle linewidth is given by evaluating the imaginary part of the phonon self-energy in Eq. 2.61 at the adiabatic phonon frequency[2], i.e. $\gamma^{\mathrm{RS}}_{\mathbf{q}\nu} = -\mathrm{Im}\tilde{\Pi}_{\mathbf{q}\nu}(\omega_{\mathbf{q}\nu})$:

$$\gamma^{\mathrm{RS}}_{\mathbf{q}\nu} = \frac{\pi}{N_{\mathbf{k}}} \sum_{\mathbf{k}}^{1\mathrm{BZ}} \sum_{mn} \left| g^{\nu}_{mn}(\mathbf{k},\mathbf{q}) \right|^2 \big(f(\varepsilon_{\mathbf{k}n}) - f(\varepsilon_{\mathbf{k}+\mathbf{q}m}) \big) \times \delta(\varepsilon_{\mathbf{k}n} - \varepsilon_{\mathbf{k}+\mathbf{q}m} + \omega_{\mathbf{q}\nu}). \tag{2.62}$$

Following the seminal work of Allen [128], we can consider that the phonon frequencies are much smaller than the electron energies. From this, and taking into account that at zero temperature the Fermi-Dirac occupation factors are unit step functions, i.e. $f(\varepsilon_{\mathbf{k}n}) = \theta(\varepsilon_{\mathrm{F}} - \varepsilon_{\mathbf{k}n})$, it is deduced that the factor $f(\varepsilon_{\mathbf{k}n}) - f(\varepsilon_{\mathbf{k}+\mathbf{q}m})$ can be substituted by the following expression:

$$f(\varepsilon_{\mathbf{k}n}) - f(\varepsilon_{\mathbf{k}+\mathbf{q}m}) = \theta(\varepsilon_{\mathbf{k}n}) - \theta(\varepsilon_{\mathbf{k}+\mathbf{q}m}) \approx \omega_{\mathbf{q}\nu}\delta(\varepsilon_{\mathbf{k}n} - \varepsilon_{\mathrm{F}}). \tag{2.63}$$

Substituting Eq. 2.63 into Eq. 2.62 and assuming that $\omega_{\mathbf{q}\nu} \ll |\varepsilon_{\mathbf{k}n} - \varepsilon_{\mathbf{k}+\mathbf{q}m}|$, we arrive to the following simplified expression of the phonon linewidth

$$\gamma^{\mathrm{RS}}_{\mathbf{q}\nu} = \frac{\omega_{\mathbf{q}\nu}\pi}{N_{\mathbf{k}}} \sum_{\mathbf{k}}^{1\mathrm{BZ}} \sum_{mn} \left| g^{\nu}_{mn}(\mathbf{k},\mathbf{q}) \right|^2 \delta(\varepsilon_{\mathbf{k}n} - \varepsilon_{\mathbf{k}+\mathbf{q}m}) \delta(\varepsilon_{\mathbf{k}n} - \varepsilon_{\mathrm{F}}). \tag{2.64}$$

The latter approximation can be also used in Eq. 2.59, from which the FS-averaged electron-phonon coupling strength can be expressed in terms of $\gamma^{\mathrm{RS}}_{\mathbf{q}\nu}$ as follows:

$$\lambda = \frac{1}{N_{\mathbf{q}}} \sum_{\mathbf{q}}^{1\mathrm{BZ}} \sum_{\nu} \lambda_{\mathbf{q}\nu} = 2 \int_0^{\infty} \mathrm{d}\omega \frac{\alpha^2 F(\omega)}{\omega}, \tag{2.65}$$

where $\lambda_{\mathbf{q}\nu}$ is the electron-phonon coupling strength related to the phonon mode $|\mathbf{q}\nu\rangle$, defined as:

$$\lambda_{\mathbf{q}\nu} = \frac{2}{\pi N_{\mathrm{F}}} \frac{\gamma^{\mathrm{RS}}_{\mathbf{q}\nu}}{\omega^2_{\mathbf{q}\nu}}, \tag{2.66}$$

and the FS-averaged Eliashberg spectral function is defined as:

$$\alpha^2 F(\omega) = \frac{1}{\pi N_{\mathrm{F}}} \frac{1}{N_{\mathbf{q}}} \sum_{\mathbf{q}}^{1\mathrm{BZ}} \sum_{\nu} \frac{\gamma^{\mathrm{RS}}_{\mathbf{q}\nu}}{\omega_{\mathbf{q}\nu}} \delta(\omega - \omega_{\mathbf{q}\nu}). \tag{2.67}$$

[2]The same result can be obtained from the Fermi's golden rule (Appendix D).

From the perspective of phonons, one can also evaluate the strength of the electron-phonon coupling by means of the FS-averaged squared electron-phonon matrix element for each phonon mode $|\mathbf{q}\nu\rangle$, which is equivalent to a sort of electronphonon weighted nesting function, defined by:

$$\langle |g_{\mathbf{q}\nu}|^2 \rangle = \frac{1}{N_\mathrm{F}} \frac{1}{N_\mathbf{k}} \sum_{\mathbf{k}mn} |g^\nu_{mn}(\mathbf{k},\mathbf{q})|^2 \delta(\varepsilon_{\mathbf{k}n} - \varepsilon_{\mathbf{k}+\mathbf{q}m} \pm \omega_{\mathbf{q}\nu}) \delta(\varepsilon_{\mathbf{k}n} - \varepsilon_\mathrm{F}). \quad (2.68)$$

2.5.2 McMillan-Allen-Dynes formula

Undoubtedly, the most spectacular physical phenomenon due to the electron-phonon interaction is the phonon-mediated superconductivity [2, 5]. Briefly said, in the superconducting state, the many-body system appears as a condensate formed by electron pairs, the so called Cooper pairs, whose pairing mechanism is provided by the electron-phonon interaction [129, 130]. In this regard, the appropriate theoretical framework for calculating the temperature up to which the material is superconductor, i.e. the superconducting critical temperature T_c, is the Eliashberg theory, which implies solving the set of the so-called Eliashberg equations [131, 132].

Nevertheless, most first principles calculations of the phonon-mediated superconducting critical temperature in solids rely on a semi-empirical expression first introduced by McMillan [133] and then refined by Allen and Dynes [134]. Within this approach, the superconducting critical temperature is approximated by:

$$T_\mathrm{c} = \frac{\omega_{\log}}{1.2} \exp\left[-\frac{1.04(1+\lambda)}{\lambda - \mu^*(1+0.62\lambda)} \right], \quad (2.69)$$

where $\omega_{\log}$ is the logarithmic average of the phonon frequencies, defined as:

$$\begin{aligned} \omega_{\log} &= \exp\left[\frac{1}{\lambda} \int_0^\infty \mathrm{d}\omega \frac{\alpha^2F^+(\omega) + \alpha^2F^-(\omega)}{\omega} \log\omega \right] \\ &= \exp\left[\frac{2}{\lambda} \int_0^\infty \mathrm{d}\omega \frac{\alpha^2F(\omega)}{\omega} \log\omega \right], \end{aligned} \quad (2.70)$$

where λ is the FS-averaged electron-phonon coupling strength (Eq. 2.59 and 2.65) and μ^* is a parameter describing the Coulomb repulsion. Throughout this thesis, the McMillan-Allen-Dynes formula in Eq. 2.69 is taken for calculating the superconducting critical temperature, with the Coulomb potential μ^* treated as an adjustable parameter. It must also be said that it generally yields results in good agreement with experiments [132], even though this procedure introduces a large uncertainty in the value of T_c, since it is based on quantities averaged on the Fermi surface.

2.6 Electron-phonon interaction using Wannier interpolation

First principles calculations of the electron-phonon interaction require large 1BZ-summations over electron states and phonon modes of functions, since they usually exhibit strong variations along the Fermi surface or other $\{\mathbf{k}, \mathbf{q}, \omega\}$ phase-spaces. This inconvenient can be easily appreciated by looking for instance, at the retarded electron and phonon self-energies in Eq 2.18 and Eq. 2.19, where whenever the difference between electron energies approaches the phonon frequency, the denominators become small and the function to sum large. Compared to self-consistent first principles DFT calculations, which are typically converged using meshes of the order of $10 \times 10 \times 10$ **k**-points [93, 94], the numerical convergence of the electron-phonon interaction calculations with respect to the **k** and **q**-point grids needs a very large number of points ($\geqslant 10^6$), which implies the use of much finer meshes [4]. However, determining the Kohn-Sham electron wave functions $\psi_{\mathbf{k}n}(\mathbf{r})$ and energies $\varepsilon_{\mathbf{k}n}$, but mostly the adiabatic phonon frequencies $\omega_{\mathbf{q}\nu}$ and polarization vectors $\boldsymbol{\epsilon}^s_{\mathbf{q}\nu}$ together with the first-order derivatives of the Kohn-Sham effective potential $\partial V_{\mathrm{KS}}(\mathbf{r})/\partial u^\alpha_s(\mathbf{q})$, and hence the electron-phonon matrix elements $g^\nu_{mn}(\mathbf{k}, \mathbf{q})$, is a prohibitive task in such fine grids. In fact, even the non-selfconsistent solution of the Kohn-Sham Schrödinger equation (Eq. 1.13) turns out to be impracticable for so many points. In order to overcome this challenge, the development of interpolation schemes based on maximally localized Wannier functions has turned out in the last years to be a very useful tool to obtain not only the Kohn-Sham energies [135–137] but also the electron-phonon matrix elements in very fine **k** and **q**-point meshes [4, 138–140], making thus converged first principles calculations of the electron-phonon interaction affordable.

2.6.1 Maximally localized Wannier functions

As seen in Sec. 1.3.2, the Kohn-Sham electron states $|\psi_{\mathbf{k}n}\rangle$ are Bloch states usually expressed in terms of lattice-periodic functions $u_{\mathbf{k}n}(\mathbf{r})$ (Eq. 1.17) [6]. In order to interpolate them, it is advantageous to alternatively describe Bloch states in terms of linear combinations of functions localized in the real space, i.e. the so-called Wannier functions [142].

To this end, the gauge freedom of Bloch states in the reciprocal space can be exploited in order to get functions that are localized in the real space. Indeed, Bloch states posses an inherent arbitrary phase at each momentum **k**, by which, if $|\psi_{\mathbf{k}n}\rangle$ is a valid Bloch state of the system, then the rotated state $|\tilde{\psi}_{\mathbf{k}n}\rangle = e^{i\theta_{\mathbf{k}n}} |\psi_{\mathbf{k}n}\rangle$ is equally valid, with $\theta_{\mathbf{k}n}$ being any real and periodic function in the reciprocal space. In this respect, the basic properties of Fourier transforms state that the smoother a reciprocal-space object is, the sharper (more localized) is the transformed real-space object. Therefore,

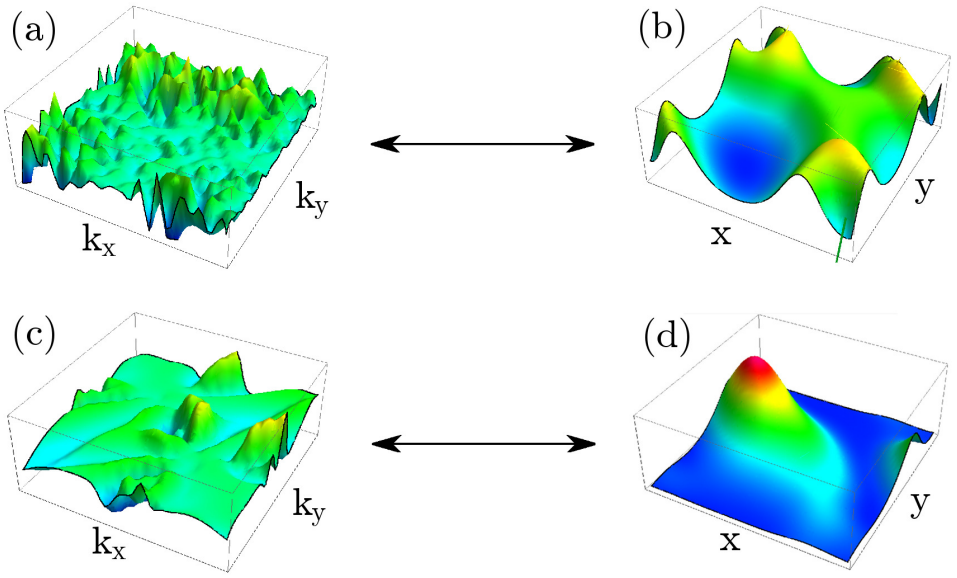

Figure 2.5. Illustrative explanation of the maximally localized Wannier rotation on Bloch states. Panel (a) shows *a priori* wrinkled Bloch wave functions in the reciprocal space (left) and its corresponding delocalized Fourier transform function in the real space (right). Panel (b) shows smooth Wannier rotated Bloch wave functions in the reciprocal space (left) and its corresponding highly localized Fourier transform, i.e. the maximally localized Wannier function, in the real space. Reproduced with permission from Ref. [141] by Julen Ibañez Azpiroz.

the goal is to construct a set of $\theta_{\mathbf{k}n}$ for which the rotated Bloch functions are as smooth as possible in the reciprocal space in order to obtain Wannier functions as localized as possible in the real space by a Fourier transform.

In the most general case, for a chosen set of M Kohn-Sham electron bands well-separated from all the other bands by finite energy gaps all over the 1BZ, one can generalize the gauge freedom of the Bloch states at each momentum $\mathbf{k}$ by means of a $M \times M$ unitary matrix $U_{mn}(\mathbf{k})$ as follows [135–137]:

$$|\tilde{\psi}_{\mathbf{k}n}\rangle = \sum_{m}^{M} U_{mn}(\mathbf{k}) \, |\psi_{\mathbf{k}m}\rangle \, , \tag{2.71}$$

where $|\tilde{\psi}_{\mathbf{k}n}\rangle$ are the so-called Wannier rotated Bloch states. In this way, the Wannier functions, which are intended to be centered at the Bravais lattice vector $\mathbf{T}$ and are normalized as: $\langle W_{\mathbf{T}n} | W_{\mathbf{T}'n'}\rangle = \delta_{\mathbf{T}\mathbf{T}'}\delta_{nn'}$, are defined by the following Fourier transforms:

$$|W_{\mathbf{T}n}\rangle = \frac{1}{N_{\mathbf{k}}} \sum_{\mathbf{k}}^{1\mathrm{BZ}} e^{-i\mathbf{k}\cdot\mathbf{T}} \, |\tilde{\psi}_{\mathbf{k}n}\rangle = \frac{1}{N_{\mathbf{k}}} \sum_{\mathbf{k}}^{1\mathrm{BZ}} e^{-i\mathbf{k}\cdot\mathbf{T}} \sum_{m} U_{mn}(\mathbf{k}) \, |\psi_{\mathbf{k}m}\rangle \, . \tag{2.72}$$

The most widely used method for constructing $U_{mn}(\mathbf{k})$ is by imposing the minimization of the quadratic spread of the Wannier functions around their centers in the real space, i.e. maximizing the real space localization. The quadratic spread functional of the Wannier functions is defined as [135–137]:

$$\Omega = \sum_{n} \big(\langle W_{\mathbf{0}n} | r^2 | W_{\mathbf{0}n} \rangle - \langle W_{\mathbf{0}n} | \mathbf{r} | W_{\mathbf{0}n} \rangle^2 \big), \tag{2.73}$$

By expressing the latter in terms of the Bloch states using Eq. 2.72, we minimize Ω with respect to $U_{mn}(\mathbf{k})$ by means of an iterative numerical procedure [135–137]. The resulting Wannier functions are the so-called maximally localized Wannier functions (MLWFs). The impact of the maximally localized Wannier rotation on the Bloch states is illustratively explained in Fig. 2.5. In Fig. 2.5(a), the direct Fourier transform of *a priori* wrinkled Bloch states $|\psi_{\mathbf{k}n}\rangle$ in the reciprocal space (left panel) turns out to be delocalized in the real space (right panel). In Fig. 2.5(b), the Fourier transform of smooth Wannier rotated Bloch states $|\tilde{\psi}_{\mathbf{k}n}\rangle$ in the reciprocal space (left panel) turns out to be highly localized in the real space, i.e. the maximally localized Wannier function (right panel). In this thesis, the calculation of MLWFs is done by means of the WANNIER90 post-processing algorithm [143].

2.6.2 Interpolation of the electron band structure

Among the several interesting applications of the MLWFs, one can use the real space localization property for efficient interpolations of the electron band structure in the reciprocal space from a typical DFT coarse $\mathbf{k}$-point mesh to a fine $\mathbf{k}'$-point mesh. Indeed, once the unitary matrices $U_{mn}(\mathbf{k})$ are calculated, the Wannier rotated Kohn-Sham Hamiltonian can be constructed on the coarse mesh by means of Eq. 2.71:

$$\begin{aligned} \tilde{H}^{mn}_{\mathrm{KS}}(\mathbf{k}) = \langle \tilde{\psi}_{\mathbf{k}m} | \hat{H}_{\mathrm{KS}} | \tilde{\psi}_{\mathbf{k}n} \rangle &= \sum_{i,j}^{M} \big(U_{im}(\mathbf{k}) \big)^* \langle \psi_{\mathbf{k}i} | \hat{H}_{\mathrm{KS}} | \psi_{\mathbf{k}j} \rangle \, U_{jn}(\mathbf{k}) \\ &= \sum_{i,j}^{M} \big(U_{im}(\mathbf{k}) \big)^* \varepsilon_{\mathbf{k}i} \delta_{ij} U_{jn}(\mathbf{k}) = \sum_{i}^{M} \big(U_{im}(\mathbf{k}) \big)^* \varepsilon_{\mathbf{k}i} U_{in}(\mathbf{k}). \end{aligned} \tag{2.74}$$

The Wannier rotated Hamiltonian matrices can be then Fourier transformed to the real space as follows:

$$\tilde{H}^{mn}_{\mathrm{KS}}(\mathbf{T}) = \langle W_{\mathbf{0}m} | \hat{H}_{\mathrm{KS}} | W_{\mathbf{T}n} \rangle = \frac{1}{N_{\mathbf{k}}} \sum_{\mathbf{k}}^{1\mathrm{BZ}} e^{-i\mathbf{k}\cdot\mathbf{T}} \tilde{H}^{mn}_{\mathrm{KS}}(\mathbf{k}). \tag{2.75}$$

Figure 2.6 shows an example for the case of MoS_2. Panel (a) shows how the maximally localization of the Wannier functions in the real space makes

$\tilde{H}^{mn}_{\mathrm{KS}}(\mathbf{T})$ spatially decay from the center of the Bravais lattice $\mathbf{T} = 0$ to the boundaries of the supercell crystal. Indeed, the boundary supercell components and those beyond are negligible with respect to the lattice-center components. Therefore, the inverse Fourier transform of $\tilde{H}^{mn}_{\mathrm{KS}}(\mathbf{T})$ can be safely taken to any other $\mathbf{k}'$-point on the fine mesh as:

$$\tilde{H}^{mn}_{\mathrm{KS}}(\mathbf{k}') = \sum_{\mathbf{T}} e^{i\mathbf{k}'\cdot\mathbf{T}} \tilde{H}^{mn}_{\mathrm{KS}}(\mathbf{T}). \tag{2.76}$$

Finally, by diagonalizing $\tilde{H}^{mn}_{\mathrm{KS}}(\mathbf{k}')$ one obtains the electron energies $\varepsilon_{\mathbf{k}'n}$ on the fine mesh for the chosen M electron bands, completing then the interpolation of the electron band structure based on MLWFs. Likewise, the unitary matrices $U_{mn}(\mathbf{k}')$ are formed by the eigenvectors of $\tilde{H}^{mn}_{\mathrm{KS}}(\mathbf{k}')$ and Bloch states on the fine mesh can be constructed by Fourier antitransforming Eq. 2.72:

$$|\psi_{\mathbf{k}n}\rangle = \sum_m U_{nm}(\mathbf{k}')\,|\tilde{\psi}_{\mathbf{k}m}\rangle = \sum_m U_{nm}(\mathbf{k}') \sum_{\mathbf{T}} e^{i\mathbf{k}'\cdot\mathbf{T}}\,|W_{\mathbf{T}n}\rangle \tag{2.77}$$

It is worth noting that the Wannier interpolation of the Kohn-Sham Hamiltonian from the coarse $\mathbf{k}$-point mesh to the fine $\mathbf{k}'$-point mesh is much faster than solving non-selfconsistently the Kohn-Sham Schrödinger equation on the fine $\mathbf{k}'$-point mesh. Therefore, this technique turns out to be extremely useful when studying electronic properties as the DOS (Eq. 1.26) or electronic response functions (Eq. 1.60).

2.6.3 Interpolation of the electron-phonon matrix elements

At this point, one can take advantage of the Wannier interpolation of the electron band structure (Sec. 2.6.2) for interpolating the electron-phonon matrix elements and improve the convergence of first principles calculations of the electron-phonon interaction [4, 138–140]. In the coarse electron momentum $\mathbf{k}$ and phonon momentum $\mathbf{q}$ meshes, the potential change matrix elements defined in Eq. 2.7 can be Wannier rotated by means of Eq. 2.71 as follows:

$$\tilde{g}^{s\alpha}_{mn}(\mathbf{k},\mathbf{q}) = \sum_{i,j} \big(U_{im}(\mathbf{k}+\mathbf{q})\big)^* g^{s\alpha}_{ij}(\mathbf{k},\mathbf{q}) U_{jn}(\mathbf{k}). \tag{2.78}$$

The Wannier rotated potential change matrix elements can be the Fourier transformed to the real space as follows:

$$\begin{aligned} \tilde{g}^{s\alpha}_{mn}(\mathbf{T_e},\mathbf{T_p}) &= \left\langle W_{\mathbf{0}m} \middle| \frac{\partial V_{\mathrm{KS}}}{\partial u^\alpha_s} \middle| W_{\mathbf{T_e}m} \right\rangle \\ &= \frac{1}{N_{\mathbf{k}} N_{\mathbf{q}}} \sum_{\mathbf{k},\mathbf{q}}^{1\mathrm{BZ}} e^{-i(\mathbf{k}\cdot\mathbf{T_e}+\mathbf{q}\cdot\mathbf{T_p})} \tilde{g}^{s\alpha}_{mn}(\mathbf{k},\mathbf{q}), \end{aligned} \tag{2.79}$$

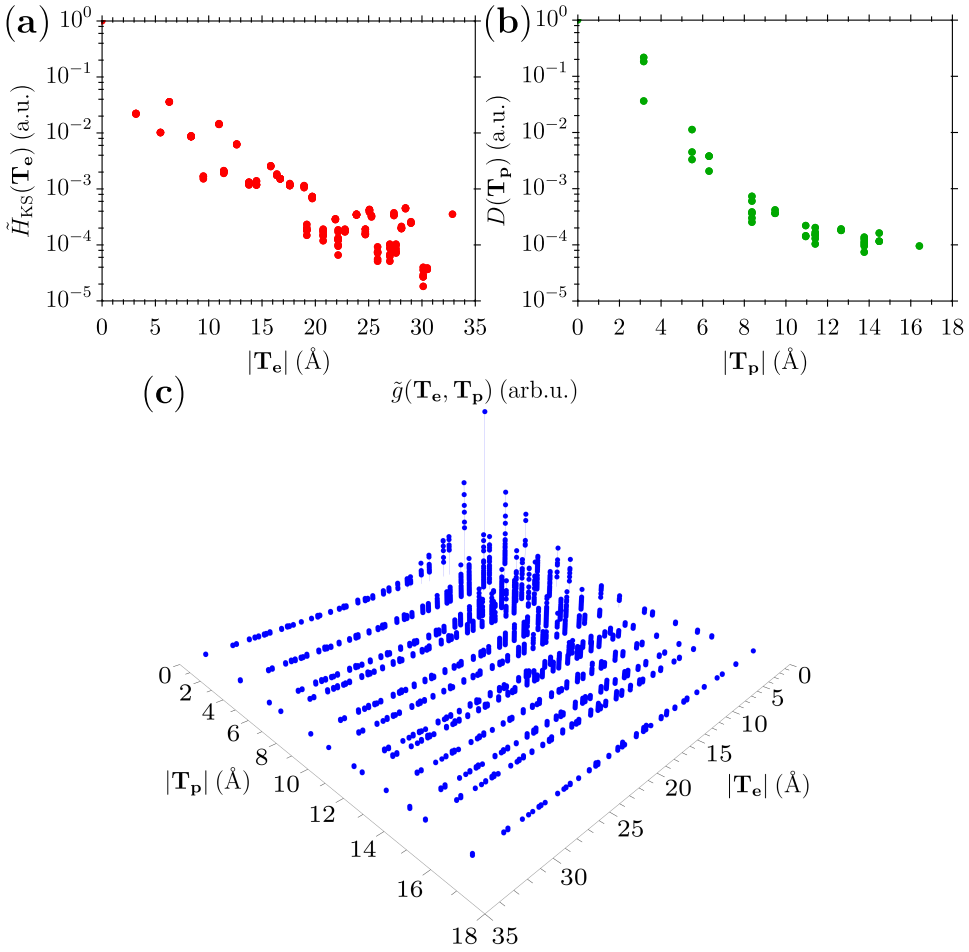

Figure 2.6. Spatial decay in logarithmic scale of the largest components of the Fourier transfoms of (a) the Wannier rotated Kohn-Sham Hamiltonian $\tilde{H}^{mn}_{\mathrm{KS}}(\mathbf{T_e})$ energies and (b) the dynamical matrix $D^{\alpha\alpha'}_{ss'}(\mathbf{T_p})$. $\mathbf{T_e}$ and $\mathbf{T_p}$ represent the Bravais lattice vectors for the MLWFs in Eq. 2.72 and the first-order derivative of the Kohn-Sham potential with respect to the ionic displacement, respectively. (c) Spatial decay of the Fourier transform of the Wannier rotated potential change matrix elements $\tilde{g}^{s\alpha}_{mn}(\mathbf{T_e}, \mathbf{T_p})$. The data are plotted as a function of distance along several directions and correspond to the undoped MoS_2 monolayer studied in Chapter 4.

where $\mathbf{T_e}$ and $\mathbf{T_p}$ represent the Bravais lattice vectors for the MLWFs in Eq. 2.72 and the first-order derivative of the Kohn-Sham potential with respect to the displacement of the s-th ion, respectively. Due to the spatial localization of both the MLWFs and the ionic displacement perturbations, the Fourier transformation of the potential change matrix elements in the Wannier representation $\tilde{g}^{s\alpha}_{mn}(\mathbf{T_e}, \mathbf{T_p})$ decays rapidly with both $\mathbf{T_e}$ and $\mathbf{T_p}$ compared to the simple Fourier transformation in the Bloch representation $g^{s\alpha}_{mn}(\mathbf{T_e}, \mathbf{T_p})$. This is clearly shown in Fig. 2.6(c) for the largest components

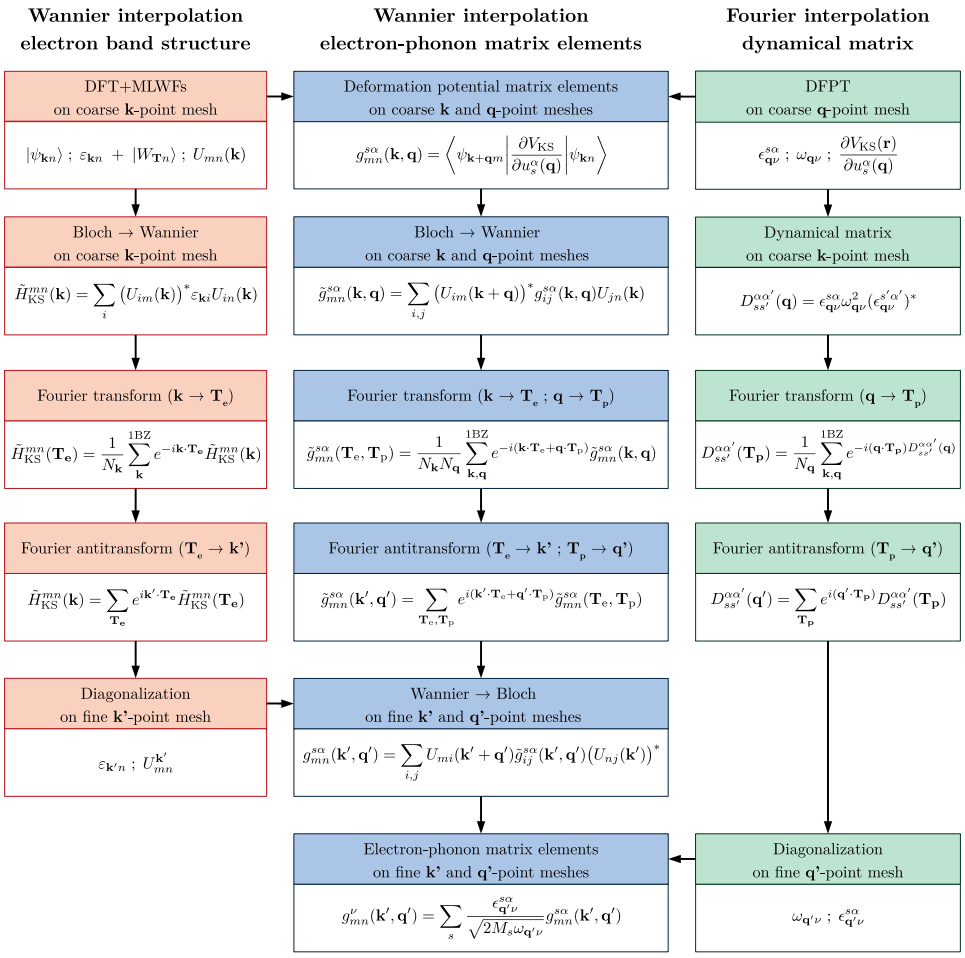

Figure 2.7. Schematic representation of the interpolation scheme based on maximally localized Wannier functions of the electron-phonon matrix elements. Red boxes represent the Wannier interpolation of the electron band structure and green boxes represent the Fourier interpolation of the dynamical matrix, both indispensable for the Wannier interpolation of the electron-matrix elements described in blue boxes.

of the potential change matrix elements of the MoS_2 monolayer. Therefore, one can neglect terms in the boundary and outside the supercell crystal, and the Fourier antitransform of Eq. 2.79 can be safely done in order to obtain the Wannier rotated potential change matrix elements on the fine electron momentum $\mathbf{k}'$ and phonon momentum $\mathbf{q}'$-point meshes as follows:

$$\tilde{g}^{s\alpha}_{mn}(\mathbf{k}',\mathbf{q}') = \sum_{\mathbf{T}_e,\mathbf{T}_p} e^{i(\mathbf{k}'\cdot\mathbf{T}_e+\mathbf{q}'\cdot\mathbf{T}_p)}\tilde{g}^{s\alpha}_{mn}(\mathbf{T}_e,\mathbf{T}_p). \tag{2.80}$$

The Wannier rotated potential change matrix elements are then transformed to the Bloch representation with the knowledge of the unitary matrices

$U_{mn}(\mathbf{k}')$ on the fine $\mathbf{k}'$-point mesh as follows:

$$g^{s\alpha}_{mn}(\mathbf{k}', \mathbf{q}') = \sum_{i,j} U_{mi}(\mathbf{k}' + \mathbf{q}') g^{s\alpha}_{ij}(\mathbf{k}', \mathbf{q}') \big(U_{nj}(\mathbf{k}')\big)^*, \tag{2.81}$$

and finally, one obtains the electron-phonon matrix elements $g^{\nu}_{mn}(\mathbf{k}', \mathbf{q}')$ on the fine $\mathbf{k}'$ and $\mathbf{q}'$-point grids by means of Eq. 2.6. The frequencies and polarization vectors $\epsilon^{s\alpha}_{\mathbf{q}'\nu}$ and $\omega_{\mathbf{q}'\nu}$ on the fine $\mathbf{q}'$-point mesh are obtained by simply Fourier interpolating the dynamical matrix (Eq. 1.53), whose Fourier transform is also highly localized in the real space, as seen in Fig. 2.6(b) for the largest components of the MoS_2 monolayer. Figure 2.7 illustrates schematically the steps to follow in the Wannier interpolation procedure of the electron-phonon matrix elements [4, 138–140].

Chapter 3

Electron-phonon interaction at the Tl/Si(111) surface

At the surface, crystals are characterized by the loss of periodicity and the corresponding breakdown of the inversion symmetry with respect to the surface plane. This makes the potential felt by the electrons be different from that of the bulk, giving rise to the so-called surface electron states, whose density probability amplitudes are strongly localized near the surface of the material and exponentially decay into the bulk [144, 145]. Similarly, the lack of the inversion symmetry also promotes the existence of the so-called surface phonon modes, whose polarization vector amplitudes mainly involve the vibration of ions close to the surface [146, 147]. In most of the cases, the surface electron states and the potential changes induced by the surface phonon modes are localized in the real space, leading to a large overlap that tends to enlarge the electron-phonon matrix elements (Eq. 2.6). In this regard, the electron-phonon interaction has been investigated in several surface systems, where it has been established that, as a general rule, the coupling is enhanced [41–46].

In non-magnetic materials, the combination of both time-reversal symmetry, i.e. $\varepsilon_{\mathbf{k}n}(\uparrow) = \varepsilon_{-\mathbf{k}n}(\downarrow)$, and inversion symmetry, i.e. $\varepsilon_{\mathbf{k}n}(\uparrow) = \varepsilon_{-\mathbf{k}n}(\uparrow)$, implies that the electron states with the same band index n at the same momentum $\mathbf{k}$ but with opposite spin directions must be spin-degenerate, i.e. $\varepsilon_{\mathbf{k}n}(\uparrow) = \varepsilon_{\mathbf{k}n}(\downarrow)$. With the breakdown of the inversion symmetry at surfaces, only the time-reversal symmetry is maintained, and the spin-degeneracy condition is released, i.e. $\varepsilon_{\mathbf{k}n}(\uparrow) \neq \varepsilon_{\mathbf{k}n}(\downarrow)$. Under these conditions, the spin-orbit coupling, far from be a mere relativistic energy correction, introduces important qualitative changes in the electronic properties of surface materials, such as the generation of spin-split and spin-polarized electron states, even in nominally non-magnetic surfaces. This is the so-called Rashba effect [148]. The first experimental observation of spin-split surface electron states was made by LaShell *et al.* in 1996 on the Au(111)

noble surface ($Z = 79$) by an ARPES experiment [149]. Later, the interpretation of spin-polarized bands was confirmed by an spin-resolved ARPES experiment [150], in good agreement with theoretical calculations [151]. It turns out that both the spin-splitting and the spin-polarization of the surface states on the Au(111) surface are well described with the Rashba model, which approximates in a simple way the effects of the spin-orbit coupling on a two-dimensional (2D) free electron gas. In the Rashba model, the original spin-degenerate 2D parabolic band is spin-split into two isotropic spin-split parabolas with opposite chiral spin-polarizations lying on the surface plane and perpendicular to the electron momentum (Appendix E). Since then, additional Rashba-like spin-splittings have been discovered in many other clean metallic terminations [47, 48, 152–159], encouraged by an increasing interest in non-magnetic surfaces with strong spin-orbit coupling as a new promising source for emergent spintronic applications [62–67].

Moreover, large anisotropic spin-splittings and peculiar spin-polarization structures that deviate from the Rashba model have been theoretically predicted and experimentally detected during the last decade on a large variety of clean surfaces covered by heavy elements, in order to take advantage of their strong atomic spin-orbit interaction [49–51]. This was first reported by Ast *et al.* in 2007 when analyzing the spectrum of the Ag(111) surface ($Z = 47$) doped with the heavy element Bi ($Z = 83$) using ARPES techniques [160]. They concluded that the measured giant spin-splitting of ~ 200 meV results from the additional breakdown of the surface in-plane inversion symmetry, leading thus to a considerably out-of-plane rotation of the spin-polarization. The potential technological importance of this finding for possible spintronic applications [62–67] accelerated the search for similar spin-splitting effects specially on semiconductor surfaces, such as Si ($Z = 14$) and Ge ($Z = 32$), covered by heavy element ($Z > 79$) monolayers [52–61]. In particular, the semiconductor Si(111) termination covered by a Tl monolayer ($Z = 81$), i.e. the Tl/Si(111) surface, exhibits the largest spin-splitting energy (~ 600 meV) reported in literature, due to its specific crystal structure together with the strong atomic spin-orbit coupling of the heavy element Tl adatoms [161–166]. These systems exhibit a set of well-defined and exceptionally large spin-split surface states within the bulk band gap near the Fermi level, accompanied by out-of-plane spin-polarization patterns. The latter ensure a robust spin-dependent 2D character of the electronic transport properties, almost in the absence of any appreciable bulk contribution. Therefore, understanding the charge and spin coupled dynamics in 2D systems with strong spin-orbit coupling is of capital importance and a very active research front at the moment [68–70].

Surface band splittings due to the spin-orbit coupling can be of the order of 100 meV close to the Fermi level, as for instance on the Au(111) surface [149], competing in magnitude with typical phonon frequencies in the low-energy domain of electronic excitations. Therefore, any study of the

electron-phonon interaction at surfaces with strong relativistic effects should include the spin-orbit coupling not only as an energy correction but also as a responsible for the generation of an entire spin-polarized electronic structure that modulates the phonon-mediated electronic scattering. In this regard, the coexistence of both, spin-orbit and electron-phonon interactions, has been historically investigated considering theoretical models based on the Frhlich and Holstein Hamiltonians [72–74]. Moreover, first-principles calculations had limited to treat the role of the spin-orbit coupling in the electron-phonon interaction as simple relativistic corrections of the electron energy and phonon frequency [167, 168]. Recently, concurrent works with this thesis have illustrated some important aspects related to the spin-polarization in 2D systems. Some examples are the spin and valley-dependent phonon-mediated scattering in transition-metal dichalchogenides [76, 77] and the absence of backscattering in topological surface states [78].

In this chapter, we provide a comprehensive first principles analysis of the role played by the electron spin and the spin-orbit coupling in the electron-phonon interaction of the relativistic Tl/Si(111) surface. In Sec. 3.1.1, we briefly introduce the theoretical framework for explicitly incorporating the electron spin degree of freedom together with relativistic effects up to the spin-orbit coupling within the DFT and DFPT formalisms, as well as in practical first principles calculations of the electron-phonon interaction. Section 3.2 is devoted to present the crystal structure of the Tl/Si(111) surface, as well as its singular electronic and lattice vibrational properties calculated from first principles. In this regard, we compare relativistic results taking into account and neglecting the spin-orbit coupling, in order to appreciate its effects on the Tl/Si(111) surface. This information will be essential in Sec. 3.3 for analyzing the impact of surface state spin-polarizations induced by the spin-orbit coupling on first principles calculations of the electron-phonon interaction of the Tl/Si(111) surface. The spin-polarization of the spin-split surface states offers the possibility of explicitly investigating the spin-dependence of the electron-phonon coupling in two regimes radically different. On the one hand, Rashba model-like surface in-plane spin polarizations lead to a strong spin-dependent electron-phonon interaction. On the other hand, surface out-of-plane spin polarizations lead to a spin-suppression of the electron-phonon interaction. Finally, in Sec. 3.4 a summary of the results and the main conclusions drawn in this chapter are given.

3.1 Electron spin and relativistic effects

In this section, we will present the extension of both DFT and DFPT formalisms for including both the electron spin degree of freedom and relativistic effects up to the spin-orbit coupling, i.e. spin-DFT spin-DFPT, in Sec. 3.1.1 and 3.1.2, respectively. Section 3.1.3 will be devoted to describe the

way the electron spin enters into first principles calculations of the electron-phonon interaction through the coupling matrix elements.

3.1.1 Spin-density functional theory

The DFT formalism as described in Sec. 1.3.1 is based on non-relativistic quantum mechanics, which ignores the spin degree of freedom of the electron and the Einstein's special relativity [169]. However, the explicit treatment of the electron spin is mandatory in the determination of a wide variety of properties of matter, such as magnetism [170]. It is also mandatory for taking into account relativistic effects, which are crucial for the correct description of the electronic and lattice vibrational properties in both magnetic and non-magnetic materials [171]. In fact, non-relativistic mechanics gives results with a leading error of the order of $(v/c)^2$, where v is the electron velocity and c is the speed of light [106, 172]. For isolated atoms, this error is of the order of $(Z\alpha)^2$, with $\alpha = 1/c \approx 1/137$ the dimensionless fine structure constant, leading to too large relativistic corrections in systems containing heavy atoms [173][1]. In such cases, an extension of DFT including both the electron spin and relativistic effects, i.e. spin-DFT, is imperative.

Spin-DFT was founded a decade after the standard formalism and is based on the idea that the energy of a many-body electronic system in its fundamental state is defined as a functional not only of the electron charge density $n(\mathbf{r})$ but also of the electron spin magnetization density vector $\mathbf{m}(\mathbf{r})$ [174–177]. Within this formalism and in the absence of magnetic fields, the exact ground-state energy of the electronic system is the global minimum value of the energy functional, which is determined by the exact ground-state electron charge and spin magnetization densities[2]. As standard DFT, the system of many interacting electrons moving in an external potential is replaced by an auxiliary Kohn-Sham system of non-interacting electrons moving in an effective potential, i.e. the electronic screened external potential, on the condition that both systems have the same ground-state electron charge and spin magnetization densities, $n_0(\mathbf{r})$ and $\mathbf{m}_0(\mathbf{r})$, respectively.

Within the spin-DFT formalism, the Kohn-Sham single-electron eigenstates are generalized by two-component spinors, which explicitly incorporate the space of the electron spin spanned by $|\pm\rangle$:

$$|\psi_{\mathbf{k}n}\rangle \otimes |\pm\rangle = |\psi^{\sigma}_{\mathbf{k}n}\rangle = \begin{pmatrix} |\psi^{+}_{\mathbf{k}n}\rangle \\ |\psi^{-}_{\mathbf{k}n}\rangle \end{pmatrix}, \tag{3.1}$$

where the index σ is the quantum number accounting for the spin degree of freedom. Note that the spinorial structure of the electron wave function in

[1] $(Z\alpha)^2 \sim 30\%$ for a tungsten, or wolfram, atom with $Z = 74$.

[2] $E^0_{\mathrm{el}} = E_{\mathrm{el}}[n_0, \mathbf{m}_0] < E_{\mathrm{el}}[n, \mathbf{m}]$, $\forall\, n(\mathbf{r}) \neq n_0(\mathbf{r})$ and $\mathbf{m}(\mathbf{r}) \neq \mathbf{m}_0(\mathbf{r})$

Eq. 3.1 makes possible the non-collinear character of the spin polarization, i.e. the possibility of the electron state to be spin-polarized in any direction in space. Likewise, the electron charge and spin magnetization densities are compactly given by the charge- and spin-density 2×2 matrix, which is defined in terms of the Kohn-Sham spinors as follows:

$$\begin{aligned} n_{\sigma\sigma'}(\mathbf{r}) &= \frac{1}{N_{\mathbf{k}}} \sum_{\mathbf{k}}^{1\mathrm{BZ}} \sum_{n} f(\varepsilon_{\mathbf{k}n}) \big(\psi^{\sigma}_{\mathbf{k}n}(\mathbf{r})\big)^{*} \psi^{\sigma'}_{\mathbf{k}n}(\mathbf{r}) \\ &= \frac{1}{2} \begin{pmatrix} n(\mathbf{r}) + m_z(\mathbf{r}) & m_x(\mathbf{r}) - i m_y(\mathbf{r}) \\ m_x(\mathbf{r}) + i m_y(\mathbf{r}) & n(\mathbf{r}) - m_z(\mathbf{r}) \end{pmatrix}, \end{aligned} \tag{3.2}$$

From here, the charge density is explicitly given by:

$$n(\mathbf{r}) = \frac{1}{N_{\mathbf{k}}} \sum_{\mathbf{k}}^{1\mathrm{BZ}} \sum_{n} \sum_{\sigma} f(\varepsilon_{\mathbf{k}n}) \big|\psi^{\sigma}_{\mathbf{k}n}(\mathbf{r})\big|^2, \tag{3.3}$$

and the spin magnetization density vector is explicitly given by:

$$\mathbf{m}(\mathbf{r}) = \frac{1}{N_{\mathbf{k}}} \sum_{\mathbf{k}}^{1\mathrm{BZ}} \sum_{n} \sum_{\sigma\sigma'} f(\varepsilon_{\mathbf{k}n}) \big(\psi^{\sigma}_{\mathbf{k}n}(\mathbf{r})\big)^{*} \boldsymbol{\sigma}_{\sigma\sigma'} \psi^{\sigma'}_{\mathbf{k}n}(\mathbf{r}), \tag{3.4}$$

where $\boldsymbol{\sigma} = (\sigma_x, \sigma_y, \sigma_z)$ are the 2×2 Pauli matrices, related to the spin angular momentum operator as: $\hat{\mathbf{S}} = \frac{1}{2}\hat{\boldsymbol{\sigma}}$, and defined as:

$$\sigma_x = \begin{pmatrix} 0 & 1 \\ 1 & 0 \end{pmatrix}, \quad \sigma_y = \begin{pmatrix} 0 & -i \\ i & 0 \end{pmatrix}, \quad \sigma_z = \begin{pmatrix} 1 & 0 \\ 0 & -1 \end{pmatrix}. \tag{3.5}$$

The Kohn-Sham spinor wave functions in Eq. 3.1 are the solutions of the generalization of the Schrödinger equation in Eq. 1.13 for spin-$\frac{1}{2}$ particles, i.e. the so-called Schrödinger-Pauli equation [178]. The latter takes into account the interaction of electrons with a magnetic field $\mathbf{B}(\mathbf{r})$, described by the magnetic vector potential $\mathbf{A}(\mathbf{r})$, such that $\mathbf{B}(\mathbf{r}) = \boldsymbol{\nabla} \times \mathbf{A}(\mathbf{r})$. Neglecting current contributions, the Kohn-Sham Schrödinger-Pauli equation is given by the following pair of coupled differential eigenvalue equations:

$$\sum_{\sigma'} \left[\Big(\big(\hat{\mathbf{p}} - \hat{\mathbf{A}}(\mathbf{r})\big)^2 + \hat{V}_{\mathrm{KS}}(\mathbf{r}) \Big) \delta_{\sigma\sigma'} - \frac{1}{2} \hat{\boldsymbol{\sigma}}_{\sigma\sigma'} \cdot \hat{\mathbf{B}}(\mathbf{r}) \right] \psi^{\sigma'}_{\mathbf{k}n}(\mathbf{r}) = \varepsilon_{\mathbf{k}n} \psi^{\sigma}_{\mathbf{k}n}(\mathbf{r}). \tag{3.6}$$

In this thesis, we focus on nominally non-magnetic materials, such that $\mathbf{A}(\mathbf{r}) = 0$ and $\mathbf{B}(\mathbf{r}) = 0$ in Eq. 3.6, and $\mathbf{m}(\mathbf{r}) = 0$ in Eq. 3.4, retaining only $n(\mathbf{r}) \neq 0$ in Eq. 3.2. On the other hand, we are interested in including relativistic effects in our theoretical framework. In relativistic quantum mechanics, the proper way to describe any system of spin-$\frac{1}{2}$ massive particles is the Dirac equation [179, 180]. For simplicity, the quasi-relativistic limit ($v/c \ll 1$) of the Dirac equation is adopted, which is equivalent to the Schrödinger-Pauli equation including relativistic effects up to

order $(v/c)^2$ [172] (Appendix F). In the absence of magnetic fields, the quasi-relativistic generalization of the Kohn-Sham Schrödinger equation is given by the following pair of coupled differential eigenvalue equations:

$$\sum_{\sigma'} \hat{H}^{\sigma\sigma'}_{\mathrm{KS}} \psi^{\sigma'}_{\mathbf{k}n}(\mathbf{r}) = \sum_{\sigma'} \left(-\frac{\hat{\boldsymbol{\nabla}}^2}{2}\delta_{\sigma\sigma'} + \hat{V}^{\sigma\sigma'}_{\mathrm{KS}}(\mathbf{r}) \right) \psi^{\sigma'}_{\mathbf{k}n}(\mathbf{r}) = \varepsilon_{\mathbf{k}n}\psi^{\sigma}_{\mathbf{k}n}(\mathbf{r}), \quad (3.7)$$

where the spinor coefficients $|\psi^{\pm}_{\mathbf{k}n}\rangle$ are coupled due to the spin-dependence of the relativistic Kohn-Sham potential $V^{\sigma\sigma'}_{\mathrm{KS}}(\mathbf{r})$. The latter is a 2×2 matrix in the spin-space and is defined as (Appendix F):

$$V^{\sigma\sigma'}_{\mathrm{KS}}(\mathbf{r}) = \big(V_{\mathrm{ext}}(\mathbf{r}) + V_{\mathrm{H}}(\mathbf{r}) + V_{\mathrm{xc}}(\mathbf{r}) + \Delta H_{\mathrm{mv}} + \Delta H_{\mathrm{D}}\big)\delta_{\sigma\sigma'} + \Delta H^{\sigma\sigma'}_{\mathrm{SO}}. \quad (3.8)$$

The first three terms on the right-hand side of Eq. 3.8 have been already introduced in the standard DFT formalism (Sec. 1.3.1). The fourth and fifth terms are the so-called scalar relativistic effects and correspond to the mass-velocity and Darwin corrections, ΔH_{mv} and ΔH_{D}, respectively. The latter terms are called scalar relativistic, since, despite their relativistic nature, they are spin-independent and act equivalently as an scalar interaction term for each spinor component. Finally, the sixth term corresponds to the so-called spin-orbit interaction, i.e. the coupling between the spin and the orbital angular momenta of the electron. In the quasi-relativistic limit, the spin-orbit interaction term may be written as:

$$\Delta H_{\mathrm{SO}} = \frac{1}{4c^2}\boldsymbol{\sigma}\cdot\big(\boldsymbol{\nabla}V(\mathbf{r})\times\mathbf{p}\big), \quad (3.9)$$

where $V(\mathbf{r})$ is the effective potential acting on electrons. Eq. 3.9 can be illustrated within classical elecrodynamics. An electron moving with momentum $\mathbf{p}$ in the potential $V(\mathbf{r})$ experiences a magnetic field in its rest frame of reference that arises from the relativistic Lorentz transformation including the Thomas precession of the electric field resulting from the gradient of the potential, i.e. $\mathbf{B} = -\big(\boldsymbol{\nabla}V(\mathbf{r})\times\mathbf{p}\big)/(2c^2)$ [181]. The interaction of the electron spin with this magnetic field leads to the spin-orbit coupling term: $\Delta H_{\mathrm{SO}} = -\mathbf{S}\cdot\mathbf{B}$, equivalent to Eq. 3.9.

In the absence of magnetic fields, the spin-orbit interaction is the only spin-dependent 2×2 matrix responsible of coupling the spinor coefficients in Eq. 3.7. Note that the latter can only be taken into account if the spinorial definition of the electron wave function in Eq. 3.1 is incorporated into first principles calculations. In fact, a non-collinear spin-DFT calculation is said to be fully relativistic if the spin-orbit interaction is included within the Kohn-Sham potential in Eq. 3.8, i.e. all the relativistic effects up to order $(v/c)^2$ are included. Instead, if not included, the pair of coupled eigenvalue equations in Eq. 3.7 are disconnected.

It is worth noting that relativistic effects originate close to the ionic cores in solids, while the intersticial regions remain well-described in the

non-relativistic limit [171]. In practice, spin-DFT calculations include relativistic interaction terms up to the spin-orbit coupling in a self-consistent manner within the pseudopotentials that form the external potential acting on electrons (Appendix B) [81]. Moreover, within spin-DFT, $V_{\rm xc}$ is commonly approximated either with the so-called spin-LDA [182] or spin-GGA [183, 184], although it has also been seen that the differences using non-relativistic exchange-correlation energy functionals in relativistic calculations are small [185–188]. In summary, Eqs. 3.3−3.8 compose the set of relativistic spin-dependent Kohn-Sham equations that must be self-consistently solved as the standard and spin-independent DFT scheme in Fig. 1.1.

3.1.2 Spin-density functional perturbation theory

The incorporation of the electron spin into the DFPT formalism is easily done by starting from the spin-density 2×2 matrix in Eq. 3.2 and following the same derivations as in Sec. 1.4 for the spin-independent theory. Thereby, one first arrives to the following expression of the dynamical matrix:

$$D_{ss'}^{\alpha\alpha'}(\mathbf{q}) = \frac{1}{\sqrt{M_s M_{s'}}}\Bigg[\sum_{\sigma\sigma'}\int\left(\frac{\partial n_{\sigma\sigma'}(\mathbf{r})}{\partial u_{s'}^{\alpha'}(\mathbf{q})}\right)^{*}\frac{\partial V_{\rm ext}^{\sigma\sigma'}(\mathbf{r})}{\partial u_s^{\alpha}(\mathbf{q})}{\rm d}\mathbf{r} + \sum_{\sigma\sigma'}\int n_{\sigma\sigma'}(\mathbf{r})\frac{\partial^2 V_{\rm ext}^{\sigma\sigma'}(\mathbf{r})}{\left(\partial u_s^{\alpha}(\mathbf{q})\right)^{*}\partial u_{s'}^{\alpha'}(\mathbf{q})}{\rm d}\mathbf{r} + \frac{\partial^2 E_{\rm ion}}{\left(\partial u_s^{\alpha}(\mathbf{q})\right)^{*}\partial u_{s'}^{\alpha'}(\mathbf{q})}\Bigg]_{u=0}, \tag{3.10}$$

where the electron spin is included through the product between the first-order derivatives with respect to the ionic displacements of the spin-density and the external potential, which are spin-dependent 2×2 matrices. In this way, one arrives to the following set of equations:

$$\frac{\partial V_{\rm KS}^{\sigma\sigma'}(\mathbf{r})}{\partial u_s^{\alpha}(\mathbf{q})} = \frac{\partial V_{\rm ext}^{\sigma\sigma'}(\mathbf{r})}{\partial u_s^{\alpha}(\mathbf{q})} + \int K_{\tau\tau'}^{\sigma\sigma'}(\mathbf{r},\mathbf{r}')\frac{\partial n^{\tau\tau'}(\mathbf{r}')}{\partial u_s^{\alpha}(\mathbf{q})}{\rm d}\mathbf{r}', \tag{3.11}$$

$$\frac{\partial n_{\sigma\sigma'}(\mathbf{r})}{\partial u_s^{\alpha}(\mathbf{q})} = \frac{1}{N_{\mathbf{k}}}\sum_{\mathbf{k}}^{\rm 1BZ}\sum_{n} f(\varepsilon_{\mathbf{k}n})\times \left(\left(\frac{\partial\psi_{\mathbf{k}n}^{\sigma}(\mathbf{r})}{\partial u_s^{\alpha}(\mathbf{q})}\right)^{*}\psi_{\mathbf{k}n}^{\sigma'}(\mathbf{r}) + \left(\psi_{\mathbf{k}n}^{\sigma}(\mathbf{r})\right)^{*}\frac{\partial\psi_{\mathbf{k}n}^{\sigma'}(\mathbf{r})}{\partial u_s^{\alpha}(\mathbf{q})}\right), \tag{3.12}$$

$$\sum_{\sigma'}\hat{H}_{\rm KS}^{\sigma\sigma'}\frac{\partial\psi_{\mathbf{k}n}^{\sigma'}(\mathbf{r})}{\partial u_s^{\alpha}(\mathbf{q})} + \frac{\partial\hat{V}_{\rm KS}^{\sigma\sigma'}}{\partial u_s^{\alpha}(\mathbf{q})}\psi_{\mathbf{k}n}^{\sigma'}(\mathbf{r}) = \frac{\partial\varepsilon_{\mathbf{k}n}}{\partial u_s^{\alpha}(\mathbf{q})}\psi_{\mathbf{k}n}^{\sigma}(\mathbf{r}) + \varepsilon_{\mathbf{k}n}\frac{\partial\psi_{\mathbf{k}n}^{\sigma}(\mathbf{r})}{\partial u_s^{\alpha}(\mathbf{q})}, \tag{3.13}$$

$$\frac{\partial\varepsilon_{\mathbf{k}n}}{\partial u_s^{\alpha}(\mathbf{q})} = \sum_{\sigma\sigma'}\left\langle\psi_{\mathbf{k}n}^{\sigma}\middle|\frac{\partial\hat{V}_{\rm KS}^{\sigma\sigma'}}{\partial u_s^{\alpha}(\mathbf{q})}\middle|\psi_{\mathbf{k}n}^{\sigma'}\right\rangle, \tag{3.14}$$

which conform the set of spin-dependent coupled Sternheimer equations that must be self-consistently solved as the spin-independent DFPT scheme in Fig. 1.2. It is worth noting that, in the spin-dependent case, the Hartree and exchange-correlation kernel in Eq. 3.11, as well as the spin-density response functions within the linear response theory, is a spin-dependent 4×4 matrix [166].

3.1.3 Coupled spin and electron-phonon matrix elements

As seen above, the main features of the spin-dependent formalism are the spinorial structure of the Kohn-Sham electron states in Eq. 3.1 and the 2×2 matrix structure of the change in both electron spin-density in Eq. 3.12 and spin-dependent Kohn-Sham potential in Eq. 3.11. Thus, in first principles calculations of the electron-phonon interaction, the electron spin is included within the electron-phonon matrix elements, which now become the scalar product between Kohn-Sham spinors via the phonon-induced change of the spin-dependent 2×2 Kohn-Sham potential:

$$\begin{aligned} g^{\nu}_{mn}(\mathbf{k},\mathbf{q}) &= \sum_{s\alpha} \frac{\epsilon^{s\alpha}_{\mathbf{q}\nu}}{\sqrt{2M_s\omega_{\mathbf{q}\nu}}} g^{s\alpha}_{mn}(\mathbf{k},\mathbf{q}) \\ &= \sum_{s\alpha} \frac{\epsilon^{s\alpha}_{\mathbf{q}\nu}}{\sqrt{2M_s\omega_{\mathbf{q}\nu}}} \sum_{\sigma\sigma'} \left\langle \psi^{\sigma}_{\mathbf{k}+\mathbf{q}m} \middle| \frac{\partial \hat{V}^{\sigma\sigma'}_{\mathrm{KS}}}{\partial u^{\alpha}_{s}(\mathbf{q})} \middle| \psi^{\sigma'}_{\mathbf{k}n} \right\rangle, \end{aligned} \tag{3.15}$$

We emphasize that, from the above equation, the electron-phonon matrix element measures the phonon-mediated electronic scattering amplitude between the general Kohn-Sham spinorial states $|\psi_{\mathbf{k}n}\rangle$ and $|\psi_{\mathbf{k}+\mathbf{q}m}\rangle$. Therefore, this terms accounts for both phonon-induced spin-conserving ($\sigma = \sigma'$) and spin-flip ($\sigma \neq \sigma'$) transitions due to the electron-phonon interaction. The spin-flip contributions to the electron-phonon coupling strength in non-magnetic materials are usually several orders of magnitude smaller than the spin-conserving contributions [189].

3.2 The Tl/Si(111) surface: electrons and phonons

In this section, we start describing the crystal structure of the Tl/Si(111) surface in Sec. 3.2.1. This is essential for understanding the first principles calculated ground-state electronic properties and lattice vibrational properties in Sec. 3.2.3 and Sec. 3.2.4, respectively. The computational methods are described in Sec. 3.2.2.

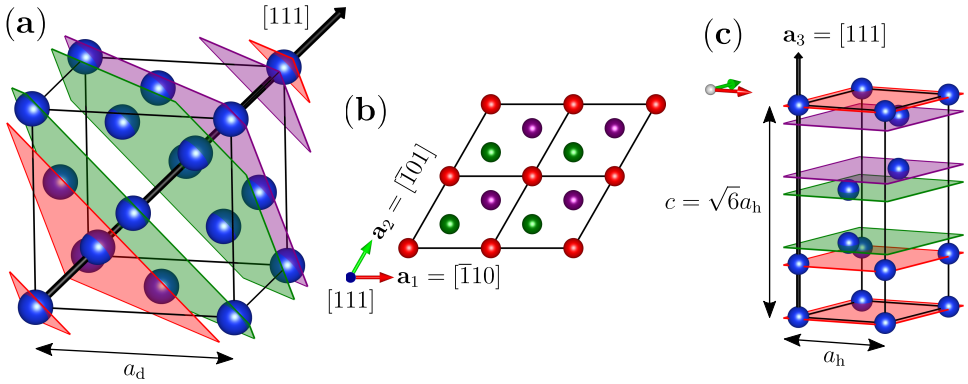

Figure 3.1. Crystal structure of the bulk silicon. (a) Along the [111] lattice direction, the conventional cubic unit cell of the diamond structure is formed by six (111) lattice planes with 2D hexagonal structure, stacked in an AABBCC arrangement, with A, B and C planes represented by red, green and magenta colors, respectively. (b) Top view of the in-plane 2D hexagonal structure. Red, green and magenta spheres represent the different relative atomic positions in the (111) plane according to the A, B and C arrangements, respectively. (c) The unit cell of the 2D hexagonal layered structure.

3.2.1 The crystal structure of the Tl/Si(111) surface

The substrate material of the Tl/Si(111) surface consists of the bulk silicon, which crystallizes in the diamond structrure with an experimental lattice parameter $a_d = 5.43$ Å [6] and whose conventional cubic unit cell is shown in Fig. 3.1(a). Along the [111] lattice direction (black vector), the diamond conventional unit cell can be seen as formed by six (111) lattice planes with 2D hexagonal structure that are stacked in a AABBCC arrangement, as represented by the red (A), green (B) and magenta (C) planes. Taking the [111] stacking direction as the cartesian $\hat{\mathbf{z}}$-axis, the unit cell of the 2D hexagonal layered structure (Fig. 3.1(b)) is described by the following direct lattice vectors:

$$\mathbf{a}_1 = a_h\hat{\mathbf{x}},\ \mathbf{a}_2 = -\frac{a_h}{2}(\hat{\mathbf{x}} + \sqrt{3}\hat{\mathbf{y}}),\ \text{and}\ \mathbf{a}_3 = c\,\hat{\mathbf{z}}, \tag{3.16}$$

and a basis of six atoms, or layers, one for each (111) lattice plane within the diamond conventional unit cell, whose positions in crystal coordinates are gathered in Table 3.1. The in-plane 2D hexagonal lattice parameter a_h is related to that of the diamond structure, a_d, by $a_h = a_d/\sqrt{2}$, and the lattice parameter perpendicular to the hexagonal plane is given by $c = \sqrt{6}a_h$. Figure 3.1(c) shows the conventional unit cell for the 2D hexagonal layered structure. Indeed, this is the crystal unit cell we will use for simulating the bulk silicon oriented along the [111] diamond lattice direction, and referred to as Si(111) in the following.

Table 3.1. The six atom basis of the hexagonal layered crystal unit cell.

Atom	Arrangement	Crystal coordinates		
		$\mathbf{a}_1$	$\mathbf{a}_2$	$\mathbf{a}_3$
1	A	0	0	0
2	A	0	0	1/4
3	B	1/3	1/3	1/3
4	B	1/3	1/3	7/12
5	C	2/3	2/3	2/3
6	C	2/3	2/3	11/12

Bulk thallium crystallizes in a standard hexagonal close-packed structure [6], and therefore, Tl adatoms represent an ideal candidate to deposit on top of the Si(111) substrate. Among the three possible adsorbing sites, low-energy electron diffraction (LEED) and x-ray scattering (XRS) experiments [190, 191], as well as first principles calculations [192], have confirmed that the so-called T_4 site represents the most stable binding configuration for the adsorption of Tl adatoms. In fact, when every T_4 site of the bulk-truncated Si(111) termination is covered by a Tl adatom, a well-ordered (1×1) Tl monolayer formed over the Si(111) surface is obtained, i.e. the Tl/Si(111) surface. This can be better understood by looking at Fig. 3.2, where the top and bottom panels represent the side and top view, respectively, of (a) the bulk-truncated Si(111) surface and (b) the Tl/Si(111) surface. In comparison with the bare Si(111) termination that presents an AABBCC arrangement, the Tl overlayer breaks with the stacking order and is arranged as the next-to-last Si layer, i.e. the T_4 site, leading to an AABBCB arrangement that conserves the 2D hexagonal layered crystal structure with lattice parameter a_{h} (red lines in Figs. 3.2(a) and(b)).

The Tl/Si(111) surface belongs to the $P3m1$ space group, exhibiting a C_{3v} symmetry, composed of a C_3 three-fold rotational symmetry and three σ_v mirror planes along the equivalent $[11\overline{2}]$ diamond lattice directions, represented by black lines in Fig. 3.2(c). Figure 3.2(d) displays the reciprocal lattice centered in the 2D surface BZ (SBZ) together with the high-symmetry $\overline{\Gamma}$, $\overline{\mathrm{M}}$ and $\overline{\mathrm{K}}(\overline{\mathrm{K}'})$ points represented by dots. While the whole C_{3v} symmetry is found at the $\overline{\Gamma}$ point, at the $\overline{\mathrm{M}}$ point the C_3 symmetry is lost but the specular symmetry (C_{1h}) is maintained. Conversely, at the $\overline{\mathrm{K}}(\overline{\mathrm{K}'})$ points, the C_3 symmetry is maintained but the mirror symmetry is lost. These symmetry considerations will be useful later for explaining the particular spin-polarization texture of spin-split surface states at the Tl/Si(111) surface.

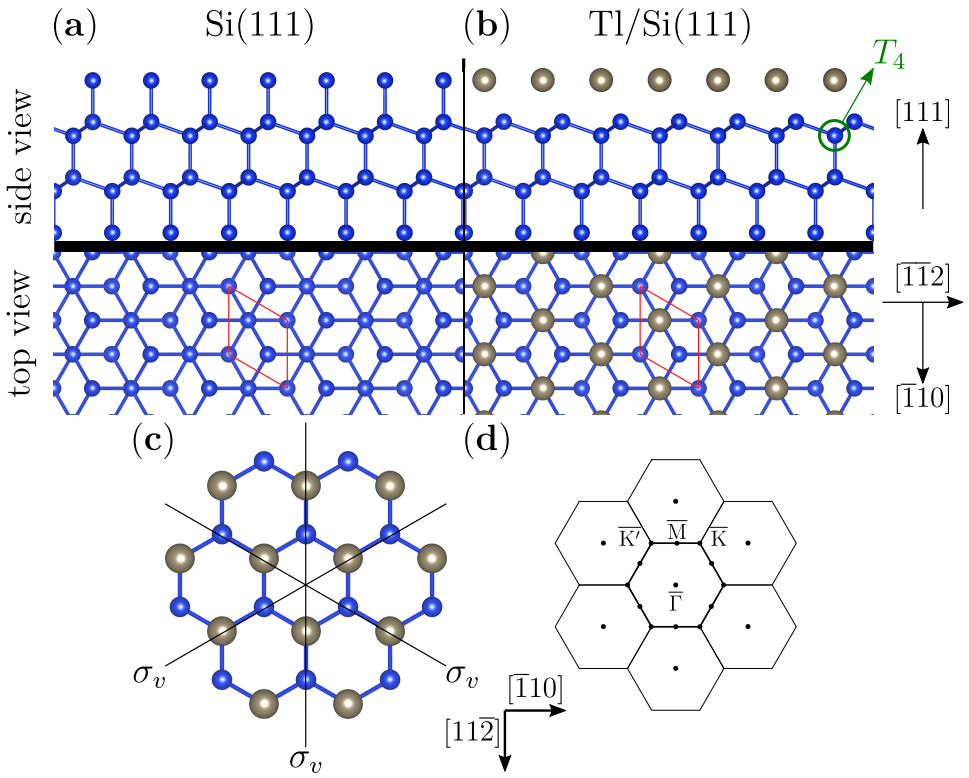

Figure 3.2. Side view (top) and top view (bottom) of (a) the bulk-truncated Si(111) and (b) the Tl/Si(111) surfaces. Big gray and small blue spheres represent the Tl monolayer and the Si substrate layers, respectively. The solid red lines display the in-plane 2D hexagonal unit cell with lattice parameter a_{h}. (c) Crystal structure of the Tl/Si(111) surface showing only the Tl monolayer and the last Si layer. The σ_v mirror planes are indicated by black lines. (d) Corresponding surface Brillouin zone with the high-symmetry points ($\overline{\Gamma}$, $\overline{\mathrm{M}}$ and $\overline{\mathrm{K}}(\overline{\mathrm{K}'}$)) indicated by black dots.

3.2.2 Computational methods

All the self-consistent first principles calculations have been performed within the non-collinear spin-DFT [174–177] and spin-DFPT [33] formalisms as implemented in the Quantum Espresso package [93, 94]. The exchange-correlation energy has been approximated within the Perdew-Burke-Ernzerhof (PBE) spin-GGA parametrization [90, 185]. An energy cutoff of 50 Ry has been used for the converged plane wave expansion. The norm-conserving pseudopotential approximation [97] has been used to include the $3s^2 3p^2 3d^0$ valence electrons in the case of the Si atom, and the $6s^2 6p^1 6d^0$ valence electrons in the case of the Tl atom. Likewise, fully relativistic pseudopotentials [188] have been constructed in order to take into account relativistic effects up to the spin-orbit interaction.

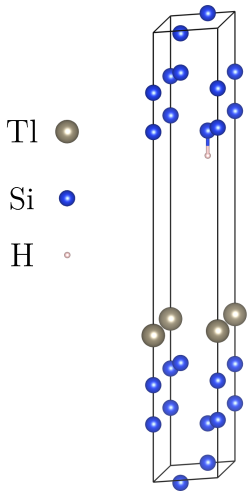

Figure 3.3. Schematic representation of the crystal unit cell employed for modeling the Tl/Si(111) surface using the slab technique. The hydrogen adlayer covering the opposite side of the slab is introduced in order to saturate the silicon dangling bonds.

The bulk Si(111) is simulated by the crystal unit cell shown in Fig. 3.1(c). A variable cell relaxation of the diamond structure using the present Si pseudo-potential gives a relaxed lattice parameter $a_{\mathrm{d}} = 5.47$ Å, which has a relative error less than 1% compared to the experimental value [6]. This value leads to the 2D hexagonal lattice parameter $a_{\mathrm{h}} = 3.87$ Å. The ground-state electronic properties of the bulk Si(111) are evaluated considering a $16 \times 16 \times 8$ Monkhorst-Pack **k**-point mesh in combination with fixed occupation factors, since the bulk silicon is a well-known semiconductor [6]. The lattice vibrational properties are obtained from a calculation of the dynamical matrices on a $4 \times 4 \times 2$ **q**-point mesh.

On the other hand, the Tl/Si(111) surface is a semi-infinite material that can not be simply reduced to a crystal unit cell repeated along the three direct lattice vectors in the real space, since periodicity is lost along the direction perpendicular to the surface. Thus, we simulate the Tl/Si(111) surface by means of the so-called slab technique. Within this procedure, the crystal unit cell must contain a sufficient amount of atoms along the surface-perpendicular direction in order to reproduce the properties of both, the bulk and the surface, and also needs to hold enough vacuum between the two sides of the slab for avoiding any interplay between the adjacent terminations. Figure 3.3 exhibits the crystal unit cell used for simulating the Tl/Si(111) surface, where the in-plane 2D hexagonal structure of the bulk Si(111) is maintained along the plane parallel to the surface. The considered slab consists of ten Si layers with a Tl monolayer on one termination of the slab. The silicon dangling bonds at the other end of the slab are saturated by

inserting a single hydrogen coverage [165, 166]. This is a common and safe procedure, since surface electron states associated to the hydrogen overlayer have usually binding energies well below the Fermi level, with a negligible interplay for the physical phenomena we are interested in. Besides, each slab is separated by a vacuum distance of 10.0 Å. Note that both the number of Si atoms for modeling the substrate and the vacuum distance considered are smaller than in previous works [165], in order to reduce the computational cost for the phonon calculations. The ground-state electronic properties of the Tl/Si(111) surface have been evaluated considering a 24×24 Monkhorst-Pack **k**-point mesh in combination with a fixed occupation smearing, since the Tl/Si(111) surface is a semiconductor with a gap [165, 166]. The lattice vibrational properties have been evaluated from dynamical matrices computed on a 8×8 **q**-point mesh. The equilibrium ionic positions are obtained by lattice geometry optimization (Sec. 1.4.1) with all the atomic forces relaxed up to at least 10^{-6} Ry/a_0.

3.2.3 Ground-state electronic properties

We focus now on the ground-state electronic properties of the Tl/Si(111) surface. The left-hand sides of Fig. 3.4 (a) and (b) display the electron band structure of the Tl/Si(111) surface with respect to the Fermi level (horizontal dotted black line) in the eV and meV range, respectively, while the right-hand sides show the corresponding DOS. The solid blue and dashed orange lines represent the calculations considering scalar relativistic effects and fully relativistic effects including the spin-orbit coupling, respectively. The shaded gray area illustrates the bulk band projection of the Si(111) substrate, which covers the energy continuum of all the electron states belonging to the bulk. Indeed, representing the band structure of the Tl/Si(111) surface along with the silicon bulk band projection is a valuable practice in order to distinguish the so-called surface states of pure 2D character from the so-called surface resonances of 3D nature. The surface states correspond to the energies that are not degenerate with the bulk continuum and emerge outside of it within the bulk forbidden band gap structure. Conversely, the surface resonances correspond to the energies that are degenerate with the bulk band projection. They can mix with bulk states and form states that propagate deep into the bulk.

In the case of the Tl/Si(111) termination, our scalar relativistic calculations clearly exhibit two spin-degenerate surface bands, labeled S_1 for the highest energy occupied surface states and S_2 for the lowest energy unoccupied surface states, lying within the forbidden silicon bulk band gap projection in the $(-1, 1)$ eV energy range. Likewise, a semiconductor state with an energy gap of ~ 380 meV is described. When the spin-orbit coupling is included, the S_1 surface band spin-splits into the $S_1^{\downarrow}$ and $S_1^{\uparrow}$ surface bands, dominating the low-energy region below the Fermi level. The S_2 surface band

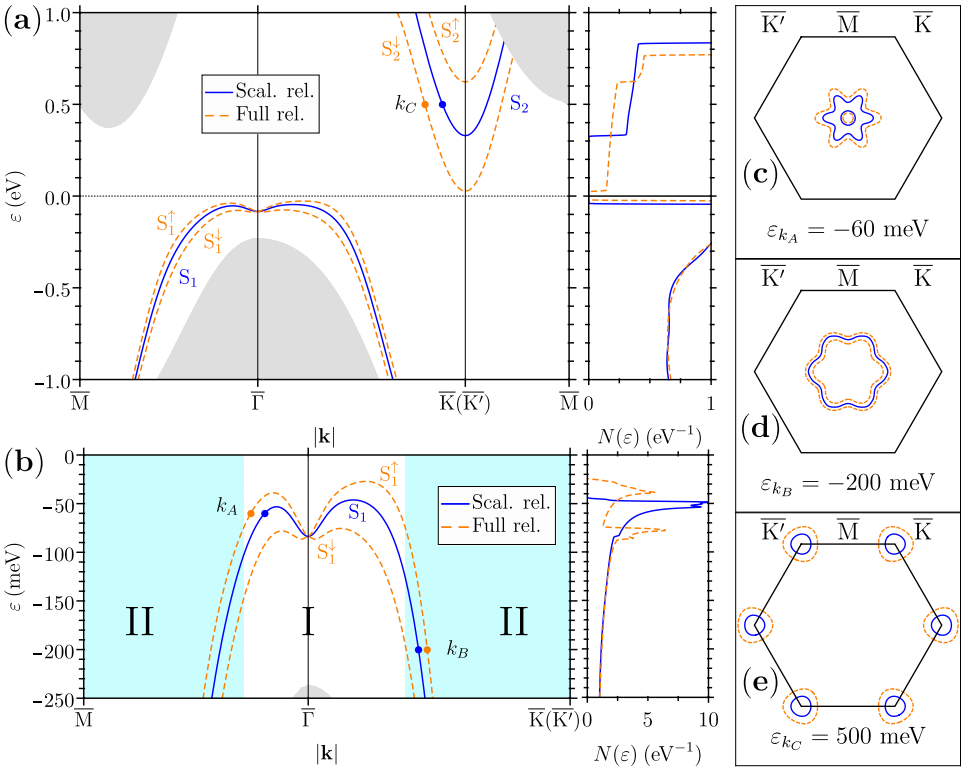

Figure 3.4. Electron band structure for the (a) eV and (b) meV energy ranges (left) and the corresponding DOS (right) of the Tl/Si(111) surface. The scalar and fully relativistic calculations are represented by solid blue and dashed orange lines, respectively. The gray shaded area in (a) denotes the bulk band projection of the Si(111) substrate. The energy contours of the surface states at (c) $\mathbf{k} = k_A$ with $\varepsilon_{k_A} = -60$ meV, (d) $\mathbf{k} = k_B$ with $\varepsilon_{k_B} = -200$ meV and (e) $\mathbf{k} = k_C$ with $\varepsilon_{k_C} = 500$ meV.

spin-splits into the $S_2^\downarrow$ and $S_2^\uparrow$ surface bands, yielding the strongest spin-split energy known in literature ($\sim$ 600 meV at the $\overline{\mathrm{K}}(\overline{\mathrm{K}'})$ points), dominating the low-energy region above the Fermi level. Thereby, the band gap strongly decreases up to a value of $\sim$ 60 meV. These calculations show an excellent agreement with photoemission measurements [161–164] and previous theoretical studies [165, 166]. Above the Fermi level, the strong spin-splitting assures that only intra-band electronic transitions will occur within the low-energy phase space (Fig. 3.4(a)). In contrast, below the Fermi level, the spin-splitting is not so large and the low-energy phase space is separated in two regions (Fig. 3.4(b)): region I (white shaded area), where intra-band electronic transitions between spin-split $S_1^\uparrow$ surface states dominate, and region II (cyan shaded area), where both intra-band and inter-band transitions are equally accessible for both spin-split $S_1^\uparrow$ and $S_1^\downarrow$ surface states.

Figures 3.4(c)-(e) represent the scalar (solid blue lines) and fully relativistic (dashed orange lines) constant energy contours for three selected representative momenta in the electron band structure plots in Figs. 3.4(a)-(b): k_A and k_B near the $\overline{\Gamma}$ point for the occupied surface bands, and k_C in the unoccupied $\overline{\mathrm{K}}(\overline{\mathrm{K}'})$ valley. The binding energies at k_A, k_B and k_C the energies are -60 meV, -200 meV and 500 meV, respectively. While the contours of the unoccupied surface band appear rather isotropic around the $\overline{\mathrm{K}}(\overline{\mathrm{K}'})$ valleys, the contours corresponding to the occupied surface bands present a hexagonal (daisy-flower-like) anisotropy. These features explain the 2D step-like structure of the DOS in the right side of Fig. 3.4(a) corresponding to the unoccupied quasi-parabolic valleys, as well as the one dimensional (1D)-like character at the top of the DOS right side of Fig. 3.4(b) corresponding to the occupied surface bands. Note that in the fully relativistic case, two 1D-like singularities distanced from about 40 meV are exhibited, one for each spin-split surface band.

Spin-polarization of the spin-split surface states

Together with the surface ground-state electronic structure, it is relevant to study the spin-polarization pattern of the spin-split surface states. The latter is defined as the expectation value of the Pauli spin-operator, i.e. $\mathbf{m}_{\mathbf{k}n} = \langle \psi_{\mathbf{k}n} | \boldsymbol{\sigma} | \psi_{\mathbf{k}n} \rangle$. This quantity measures the $\mathbf{k}$-dependence of the spin quantization axis for each spin-split surface band of index n, which due to its intrinsic strong spin-orbit coupling and the symmetry of the crystal exhibits a peculiar structure that deviates considerably from the Rashba model [193]. Figure 3.5 displays the calculated momentum-resolved spin-polarization texture of the spin-split surface bands $\mathrm{S}_1^{(\downarrow,\uparrow)}$ (top) and $\mathrm{S}_2^{(\downarrow,\uparrow)}$ (bottom) of the Tl/Si(111) surface. The black arrows and the color code represent the surface in-plane and out-of-plane components of the spin-polarization, respectively. Due to time-reversal symmetry, the surface states are spin-polarized in nearly opposite directions for each pair of spin-split bands, thereby assuring the non-magnetization of the material. A net spin-polarization exists for each spin-split surface band at any $\mathbf{k}$-point on the SBZ, except at the $\overline{\Gamma}$ and $\overline{\mathrm{M}}$ points. At these high symmetry points, the inversion symmetry due to the mirror plane in combination with the time-reversal symmetry forces the spin-degeneracy [194].

Close to the $\overline{\Gamma}$ point, the electron spin is chirally polarized in the plane of the surface and perpendicular to the momentum $\mathbf{k}$ for each spin-split surface band. In addition, each pair of spin-split surface bands are spin-polarized in the opposite direction, analogously to the Rashba model (Appendix E) [148]. However, the surface-perpendicular component of the spin polarization increases to the detriment of its in-plane components as we move away from the SBZ center along the $\overline{\Gamma\mathrm{K}}$ direction, until the spin is totally polarized perpendicular to the surface at the $\overline{\mathrm{K}}$ valley. The same happens along the

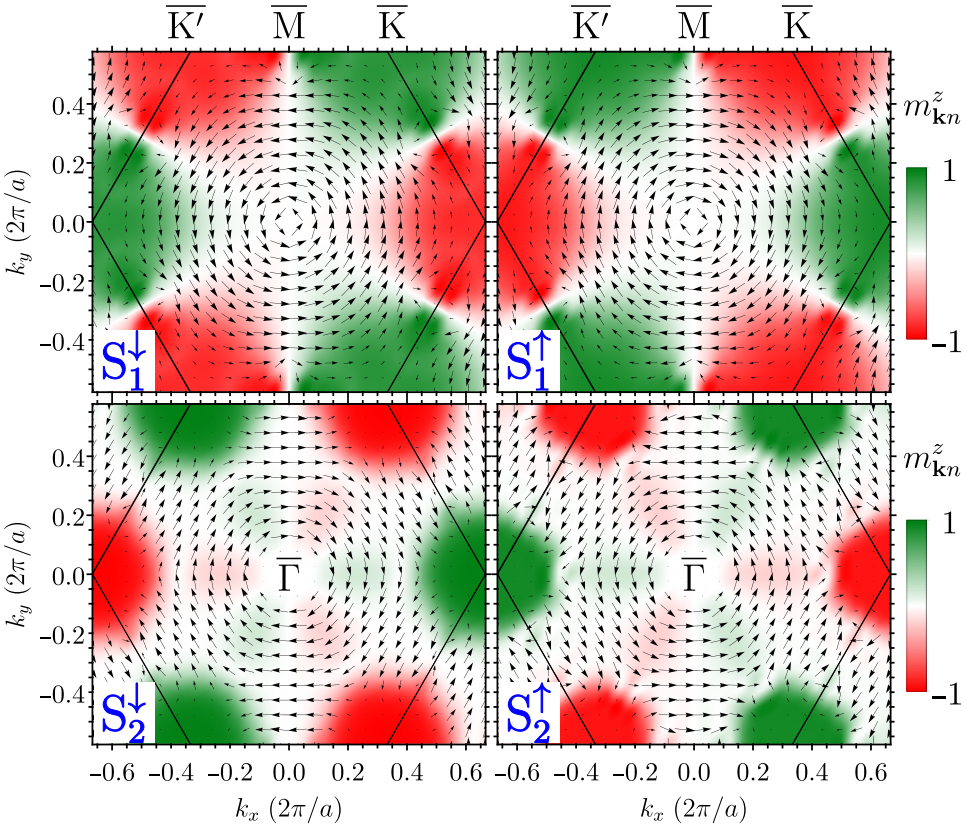

Figure 3.5. Momentum-dependent spin-polarization maps of the $S_1^{(\downarrow,\uparrow)}$ and $S_2^{(\downarrow,\uparrow)}$ surface bands in the surface BZ. Arrows (black) represent the in-plane component $m^x_{\mathbf{k}n}\,\hat{\mathbf{x}} + m^y_{\mathbf{k}n}\,\hat{\mathbf{y}}$, while the background color code shows the surface-perpendicular component $m^z_{\mathbf{k}n}$.

$\overline{\Gamma\mathrm{K}'}$ direction, with the spin at the $\overline{\mathrm{K}'}$ point being polarized in the opposite direction to $\overline{\mathrm{K}}$ for each spin-split surface band. The latter indicates that intraband backscattering between the spin-polarized $\overline{\mathrm{K}}$ and $\overline{\mathrm{K}'}$ valleys should be strongly suppressed in this system. Conversely, along the $\overline{\Gamma\mathrm{M}}$ direction, the surface states keep the Rashba model-like pure in-plane spin-polarization perpendicular to $\mathbf{k}$.

The different features of the spin-polarization can be rationalized in terms of orbital compositions looking at the cross product entering the spin-orbit coupling in Eq. 3.9. While the highest occupied $S_1/S_1^{(\downarrow,\uparrow)}$ surface states at the $\overline{\Gamma}$ point have a predominant out-of-plane polarized Tl and close-to-surface Si p_z orbital character, the lowest unoccupied $S_2/S_2^{(\downarrow,\uparrow)}$ surface states at the $\overline{\mathrm{K}}(\overline{\mathrm{K}'})$ points have a predominant in-plane polarized Tl $p_x + p_y$ orbital character. Since, close to the $\overline{\Gamma}$ point, the potential gradient is oriented along the surface-perpendicular direction $\hat{\mathbf{z}}$, the cross product $\boldsymbol{\nabla} V(\mathbf{r}) \times \mathbf{k}$ is parallel to the surface plane and perpendicular to the electron momentum,

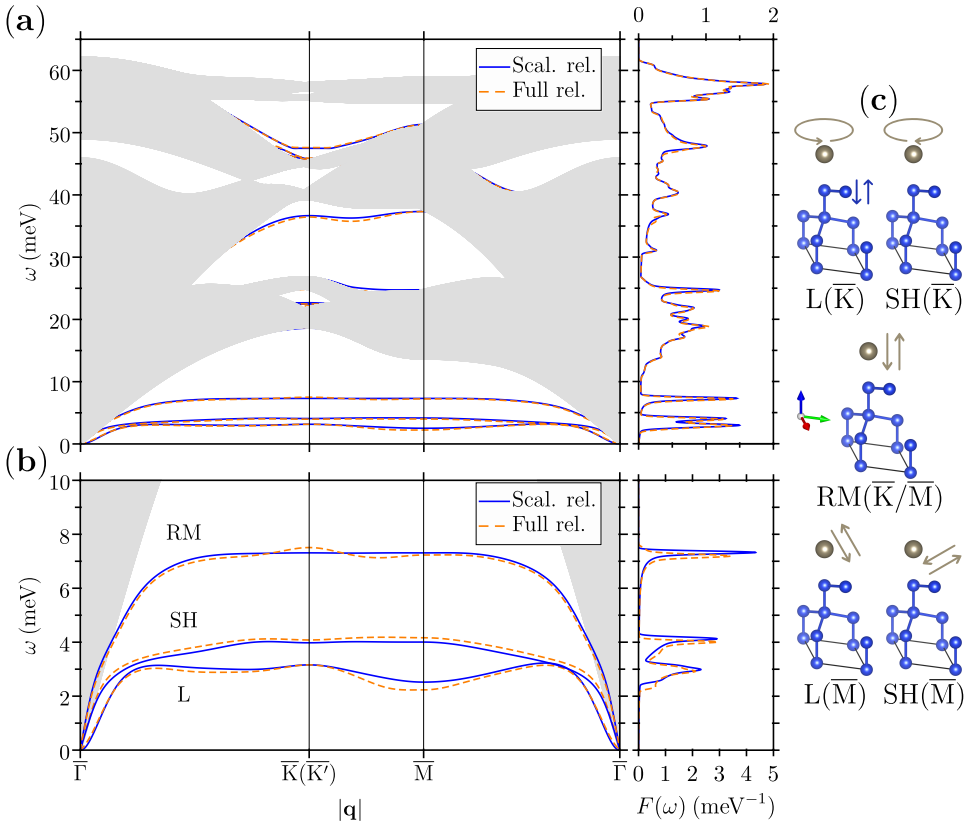

Figure 3.6. Phonon dispersion relation for the (a) 0-65 meV and (b) 0-10 meV frequency ranges (left) and the corresponding phDOS (right) of the Tl/Si(111) surface. The scalar and fully relativistic calculations are represented by solid blue and dashed orange lines, respectively. The gray shaded area denotes the bulk projection of the Si(111) substrate. (c) Schematic representation of the surface phonon modes with in-plane longitudinal (L) and shear horizontal (SH) polarization at $\mathbf{q} = \overline{\mathrm{K}}$ and $\overline{\mathrm{M}}$, and the out-of-plane Rayleigh mode (RM).

yielding a spin polarized in the plane. At the $\overline{\mathrm{K}}(\overline{\mathrm{K}'})$ point, however, the potential gradient is constrained in the plane of the surface, and thus, the spin aligns in the direction perpendicular to the plane.

3.2.4 Lattice vibrational properties

Let us now analyze the lattice vibrational properties of the Tl/Si(111) surface. The left-hand sides of Fig. 3.6(a) and (b) display the phonon dispersion relation of the Tl/Si(111) surface for the complete 0-65 meV and the low-frequency 0-10 meV vibrational frequency ranges, respectively, while the right-hand sides show the corresponding phDOS. The solid blue and dashed orange lines represent the lattice vibrational structure resulting from self-consistent DFPT calculations performed with scalar and fully relativistic

effects, respectively. The shaded gray area illustrates the bulk projection of the Si(111) substrate, which covers the frequency continuum of all the phonon modes belonging to the bulk. Similar to electrons, the so-called surface phonon modes are the branches emerging outside the bulk projection, while the branches within the bulk continuum are called surface vibrational resonances. From Fig. 3.6(a), we notice that there is no appreciable difference between the scalar and fully relativistic calculations in the vibrational structure. Figure 3.6(b) shows the three low-frequency acoustic surface phonon modes, which correspond fundamentally to localized vibrations connected to the Tl adatom displacements, as schematically represented in Fig. 3.6(c). Ordered by increasing frequency, we label these phonon branches according to their polarization. These are: the lowest-frequency in-plane polarized longitudinal (L) and transversal or shear horizontal (SH) modes, and the highest-frequency out-of-plane polarized Rayleigh mode (RM). In Fig. 3.6(c), we represent the polarization amplitudes for the L, SH and RM vibrational modes at the $\overline{\mathrm{K}}(\overline{\mathrm{K}'})$ and $\overline{\mathrm{M}}$ points. While the RM mode maintains an out-of-plane polarized vibration and a rather dispersionless branch at frequency of about 7 meV through the SBZ, L and SH branches exhibit a more heterogeneous behavior with frequencies roughly centered at 3 and 4 meV. Note that the chiral in-plane polarized modes at the $\overline{\mathrm{K}}(\overline{\mathrm{K}'})$ points are non-degenerate due to the broken symmetry, as seen experimentally in other 2D materials [195].

3.3 Coupled spin and electron-phonon interaction

In this section, we investigate the precise role played by the peculiar electron spin-polarization in Fig. 3.5 and the spin-orbit interaction in the electron-phonon interaction of the Tl/Si(111) surface. To this end, we proceed to compare scalar and fully relativistic first-principles calculations of the state-dependent Eliashberg functions, $\alpha^2 F^{\pm}_{\mathbf{k}n}$, and the electron-phonon coupling strength, $\lambda_{\mathbf{k}n}$, for the low-energy range close to the Fermi level. We divide the analysis in two different regimes: i) the lowest energy unoccupied surface states (Sec. 3.3.2) and ii) the highest energy occupied surface states (Sec. 3.3.3), due to their different spin textures. The computational methods are described in Sec. 3.3.1.

3.3.1 Computational methods

The electron-phonon matrix elements in Eq. 3.15 have been calculated considering the full-spinor Kohn-Sham electron states together with the spin-dependent first-order derivatives of the Kohn-Sham potential with respect to the ionic displacements. We considered a coarse grid of 24×24 **k**-points for electrons and one of 8×8 **q**-points for phonons. The SBZ integrals involved in the computation of $\alpha^2 F^{\pm}_{\mathbf{k}n}$ (Eq. 2.54) and $\lambda_{\mathbf{k}n}$ (Eq. 2.58) were performed

in very fine **k**-point and **q**-point grids by means of the Wannier interpolation scheme of electron-phonon matrix elements (Sec. 2.6.3). The Wannier interpolation was limited to the surface bands. Therefore, the sum over the electron band index runs over the S_1 and S_2 surface states for the scalar relativistic case, and $S_1^{(\downarrow,\uparrow)}$ and $S_2^{(\downarrow,\uparrow)}$ surface states for the fully relativistic case. For the phonon branch index, we considered all the phonon modes. In order to obtain numerically converged results, the SBZ integrals below the Fermi level are computed on fine 1000×1000 **k**-point and 1000×1000 **q**-point meshes. The delta functions $\delta(\varepsilon_{\mathbf{k}n} - \varepsilon_{\mathbf{k}+\mathbf{q}m} \pm \omega_{\mathbf{q}\nu})$ and $\delta(\omega - \omega_{\mathbf{q}\nu})$ were replaced by Gaussian functions, $\delta(x) = (\sigma\sqrt{2\pi})^{-1} \exp[-(x/\sigma)^2/2]$, with a smearing value of $\sigma = 2$ meV and 0.1 meV, respectively. On the other hand, converged SBZ integrals above the Fermi level are obtained on fine 3000×3000 **k**-point and 1500×1500 **q**-point meshes with the delta functions $\delta(\varepsilon_{\mathbf{k}n} - \varepsilon_{\mathbf{k}+\mathbf{q}m} \pm \omega_{\mathbf{q}\nu})$ and $\delta(\omega - \omega_{\mathbf{q}\nu})$ replaced by Gaussian functions with a smearing value of $\sigma = 6$ meV and 0.1 meV, respectively.

3.3.2 Spin-suppression of the electron-phonon interaction

We start focusing on the role played by the electron spin and the spin-orbit coupling in the electron-phonon interaction of the lowest energy unoccupied surface states in the Tl/Si(111) surface. Figure 3.7(a) shows the calculated $\lambda_{\mathbf{k}n}$ for the scalar relativistic S_2 surface band (solid blue line) and for the fully relativistic spin-split $S_2^{\downarrow}$ surface band (dashed orange line), as a function of the momentum **k** around the bottom of the $\overline{\mathrm{K}}$ valley along the high symmetry $\overline{\Gamma\mathrm{K}}$ and $\overline{\mathrm{KM}}$ directions. For the spin-split $S_2^{\uparrow}$ surface band, the phonon-mediated scattering with bulk electron states dominates and it is outside of the scope of this work. The contribution of the three low-frequency acoustic phonon modes represents 95% of the electron-phonon coupling strength of the lowest energy unoccupied surface states around the $\overline{\mathrm{K}}$ point, putting in evidence the large surface character of the electron-phonon interaction. This figure reflects the strinking quantitative and qualitative differences between the scalar and fully relativistic results. At $\overline{\mathrm{K}}$, the electron-phonon coupling strength for the spin-split $S_2^{\downarrow}$ surface state nearly vanishes ($\lambda_{\overline{\mathrm{K}},S_2^{\downarrow}} < 0.01$), which is in complete constrast with its spin-degenerate S_2 counterpart, where we find that $\lambda_{\overline{\mathrm{K}},S_2} = 0.35$. Likewise, moving away from the center of the $\overline{\mathrm{K}}$ valley, our calculations show that the mass enhancement parameter for the scalar relativistic surface band $\lambda_{\mathbf{k},S_2}$ remains about one order of magnitude stronger than that for the fully relativistic one $\lambda_{\mathbf{k},S_2^{\downarrow}}$. The reason of the step-like structure of $\lambda_{\mathbf{k},S_2}$ observed in the immediate vicinity of the $\overline{\mathrm{K}}$ point is that phonon-emitting electron scattering is not energetically accessible at the bottom of the $\overline{\mathrm{K}}$ valley. Hence, the term $\delta(\varepsilon_{\mathbf{k}n} - \varepsilon_{\mathbf{k}+\mathbf{q}m} + \omega_{\mathbf{q}\nu})$ does not contribute to Eq. 2.58, or equivalently the term $\alpha^2 F^{+}_{\mathbf{k}n}(\omega) = 0$ in Eq. 2.57. In fact, only phonon-emitting hole scattering processes are possible, which

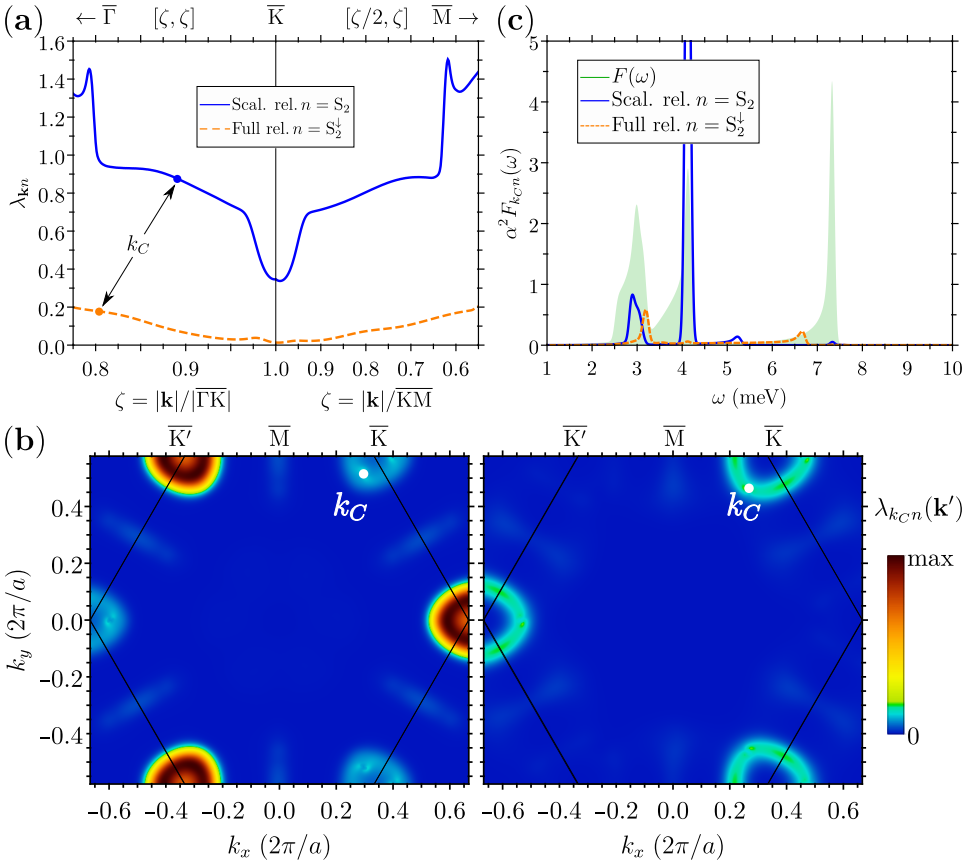

Figure 3.7. (a) State-dependent electron-phonon coupling strength $\lambda_{\mathbf{k}n}$ for the lowest energy unoccupied surface states around the $\overline{\mathrm{K}}$ valley along the high symmetry $\overline{\Gamma\mathrm{K}}$ and $\overline{\Gamma\mathrm{M}}$ directions. The solid blue and dashed orange lines display the results for the scalar relativistic S_2 and the fully relativistic spin-split $S_2^{\downarrow}$ surface bands, respectively. (b) $\mathbf{k}'$ momentum-resolved contribution map within the SBZ to $\lambda_{\mathbf{k}n}$ at the electron momentum $\mathbf{k} = k_C$ for the scalar S_2 (left) and the spin-split $S_2^{\downarrow}$ (right) surface bands. k_C is shown in Fig. 3.4(a). The color code represents the intensity of the $\lambda_{\mathbf{k}n}(\mathbf{k}')$ contribution. (c) The Eliashberg function, $\alpha^2 F_{\mathbf{k}n}(\omega)$, evaluated at $\mathbf{k} = k_C$ for the scalar S_2 and the spin-split $S_2^{\downarrow}$ surface bands, represented by the solid blue and dashed orange lines, respectively. The green area represents the phDOS in meV^{-1}.

means that solely the term $\delta(\varepsilon_{\mathbf{k}n} - \varepsilon_{\mathbf{k}+\mathbf{q}m} - \omega_{\mathbf{q}\nu})$ contributes to Eq. 2.58, or equivalently the term $\alpha^2 F^{-}_{\mathbf{k}n}(\omega) \neq 0$ in Eq. 2.57. However, as soon as the difference between the scalar S_2 surface state energy and that of the bottom of the valley equals, or is greater than, the smallest surface phonon frequency, i.e. $|\varepsilon_{\mathbf{k},S_2} - \varepsilon_{\overline{\mathrm{K}},S_2}| \geqslant \omega_{\mathrm{min}}$, phonon-emitting electron scattering events are also allowed, resulting in $\lambda_{\mathbf{k},S_2} \geqslant 0.7 = 2\lambda_{\overline{\mathrm{K}},S_2}$. As the momentum $\mathbf{k}$ moves further away from the center of the $\overline{\mathrm{K}}$ valley and the energy $\varepsilon_{\mathbf{k},S_2}$ increases, the electron-phonon coupling strength grows smoothly, following

the same trend as the DOS in the righ-hand side of Fig. 3.4(a). For the relativistic case, as the energy $\varepsilon_{\mathbf{k},S_2^{\downarrow}}$ increases, the electron-phonon coupling strength $\lambda_{\mathbf{k},S_2^{\downarrow}}$ increases smoothly up to values always not larger than 0.2 for the fully relativistic spin-split $S_2^{\downarrow}$ surface states.

Figure 3.7(b) represents the contribution[3] maps from each $\mathbf{k}'$-point on the SBZ to $\lambda_{\mathbf{k}n}$ (Eq. 2.58) for the scalar relativistic S_2 (left) and the fully relativistic spin-split $S_2^{\downarrow}$ (right) surface states at the fixed momentum $\mathbf{k} = k_C$ close to the $\overline{\mathrm{K}}$ point (left panel of Fig. 3.4(a)). Note that we have $\lambda_{k_C,S_2} = 0.88$ and $\lambda_{k_C,S_2^{\downarrow}} = 0.18$ (blue and orange dots, respectively, in Fig. 3.7(a)). The most obvious difference between the two maps appear at the momentum $\mathbf{k}' = \overline{\mathrm{K}'}$, where the contribution is maximum in the scalar relativistic case but results to be negligible in the fully relativistic one. This distinction can be rapidly rationalized by means of spinor overlap arguments. As seen in the bottom panels of Fig. 3.5, the spin-split unoccupied surface spinor states near the $\overline{\mathrm{K}}$ and $\overline{\mathrm{K}'}$ points have surface-perpendicular and opposite spin-polarizations. Therefore, phonon-mediated spin-flip $\overline{\mathrm{K}} \leftrightarrow \overline{\mathrm{K}'}$ inter-valley electronic transitions are strongly suppressed in the fully relativistic case. This is in complete contrast with the scalar relativistic case, where the spin-conserving inter-valley scattering channels are perfectly accessible and dominate the electron-phonon interaction (color code in Fig. 3.7(b)). On the other hand, the phonon-mediated spin-conserving $\overline{\mathrm{K}} \leftrightarrow \overline{\mathrm{K}}$ ($\overline{\mathrm{K}'} \leftrightarrow \overline{\mathrm{K}'}$) intra-valley electronic transitions count in the same manner for both scalar and fully relativistic cases, although with a noticeably smaller probability than the spin-conserving inter-valley processes.

In Fig. 3.7(c), we present the low-frequency range of the state-dependent Eliashberg spectral functions (Eq. 2.54) for the scalar relativistic S_2 and the fully relativistic $S_2^{\downarrow}$ surface states at $\mathbf{k} = k_C$, represented by the solid blue and dashed orange lines, respectively. The green area represents the phDOS in the right-hand side of Fig. 3.6(b). It is appreciated that both scalar and fully relativistic functions exhibit moderate peaks at frequencies near 3 meV and higher frequencies. These moderate peak indicate that the surface electrons at the unoccupied $\overline{\mathrm{K}}$ valley are weakly coupled to the longitudinal surface in-plane polarized and out-of-plane polarized acoustic phonon branches. However, while almost absent in the fully relativistic case, an outstandingly strong peak is also present at frequencies near 4 meV for the scalar relativistic $\alpha^2F_{\mathbf{k}n}(\omega)$. This evidences the strong coupling of surface electrons at the unoccupied $\overline{\mathrm{K}}$ valley to the transversal in-plane polarized acoustic phonon branch. This strong coupling is expected due to the surface in-plane p_x+p_y orbital character of the lowest energy unoccupied surface states at the $\overline{\mathrm{K}}$ valley (Sec. 3.2.3). Indeed, the most striking effect of including the electron spin in $\alpha^2F_{\mathbf{k}n}(\omega)$ is the suppression of the large

[3]The $\mathbf{k}'$-point contribution to $\lambda_{\mathbf{k}n}$ is defined such that: $\lambda_{\mathbf{k}n} = \sum_{\mathbf{k}'} \lambda_{\mathbf{k}n}(\mathbf{k}')/N_{\mathbf{k}'}$

peak at $\omega \approx 4$ meV in the fully relativistic case. This peak appears more than three orders of magnitude smaller than that of the scalar relativistic case, which is explained by the suppression of the phonon-mediated spin-flip inter-valley electronic scattering.

3.3.3 Spin-dependent strong electron-phonon interaction

We come now to describe the role played by the electron spin and the spin-orbit coupling in the the electron-phonon interaction of the highest energy occupied surface states in the Tl/Si(111) surface. Figure 3.8(a) shows the calculated $\lambda_{\mathbf{k}n}$ for the scalar S_1 (solid blue line) and the fully relativistic spin-split $S_1^{\uparrow}$ (short-dashed dark-orange line) and $S_1^{\downarrow}$ (long-dashed light-orange line) surface bands, as a function of the momentum $\mathbf{k}$ close to the $\overline{\Gamma}$ point along the high symmetry $\overline{\Gamma\mathrm{M}}$ and $\overline{\Gamma\mathrm{K}}$ directions. It is worth noting that the contribution of the three low-frequency acoustic phonon modes represents 90% of the electron-phonon coupling strength of the highest energy occupied surface states around the $\overline{\Gamma}$ point, reflecting the large surface character of the electron-phonon interaction. Regions I (white shaded area) and II (cyan shaded area) correspond to those in Fig. 3.4(b). In the fully relativistic case, $\lambda_{\mathbf{k}n}$ are damped by up to a factor of 3 compared to the scalar relativistic results within the region I, while they are of the same order of the scalar results within the region II. It is interesting that the largest values of the electron-phonon coupling strength for both scalar and fully relativistic cases are obtained within the region I, with $\lambda_{S_2} \sim 2.2$ and $\lambda_{S_2^{\uparrow}} \sim 1.4$, respectively. Indeed, the enhancement of the electron-phonon interaction in the region I is directly connected to the 1D-like DOS singularities of the occupied surface bands (right panel of Fig. 3.4(b)).

Figure 3.8(b) and (c) show the contribution map from each $\mathbf{k}'$-point on the SBZ to $\lambda_{\mathbf{k}n}$ for the scalar relativistic S_1 (left) and the fully relativistic spin-split $S_1^{\uparrow}$ (right) surface states at $\mathbf{k} = k_A$ within the region I and $\mathbf{k} = k_B$ within the region II, respectively. Note that we have $\lambda_{k_A,S_1} = 1.85$ and $\lambda_{k_A,S_1^{\uparrow}} = 0.65$, represented by the blue and orange dots, respectively, in the region I of Fig. 3.8(a), and $\lambda_{k_B,S_1} = 0.42$ and $\lambda_{k_B,S_1} = 0.50$, represented by the blue and orange dots, respectively, in the region II. While the contribution maps displayed in the left and right panels of Fig. 3.8(c) are very similar, Fig. 3.8(b) shows that the fully relativistic contributions are strongly weakened comparing to the scalar relativistic case. This weakening is easily understood in terms of spin-state overlaps. Let us recall that the spin-polarizations of the occupied spin-split surface states follow a Rashba model [148] showing an in-plane chiral spin-polarization near the $\overline{\Gamma}$ point (top panels of Fig. 3.5). As explained in detail in Appendix E, in the Rashba model, the spinor overlaps between two states at momenta $\mathbf{k}$ and $\mathbf{k}'$ within the same spin-split band (intra-band electronic scattering) appear modu-

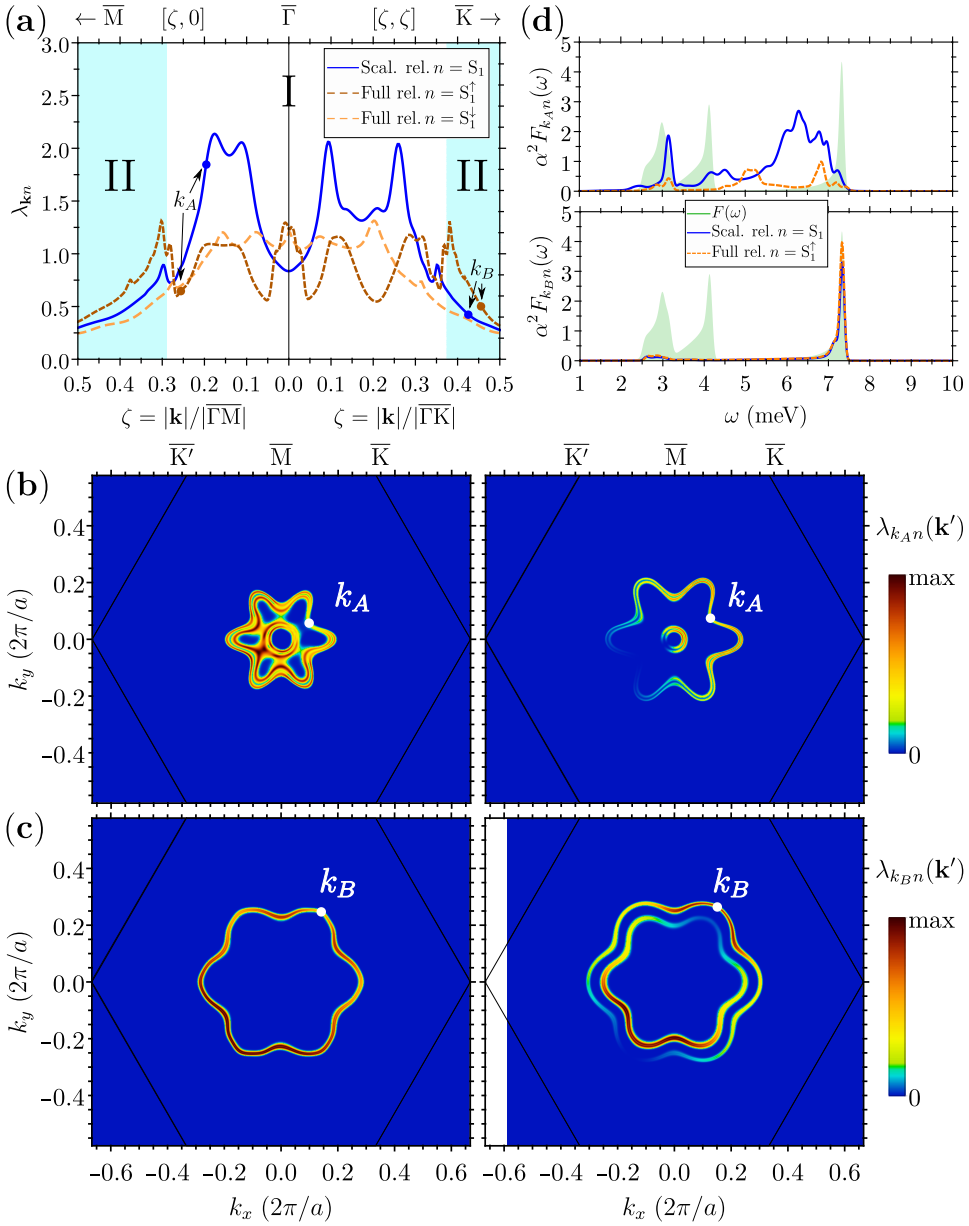

Figure 3.8. (a) State-dependent electron-phonon coupling strength $\lambda_{\mathbf{k}n}$ for the highest energy occupied surface states around the $\overline{\Gamma}$ point along the high symmetry $\overline{\Gamma M}$ and $\overline{\Gamma K}$ directions. The solid blue, short-dashed dark-orange and long-dashed light-orange lines display the results for the scalar relativistic S_1 and the fully relativistic spin-split $S_1^{\uparrow}$ and $S_1^{\downarrow}$ surface bands, respectively. Regions I and II correspond to the ones in Fig. 3.4. (b) and (c) $\mathbf{k}'$ momentum-resolved contribution map within the SBZ to $\lambda_{\mathbf{k}n}$ for the scalar S_1 (left) and spin-split $S_1^{\uparrow}$ surface bands at the electron momentum $\mathbf{k} = k_A$ (region I) and $\mathbf{k} = k_B$ (region II), respectively. k_A and k_B are shown in Fig. 3.4 (b). (d) The Eliashberg function $\alpha^2 F_{\mathbf{k}n}(\omega)$ evaluated at $\mathbf{k} = k_A$ (top) and $\mathbf{k} = k_B$ (bottom) for the scalar S_1 and the spin-split $S_1^{\uparrow}$ surface bands, represented by the solid blue and dashed orange lines, respectively. The green area represents the phDOS in meV^{-1}.

lated by the factor $(1+\cos\theta)/2$ with respect to the spin-independent case, where θ is the angle between $\mathbf{k}$ and $\mathbf{k}'$. Still, the spinor overlaps between two states belonging to different spin-split bands (inter-band electronic scattering), appear modulated by the factor $(1-\cos\theta)/2$ with respect to the spin-independent case. It is interesting to see that at momenta for which both inter-band and intra-band scattering channels are allowed (region II), the sum of the latter factors gives the unity and one recover the same structure as in the spin-independent case. This is actually what happens for the electron-phonon coupling strength at k_B within the region II, where the spin-split contribution map (right panel of Fig. 3.8(c)) are qualitatively similar to that of the spin-degenerate case (left panel of Fig. 3.8(c)), leading to mass enhancement parameters quantitatively similar. Following this argument, we observe that, at k_A within the region I, only intra-band contributions are energetically accessible for the spin-split $S_1^{\uparrow}$ surface states. In this regard, it is shown that the fully relativistic contribution map (right panel Fig. 3.8(b)) is modulated by the geometrical factor $(1+\cos\theta)/2$ compared to the scalar relativistic contribution map (left panel Fig. 3.8(b)).

In Fig. 3.8(d), we present the low-frequency range of $\alpha^2F_{\mathbf{k}n}(\omega)$ for the scalar relativistic S_1 and fully relativistic $S_1^{\uparrow}$ surface states, represented by the solid blue and dashed orange lines at $\mathbf{k}=k_A$ (top) and $\mathbf{k}=k_B$ (bottom), respectively. The green area represents the phDOS associated with the low-frequency acoustic phonon modes. We observe that, at the momentum k_A, the Eliashberg spectral functions exhibit a quite spread spectral distribution exhibiting a moderate peak at $\omega=3$, but with most of the spectral weight at higher frequencies. This indicates that a stronger coupling of the occupied surface electrons to the out-of-plane acoustic phonon branch. It is worth noting that spin-dependent function exhibits a reduced spectral structure similar in shape to the spin-independent case, putting in evidence the modulation of the contributions to the electron-phonon coupling strength in the region I. Moreover, at the momentum k_B, both spin-independent and spin-dependent $\alpha^2F_{\mathbf{k}n}(\omega)$ show almost the same spectral structure. This is consistent with the fact that the electron-phonon coupling strengths and that the corresponding contribution maps are practically equivalent for both cases. Note also that for this momentum almost all the spectral weight is collected in one single peak at $\omega\approx 7$ meV, indicating the strong coupling of the occupied surface electrons to the out-of-plane acoustic phonon branch. This strong coupling is expected due to the surface out-of-plane p_z orbital character of the highest energy occupied surface states at the $\overline{\Gamma}$ point (Sec. 3.2.3)

3.4 Conclusions

In this chapter, we have demonstrated the fundamental role played by the electron spin and the relativistic effects on the dynamics of surface electrons

at the Tl/Si(111) surface. We have shown that the spin-orbit induced spin-polarization of the surface states governs the electron-phonon interaction and enters in a decisive way by modulating the electron-phonon matrix elements.

To this end, in Sec. 3.1, we have introduced the theoretical formalism for including the electron spin and relativistic effects up to the spin-orbit coupling into self-consistent first principles DFT and DFPT calculations, as well as into electron-phonon interaction first principles calculations. In Sec. 3.2, we have presented the calculated ground-state electronic and lattice vibrational properties of the Tl/Si(111) surface and the Si(111) bulk, as well as compared both in order to properly identify the surface electron states and phonon modes. We have observed that the inclusion of the electron spin and the spin-orbit coupling induce the spin-splitting of the surface band structure together with the generation of fully spin-polarized surface states. In this regard, peculiar spin-polarization textures with surface out-of-plane finite components that deviate from the Rashba model are obtained due to strong surface in-plane potential gradients, as well as strong spin-splitting energies as large as 600 meV. In Sec. 3.3, we have calculated the surface state-dependent electron-phonon coupling strengths and Eliashberg spectral functions.

For the lowest energy unoccupied surface bands, the spin-dependent electron-phonon coupling strength appears strongly weakened compared to the spin-independent one, due to the spin-suppression of the inter-valley electron-phonon matrix elements, as these states exhibit a strong collinear spin-valley structure. Therefore, surface electrons can not backscatter in this case and only intra-valley phonon-mediated electronic scattering is accessible, which are so small close to the bottom of the valley that the electron-phonon interaction is practically absent. This condition makes the low-energy range of unoccupied surface states at the Tl/Si(111) an ideal scenario that opens up an avenue to greatly improve the efficiency of spin currents for silicon spintronics applications.

For the highest energy occupied surface bands, while the restriction imposed by the spin-polarization should also apply to the occupied surface bands (S_1), the spin-dependent electron-phonon coupling strength remains remarkably high with $\lambda_{\max} \sim 1.4$. In this case, spin-dependent contributions to the coupling strength are not spin-suppressed but modulated by a smooth scattering angular-dependent geometrical factor that includes no backscattering. Thereby, a strong electron-phonon interaction regime is reached in the presence of the spin-orbit interaction. This result opens up new theoretical perspectives since, for instance, spin-polarized polaron-like states may be favored, which clearly demands a deeper understanding of the transport properties in this surface. We believe that this work should stimulate further experimental and theoretical investigations in this research front.

Chapter 4

Electron-phonon interaction at the MoS_2 monolayer

One of the main goals of this thesis is to explore the effects beyond the adiabatic approximation due to the electron-phonon interaction, i.e. non-adiabatic effects. These effects can be traced back by comparing theoretically calculated electron and phonon spectral functions including the effects due to the electron-phonon coupling with electron band structures and phonon dispersion relations resulting from DFT and DFPT calculations, respectively. In this respect, first principles calculations of both, renormalized electron band structures and phonon dispersion relations, are of paramount importance for the experimental community in order to explain the features observed in both, electron and phonon spectral measurements, respectively. In order to illustrate the typical signatures of the coupling between electrons and phonons, it is instructive to consider a coupled electron-phonon system within the Einstein model. The latter consists of a single non-interacting electron band dispersing linearly with energy $\varepsilon_{\mathbf{k}} = v_{\mathrm{F}}|\mathbf{k}|$ and one non-interacting dispersionless optical phonon mode with frequency ω_{o} that interact with each other at zero temperature[1].

With respect to electrons, the most significant manifestation of the electron-phonon coupling in the interacting electron spectral functions are the so-called "kinks" at energies around to the phonon frequency ω_{o} [4]. This typical feature distorts the non-interacting electron band structure close to the Fermi level and exhibits several peaks evidencing the breakdown of the single-quasiparticle picture. This physical phenomenon was already predicted qualitatively by Engelsberg and Schrieffer in the early 1960s by analytically studying a coupled electron-phonon system within the Einstein and Debye models taking into account the whole complex energy plane [37]. More recently, Eiguren *et al.* generalized the previous method in combina-

[1] The reader is referred to Appendix C for a detailed description of the coupled electron-phonon system within the Einstein model.

tion with *ab initio* calculations for quantitative studies in realistic materials, where the importance of the complex nature of both quasi-particle energy and its renormalization factor were highlighted [35, 36]. Connecting with this, we mention that a proper evaluation of the electron quasi-particle band structure taking into account the complex energy plane (Eq. 2.26) shows that the electron-phonon interaction splits the one non-interacting electron band into two different quasi-particle bands, dividing the electron spectrum in two regions: one for energies below ω_o and the other one above it. On the one hand, electron states at energies below ω_o do not have sufficient energy for decaying by emitting any phonon, and therefore, are well-defined electron quasi-particles with idealized infinite lifetime. However, from a quantum many-body point of view, these electron states are allowed to simultaneously emit and reabsorb phonons by means of virtual processes, leading to the formation of a heavy cloud of phonons that dresses them and leads to an increase of their effective band mass, or equivalently a reduction of their effective band velocity, similar to polarons in insulators. On the other hand, electrons at energies above ω_o do have sufficient energy for decaying by the emission of phonons, and therefore, have a finite lifetime. In this case, virtual processes are less probable in favor of real emissions of phonons, leading to a decrease of the electron effective band mass, or equivalently an increase of the effective band velocity. On the experimental side, photoemission kinks have been observed in many ARPES experiments [196–202] and reported in first principles calculations [203–205].

With respect to phonons, the most significant manifestation of the electron-phonon interaction in the interacting phonon spectral functions are Kohn anomalies [206]. These features correspond to sharp dips or frequency softenings in the phonon dispersion relations as a result of an abrupt change in the electronic screening due to lattice vibrations, when occupied and unoccupied electron states close to the FS are effectively connected by a phonon mode [5]. Contrary to the possible kinks in photoemission spectra, the Kohn anomalies are usually well captured by first principles DFPT calculations, as demonstrated by the good agreement with some experimental measurements [207–210]. The reason of this good agreement lies in the fact that the calculation of phonons even within the adiabatic approximation includes the static contribution to the electronic screening of lattice vibrations (Eq. 1.61). Moreover, the dynamical contributions beyond the adiabatic approximation can usually be neglected even in metals, since the electron energies are usually much larger than typical phonon frequencies. Nevertheless, the possibility of large non-adiabatic frequency corrections to phonon branches in the long-wavelength limit was already proposed in the late 1950s and early 1960s [37, 131], as well as in subsequent theoretical studies in simple models [211–214]. Since then, a great effort has been made in order to detect those effects. In fact, it has been only recently that these effects have been identified by comparing experimental and theoretical results [104, 215–226].

In all these referenced systems, an approximated *ab initio* lattice vibrational theory including non-adiabatic effects due to the electron-phonon interaction has proved to be essential in order to interpret the experiments, which otherwise could not be explained. In recent literature, the detection of non-adiabatic effects has been mostly limited to phonons in the BZ center, and the renormalization frequencies and the lifetimes of phonon modes have always been calculated using the Brillouin-Wigner or Rayleigh-Schrödinger perturbation theory (Eq. 2.44). Indeed, a proper evaluation of the phonon quasi-particle dispersion relation taking into account the complex frequency plane (Eq. 2.41) as it is done in this thesis was missing.

In this context, the electric field effect has recently emerged as an ideal route for easily tuning the Fermi level, and hence, tailoring the nature and strength of many-body interactions in 2D semimetal and semiconductors via carrier-doping [227, 228]. Thereby, the possibility of systematic doping, together with many experiments performed in an electron-doped MoS_2 monolayer top-gated field effect transistor, have recently revealed signatures of a strong electron-phonon interaction in electron and phonon spectra, posing a challenge for a proper theoretical interpretation. On the one hand, Raman experiments have uncovered the strong sensitivity to electron-doping of the BZ center optical phonons with dominant out-of-plane polarization, which exhibit an increasing frequency softening at low carrier concentrations ($\rho < 2 \times 10^{13}$ cm^{-2}) [229]. Although this effect was first understood by means of adiabatic phonon calculations, later works focussing on the small momentum range have pointed out the importance of non-adiabatic corrections when increasing the electron-doping concentration ($\rho \sim 5 \times 10^{13}$ cm^{-2}) [230, 231]. On the other hand, ARPES experiments at larger doping concentrations ($\rho > 5 \times 10^{13}$ cm^2) have revealed an unprecedented electron photoemission spectrum showing an unambiguous doubly split structure related to phonons [232]. These results go hand in hand with the spin-valley locking superconductivity experimentally found in this system [233–236], which has been theoretically explained by a considerable strengthening of the electron-phonon interaction upon doping [237–240].

In this chapter, we provide a comprehensive first principles analysis of the effects due to the electron-phonon interaction on both, the electron and phonon spectral functions of the electron-doped MoS_2 monolayer. Section 4.1 is devoted to present the crystal structure of the MoS_2 monolayer, as well as the doping-dependent electronic and lattice vibrational structures calculated from first principles. We observe that deep changes in the Fermi surface upon doping promote the generation of Kohn anomalies in the adiabatic phonon dispersion relation in agreement with previous calculations [237–239] and become lattice instabilities at larger doping values. In Sec. 4.2, we present the calculated phonon spectral function as a function of electron-doping and including non-adiabatic effects due the electron-phonon interaction. At momenta away from the BZ center, the frequency of the

phonon modes are barely affected but large spectral broadenings are reported, indicating that phonons acquire finite lifetimes that decrease upon doping. More interestingly, at momenta close to the BZ center, larger frequency hardenings and sharper dispersions upon doping emerge for the optical phonon branches, accompanied by an intricate and broadened phonon spectral function. The latter results are illustrated by means of a simple analytical Einstein-like model. Likewise, we explain the emergent spectrum in terms of a multiple-phonon quasi-particle picture which puts in evidence the splitting of the optical phonon branch induced by the electron-phonon interaction. In Sec. 4.3, we present the calculated electron spectral function as a function of electron-doping and including effects due the electron-phonon interaction. A genuine electron spectral function equivalent to the experimentally measured one [232] is obtained. A combination of first principles calculations of the electron-phonon interaction and a consistent complex energy plane analysis of electron quasi-particle poles sheds light into the physical origin of the intricate photoemission spectrum and reveal that – at least – three coexisting quasi-particle bands are present. Finally, in Sec. 4.4, a summary of the results and the main conclusions drawn in this chapter are given.

4.1 The MoS_2 monolayer: electrons and phonons

We start this section by describing the crystal structure of the MoS_2 monolayer in Sec. 4.1.1. The first principles calculated ground-state electronic properties and lattice vibrational properties of the undoped semiconductor monolayer are presented in Sec. 4.1.3. This is an important step before referring to the electron-doped metallic monolayer. The first principles calculated ground-state electronic properties and lattice vibrational properties of the doped metal monolayer are presented in Sec. 4.1.4. Our calculations cover electron-doping concentrations ranging up to $\rho = 0.15\ e/\text{u.c.}$, or equivalently $\rho \approx 17 \times 10^{13}\ e/\text{cm}^2$. The deep changes in the Fermi surface shape upon doping promote the access of an increasing number of nesting channels. This explains the fluctuations of the doping-dependent lattice vibrational structure, when rationalized in terms of phonon-mediated and spin-conserving electronic scattering transitions. This is an imperative step before analyzing the electron-phonon interaction and serves as a preliminary diagnosis of the coupling dependence on doping. The computational methods are described in Sec. 4.1.2.

4.1.1 The crystal structure of the MoS_2 monolayer

This material crystallizes in a hexagonal close-packed structure and is composed of two planes of sulfur (S) atoms with an intercalated plane of molybdenum (Mo) atoms, which are bound to S atoms in a trigonal prismatic

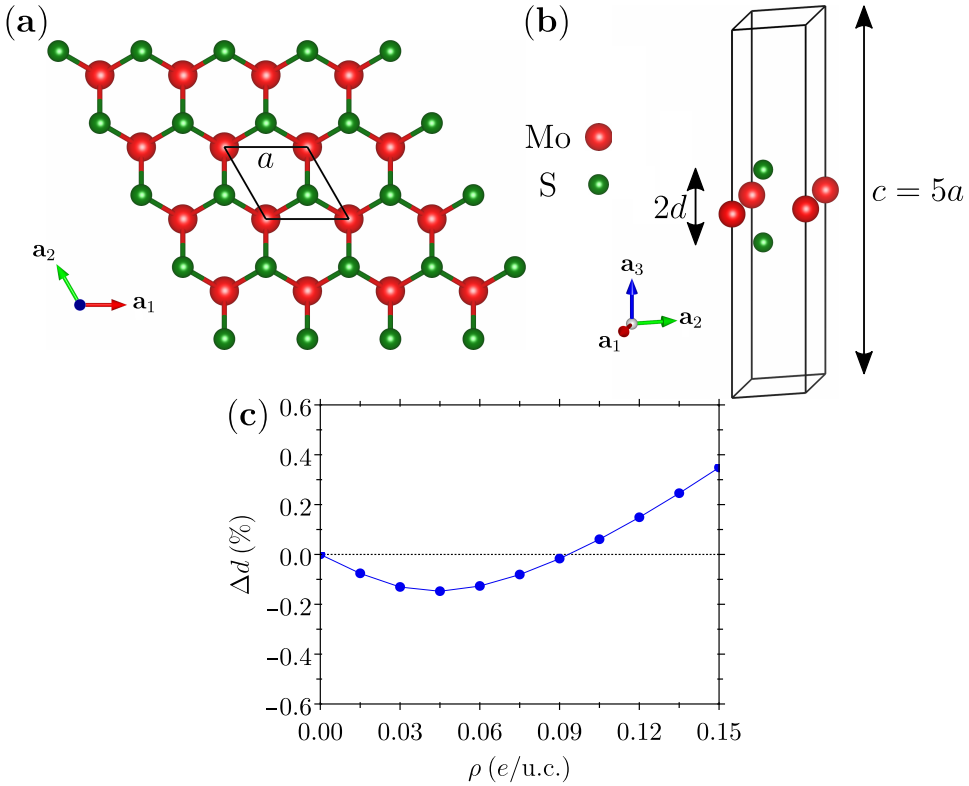

Figure 4.1. (a) Top and (b) side view of the crystal unit cell employed for modeling the MoS_2 monolayer using the slab technique. Green and red spheres represent Mo and S atoms, respectively. a represents the in-plane lattice parameter, set equal to $a = 3.16$ Å, and d represents the distance between Mo and S atomic planes. The height of the unit cell is fixed equal to $c = 5a = 15.80$ Å. (c) The change in the inter-planar distance d as a function of the electron-doping concentration ρ. In the undoped case, the relaxed inter-planar distance is equal to $d = 1.56$ Å, equivalent to a Mo-S bond length of 2.40 Å and a vacuum distance of 12.68 Å.

arrangement. The crystal structure of this system has the $P6m2$ symmetry space group, equivalent to the D_{3h} symmetry point group, without inversion symmetry [241]. Since the material is correctly described by one isolated single layer, we resort to the slab technique. Figures 4.1(a) and (b) show the top and side views, respectively, of the unit cell of the MoS_2 monolayer, which is described by the following direct lattice vectors:

$$\mathbf{a}_1 = a\,\hat{\mathbf{x}}, \quad \mathbf{a}_2 = \frac{a}{2}(-\hat{\mathbf{x}} + \sqrt{3}\hat{\mathbf{y}}), \quad \text{and} \quad \mathbf{a}_3 = c\,\hat{\mathbf{z}}, \tag{4.1}$$

where a represents the in-plane lattice parameter, which has been taken equal to the experimental bulk value, $a = 3.16$ Å [242], and c is the height of the unit cell, which has been set equal to $c = 5a = 15.80$ Å. This is a large enough vacuum space in order to avoid any interplay between adjacent MoS_2

Table 4.1. The three atom basis of the MoS_2 monolayer crystal unit cell.

Atom	Crystal coordinates		
	$\mathbf{a}_1$	$\mathbf{a}_2$	$\mathbf{a}_3$
S	$-1/3$	0	d/c
Mo	0	0	0
S	$-1/3$	$1/3$	$-d/c$

slabs. The unit cell has a basis of three atoms, whose positions in crystal coordinates are gathered in Table 4.1, where d represents the distance between the Mo and S atomic planes, or simply the inter-planar distance. For all the cases considered in this chapter, i.e. with and without considering doping, the equilibrium cell geometry of the monolayer is determined by relaxing all atomic forces up to at least 10^{-6} Ry/a_0. In this regard, Fig. 4.1(c) shows the evolution of the change in the relaxed inter-atomic planar distance d as a function of the considered electron-doping concentrations ρ. As a reference, the relaxed inter-planar distance for the undoped monolayer is equal to $d = 1.56$ Å, equivalent to a Mo-S bond length of 2.40 Å, which is in good agreement with previous theoretical calculations [241]. The SBZ of the MoS_2 monolayer is the same as that of the Tl/Si(111) surface (Fig. 3.2(d)).

4.1.2 Computational methods

All the self-consistent first-principles calculations have been performed within the noncollinear spin-DFT [174–177] and DFPT [33] formalisms as implemented in the Quantum Espresso package [93, 94]. The exchange-correlation energy has been approximated using the Perdew-Zunger (PZ) spin-LDA parametrization [88]. An energy cutoff of 80 Ry has been used for the converged planewave basis expansion. The norm-conserving pseudopotential approximation [97] has been employed to include the $4d^5 5s^1 5p^0$ valence electron states in the case of the Mo atom ($Z = 42$), and the $3s^2 3p^4 3d^0$ valence electrons in the case of the S atom ($Z = 16$). Likewise, fully relativistic pseudopotentials [188, 243] have been constructed in order to take into account relativistic effects up to the spin-orbit interaction.

In the case of the undoped semiconductor MoS_2 monolayer (Sec. 4.1.3), the ground-state electronic properties are evaluated considering a 32×32 Monkhorst-Pack **k**-point mesh in combination with fixed Fermi-Dirac occupation factors. The corresponding lattice vibrational properties are evaluated based on the calculation of the dynamical matrices on a 8×8 **q**-point mesh. In the case of the doped metal MoS_2 monolayer (Sec. 4.1.4), the ground-state electronic properties are evaluated considering a 32×32 Monkhorst-Pack **k**-point mesh and Fermi-Dirac occupation factors are taken

into account with a spreading value of 5 mRy, more suitable for metals with a well-defined FS. The corresponding lattice vibrational properties are evaluated based on the calculation of the dynamical matrices on a 8×8 **q**-point mesh. Electron-doping effects are self-consistently simulated by the addition of excess electronic charge into the unit cell, which is compensated by a uniform positive jellium background in order to remove divergences [93, 94].

It is worth noting that, unlike in the undoped case, the dynamical matrices of the doped monolayer are not directly taken from the DFPT calculations but have been obtained by means of an additional non-selfconsistent procedure. For the doped monolayer, DFPT calculations are based on previous converged DFT calculations, which include BZ summations on a coarse 32×32 **k**-point mesh and Fermi-Dirac occupation factors are taken into account with a spreading value of 5 mRy, i.e. equivalent to an energy of $\sim$ 68 meV and a temperature of $\sim$ 790 K. In fact, this energy is enough to produce a remarkable smoothing of the Fermi surface that can mask pronounced changes of its structure, which are at the origin of several interesting phenomena such as Kohn anomalies. It would be desirable to perform DFPT calculations with smaller smearing broadening values in order to have a better description of the topology of the Fermi surface. This demands finer **k**-point meshes for achieving converged results, making self-consistency computationally prohibitive. Nevertheless, one can take advantage from the first term on the right-hand side of Eq. 1.61, whose explicit expression can be cast in the form of Eq. 2.22, as in the scheme proposed in Ref. [104]. In fact, note that the latter term is already accessible from DFT and DFPT calculations. Thus, the idea is to compute a non-selfconsistent and converged 1BZ summation of the first term on the right-hand side of Eq. 1.61 in a finer **k**-point mesh and with a smaller smearing broadening by means of Wannier interpolation techniques (Sec. 2.6) and substitute it with the one coming directly from DFPT calculations on the dynamical matrix. In this way, we have used a fine 720×720 **k**-point mesh and Fermi-Dirac occupation factors are taken into account with a spreading value of 5 meV, i.e. equivalent to a temperature of $\sim$ 60 K. In a next step, the adiabatic phonon modes are obtained by solving the secular eigenvalue problem of the so resulting dynamical matrix, $\det\left|D^{\alpha\alpha'}_{ss'}(\mathbf{q}) - \omega^2\right| = 0$.

4.1.3 The undoped semiconductor MoS_2 monolayer

In this section, we present the calculated electronic and lattice vibrational properties of the undoped MoS_2 monolayer.

Ground-state electronic properties

We start presenting the calculated electronic properties of the undoped MoS_2 monolayer, whose electron band structure in the eV range is shown in

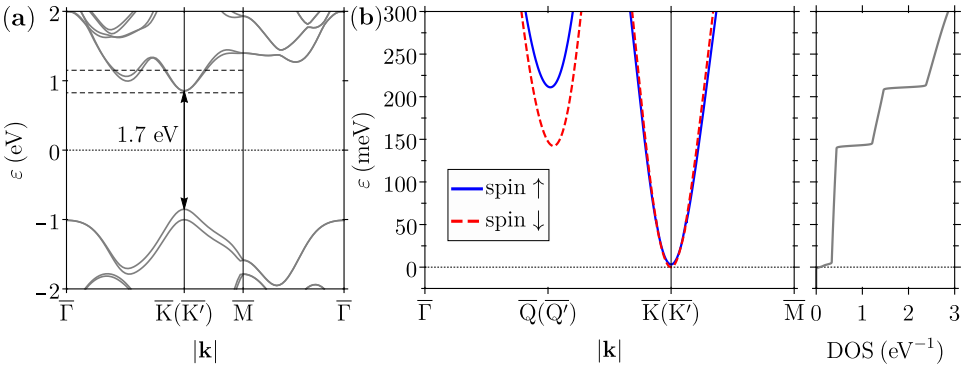

Figure 4.2. (a) Electron band structure of the undoped MoS_2 monolayer on the eV range of energy and centered on the semiconducting direct energy band gap of about 1.7 eV at the $\overline{\mathrm{K}}(\overline{\mathrm{K}}')$ high-symmetry points. (b) Zoom in of the unoccupied low-energy conduction-band structure delimited by the horizontal dashed black lines in (a) (left) and the corresponding DOS (right) of the undoped MoS_2 monolayer on the meV range of energy. Solid blue and dashed red lines represent opposite full out-of-plane spin-polarized bands.

Fig. 4.2(a). The undoped semiconductor monolayer exhibits a direct energy band gap of about 1.7 eV at the high-symmetry $\overline{\mathrm{K}}(\overline{\mathrm{K}}')$ points, which is in good agreement with previous experimental and theoretical values [244–250]. Figure 4.2(b) displays the zoom in of the unoccupied low-energy conduction-band structure of the undoped MoS_2 monolayer, delimited by horizontal dashed black lines in Fig. 4.2(a), (left) and its corresponding DOS (right). This electron momentum and energy $(\mathbf{k}, \varepsilon)$ region represents the phase-space available when adding finite electron-doping concentrations to the system (Sec. 4.1.4). The low-energy conduction-band structure consists of a distribution of valleys located at the high-symmetry $\overline{\mathrm{K}}(\overline{\mathrm{K}}')$ points and the $\overline{\mathrm{Q}}(\overline{\mathrm{Q}}')$ points, which are at about half way along the equivalent $\overline{\Gamma\mathrm{K}}(\overline{\Gamma\mathrm{K}}')$ directions. The main energy conduction-band minimum is predicted at the bottom of the $\overline{\mathrm{K}}(\overline{\mathrm{K}}')$ valleys, while an additional second minimum is also predicted at the bottom of the $\overline{\mathrm{Q}}(\overline{\mathrm{Q}}')$ valleys about 140 meV higher in energy. The conduction-valleys are split in energy by the action of the spin-orbit interaction and present opposite full out-of-plane spin-polarizations in the whole SBZ, which are represented by the solid blue and dashed red lines. While the spin-orbit (SO) interaction induces an energy splitting of $\Delta_{\mathrm{SO}} \sim 80$ meV at the $\overline{\mathrm{Q}}(\overline{\mathrm{Q}}')$ conduction-valleys, the $\overline{\mathrm{K}}(\overline{\mathrm{K}}')$ conduction-valleys appear almost spin-degenerated ($\Delta_{\mathrm{SO}} \leqslant 3$ meV). The latter is in clear contrast with the case of the occupied high-energy valence-states at $\overline{\mathrm{K}}(\overline{\mathrm{K}}')$ points, where a large spin-splitting of about $\Delta_{\mathrm{SO}} \sim 150$ meV is obtained.

The full out-of-plane spin-polarization can be easily understood due to the pure 2D nature of the MoS_2 monolayer, where both the electron momentum $\mathbf{k}$ and the effective potential, as well as its gradient asymmetry

Table 4.2. Orbital composition in percentage for the low-energy conduction-states (LE-CS) at the $\overline{\mathrm{Q}}(\overline{\mathrm{Q}'})$ and $\overline{\mathrm{K}}(\overline{\mathrm{K}'})$ points, and the high-energy valence-state (HE-VS) at the $\overline{\mathrm{K}}(\overline{\mathrm{K}'})$ points of the undoped MoS_2 monolayer. For each orbital angular momentum l, we distinguish between the combinations of orbitals m aligned parallel ($\parallel$) or perpendicular ($\perp$) to the monolayer (x, y) plane.

Atom	l_m	LE-CS at $\overline{\mathrm{Q}}(\overline{\mathrm{Q}'})$	HE-VS at $\overline{\mathrm{K}}(\overline{\mathrm{K}'})$	LE-CS at $\overline{\mathrm{K}}(\overline{\mathrm{K}'})$
S	s	1 %	0 %	0 %
S	$p_x + p_y$ ($\parallel$)	32 %	22 %	16 %
S	p_z ($\perp$)	14 %	0 %	0 %
Mo	s	1 %	0 %	5 %
Mo	$p_x + p_y$ ($\parallel$)	0 %	1 %	0 %
Mo	p_z ($\perp$)	0 %	0 %	0 %
Mo	$d_{xy} + d_{x^2-y^2}$ ($\parallel$)	44 %	77 %	0 %
Mo	$d_{z^2} + d_{zx} + d_{zy}$ ($\perp$)	8 %	0 %	79 %

$\boldsymbol{\nabla} V(\mathbf{r})$, are constrained parallel to the monolayer plane (x, y). The corresponding cross product $\big(\mathbf{k} \times \boldsymbol{\nabla} V(\mathbf{r})\big)$ points out of the plane and couples to the spin, forcing it to align perpendicular to the plane [251]. For this reason, the spin-orbit coupling term is expected to be larger for the electron states with more in-plane orbital character. The orbital composition of the low-energy conduction-states (LE-CS) at the $\overline{\mathrm{K}}(\overline{\mathrm{K}'})$ and $\overline{\mathrm{Q}}(\overline{\mathrm{Q}'})$ points, as well as for the high-energy valence-state (HE-VS) at the $\overline{\mathrm{K}}(\overline{\mathrm{K}'})$ points is gathered in Table 4.2. We define $P_{\mathbf{k}n}^{Xlm}$ as the squared module of the projections of the Kohn-Sham states $|\psi_{\mathbf{k}n}\rangle$ and the the orthogonalized X atomic pseudo-states $|\varphi_{Xlm}^{\mathrm{PS}}\rangle$ with $\{l, m\}$ orbital angular momentum quantum numbers (Appendix B), as follows:

$$P_{\mathbf{k}n}^{Xlm} = \frac{\big|\langle \varphi_{Xlm}^{\mathrm{PS}} | \psi_{\mathbf{k}n} \rangle\big|^2}{\langle \psi_{\mathbf{k}n} | \psi_{\mathbf{k}n} \rangle}. \tag{4.2}$$

From Table 4.2, we appreciate that the states at $\overline{\mathrm{Q}}(\overline{\mathrm{Q}'})$ conduction-valleys and the valence-states at the $\overline{\mathrm{K}}(\overline{\mathrm{K}'})$ points are mainly composed of in-plane polarized orbitals, and therefore, exhibit larger spin-splittings. Conversely, the $\overline{\mathrm{K}}(\overline{\mathrm{K}'})$ conduction-valleys have a predominant out-of-plane polarized orbital character, and thus, present a much smaller spin-splitting, which is almost unappreciable. We finish this section by noting that the orbital composition of the conduction-valley structure of the undoped MoS_2 monolayer remains almost unchanged upon doping.

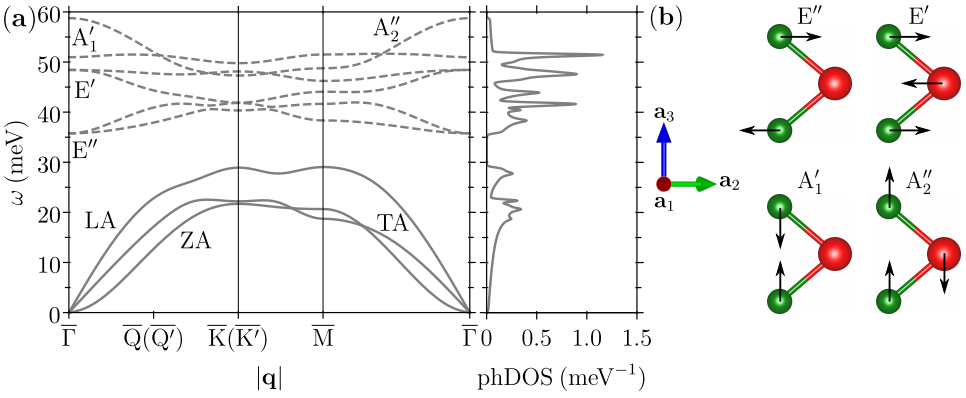

Figure 4.3. (a) Phonon dispersion relation (left) and the corresponding phDOS (right) of the undoped MoS_2 monolayer. Acoustic and optical lattice normal modes are represented by solid and dashed gray lines, respectively, and are well separated by a frequency gap of about 6 meV. (b) Schematic representation of the polarization vectors for the E″, E′, A_1' and A_2'' optical phonon branches at $\mathbf{q} = \overline{\Gamma}$.

Lattice vibrational properties

We come now to present the calculated lattice vibrational properties of the undoped MoS_2 monolayer, whose phonon dispersion relation (left) and its corresponding phDOS (right) are shown in Fig. 4.3(a). The set of low-frequency acoustic vibrational modes (solid gray lines) is completely separated from the set of high-frequency optical modes (dashed gray lines) by a gap of about 6 meV. The in-plane vibrating longitudinal (LA) and transverse (TA) acoustic phonon branchs present a linear dispersion near the $\overline{\Gamma}$ point and have higher frequency than the out-of-plane polarized acoustic (ZA) branch, showing the typical parabolic dispersion for one-layered systems [252].

Regarding the optical phonon modes, the corresponding polarization vectors at the $\mathbf{q} = \overline{\Gamma}$ point are schematically represented in Fig. 4.3(b). The E″ and E′ vibrational branches correspond to two pairs of in-plane longitudinal (LO) and transverse (TO) optical modes. While the E″ modes correspond to the in-plane vibrations of the S atoms in counterphase, the E′ modes correspond to the in-plane vibrations of the Mo and S atoms in counterphase to each other. In addition, while the E″ branches are degenerated at the $\overline{\Gamma}$ point with a frequency of 36 meV, the E′ branches are split with a LO-TO splitting of 0.5 meV at frequencies between 48 and 49 meV. The A_1' vibrational modes correspond to the almost dispersionless optical branch with the S atoms vibrating counterphase in out-of-plane direction and with a frequency of 51 meV at the $\overline{\Gamma}$ point. It is important to note for the following discussion that the Mo atoms remain static for the A_1' mode at $\mathbf{q} = \overline{\Gamma}$, while at $\mathbf{q} = \overline{Q}(\overline{Q'})$, $\overline{K}(\overline{K'})$ and $\overline{M}$ these atoms exhibit in-plane vibrations. Finally, the A_2'' phonon modes correspond to the highest-frequency optical

branch, with the Mo and S atoms vibrating counterphase in out-of-plane direction and with a frequency of 59 meV at the $\overline{\Gamma}$ point.

4.1.4 The electron-doped metallic MoS_2 monolayer

In this section, we present the calculated electronic and lattice vibrational properties of the MoS_2 monolayer as a function of doping. Our calculations cover electron-doping concentrations ranging up to $\rho = 0.15$ e/u.c., or equivalently $\rho \approx 17 \times 10^{13}$ e/cm^2.

Doping-dependent electronic properties

We start analyzing the evolution of the electronic properties of the MoS_2 monolayer as a function of doping. Figure 4.4 shows the low-energy electron conduction-valley structure (left) and its corresponding DOS (right), while Fig. 4.5 displays the resulting Fermi surface contours, for all the electron-doping levels considered in this work. Following the convention adopted in Fig. 4.2(b), the solid blue and dashed red lines in Fig. 4.4 and contours in Fig. 4.5 represent opposite full out-of-plane spin-polarized conduction-valleys and Fermi sheets, respectively. Besides, in Fig. 4.4, the dashed-dotted green lines delimit the shaded green area that represent the energy window within which an electron-hole pair can energetically be excited by the emission or absorption of a phonon with maximum frequency $\omega_{\text{max}} = 60$ meV, which is about the maximum frequency of the actual vibrational structure (Fig. 4.3(a)).

It is worth noting the high sensitivity of the energy difference between the bottom of the $\overline{\text{K}}(\overline{\text{K}'})$ and $\overline{\text{Q}}(\overline{\text{Q}'})$ conduction-valleys upon doping. In fact, the energy difference decreases as the electron-doping concentration increases, and eventually becomes negative with even higher doping (Fig. 4.4). This relative energy shift has been already observed in previous theoretical works [237, 253]. It has been explained in terms of a higher Coulomb repulsion for the more localized electron states at the $\overline{\text{K}}(\overline{\text{K}'})$ valleys, with a prevalent out-of-plane orbital character, compared to the more spread states at the $\overline{\text{Q}}(\overline{\text{Q}'})$ valleys, with a prevalent in-plane orbital character (Table 4.2). Figure 4.4 highlights the importance of self-consistently incorporating the effects of doping on both the calculation of the electronic ground state and the lattice vibrational properties, where the correct band structure is necessary in order to appropriately account for the electrostatic screening (Eq. 1.60).

The progressive population of the conduction-valley structure with increasing electron-doping concentrations (Fig. 4.4) promotes the gradual emergence of multiple and fully out-of-plane spin-polarized Fermi sheets, which in turn results in an increasing number of possible electron-phonon scattering channels. From the deep changes in the Fermi surface shape (Fig. 4.5), one can distinguish three different electron-doping regimes:

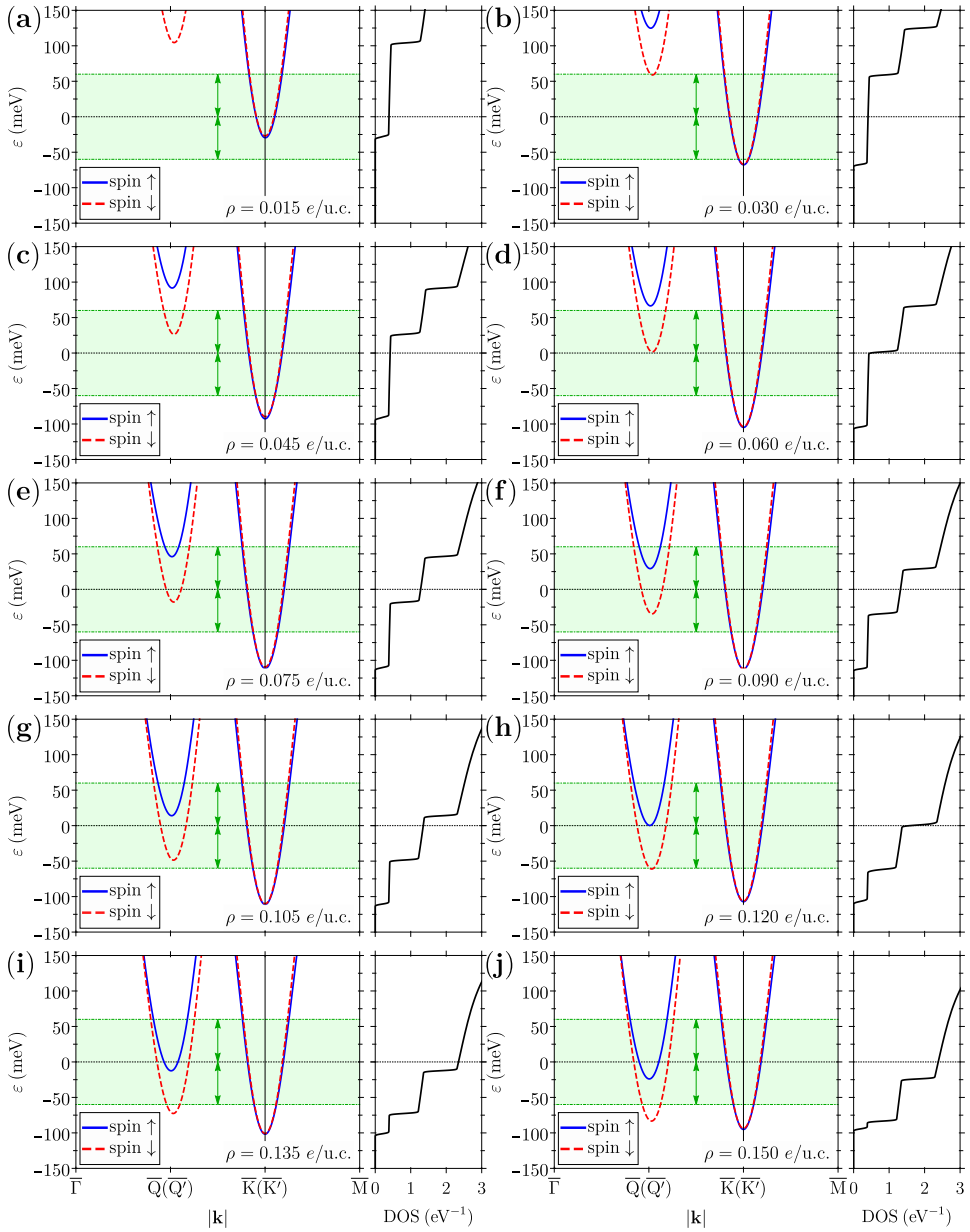

Figure 4.4. Low-energy electron conduction-band structure (left) and its corresponding DOS (right) of the MoS_2 monolayer for the electron-doping concentrations $\rho = 0.015$ (a), 0.030 (b), 0.045 (c), 0.060 (d), 0.075 (e), 0.090 (f), 0.105 (g), 0.120 (h), 0.135 (i) and 0.150 e/u.c. (j). Solid blue and dashed red lines represent opposite full out-of-plane spin-polarized bands. The Fermi level is set to zero (horizontal dotted black line). Horizontal dashed-dotted green lines delimit the energy window (shaded green areas) within which an electron-hole pair can be excited (relaxed) by the decay (emission) of a phonon with maximum frequency $\omega_{\max} = 60$ meV.

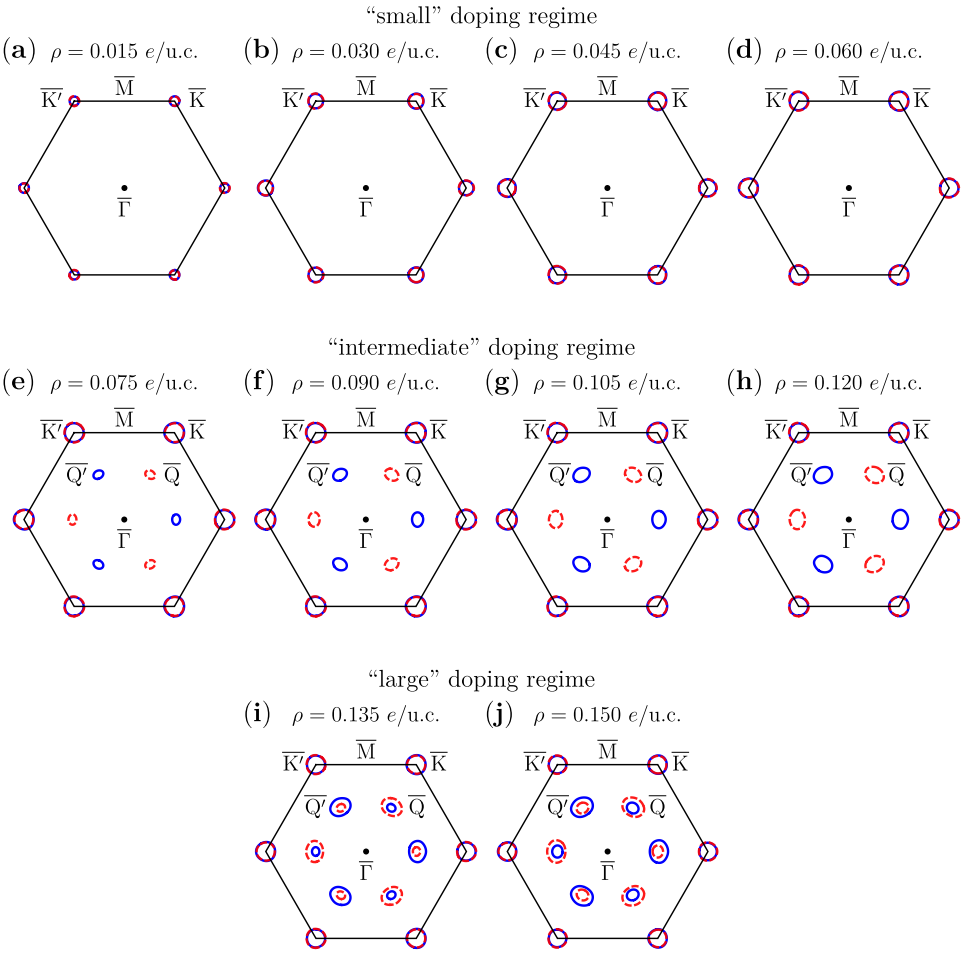

Figure 4.5. Fermi surface contour map of the MoS_2 monolayer for the electron-doping concentrations ρ = 0.015 (a), 0.030 (b), 0.045 (c), 0.060 (d), 0.075 (e), 0.090 (f), 0.105 (g), 0.120 (h), 0.135 (i) and 0.150 e/u.c. (j). Solid blue and dashed red contours represent the opposite full out-of-plane spin-polarized Fermi sheets. In the "small" doping regime (panels (a)-(d)), the almost spin-degenerated $\overline{\mathrm{K}}(\overline{\mathrm{K}'})$ conduction-valleys are only occupied. In the "intermediate" doping regime (panels (e)-(h)), the lower spin-split $\overline{\mathrm{Q}}(\overline{\mathrm{Q}'})$ conduction-valleys get also populated. In the "large" doping regime, the upper spin-split $\overline{\mathrm{Q}}(\overline{\mathrm{Q}'})$ conduction-valleys become finally filled.

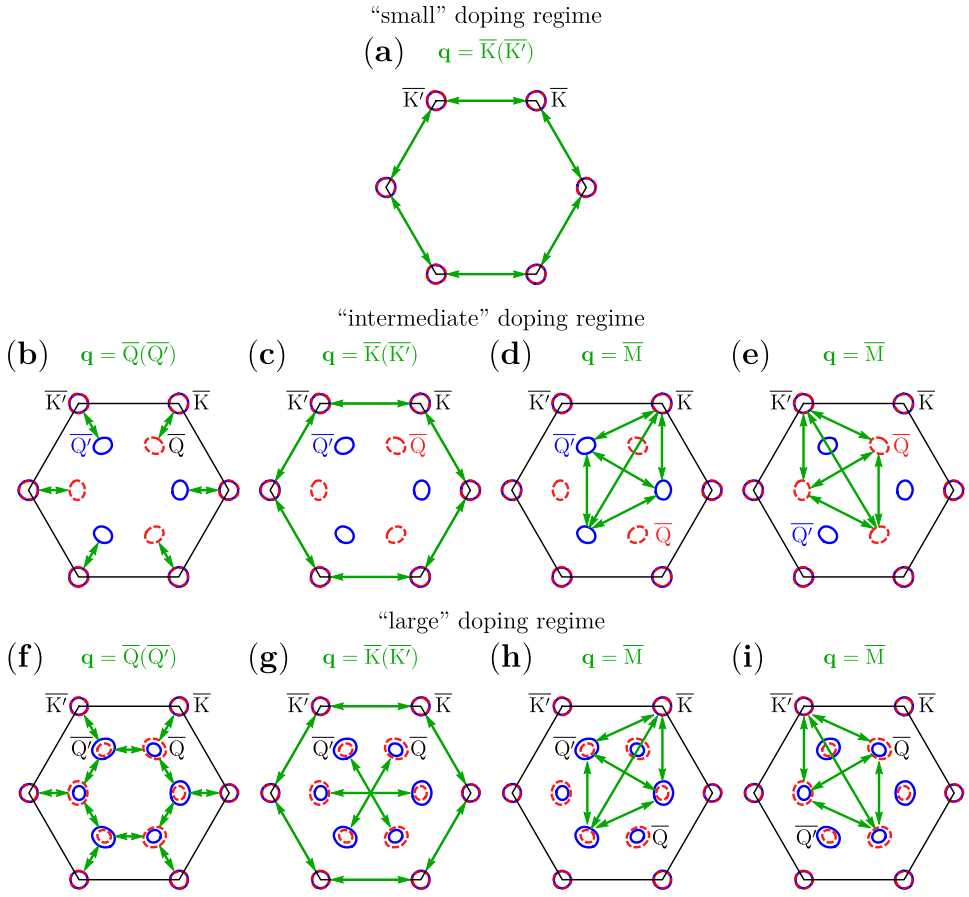

Figure 4.6. Fermi surface nesting wave vectors (green arrows) connecting different Fermi sheets within the SBZ as a function of the electron-doping regime. Solid blue and dashed red contours represent the opposite full out-of-plane spin-polarized Fermi sheets. In the "small" doping regime, $\overline{\mathrm{K}} \leftrightarrow \overline{\mathrm{K}'}$ nesting connections mediated by $\mathbf{q} = \overline{\mathrm{K}}(\overline{\mathrm{K}'})$ are only allowed (panel (a)). In the "intermediate" doping regime, allowed nesting connections include: $\overline{\mathrm{K}} \leftrightarrow \overline{\mathrm{Q}}$ and $\overline{\mathrm{K}'} \leftrightarrow \overline{\mathrm{Q}'}$ transitions, as well as $\overline{\mathrm{Q}} \leftrightarrow \overline{\mathrm{Q}'}$ transitions, mediated by $\mathbf{q} = \overline{\mathrm{Q}}(\overline{\mathrm{Q}'})$ (panel (b)); $\overline{\mathrm{K}} \leftrightarrow \overline{\mathrm{K}'}$ transitions, as well as $\overline{\mathrm{Q}} \leftrightarrow \overline{\mathrm{Q}'}$ transitions, mediated by $\mathbf{q} = \overline{\mathrm{K}}(\overline{\mathrm{K}'})$ (panel (c)); and $\overline{\mathrm{K}} \leftrightarrow \overline{\mathrm{Q}'}$ and $\overline{\mathrm{K}'} \leftrightarrow \overline{\mathrm{Q}}$ transitions, as well as channels connecting equivalent $\overline{\mathrm{Q}}$ or $\overline{\mathrm{Q}'}$ Fermi sheets, mediated by $\mathbf{q} = \overline{\mathrm{M}}$ (panels (d) and (e)). In the "large" doping regime, the same nesting connections as for the "intermediate" regime mediated by $\mathbf{q} = \overline{\mathrm{Q}}(\overline{\mathrm{Q}'})$, $\overline{\mathrm{K}}(\overline{\mathrm{K}'})$ and $\overline{\mathrm{M}}$ are represented in panels (f), (g), and (h) and (i), respectively.

- The "small" doping regime. This regime is found for electron-doping concentrations $\rho \leqslant 0.06$ e/u.c. ($\rho \lessapprox 7 \times 10^{13}$ e/cm^2). In this case, only the almost spin-degenerate $\overline{\mathrm{K}}(\overline{\mathrm{K}'})$ conduction-valleys are occupied (Figs. 4.4(a)-(d)). The corresponding Fermi sheets around the $\overline{\mathrm{K}}(\overline{\mathrm{K}'})$ points are the only ones present (Figs. 4.5(a)-(d)).

- The "intermediate" doping regime. This regime is found for electron-doping concentrations 0.06 e/u.c $\leqslant \rho \leqslant$ 0.12 e/u.c (7×10^{13} $e/\mathrm{cm}^2 \lessapprox \rho \lessapprox 14 \times 10^{13}$ e/cm^2). In this case, the lower spin-split $\overline{\mathrm{Q}}(\overline{\mathrm{Q}'})$ conduction-valleys start populating (Figs. 4.4(e)-(h)). The corresponding out-of-plane spin-polarized Fermi sheets appear located at the equivalent $\overline{\mathrm{Q}}(\overline{\mathrm{Q}'})$ points (Figs. 4.5(e)-(h)).

- The "large" doping regime. This regime is found for electron-doping concentrations $\rho \geqslant 0.12$ e/u.c. ($\rho \gtrapprox 14 \times 10^{13}$ e/cm^2). In this case, the upper spin-split $\overline{\mathrm{Q}}(\overline{\mathrm{Q}'})$ conduction-valleys, i.e. the whole conduction-valley structure, become finally filled (Figs. 4.4(i) and (j)). At the equivalent $\overline{\mathrm{Q}}(\overline{\mathrm{Q}'})$ points, two opposite full out-of-plane spin-polarized Fermi sheets are present (Figs. 4.5(i) and (j)).

In order to continue the discussion, it is important to analyze how the changing in the Fermi surface shape upon doping affects the nesting properties of the MoS_2 monolayer. The Fermi surface nesting describes the connection of different Fermi sheets, or different parts of the same Fermi sheet, by means of a given wave vector $\mathbf{q}$. This function is correctly expressed by considering the imaginary part of the non-interacting density-response function (Eq. 1.60) in the static limit ($\omega \to 0$) assuming constant matrix elements [254]:

$$\lim_{\omega \to 0} \frac{\mathrm{Im}\chi^0_{\mathbf{q}}(\omega)}{\omega} = \frac{1}{N_{\mathbf{k}}} \sum_{\mathbf{k}} \delta(\varepsilon_{\mathbf{k}n} - \varepsilon_{\mathrm{F}}) \delta(\varepsilon_{\mathbf{k}+\mathbf{q}m} - \varepsilon_{\mathrm{F}}). \tag{4.3}$$

We conclude that the more pieces of the Fermi surface are connected to each other in the above way, the stronger is the nesting. This is a valuable information, as we will see in the following lines.

Apart from the trivial $\mathbf{q} = \overline{\Gamma}$ wave vector that gives rise to intra-valley electronic transitions, the possible nesting momenta $\mathbf{q}$ connecting the different Fermi sheets, i.e. inter-valley transitions, of the doped MoS_2 monolayer are schematically represented by green arrows in Fig. 4.6, in the following way:

- $\mathbf{q} = \overline{\mathrm{Q}}(\overline{\mathrm{Q}'})$, which connects the Fermi sheet of the $\overline{\mathrm{K}}$ valley with those of the $\overline{\mathrm{Q}}$ valleys and the Fermi sheet of the $\overline{\mathrm{K}'}$ valley with those of the $\overline{\mathrm{Q}'}$ valleys. It also leads to $\overline{\mathrm{Q}} \leftrightarrow \overline{\mathrm{Q}'}$ transitions (Figs. 4.6(b) and (f)).

- $\mathbf{q} = \overline{\mathrm{K}}(\overline{\mathrm{K}'})$, which connects the Fermi sheets of the $\overline{\mathrm{K}}$ and $\overline{\mathrm{K}'}$ valleys (Fig. 4.6(a)). It also leads $\overline{\mathrm{Q}} \leftrightarrow \overline{\mathrm{Q}'}$ transitions (Figs. 4.6(c) and (g)).

- $\mathbf{q} = \overline{\mathrm{M}}$, which connects the Fermi sheet of the $\overline{\mathrm{K}}$ valley with those of the $\overline{\mathrm{Q}'}$ valleys and the Fermi sheet of the $\overline{\mathrm{K}'}$ valley with those of the $\overline{\mathrm{Q}}$ valleys (Figs. 4.6(d) and (e)). It also connects the $\overline{\mathrm{Q}'}$ valleys with themselves and the $\overline{\mathrm{Q}}$ valleys with themselves (Figs. 4.6(h) and (i)).

Note that, while all the previous possible nesting mechanisms are allowed within the electronic structure of the "intermediate" and "large" electron-doping regimes, in the case of the "small" doping regime only the wave vector $\mathbf{q} = \overline{\mathrm{K}}(\overline{\mathrm{K}'})$ is allowed to mediate inter-valley transitions. It is also important to bear in mind that the spin-polarization modulates and inhibits the electron-phonon interaction. For instance, the scattering channels connecting the $\overline{\mathrm{Q}}$ and $\overline{\mathrm{Q}'}$ conduction-valleys driven by phonons with momenta $\mathbf{q} = \overline{\mathrm{Q}}(\overline{\mathrm{Q}'})$ and $\overline{\mathrm{K}}(\overline{\mathrm{K}'})$ (Figs. 4.6(b) and (c)) are expected to be suppressed, since both electron states present opposite spin-polarizations.

Doping-dependent lattice vibrational properties

We come now to analyze the evolution of the lattice vibrational properties of the MoS_2 monolayer as a function of doping. This step provides an initial valuable examination of the interaction. The presence of frequency softenings in the lattice vibrational structure gives a first indication of strong electron-phonon couplings. Figure 4.7 compares the undoped (solid gray lines) and doped (dashed magenta lines) adiabatic phonon dispersion relations of the MoS_2 monolayer (left) and their corresponding phDOS (right) for the all the electron-doping levels considered in this study. In connection with Sec. 4.1.4, we recall that Figs. 4.7(a)-(d) correspond to the "small" doping regime, Figs. 4.7(e)-(h) to the "intermediate doping regime", and Figs. 4.7(i) and (j) to the "large" doping regime.

Let us start with the "small" doping regime (Figs. 4.7(a)-(d)). In this range, a significant frequency dip of about 5 meV is reported for the A_1' optical phonon branch at momenta near $\mathbf{q} = \overline{\Gamma}$ and $\overline{\mathrm{M}}$. An even larger frequency softening of about 10 meV is obtained for the LA acoustic branch at momenta near $\mathbf{q} = \overline{\mathrm{M}}$. This indicates that the A_1' phonon mode with momentum $\mathbf{q} = \overline{\Gamma}$ is effectively coupled to the electron states at the $\overline{\mathrm{K}}(\overline{\mathrm{K}'})$ valleys by spin-conserving intra-valley electronic scattering processes. This coupling is explained by looking at the polarization vector of the A_1' phonon mode with momentum $\mathbf{q} = \overline{\Gamma}$ (Fig. 4.3(b)) and the orbital character of the electron states at the $\overline{\mathrm{K}}(\overline{\mathrm{K}'})$ conduction-valleys (Table 4.2). Both are both of out-of-plane nature, leading to a large overlap in the electron-phonon matrix elements. Likewise, the softening of both the A_1' and LA phonon modes at $\mathbf{q} = \overline{\mathrm{M}}$ puts in evidence the presence of effective phonon-mediated spin-conserving $\overline{\mathrm{K}'} \leftrightarrow \overline{\mathrm{Q}}$ (Fig. 4.6(c)) and $\overline{\mathrm{K}} \leftrightarrow \overline{\mathrm{Q}'}$ (Fig. 4.6(d)) inter-valley electronic scattering processes. This coupling is also explained by the large overlap resulting from the in-plane nature of the LA and A_1' phonon modes at $\mathbf{q} = \overline{\mathrm{M}}$ and the empty and occupied electron states at the $\overline{\mathrm{Q}}(\overline{\mathrm{Q}'})$ and

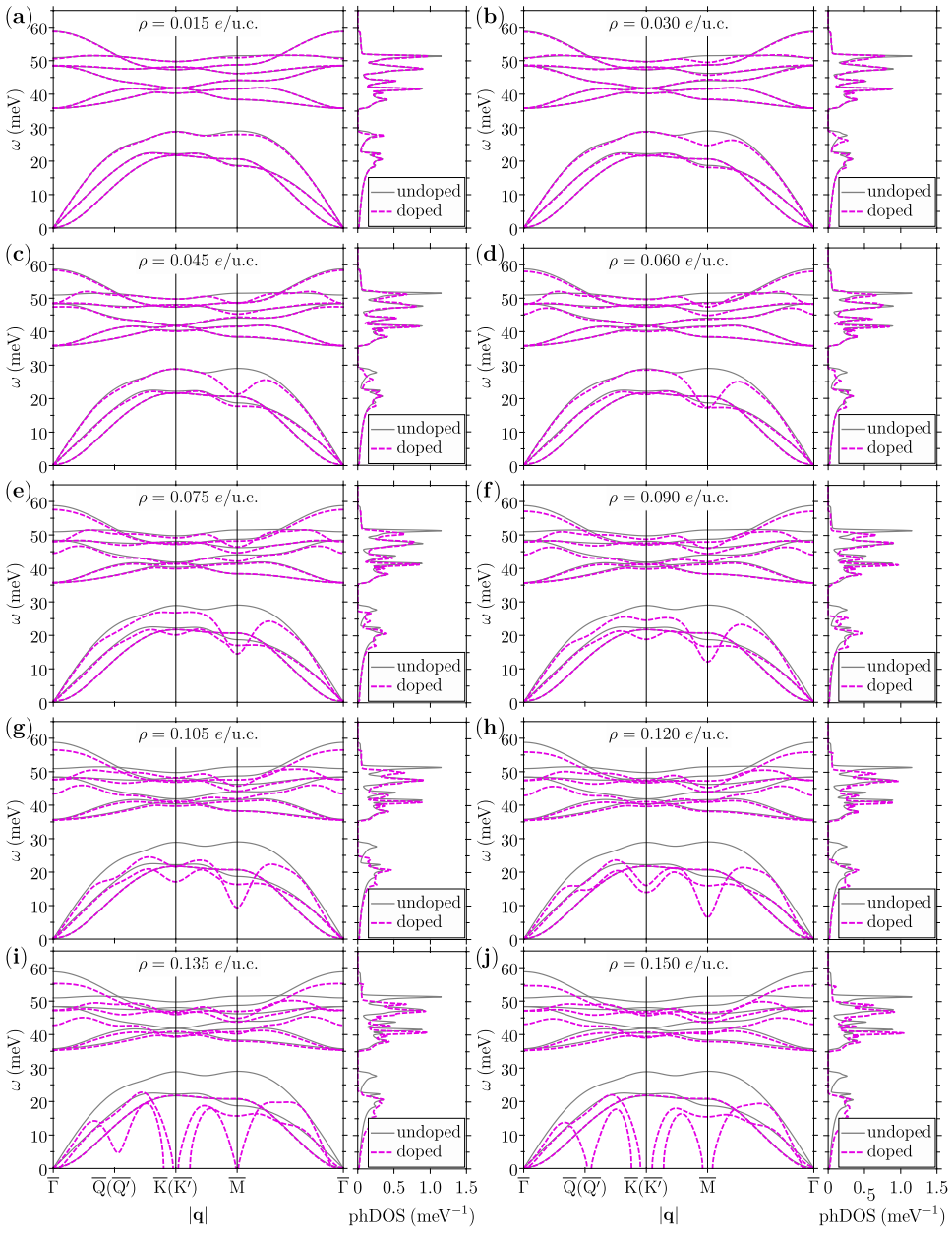

Figure 4.7. Phonon dispersion relation (left) and its corresponding phDOS (right) of the MoS_2 monolayer for the electron-doping concentrations $\rho = 0.015$ (a), 0.030 (b), 0.045 (c), 0.060 (d), 0.075 (e), 0.090 (f), 0.105 (g), 0.120 (h), 0.135 (i) and 0.150 e/u.c. (j). Solid gray and dashed magenta lines represent the undoped and doping-dependent phonon branches, respectively. Note that the doping-dependent results are derived from the non-selfconsistent procedure described in Sec. 4.1.4.

$\overline{\mathrm{K}}(\overline{\mathrm{K}'})$ conduction-valleys, respectively. It is also worth noting the absence of any doping-effect on the phonon modes at $\mathbf{q} = \overline{\mathrm{K}}(\overline{\mathrm{K}'})$, even when nesting is possible for these momenta (Fig. 4.6(a)). This is an indication of the lack of effective coupling between the phonon modes at $\mathbf{q} = \overline{\mathrm{K}}(\overline{\mathrm{K}'})$ and the electron states at the Fermi level.

In the intermediate doping regime, additional frequency dips appear for the in-plane polarized acoustic and the optical E'' and A_1' phonon branches at momenta near $\mathbf{q} = \overline{\mathrm{Q}}(\overline{\mathrm{Q}'})$ and $\overline{\mathrm{K}}(\overline{\mathrm{K}'})$ (Figs. 4.7(e)-(h)). The Kohn anomalies for the A_1' vibrational branch at $\mathbf{q} = \overline{\Gamma}$ and $\overline{\mathrm{M}}$, as well as for the LA phonon mode at $\mathbf{q} = \overline{\mathrm{M}}$, are intensified, with impressive softening values larger than 10 meV. This enhancement of the screening directly results from the increase in the number of Fermi sheets at these electron-doping levels. This gives rise to additional effective phonon-mediated spin-conserving electronic scattering channels connecting occupied and unoccupied states between the $\overline{\mathrm{K}}(\overline{\mathrm{K}'})$ and $\overline{\mathrm{Q}}(\overline{\mathrm{Q}'})$ conduction-valleys (Figs. 4.6(b) and (c)), as well as the $\overline{\mathrm{Q}}(\overline{\mathrm{Q}'})$ valleys with themselves (Figs. 4.6(d) and (e)). As before, the strong couplings can be rationalized in terms of large electron-phonon matrix elements resulting from large overlaps between the potential changes induced by the lattice vibrational normal modes and the electron states.

Finally, within the large doping regime, the in-plane polarized acoustic Kohn anomalies develop instabilities at $\mathbf{q} = \overline{\mathrm{Q}}(\overline{\mathrm{Q}'})$, $\overline{\mathrm{K}}(\overline{\mathrm{K}'})$ and $\overline{\mathrm{M}}$ (Figs. 4.7(i) and (j)). At these electron-doping levels, the whole spin-polarized conduction-valley structure is occupied (Figs. 4.4(i) and (j)), and therefore, the number of Fermi surface nesting channels is maximum (Fig. 4.6). Indeed, in this range, the electrostatic screening is so large that a phase transition of the crystal is energetically favorable, as proposed in Ref. [238].

The insensitivity to the electron-doping for the ZA, E'' and A_2'' vibrational branches has been numerically obtained, as expected from symmetry arguments [238, 255]. For these reasons, we exclude these phonon modes from the following discussion.

4.2 Electron-phonon effects on the phonon spectral function

In this section, we present a comprehensive *ab initio* analysis of the non-adiabatic effects due to the electron-phonon interaction on the phonon spectral function of the electron-doped MoS_2 monolayer as a function of doping. Figure 4.8 represents the calculated phonon spectral function for all the electron-doping levels in which the lattice is stable. The dashed black lines show the corresponding adiabatic phonon dispersions (dashed magenta lines in Fig. 4.7). The color code represents the height of the phonon spectral function. The differences between the adiabatic phonon branches and the

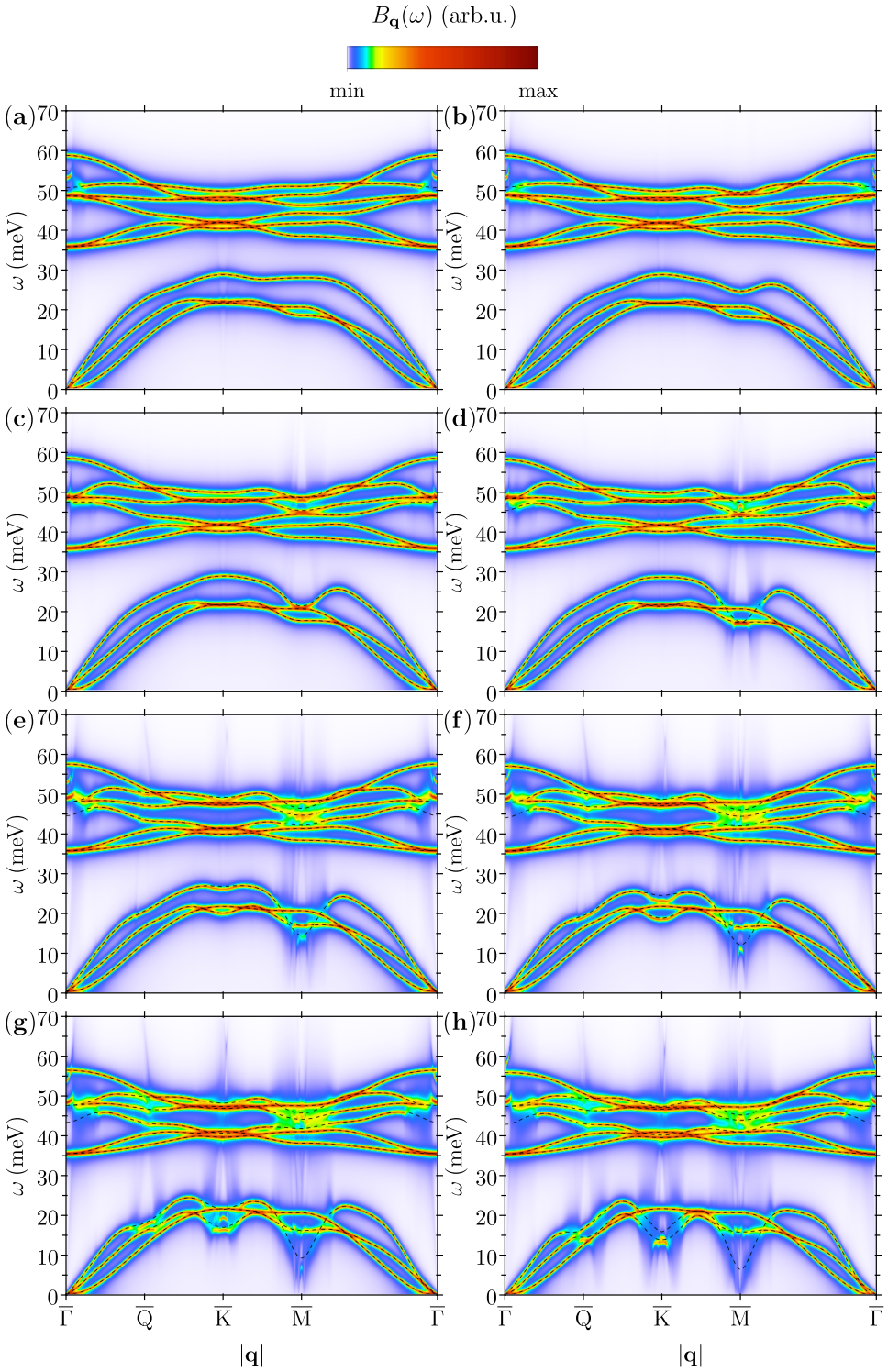

Figure 4.8. Density plot of the phonon spectral function of the MoS_2 monolayer for the electron-doping concentrations $\rho = 0.015$ (a), 0.030 (b), 0.045 (c), 0.060 (d), 0.075 (e), 0.090 (f), 0.105 (g) and 0.120 e/u.c. (h). The color code scale represents the height of the spectral function. Dashed black lines represent the adiabatic phonon dispersion relations.

main features defined by the phonon spectral function allow to appreciate the non-adiabatic corrections induced by the electron-phonon interaction. We divide the analysis in two different parts: Secs. 4.2.2 and 4.2.3 are devoted to the large momentum regime ($\mathbf{q} \gg \overline{\Gamma}$) and the small momentum regime ($\mathbf{q} \to \overline{\Gamma}$), respectively. For the phonon modes driving effective electronic inter-valley scattering $\mathbf{q} \gg \overline{\Gamma}$, large spectral broadenings are identified. For the long-wavelength optical phonon modes with $\mathbf{q} \to \overline{\Gamma}$, responsible for intra-valley scattering, large frequency hardenings and sharp dispersions accompanied by intricate spectral structures emerge. In Sec. 4.2.4, we rationalize the emergent spectrum within the small momentum regime in terms of a multiple-phonon quasi-particle picture, which explicitly accounts for the splitting of the adiabatic optical phonon branch induced by the electron-phonon interaction. The computational methods are described in Sec. 4.2.1.

4.2.1 Computational methods

The potential change matrix elements in Eq. 2.7 have been calculated considering the full-spinor Kohn-Sham electron states and the spin-dependent first-order derivatives of the Kohn-Sham potential with respect to the ionic displacements on coarse 16×16 **k**-point and 8×8 **q**-point meshes for electrons and phonons, respectively. The SBZ summations involved in the computation of the converged phonon self-energy (Eq. 2.19) and FS-averaged electron-phonon coupling strength (Eq. 2.59) are performed using fine 1800×1800 **k**-point and 1800×1800 **q**-point meshes by means of the Wannier interpolation scheme of electron-phonon matrix elements. The Wannier interpolation is limited to the spin-split low-energy conduction-bands, and therefore, the sum over the band indexes runs over the two of them. The sum over the branch index runs over all the phonon modes of the MoS_2 monolayer. The imaginary part of the phonon self-energy (Eq. 2.61) is calculated for a frequency range of $\omega \in [-100 \text{ meV}; 100 \text{ meV}]$ with a frequency step of $\Delta\omega = 0.05$ meV and replacing the delta functions $\delta(\varepsilon_{\mathbf{k}n} - \varepsilon_{\mathbf{k}+\mathbf{q}m} - \omega)$ by Gaussian functions with a broadening value of 1 meV. The Fermi-Dirac occupation factors are taken into account with a spreading value of 5 meV (~ 60 K). The real part of the phonon self-energy is recovered by means of Kramers-Kronig relations in Eq. 2.21 from the imaginary part, and the phonon spectral function is then obtained by means of Eq. 2.45. Regarding the FS-averaged electron-phonon coupling strength (Eq. 2.59), the delta functions $\delta(\varepsilon_{\mathbf{k}n} - \varepsilon_{\mathbf{k}+\mathbf{q}m} \pm \omega_{\mathbf{q}\nu})$ and $\delta(\varepsilon_{\mathbf{k}n} - \varepsilon_{\mathrm{F}})$ are replaced by Gaussian functions with a broadening of 2 meV. The superconducting critical temperatures are estimated by the semi-empirical McMillan-Allen-Dynes formula in Eq. 2.69 with Coulomb repulsion parameters ranging from $\mu^* = 0.00$ to $\mu^* = 0.25$ values.

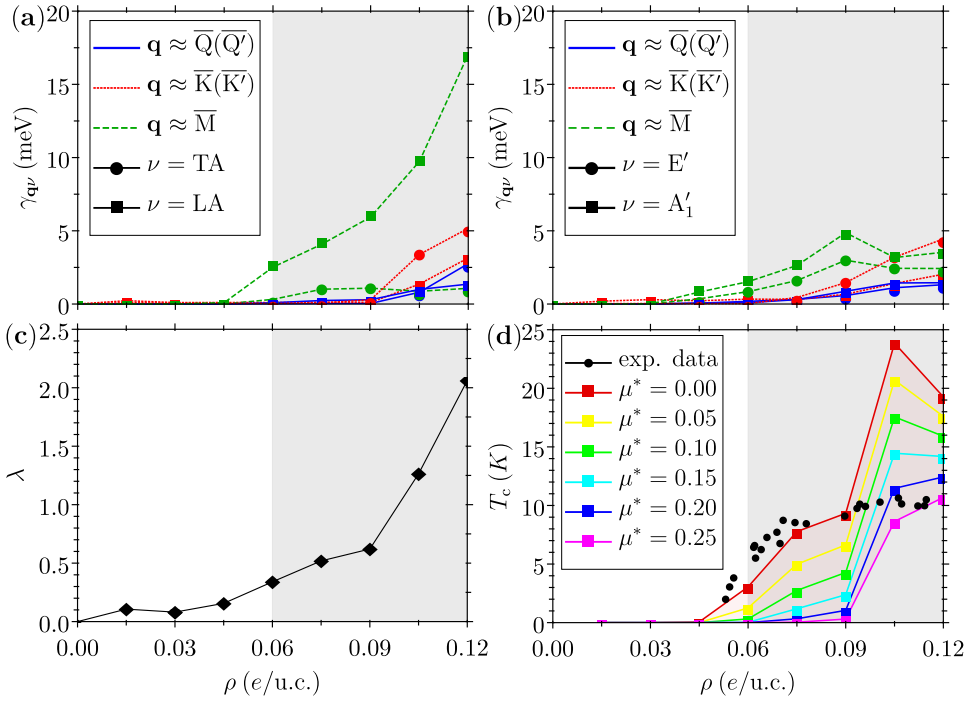

Figure 4.9. The phonon linewidth $\gamma_{\mathbf{q}\nu}$ as a function of doping for (a) acoustic and (b) optical vibrational modes at $\mathbf{q} \approx \overline{\mathrm{Q}}(\overline{\mathrm{Q}}')$, $\overline{\mathrm{K}}(\overline{\mathrm{K}}')$ and $\overline{\mathrm{M}}$, represented by solid blue, dotted red and dashed green lines. In panel (a), circles and squares represent the acoustic TA and LA phonon modes, respectively, while, in panel (b), the optical E′ and A_1' phonon modes, respectively. (c) The electron-phonon coupling strength λ and (d) the superconducting critical temperature T_c as a function of doping. Black circles are experimental data from Ref. [233] and colored lines represent T_c for the Coulomb potential parameter in the range $0.00 \leqslant \mu^* \leqslant 0.25$. The white and shaded gray areas correspond to the small and intermediate doping regime, respectively.

4.2.2 Large momentum regime ($\mathbf{q} \gg \overline{\Gamma}$)

In this section, we analyze the non-adiabatic effects induced by the electron-phonon interaction on the phonon spectral function of the doped MoS_2 monolayer within the large momentum regime. By the large momentum regime we refer to the set of wave vectors $\mathbf{q}$ away from the $\overline{\Gamma}$ point that take part in the phonon-mediated inter-valley electronic scattering. This is governed by the doping-dependent topology of the Fermi surface, as explained in Sec. 4.1.4, and comprises momenta near $\mathbf{q} = \overline{\mathrm{Q}}(\overline{\mathrm{Q}}')$, $\overline{\mathrm{K}}(\overline{\mathrm{K}}')$ and $\overline{\mathrm{M}}$.

In Fig. 4.8, we observe that the non-adiabatic electron-phonon corrections upon doping do not change appreciably the adiabatic phonon dispersions within the large momentum regime, and, to a large extent, we can say that the renormalized phonon frequencies follow the adiabatic ones, i.e. $\Omega_{\mathbf{q}\nu} \approx \omega_{\mathbf{q}\nu}$. Thus, we assume that the only significant spectral feature

related to the electron-phonon coupling is the broadening of the phonon linewidth. Thereby, the phonon linewidth is taken approximately equal to the imaginary part of the phonon self-energy in Eq. 2.61 evaluated at the adiabatic frequency itself, which is the same as one would obtain by Fermi's golden rule or the Rayleigh-Schrödinger perturbation theory approach in Eq. 2.62. Figure 4.9 represents the calculated values of $\gamma^{\mathrm{RS}}_{\mathbf{q}\nu}$ as a function of the electron-doping for the phonon modes effectively coupled to electrons and evaluated at momenta near $\mathbf{q} = \overline{\mathrm{Q}}(\overline{\mathrm{Q}'})$ (solid blue lines), $\overline{\mathrm{K}}(\overline{\mathrm{K}'})$ (dotted red lines) and $\overline{\mathrm{M}}$ (dashed green lines). We distinguish the small and intermediate doping regimes, which are represented by the white and gray areas, respectively. In Fig. 4.9(a), the LA and TA acoustic phonon branchs are represented by squares and circles, respectively. On the other hand, in Fig. 4.9(b), the A'_1 and E' optical phonon branchs are represented by squares and circles, respectively.

At small doping concentrations, only the LA and A'_1 phonon modes at $\mathbf{q} = \overline{\mathrm{M}}$ exhibit weak but appreciable linewidth broadenings. This is an expected behavior, since in this doping regime these are the only phonon modes that are effectively coupled to electrons (Sec. 4.1.4). Therefore, the LA and A'_1 phonon modes at $\mathbf{q} \approx \overline{\mathrm{M}}$ decay by exciting spin-conserving $\overline{\mathrm{K}} \leftrightarrow \overline{\mathrm{Q}'}$ ($\overline{\mathrm{K}'} \leftrightarrow \overline{\mathrm{Q}}$) inter-valley electron-hole pairs. The real electronic excitations become energetically accessible when both occupied and unoccupied states at the $\overline{\mathrm{K}}(\overline{\mathrm{K}'})$ and $\overline{\mathrm{Q}}(\overline{\mathrm{Q}'})$ valleys, respectively, are within the phonon-mediated energy window (shaded green area in Fig. 4.4). The latter, as well as the resulting finite phonon linewidth broadening, occur for electron-doping concentrations $\rho \geqslant 0.045$ e/u.c..

At intermediate doping concentrations, the in-plane polarized E' and A'_1 optical phonon modes at $\mathbf{q} \approx \overline{\mathrm{Q}}(\overline{\mathrm{Q}'})$ and $\overline{\mathrm{K}}(\overline{\mathrm{K}'})$ acquire appreciable finite linewidth broadenings. This is also an expected behavior, since in this doping regime many additional effective phonon-mediated spin-conserving inter-valley electron-hole pair excitations become energetically available (Sec. 4.1.4). Likewise, the broadening of the above discussed phonon linewidths at $\mathbf{q} \approx \overline{\mathrm{M}}$ is also enhanced. It is particularly remarkable that the LA phonon branch at this precise momentum exhibits linewidth values as large as three times that of the other modes.

Continuing with this discussion, it is important to point out that the phonon linewidth is intimately related to the electron-phonon coupling strength (Eqs. 2.65 and 2.66). The phonon linewidth is a magnitude which accounts for the electron-phonon interaction, so that the wider is the phonon linewidth the more the given phonon mode contributes to the interaction. Figure 4.9(c) represents the electron-phonon coupling strength of the MoS_2 monolayer as a function of doping. The interaction is found to be very weak within the small doping regime, exhibiting small but finite values of about $\lambda \sim 0.1$. This must result from the effective coupling of electrons to phonon modes at $\mathbf{q} \to \overline{\Gamma}$, since we have already ruled out the contributions from

phonon modes with $\mathbf{q} \gg \overline{\Gamma}$. Within the intermediate doping regime, the electron-phonon coupling strength exhibits a rapidly growing enhancement up to values of about $\lambda \sim 2$, which resembles in shape to the outstanding linewidth broadening of the LA phonon mode at $\mathbf{q} \approx \overline{\mathrm{M}}$ (green line in Fig.4.9(a)). One concludes that the electron-phonon interaction at the MoS_2 monolayer is mainly governed by the spin-conserving inter-valley electronic scattering mediated by LA phonon modes with $\mathbf{q} \approx \overline{\mathrm{M}}$. We recall that the latter includes $\overline{\mathrm{K}} \leftrightarrow \overline{\mathrm{Q}'}$ and $\overline{\mathrm{K}'} \leftrightarrow \overline{\mathrm{Q}}$ transitions, as well as transitions between equivalent $\overline{\mathrm{Q}}$ or $\overline{\mathrm{Q}'}$ valleys (Figs. 4.6(d) and (e)).

In relation to the strong coupling described in the previous paragraph, several theoretical works [237–240] have proposed the electron-phonon interaction as the mechanism responsible for the superconductivity experimentally found in gate-tuned MoS_2 thin flakes [233–236]. Indeed, the onset of superconductivity has been reported at electron-doping concentrations of $\rho \approx 6 \times 10^{13}$ e/cm^2, i.e. $\rho \approx 0.05$ e/u.c. for our modeled unit cell, which coincides with the large strengthening of the electron-phonon interaction (Fig. 4.9(c)). Figure 4.9(d) displays the calculated superconducting critical temperature T_c as a function of doping. Black circles represent the experimental data from Ref. [233], while the colored lines represent our calculations using the McMillan-Allen-Dynes semi-empirical formalism with a Coulomb potential parameter μ^* ranging from 0 to 0.25. It is seen that our calculations reproduce qualitatively the experimentally measured dome-shaped superconducting region and the order of magnitude of T_c. This is quite remarkable because the McMillan-Allen-Dynes formula assumes an average of the Fermi surface and neglects all the electronic anisotropy. In addition, T_c values computed with $\mu^* = 0$ follow the experiment up to $\rho = 0.09$ e/u.c., while for higher electron-doping concentrations calculations a value of $\mu^* = 0.2$ and 0.25 reproduces the experimental data more closely. This suggests that for smaller doping levels within the intermediate doping regime the electron-electron interaction is not dominant, but for higher concentrations regime the Coulomb repulsion is necessary in order to properly describe T_c.

4.2.3 Small momentum regime ($\mathbf{q} \to \overline{\Gamma}$)

In this section, we analyze the non-adiabatic effects induced by the electron-phonon interaction on the phonon spectral function of the doped MoS_2 monolayer within the small momentum regime ($\mathbf{q} \to \overline{\Gamma}$). In the small momentum limit, we focus on the optical phonon branches that take part in the phonon-mediated intra-valley electronic scattering. We thus avoid discussing the acoustic modes, since their coupling with electrons vanishes, $g^{\nu}_{mn}(\mathbf{k}, \mathbf{q}) \to 0$, when $\mathbf{q} \to \overline{\Gamma}$ [2].

Figure 4.10 shows the calculated phonon spectral function within the small momentum regime for all the electron-doping levels considered in this work except those within the large doping regime. In fact, this figure is a

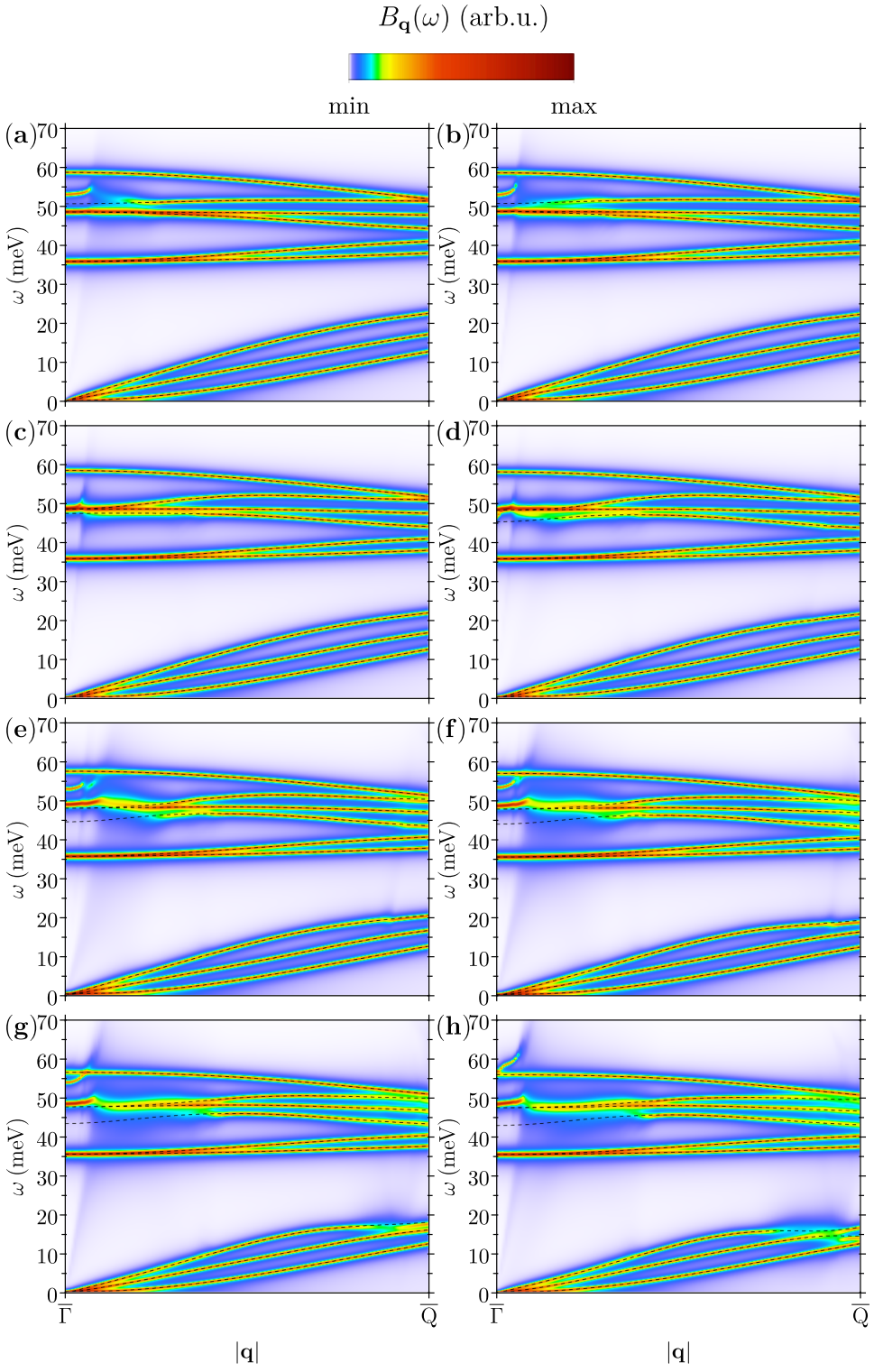

Figure 4.10. Density plot of the phonon spectral function of the MoS_2 monolayer within the small momentum regime for the electron-doping concentrations ρ = 0.015 (a), 0.030 (b), 0.045 (c), 0.060 (d), 0.075 (e), 0.090 (f), 0.105 (g) and 0.120 e/u.c. (h) near $\overline{\Gamma}$. The color code scale represents the height of the spectral function. Dashed black lines represent the adiabatic phonon dispersion relations.

zoom of Fig. 4.8 between $\overline{\Gamma}$ and $\overline{\mathrm{Q}}$. The dashed black lines show the corresponding adiabatic phonon dispersion relations. The color code represents the height of the phonon spectral function. Unlike in the large momentum regime, in this case the non-adiabatic electron-phonon effects are not only limited to the broadening of the phonon linewidth but also lead to a large hardening of the phonon frequency at $\mathbf{q} = \overline{\Gamma}$, accompanied by an increasingly steeper dispersion of the branch slightly away from the SBZ center. Therefore, the adiabatic approximation completely breaks down in this momentum regime. While at small doping concentrations only the out-of-plane polarized A_1' optical phonon branch exhibits significant spectral features (Figs. 4.8(a)-(d)), the in-plane polarized E' optical phonon modes also display appreciable spectral features within the intermediate doping regime (Figs. 4.8(e)-(h)). The latter appear rather insensitive to doping, unlike the former case. This is consistent with the fact that the corresponding electron-phonon matrix elements do not vary significantly with increasing the electron-doping concentration. The electron-phonon matrix elements obtained from first-principles calculations for the E' branches at $\mathbf{q} = \overline{\Gamma}$ interacting with electron states at $\mathbf{k} = \overline{\mathrm{K}}(\overline{\mathrm{K}'})$ are smaller than 1 meV for all the electron-doping levels. For electron states at $\mathbf{k} = \overline{\mathrm{Q}}(\overline{\mathrm{Q}'})$, the electron-phonon matrix elements are found in the range of $30 - 40$ meV for all the electron-doping levels. Henceforth, we focus exclusively on the A_1' optical phonon branch, which reveals the most interesting and complex evolution of the spectral features as a function of doping.

Coupling of the low-energy electron conduction-bands to the $\mathbf{A_1'}$ optical phonon branch at $\mathbf{q} \to \overline{\Gamma}$ within an Einstein-like model

In order to get a better insight into the physics related to the A_1' optical phonon branch at $\mathbf{q} \to \overline{\Gamma}$, we derive a simple analytic model for the MoS_2 monolayer that reproduces our first-principles results. As seen in Fig. 4.2(b), the low-energy electron conduction-band structure consists of two almost spin-degenerated valleys centered at the $\overline{\mathrm{K}}(\overline{\mathrm{K}'})$ points and two spin-split valleys centered at the $\overline{\mathrm{Q}}(\overline{\mathrm{Q}'})$ points. Thus, phonon-mediated inter-band electron-hole scattering can be neglected within the small momentum regime, since the low-energy spin-split conduction-bands are opposite spin-polarized, and only phonon-mediated intra-valley electronic scattering is considered by spin-converving arguments. In addition, we just account for conduction-valleys that are filled up to electron-doping levels in the intermediate doping regime (Figs. 4.4(a)-(h)), since the lattice becomes unstable for larger electron-doping concentrations. For this reason, the upper spin-split $\overline{\mathrm{Q}}(\overline{\mathrm{Q}'})$ conduction-valleys are not included in this analisis, as they get populated only within the large doping regime.

After these initial considerations, we formulate the Einstein-like model for simulating the MoS_2 monolayer. This consists of a free electron gas com-

Table 4.3. Ab-initio calculated parameters used in the Einstein-like model for the MoS_2 monolayer. $\varepsilon_{\rm F}^{x}$ is the energy of the Fermi level with respect to the bottom of the occupied $x = \overline{\rm K}(\overline{\rm K}')$ and $\overline{\rm Q}(\overline{\rm Q}')$ valleys, respectively. $g_{\rm o}^{x}$ are the intra-band electron-phonon matrix elements for the A_1' phonon mode at $\mathbf{q} = \overline{\Gamma}$ interacting with electron states at strictly $x = \overline{\rm K}(\overline{\rm K}')$ and $\overline{\rm Q}(\overline{\rm Q}')$ $\mathbf{k}$-momenta.

ρ (e/u.c.)	$\varepsilon_{\rm F}^{\overline{\rm K}(\overline{\rm K}')}$ (meV)	$\varepsilon_{\rm F}^{\overline{\rm Q}(\overline{\rm Q}')}$ (meV)	$g_{\rm o}^{\overline{\rm K}(\overline{\rm K}')}$ (meV)	$g_{\rm o}^{\overline{\rm Q}(\overline{\rm Q}')}$ (meV)
0.000	-	-	87	66
0.015	28	-	84	68
0.030	67	-	82	69
0.045	91	-	65	86
0.060	104	-	52	98
0.075	110	18	46	104
0.090	112	35	41	109
0.105	111	49	35	114
0.120	107	61	30	119

posed of four equivalent $\overline{\rm K}(\overline{\rm K}')$-like spin-degenerated valleys and six equivalent $\overline{\rm Q}(\overline{\rm Q}')$-like lower spin-split valleys. These bands are considered as perfectly parabolic dispersing $\varepsilon_{\mathbf{k}}^{x} = |\mathbf{k}^2|/(2m_x^*) - \varepsilon_{\rm F}^{x}$, where m_x^* the electron effective band mass and $\varepsilon_{\rm F}^{x}$ the energy of the Fermi level with respect to the bottom of the $x = \overline{\rm K}(\overline{\rm K}')$ and $\overline{\rm Q}(\overline{\rm Q}')$ conduction-valleys. The energy dispersions $\varepsilon_{\mathbf{k}}^{x}$ have been characterized by means of a fitting procedure for all the electron-doping levels and considering the $\overline{\Gamma{\rm K}}$ direction. In more detail, we obtain $m^*_{\overline{\rm K}(\overline{\rm K}')} = 0.60$ and $m^*_{\overline{\rm Q}(\overline{\rm Q}')} = 0.80$. The parameter values of $\varepsilon_{\rm F}^{x}$ are taken from first-principles calculations. The free electron gas interacts with one single optical phonon branch, which is assumed as adiabatic and disperses like the A_1' vibrational branch, i.e. $\omega_{\mathbf{q}{\rm o}} = \omega_{\mathbf{q}{\rm A}_1'}$. The coupling strength is approximated by constant electron-phonon matrix elements $g_{\rm o}^{x}$, which are obtained from the *ab initio* calculations for the A_1' phonon branch at $\mathbf{q} = \overline{\Gamma}$. All these parameters are gathered in Table 4.3 for all the electron-doping levels.

In the following, we derive the phonon self-energy that accounts for the non-adiabatic electron-phonon effects within this Einstein-like model. Adapting Eq. 2.19 to this proposed model, we find that the non-adiabatic

phonon self-energy is written as:

$$\tilde{\Pi}_{\mathbf{q}\mathrm{o}}(\omega) = \lim_{\eta\to 0^+} \frac{1}{N_{\mathbf{k}}} \sum_{\mathbf{k}}^{1\mathrm{BZ}} \sum_{x} \mathcal{N}_x \left|g_{\mathrm{o}}^x\right|^2 \times \left(\frac{f(\varepsilon_{\mathbf{k}}^x) - f(\varepsilon_{\mathbf{k}+\mathbf{q}}^x)}{\varepsilon_{\mathbf{k}}^x - \varepsilon_{\mathbf{k}+\mathbf{q}}^x + \omega + i\eta} - \frac{f(\varepsilon_{\mathbf{k}}^x) - f(\varepsilon_{\mathbf{k}+\mathbf{q}}^x)}{\varepsilon_{\mathbf{k}}^x - \varepsilon_{\mathbf{k}+\mathbf{q}}^x} \right), \tag{4.4}$$

where $\mathcal{N}_x$ is the number of equivalent valleys for $x = \overline{\mathrm{K}}(\overline{\mathrm{K}'})$ and $\overline{\mathrm{Q}}(\overline{\mathrm{Q}'})$-like valleys, i.e. $\mathcal{N}_{\overline{\mathrm{K}}(\overline{\mathrm{K}'})} = 4$ and $\mathcal{N}_{\overline{\mathrm{Q}}(\overline{\mathrm{Q}'})} = 6$. Since we are dealing with the MoS_2 monolayer, i.e. a pure 2D material, we can conveniently approach the sum in Eq. 4.4 as a 2D integral [6]:

$$\lim_{N_{\mathbf{k}}\to\infty} \frac{1}{N_{\mathbf{k}}} \sum_{\mathbf{k}}^{1\mathrm{BZ}} = A \int \frac{\mathrm{d}\mathbf{k}}{(2\pi)^2}, \tag{4.5}$$

where $A = \sqrt{3}a^2/2$ is the area of the in-plane hexagonal unit cell, with the in-plane lattice parameter $a = 3.16$ Å. Substituting Eq. 4.5 into Eq. 4.4:

$$\tilde{\Pi}_{\mathbf{q}\mathrm{o}}(\omega) = \sum_{x} \mathcal{N}_x \left|g_{\mathrm{o}}^x\right|^2 \Big(\chi_{\mathbf{q}x}^0(\omega) - \chi_{\mathbf{q}x}^0(0) \Big), \tag{4.6}$$

where $\chi_{\mathbf{q}x}^0(\omega)$ is the integral expression of the non-interacting density-response function for the 2D free electron gas, i.e. the 2D Lindhard function, at the x valley, given by:

$$\chi_{\mathbf{q}x}^0(\omega) = \lim_{\eta\to 0^+} A \int \frac{\mathrm{d}\mathbf{k}}{(2\pi)^2} \frac{f(\varepsilon_{\mathbf{k}}^x) - f(\varepsilon_{\mathbf{k}+\mathbf{q}}^x)}{\varepsilon_{\mathbf{k}}^x - \varepsilon_{\mathbf{k}+\mathbf{q}}^x + \omega + i\eta}. \tag{4.7}$$

Indeed, Eq. 4.7 has the following well-kwon analytical result [256]:

$$\chi_{\mathbf{q}x}^0(\omega) = -n_{\mathrm{F}}^x A \left(1 \pm \frac{1}{2q^2} \frac{2m_x^*\omega \mp q^2}{\left|2m_x^*\omega \mp q^2\right|} \sqrt{(2m_x^*\omega \mp q^2)^2 - (2qk_{\mathrm{F}}^x)^2} \right), \tag{4.8}$$

where and $q = |\mathbf{q}|$, and $n_{\mathrm{F}}^x = m_x^*/(2\pi)$ and $k_{\mathrm{F}}^x = \sqrt{2m_x^*\varepsilon_{\mathrm{F}}^x}$ are the DOS and the electron momentum at the Fermi level of a 2D free electron gas at the x valley. Finally, we find that the A_1' phonon spectral function accounting for the non-adiabatic electron-phonon effects within the small momentum regime for the Einstein-like model is given by:

$$B_{\mathbf{q}\mathrm{o}}(\omega) = -\frac{1}{\pi} \mathrm{Im} \left[\frac{2\omega_{\mathbf{q}\mathrm{o}}}{\omega^2 - \omega_{\mathbf{q}\mathrm{o}}^2 - 2\omega_{\mathbf{q}\mathrm{o}} \tilde{\Pi}_{\mathbf{q}\mathrm{o}}(\omega)} \right]. \tag{4.9}$$

Figure 4.11 compares the spectral function for the A_1' phonon mode of the MoS_2 monolayer obtained from *ab initio* calculations and the Einstein-like model, both evaluated within the small momentum limit along the $\overline{\Gamma\mathrm{K}}$

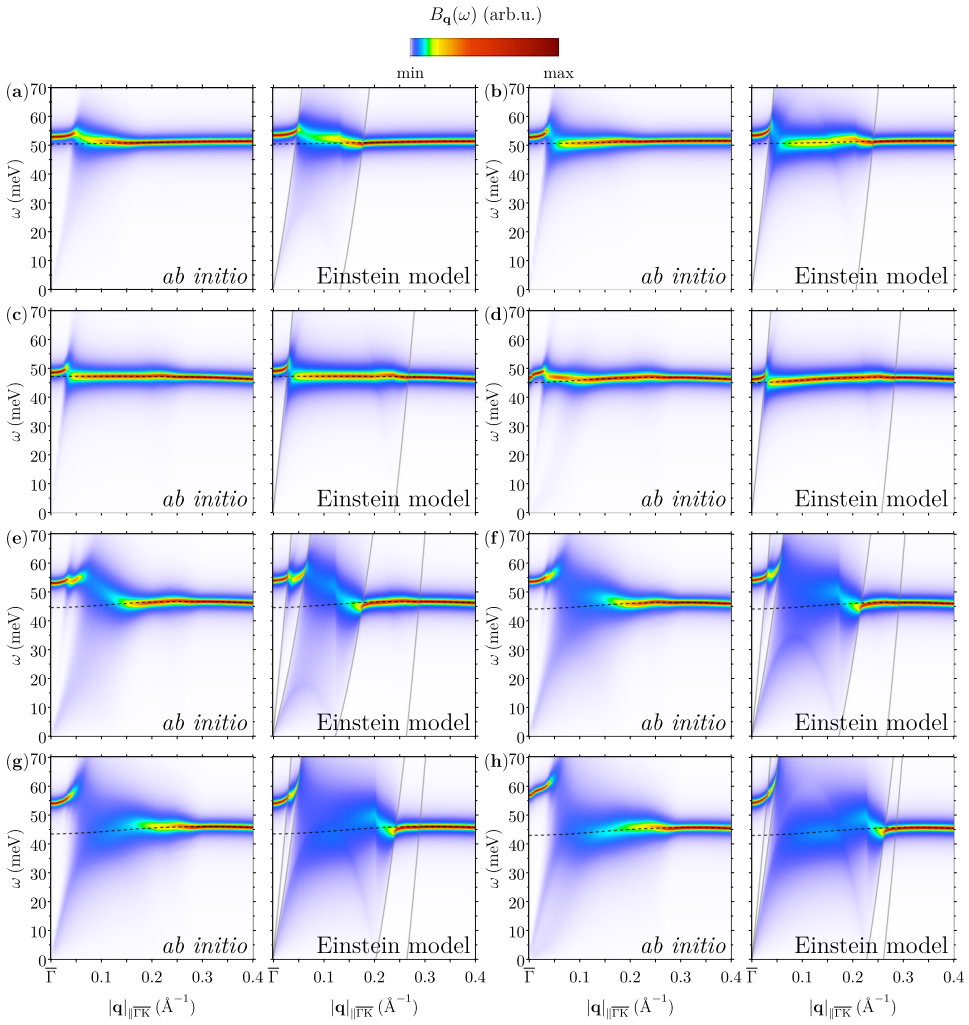

Figure 4.11. Density plot of the spectral function of the MoS_2 monolayer for the A_1' phonon mode within the small momentum regime along the $\overline{\Gamma K}$ direction obtained by means of *ab initio* calculations (left) and the Einstein-like model (right) for the electron-doping concentrations $\rho = 0.015$ (a), 0.030 (b), 0.045 (c), 0.060 (d), 0.075 (e), 0.090 (f), 0.105 (g), and 0.120 e/u.c. (h). The color code scale represents the height of the spectral function. Dashed black lines represent the adiabatic dispersion relations. Solid gray lines bound the electron-hole excitation damping continuum of the Einstein-like model. These are delimited by: $(q^2 + 2qk_{\mathrm{F}}^x)/2m_x^* \geqslant \omega \geqslant (q^2 - 2qk_{\mathrm{F}}^x)/2m_x^*$, where k_{F}^x is the Fermi momentum for each $x = \overline{\mathrm{K}}(\overline{\mathrm{K}'})$ (outer lines) and $\overline{\mathrm{Q}}(\overline{\mathrm{Q}'})$-like (inner lines) valley.

direction for all the electron-doping levels except for those within the large doping regime. The dashed black lines show the corresponding adiabatic dispersion relation for the A_1' phonon mode (dashed magenta lines in Fig. 4.7). The color code represents the height of the phonon spectral function. The good agreement between both phonon spectra for all the electron-doping levels confirms that our analytic model contains all the relevant physics of the non-adiabatic electron-phonon renormalizations.

We can observe that the intensity of the spectral effects decreases with larger carrier concentrations within the small doping regime, where only $\overline{\mathrm{K}}(\overline{\mathrm{K}'})$ intra-valley electron-hole scattering occurs (Figs. 4.11(a)-(d)). This trend is explained by the growing electronic screening that increasingly reduces the value of the screened electron-phonon matrix element $g_{\mathrm{o}}^{\overline{\mathrm{K}}(\overline{\mathrm{K}'})}$ upon doping (Table 4.3). On the other hand, the spectral effects are outstandingly enhanced as the electron-doping concentration grows within the intermediate doping regime, where $\overline{\mathrm{Q}}(\overline{\mathrm{Q}'})$ intra-valley electronic transitions are also allowed (Figs. 4.11(e)-(h)). In particular, for $\rho = 0.12$ e/u.c. in Fig. 4.11(h), the renormalization of the adiabatic branch $\omega_{\mathbf{q}\mathrm{o}}$, which has a frequency of 43.1 meV at $\mathbf{q} = \overline{\Gamma}$, results in a sharp phonon peak with maxima at frequencies $\omega \approx 57$ meV and 63 meV at $\mathbf{q} = \overline{\Gamma}$ and $|\mathbf{q}| \approx 0.05$ Å^{-1} along the $\overline{\Gamma\mathrm{K}}$ direction, respectively. These values correspond to a frequency hardening of $\sim$ 33% and 46%, respectively, being both of them larger than the largest frequency renormalization value reported so far in any material ($\sim$ 30%) [221]. This is explained by the larger values of $g_{\mathrm{o}}^{\overline{\mathrm{Q}}(\overline{\mathrm{Q}'})}$, which also increases rather unexpectedly upon doping, still within the intermediate doping regime, which is unlike $g_{\mathrm{o}}^{\overline{\mathrm{K}}(\overline{\mathrm{K}'})}$. Such a behavior has been recently explained in terms of an electrostatic screening suppression caused by out-of-plane potential changes in inequivalent multi-valley materials, which promote the enhancement of the electron-phonon interaction [230].

For all the electron-doping levels considered in Fig. 4.11, it is seen that the main renormalized phonon peak acquires an appreciable linewidth broadening at a given finite momentum $|\mathbf{q}| \approx 0.03 - 0.05$ Å^{-1} along the $\overline{\Gamma\mathrm{K}}$ direction. By exploring the phonon spectral functions of the Einstein-like model, we quickly notice that the linewidth broadening occurs as soon as the phonon peak enters within the dissipative electron-hole pair excitation continua of the $\overline{\mathrm{K}}(\overline{\mathrm{K}'})$ and $\overline{\mathrm{Q}}(\overline{\mathrm{Q}'})$ valleys, which are bounded by solid gray lines in Fig. 4.11. Indeed, the phonon modes with frequencies higher than the threshold of the Landau damping region do not decay, i.e. $\mathrm{Im}\tilde{\Pi}_{\mathbf{q}\mathrm{o}}(\omega) = 0$, leading to well-defined phonon quasi-particles with idealized infinitely long lifetimes ($\gamma_{\mathbf{q}\mathrm{o}} = 0$). Nevertheless, from a quantum many-body point of view, these phonon modes are allowed to excite virtual electron-hole pairs of lower energy, even in the absence of available energy. Therefore, one finds that in this range $\mathrm{Re}\tilde{\Pi}_{\mathbf{q}\mathrm{o}}(\omega) \neq 0$ [257]. Thereby, a dressing cloud of charge carriers is produced, which oscillates with the lattice and results in

an increase of the frequency of the phonon modes. This gives a physical explanation of the observed hardening and steeper dispersions in Fig. 4.11. Close to the left border of the Landau damping region, the undamped and highly renormalized phonon branch reaches its maximum frequency following a similar dispersion to that of the dissipative electronic continuum edge $\omega \simeq (q^2 + 2qk_{\rm F}^x)/(2m_x^*)$. At this frequency, the lattice and the dressing electronic cloud vibrate in phase. The result is that the phonon velocity coincides with the Fermi velocity, $\Omega_{\mathbf{q}_{\rm o}}/|\mathbf{q}| \approx |\mathbf{v}_{\rm F}|$ [211–213]. On the other hand, at higher momenta within the Landau damping region, phonons acquire a finite lifetime, i.e. $\gamma_{\mathbf{q}_{\rm o}} \neq 0$, since they are energetically allowed to decay by exciting real electron-hole pairs, i.e. $\mathrm{Im}\tilde{\Pi}_{\mathbf{q}_{\rm o}}(\omega) \neq 0$. Thus, for these damped phonons, virtual electron-hole pair excitations become less probable in favor of real excitations, so that $\mathrm{Re}\tilde{\Pi}_{\mathbf{q}_{\rm o}}(\omega) \to 0$ and the frequency renormalizations vanish.

Note that we have rationalized the above non-adiabatic electron-phonon spectral signatures by means of a simple Einstein-like model. Therefore, we conclude that the occurrence of this phenomenon is not unique to the doped MoS_2 monolayer and should be expected for any optical phonon branch in similar conditions as described in this section.

4.2.4 Phonon quasi-particle branch splitting

We analyze now the intricate dynamical structure of the spectral function for the strongly interacting A_1' optical phonon mode within the intermediate momentum regime. By exploring more closely Fig. 4.11, we observe that along with the above illustrated main renormalized phonon peak around $\omega \sim 55 - 65$ meV, a substantial part of the spectral weight remains in the lower frequency range of the phonon spectrum (blue area). This spectral feature develops inside the dissipative electron-hole pair excitation continuum, and thus, has quite a wide structure. While immediately close to $\mathbf{q} = \overline{\Gamma}$ its spectral weight is negligible, the low-frequency feature accumulates an increasing weight when approaching the adiabatic optical branch to the detriment of the high-frequency peak. In addition, the low-frequency spectral weight increases with the strength of the non-adiabatic electron-phonon effects, that is with the electron-phonon coupling strength upon doping. We come now to explain these spectral features in terms of phonon quasi-particle poles.

Figure 4.12(a) displays a cut of the phonon spectral function calculated from first-principles, $B_{q_s \mathrm{A}_1'}(\omega)$ (gray area), for the A_1' optical branch and $\rho = 0.12$ e/u.c., at the momentum $q_s = |\mathbf{q}| = 0.05$ Å^{-1} along the $\overline{\Gamma\mathrm{K}}$ direction. We also represent the phonon quasi-particle spectral functions obtained from solving the phonon Dyson's equation within the standard Rayleigh-Schrödinger (RS), $B^{\rm RS}_{q_s \mathrm{A}_1'}(\omega)$ (long-dashed light-blue line), and the

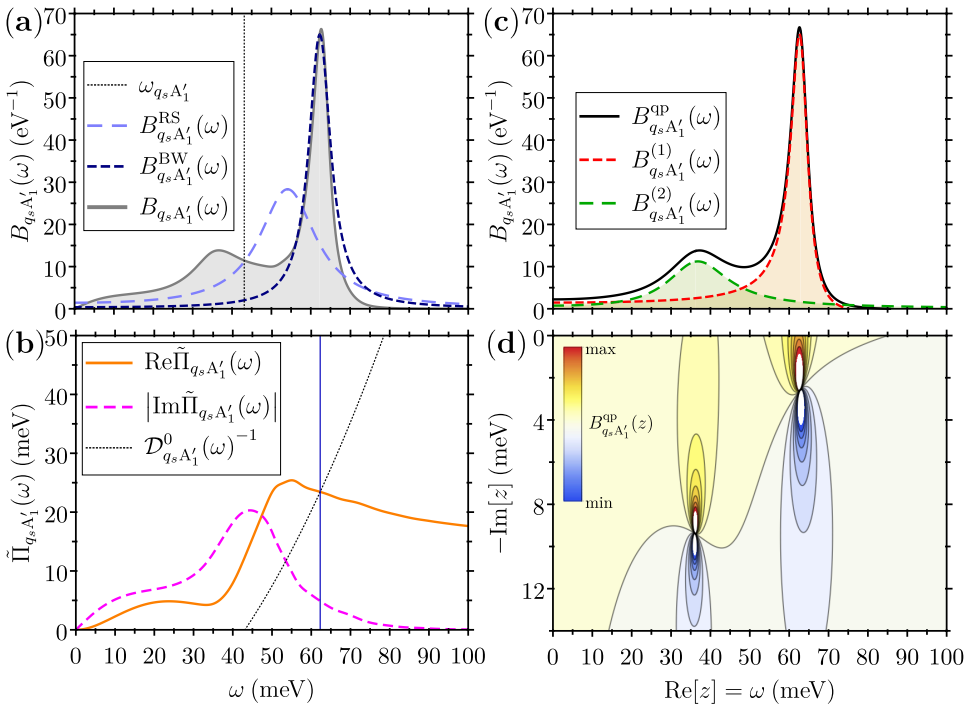

Figure 4.12. The spectral function and the self-energy for the A_1' phonon mode and $\rho = 0.12$ e/u.c. evaluated at $q_s = |\mathbf{q}| = 0.05$ Å^{-1} along the $\overline{\Gamma K}$ direction. (a) The gray area represents the *ab initio* calculated phonon spectral function, $B_{q_s A_1'}(\omega)$. The long-dashed light-blue and short-dashed dark-blue lines represent the phonon quasi-particle spectral functions obtained from the standard procedures based on the Rayleigh-Schrödinger, $B^{RS}_{q_s A_1'}(\omega)$, and Brillouin-Wigner, $B^{BW}_{q_s A_1'}(\omega)$, perturbation theory approaches. The vertical dotted black arrow indicates the adiabatic phonon spectral delta-line. (b) The solid orange and dashed magenta lines show the real and imaginary parts of $\tilde{\Pi}_{q_s A_1'}(\omega)$, respectively. The dotted black line represents the inverse of $\mathcal{D}^0_{q_s A_1'}(\omega)$, whose cut with the real part of the self-energy defines $\Omega^{BW}_{q_s A_1'}$. (c) The double-phonon quasi-particle spectral function obtained by the numerical fitting procedure, $B^{qp}_{q_s A_1'}(\omega)$, and the spectral contributions of the high-frequency, $B^{(1)}_{q_s A_1'}(\omega)$, and the low-frequency, $B^{(2)}_{q_s A_1'}(\omega)$, phonon quasi-particle poles, are represented by the solid black, short-dashed red and long-dashed green black lines, respectively. (d) Contour map of the phonon quasi-particle spectral function on the complex plane z, where the two complex poles are well-defined at $z^{(1)}_{q_s A_1'}$ and $z^{(2)}_{q_s A_1'}$. The color code represents the height of the spectral function.

Table 4.4. The phonon quasi-particle frequency, $\Omega^x_{q_s\mathrm{A}'_1}$, linewidth, $\gamma^x_{q_s\mathrm{A}'_1}$, and renormalization factor, $\mathbb{Z}^x_{q_s\mathrm{A}'_1}$, within the Rayleigh-Schrödinger (x = RS) and Brillouin-Wigner (x = BW) perturbation theory approaches, and within our numerical fitting procedure, x = (1) and (2), starting from the adiabatic frequency $\omega_{q_s\mathrm{A}'_1} = 43.1$ meV for the A'_1 optical phonon mode and $\rho = 0.12\ e$/u.c. at q_s. Recall that the quasi-particle complex poles are defined as $z^x_{q_s\mathrm{A}'_1} = \Omega^x_{q_s\mathrm{A}'_1} - i\,\gamma^x_{q_s\mathrm{A}'_1}$.

x	$\Omega^x_{q_s\mathrm{A}'_1}$ (meV)	$\gamma^x_{q_s\mathrm{A}'_1}$ (meV)	$\mathbb{Z}^x_{q_s\mathrm{A}'_1}$
RS	54.1	8.8	0.78
BW	62.3	3.4	0.69
(1)	62.9	2.6	$0.52 + i\,0.12$ ($\sim 65\%$)
(2)	36.3	9.4	$0.33 + i\,0.04$ ($\sim 35\%$)

Brillouin-Wigner (BW), $B^{\mathrm{BW}}_{q_s\mathrm{A}'_1}(\omega)$ (short-dashed dark-blue line), perturbation theory approaches (Eq. 2.44). Figure 4.12(b) shows the phonon self-energy calculated from first-principles, $\tilde{\Pi}_{q_s\mathrm{A}'_1}(\omega)$, where its real and imaginary parts are represented by the solid orange and dashed magenta lines, respectively. We also represent the inverse of the bare phonon propagator, $D^0_{q_s\mathrm{A}'_1}(\omega)^{-1}$ (dotted black lines), whose intersection with the real part of the phonon self-energy defines the frequency of the phonon quasi-particle within the Brillouin-Wigner perturbation theory approach, $\Omega^{\mathrm{BW}}_{q_s\mathrm{A}'_1}$. While the first principles quantity $B_{q_s\mathrm{A}'_1}(\omega)$ displays a double peak-like structure with maxima at $\omega \approx 36$ and 62 meV, both spectra resulting from the standard procedures (RS and BW) exhibit a single Lorentzian peaked function. The frequency, linewidth and real renormalization factor values for the latter are gathered in Table 4.4. Note that $B^{\mathrm{RS}}_{q_s\mathrm{A}'_1}(\omega)$ completely fails describing the *ab initio* phonon spectral function, while its high-frequency spectral feature at $\omega \approx 62$ mev is roughly approximated by $B^{\mathrm{BW}}_{q_s\mathrm{A}'_1}(\omega)$. This is consistent with the fact that the Brillouin-Wigner perturbation theory is only valid when $\left|\mathrm{Im}\tilde{\Pi}_{q_s\mathrm{A}'_1}(\omega)\right| \ll \mathrm{Re}\tilde{\Pi}_{q_s\mathrm{A}'_1}(\omega)$, which is satisfied in the vicinity of $\Omega^{\mathrm{BW}}_{q_s\mathrm{A}'_1}$, as it as can be seen in Fig. 4.12(b).

The low-frequency feature of $B_{q_s\mathrm{A}'_1}(\omega)$ at $\omega \approx 36$ meV develops at frequencies where the imaginary part of the self-energy is larger than the real part. It is therefore reasonable to think that this spectral feature originates from an additional phonon quasi-particle pole with larger linewidth. As seen in Sec. 2.4.1, the non-linear character of the phonon Dyson's equation in Eq. 2.41 leads to the possibility of finding several solutions, i.e. a multiple-phonon quasi-particle picture. This is properly defined when the whole complex frequency plane is considered as we will see shortly. To this end, in prin-

ciple we should need an analytic continuation of the phonon self-energy into the complex plane. Instead of this, we assume that the phonon self-energy is analytic in the entire complex plane. We numerically fit $B_{q_s\mathrm{A}_1'}(\omega)$ by meas of Eq. 2.48 in order to extract the position of the complex poles and the complex renormalization factors of the phonon quasi-particles. The result is that we find that a double complex pole picture is consistent with the dynamical structure of $B_{q_s\mathrm{A}_1'}(\omega)$. The frequency, linewidth and complex renormalization factor values of the fitted double-phonon quasi-particle structure are also gathered in Table 4.4 ((1) and (2)). Figure 4.12(c) shows the fitted double-phonon quasi-particle spectral function, $B^{\mathrm{qp}}_{q_s\mathrm{A}_1'}(\omega)$ (solid black line). In this figure we also show the spectral contributions of the high-frequency, $B^{(1)}_{q_s\mathrm{A}_1'}(\omega)$ (short-dashed red line), and low-frequency, $B^{(2)}_{q_s\mathrm{A}_1'}(\omega)$ (long-dashed green line), phonon quasi-particle poles, whose corresponding spectral weights represent about the 65% and 35% of the total, respectively. Note that the double-phonon quasi-particle spectral function fits perfectly with the phonon spectral function. Figure 4.12(d) exhibits the contour map of the doule-phonon quasi-particle spectral function in the whole complex frequency plane, with the high-frequency and low-frequency poles found at $z^{(1)}_{q_s\mathrm{A}_1'}$ and $z^{(2)}_{q_s\mathrm{A}_1'}$, respectively (Table 4.4).

Physically, the high-frequency phonon quasi-particle mode has its frequency within the dissipative electron-hole pair excitation continuum of the $\overline{\mathrm{K}}(\overline{\mathrm{K}'})$ valleys, and therefore, acquires a finite linewidth, since it is allowed to decay into $\overline{\mathrm{K}}(\overline{\mathrm{K}'})$ intra-valley electron-hole pairs excitations. However, at the same time, it is also more energetic than the threshold of the Landau damping at the $\overline{\mathrm{Q}}(\overline{\mathrm{Q}'})$ valleys. Thereby, the excitation of virtual electron-hole processes is strongly promoted, leading to a strong frequency renormalization of this phonon mode. On the other hand, the low-frequency phonon quasi-particle mode has its frequency also within the dissipative electron-hole pair excitation continuum of the $\overline{\mathrm{Q}}(\overline{\mathrm{Q}'})$ valleys. Thus, this mode decays into the corresponding electron-hole pair excitations and results highly damped, with a linewidth 3.5 times larger than that of the high-frequency mode.

The precision of the double-phonon quasi-particle picture puts in evidence the origin of the splitting of the adiabatic A_1' optical phonon mode at q_s into two different and well-defined non-adiabatic phonon modes. In order to get an even deeper insight about the phonon branch splitting as described above, we expand our phonon quasi-particle analysis to a finite momentum interval close to $\overline{\Gamma}$. Figures 4.13(a) and (b) show the frequency and linewidth dispersions, respectively, of the phonon quasi-particle modes for the A_1' optical phonon branch and $\rho = 0.12$ e/u.c. within the small momentum regime along the $\overline{\Gamma\mathrm{K}}$ direction. We compare the single-phonon quasi-particle solutions resulting from the Rayleigh-Schrödinger (light-dashed blue lines) and Brillouin-Wigner (dark-solid blue lines) perturbation theory approaches

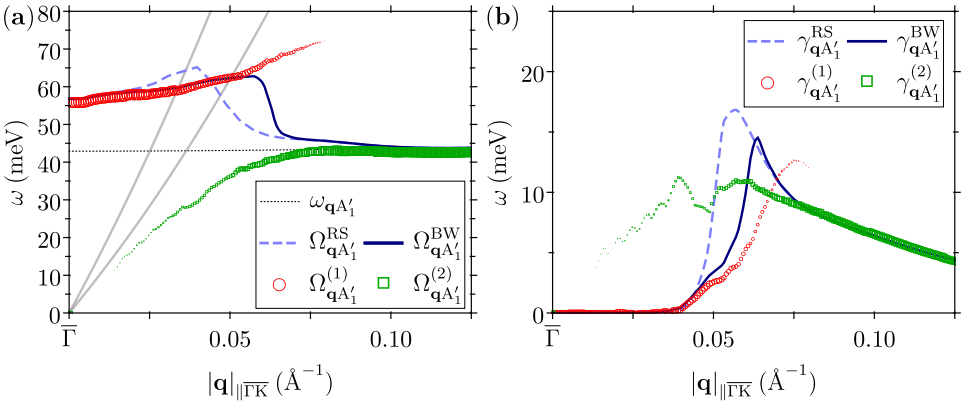

Figure 4.13. The renormalized phonon (a) frequency and (b) linewidth dispersions for the A_1' phonon mode and $\rho = 0.12$ e/u.c., within the small momentum regime along the $\overline{\Gamma K}$ direction. The adiabatic phonon dispersion $\omega_{\mathbf{q}A_1'}$ is represented by the dotted black line. The phonon quasi-particle frequencies and linewidths resulting from the Rayleigh-Schrödinger, $\Omega^{RS}_{\mathbf{q}A_1'}$ and $\gamma^{RS}_{\mathbf{q}A_1'}$, and the Brillouin-Wigner, $\Omega^{BW}_{\mathbf{q}A_1'}$ and $\gamma^{BW}_{\mathbf{q}A_1'}$, perturbation theory approaches are represented by the long-dashed light-blue and solid dark-blue lines, respectively. The frequencies and the linewidths of the high-frequency, $\Omega^{(1)}_{\mathbf{q}A_1'}$ and $\gamma^{(1)}_{\mathbf{q}A_1'}$, and low-frequency, $\Omega^{(2)}_{\mathbf{q}A_1'}$ and $\gamma^{(2)}_{\mathbf{q}A_1'}$, phonon quasi-particle modes resulting from the numerical spectral fitting procedure are represented by open red circles and open green squares, respectively. In panel (a), solid gray lines bound the electron-hole pair excitation continua in the Einstein-like model as in Fig. 4.11. The size of the markers is proportional to the spectral weight of each pole.

with the double-phonon quasi-particle structure. The high-frequency and low-frequency phonon quasi-particle poles resulting from the numerical spectral fitting procedure are represented by the open red circles and the open green squares, respectively. Note that, in panel (a), the solid gray curves represent the left bounds of the electron-hole pair excitation continua for the $\overline{K}$ and $\overline{Q}$ valleys. We observe that the results of the standard single-phonon quasi-particle results are valid very close to $\overline{\Gamma}$ and deep within the Landau damping region, while the non-adiabatic splitting of the optical branch occurs in the vicinity of the edge of the electron-hole pair excitation continua. Moving away from the $\overline{\Gamma}$ point, the renormalized high-frequency optical branch approaches the Landau damping region and an appreciable part of the spectral function is smoothly transferred into the damped low-frequency acoustic branch. Once the high-frequency peak overlaps with the electron-hole pair continua at momentum $|\mathbf{q}| \approx q_s = 0.05$ Å^{-1} along the $\overline{\Gamma K}$ direction, its linewidth broadens rapidly. This coincides with the total transfer of the spectral weight of the high-frequency branch to the emer-

gent low-frequency branch, which follows a damped dispersion similar to the adiabatic one at higher momenta.

4.3 Electron-phonon effects on the electron spectral function

In this section, we analyze the electron spectral function of the electron-doped MoS_2 monolayer considering a procedure similar to that of Sec. 4.2. In Sec. 4.3.2, we examine the doping-dependence of the electron-phonon effects on the electron spectral function. In Sec. 4.3.3, we analyze in more the detail the specific doping level for which multiple band splittings or "kinks" are observed in the electron spectral function, recently measured in ARPES experiments [232]. We rely on a reasoning of the energy-dependent structure of the imaginary part of the electron self-energy in order to understand the emergence of these spectral features. Finally, in Sec. 4.3.4, we combine our *ab initio* electron-phonon calculations with a complex energy plane analysis of the electron quasi-particle poles. We show that the singular band splitting or "kink" structure observed in the ARPES experiments can be explained by three coexisting electron quasi-particle states. One of these states, despite being strongly interacting with the accompanying virtual phonon cloud, presents an exceptionally long lifetime. The computational methods are described in Sec. 4.3.1.

4.3.1 Computational methods

The potential change matrix elements in Eq. 2.7 have been calculated considering the full-spinor Kohn-Sham electron states and the spin-dependent first-order derivatives of the Kohn-Sham potential with respect to the ionic displacements on coarse 16×16 $\mathbf{k}$-point and 8×8 $\mathbf{q}$-point meshes for electrons and phonons, respectively. The SBZ summations involved in the converged computation of the electron self-energy in Eq. 2.18, and the electron state-dependent and phonon mode-dependent electron-phonon coupling strength in Eqs. 2.58 and 2.68, respectively, are performed using fine 3000×3000 $\mathbf{k}$-point and 1500×1500 $\mathbf{q}$-point meshes by means of the Wannier interpolation scheme of electron-phonon matrix elements. As for phonons, the Wannier interpolation is limited to the spin-split low-energy conduction-bands, and therefore, the sum over the band indexes runs over the two of them. The sum over the branch index runs over all the phonon modes of the MoS_2 monolayer. The imaginary part of the electron self-energy (Eq. 2.52) is calculated for an energy range of $\omega \in [-500\text{ meV}; 500\text{ meV}]$ with an energy step of $\Delta\omega = 0.02$ meV and replacing the delta functions $\delta(\omega - \varepsilon_{\mathbf{k}+\mathbf{q}m} \pm \omega_{\mathbf{q}\nu})$ by Gaussian functions with a broadening value of 1 meV. These calculations were performed at zero temperature ($T = 0$ K). In these

conditions, the Bose-Einstein occupation factors for phonons are equal to zero and the Fermi-Dirac occupation factors for electrons are related to Heaviside step functions, $f(\varepsilon_{\mathbf{k}n}) = H(\varepsilon_{\mathrm{F}} - \varepsilon_{\mathbf{k}n})$. The real part of the electron self-energy is recovered by means of the Kramers-Kronig relations in Eq. 2.20 from the imaginary part, and the electron spectral function is then obtained by means of Eq. 2.35. Regarding the electron state-dependent and phonon mode-dependent electron-phonon coupling strength (Eqs. 2.58 and 2.68), the delta functions $\delta(\varepsilon_{\mathbf{k}n} - \varepsilon_{\mathbf{k}+\mathbf{q}m} \pm \omega_{\mathbf{q}\nu})$ and $\delta(\varepsilon_{\mathbf{k}n} - \varepsilon_{\mathrm{F}})$ are replaced by Gaussian functions with a broadening value of 1 meV.

Analytical continuation of the electron self-energy

As noted in Sec. 2.3.1, in order to find the proper complex solutions of the electron quasi-particle equation in Eq. 2.26, we need in principle to perform the analytical continuation of the electron self-energy from the upper half complex energy plane into the lower half. To this end, we calculate the electron self-energy from first principles only along the real energy axis, and then, we use a generalization of the method outlined in Ref. [36] to handle electron self-energies without assuming the particle-hole symmetry. For doing so, we use the Kramers-Kronig relations in Eq. 2.20 integrated by parts:

$$\Sigma_{\mathbf{k}n}(\omega + i\eta) = -\int_{-\infty}^{\infty} \mathrm{d}\omega' \log[\omega - \omega' + i\eta] \frac{\partial \mathrm{Im}\Sigma_{\mathbf{k}n}(\omega'')}{\partial \omega''}\bigg|_{\omega''=\omega'} + \mathrm{C}. \quad (4.10)$$

As it is known, the simple replacement of ω by z in Eq. 4.10 is not valid, as the branch-cuts introduced by the logarithmic term makes the direct numerical integration inappropriate [126]. However, we adopt a numerical strategy based on the analytical integration of $\partial \mathrm{Im}\Sigma_{\mathbf{k}n}(\omega)/\partial\omega$ as a piecewise polynomial. In this regard, we have used a cubic spline interpolation, thereby ensuring the continuity of the first and second derivatives of the latter term all over the real energy ω axis.

4.3.2 Doping-dependent electron spectral function

In this section, we analyze the evolution of the electron-phonon effects on the electron spectral function of the MoS_2 monolayer as a function of doping. Figure 4.14 represents the calculated electron spectral function for the electron-doping concentrations $\rho = 0.015$ (a), 0.030 (b), 0.045 (c) and 0.060 e/u.c. (d) within the small doping regime, and $\rho = 0.075$ (e) and 0.105 e/u.c. (f) within the intermediate doping regime. Again, we do not consider the large doping regime, since the crystal is unstable. The dashed black lines show the low-energy bare electron conduction-brand structures (Fig. 4.4). The color code represents the height of the electron spectral function. The differences between the bare electron conduction-bands and the

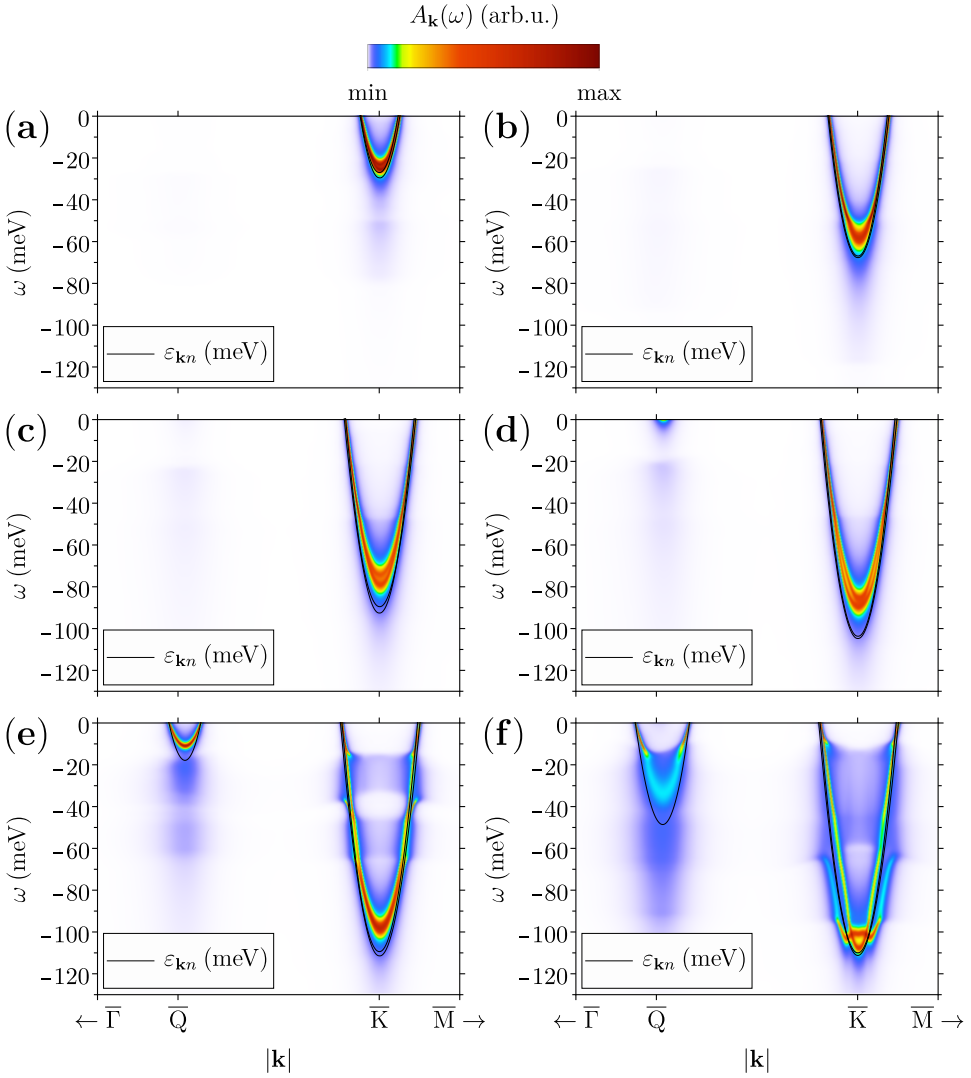

Figure 4.14. Density plot of the electron spectral function of the MoS_2 monolayer for the electron-doping concentrations $\rho = 0.015$ (a), 0.030 (b), 0.045 (c), 0.060 (d), 0.075 (e) and 0.105 e/u.c. (f). The color code scale represents the height of the spectral function. Dashed black lines represent the low-energy bare electron conduction-band structure.

main features defined by the electron spectral functions allow to appreciate the corrections induced by the electron-phonon interaction.

Within the small doping regime, only the almost spin-degenerate $\overline{\mathrm{K}}(\overline{\mathrm{K}'})$ conduction-valleys are occupied, and hence, only these appear in the simulated photoemission spectra. For the lowest electron-doping concentration (Fig. 4.14(a)), the binding energy of the $\overline{\mathrm{K}}(\overline{\mathrm{K}'})$ conduction-valleys is less than the frequency of the A_1' optical phonon mode at $\mathbf{q} = \overline{\Gamma}$, which in this case is the only interacting phonon mode (Sec. 4.2). In these conditions, the electron-phonon interaction presents two distinct spectral features [4]: a renormalized valley with heavier effective mass and a so-called satellite further down at $\omega \approx \omega_{\overline{\Gamma}\mathrm{A}_1'} = 50.6$ meV. In fact, the satellite features have been recently observed in ARPES experiments in doped oxides [205, 228, 258–260]. For larger dopings but still within the small doping regime, the binding energy of the $\overline{\mathrm{K}}(\overline{\mathrm{K}'})$ conduction-valleys is larger than the frequency of the A_1' optical phonon mode at $\mathbf{q} = \overline{\Gamma}$, and therefore, the obtained electron spectral functions resembles more the spectrum of the Einstein model (Appendix C). As seen in Fig. 4.9(c), the electron-phonon coupling strength exhibits rather small values within the small doping regime ($\lambda \sim 0.1$), and therefore, the electron-phonon effects are rather weak. Indeed, the electron spectral functions look very similar to bare electron band structures.

The situation changes drastically as we enter the intermediate doping regime. The $\overline{\mathrm{K}}(\overline{\mathrm{K}'})$ conduction-valleys become strongly renormalized exhibiting unprecedented multiple spectral band-splittings or "kinks" that reproduce the recent intricate ARPES measurements in electron-doped MoS_2 monolayer [232]. These outstanding spectral features are signatures of the strong enhancement of the electron-phonon coupling strength in this system at intermediate electron-doping concentrations ($\lambda > 0.5$) (Fig. 4.9(c)) and the onset of the superconducting state (Fig. 4.9(d)). On the other hand, the lower spin-split $\overline{\mathrm{Q}}(\overline{\mathrm{Q}'})$ conduction-valleys also get populated within the intermediate doping regime, and hence, they appear in the simulated photoemission spectra. These figures demonstrate the outstanding strength of the electron-phonon coupling in the $\overline{\mathrm{Q}}(\overline{\mathrm{Q}'})$ conduction-valleys, which exhibit multiple unequivocal satellites in the spectral function, as well as a strong spectral band-splitting with increasing doping.

4.3.3 Electron spectral function with multiple kinks

In this section, we analyze the multiple band-splitting or "kink" structure observed experimentally in the electron spectral function of the electron-doped MoS_2 monolayer at the $\overline{\mathrm{K}}(\overline{\mathrm{K}'})$ valleys [232]. We focus on the calculated electron spectral function for the doping concentration $\rho = 0.075\ e/\mathrm{u.c.}$ within the "intermediate" doping regime (Fig. 4.14(e)). To this end, it is important to do a deep inspection of the electron-phonon interaction for this specific electron-doping level. Figure 4.15(a) shows the low-energy bare elec-

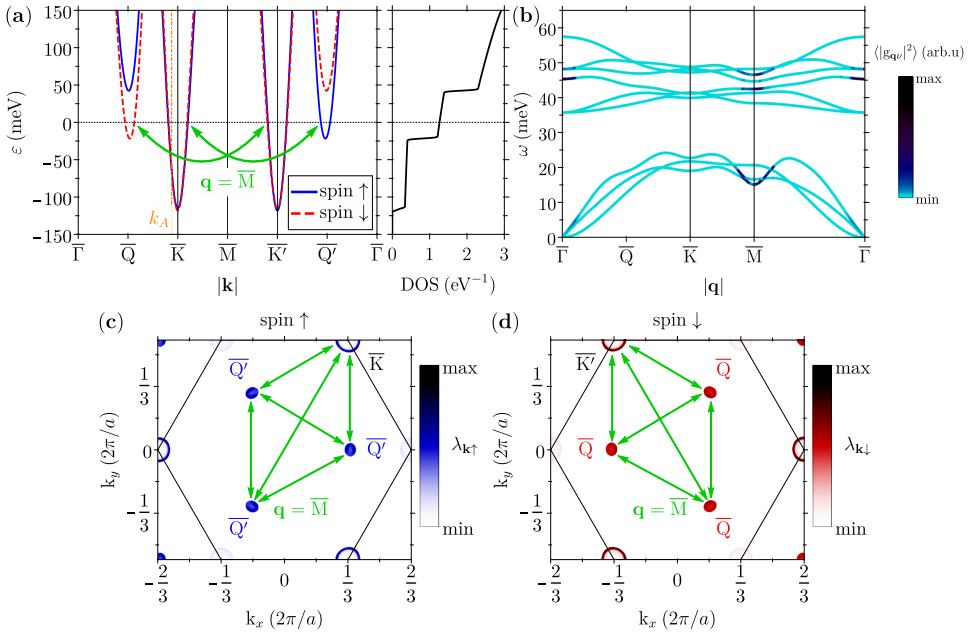

Figure 4.15. (a) Electron conduction-band structure (left) and the corresponding DOS (right) of the MoS_2 monolayer for the electron-doping concentration $\rho = 0.075\, e$/u.c.. Solid blue and dashed red lines represent opposite full out-of-plane spin-polarized bands. The Fermi level is set to zero (horizontal dotted black line). (b) Phonon dispersion relation represented by colored lines, where the color code indicates the electron-phonon weighted nesting function $\langle|g_{\mathbf{q}\nu}|^2\rangle$ for each phonon mode $|\mathbf{q}\nu\rangle$. (c) and (d) Momentum resolved state-dependent electron-phonon coupling strength $\lambda_{\mathbf{k}n}$ within the SBZ for the occupied spin-up (↑) (blue color code) and spin-down (↓) (red color code), respectively. The green arrows depict the most relevant spin-conserving phonon-mediated inter-valley electronic transitions within the "intermediate" doping regime. These are driven by phonon modes with equivalent momenta close to $\mathbf{q} = \overline{\mathrm{M}}$ and connecting the $\overline{\mathrm{Q}}'(\overline{\mathrm{Q}})$ valleys with themselves and with the outer states of the $\overline{\mathrm{K}}(\overline{\mathrm{K}}')$ valleys for the spin-up (spin-down) polarization.

tron conduction-band structure (left) and the corresponding DOS (right). The solid blue and dashed red lines represent opposite full out-of-plane spin-polarized conduction-valleys. The almost spin-degenerate $\overline{\mathrm{K}}(\overline{\mathrm{K}}')$ valleys and the lower spin-split $\overline{\mathrm{Q}}(\overline{\mathrm{Q}}')$ valleys are occupied, with binding energies of $\varepsilon_{\overline{\mathrm{K}}(\overline{\mathrm{K}}')} = -118$ meV and $\varepsilon_{\overline{\mathrm{Q}}(\overline{\mathrm{Q}}')} = -22$ meV, respectively. Note that the latter energy is located within the phonon frequency range. Figure 4.15(b) displays the adiabatic phonon dispersion relation with the color code representing the electron-phonon weighted nesting function, or equivalently the FS-averaged squared electron-phonon matrix element, $\langle|g_{\mathbf{q}\nu}|^2\rangle$ for each phonon mode $|\mathbf{q}\nu\rangle$ (Eq. 2.68). Figures 4.15(c) and (d) show the momentum-resolved electron-phonon coupling strength, $\lambda_{\mathbf{k}n}$, within the SBZ for the occupied electron states with spin-up and spin-down polarizations, respectively.

Indeed, the large values of $\langle|g_{\mathbf{q}\nu}|^2\rangle$ for the acoustic (A) and the optical (O) phonon modes at momentum $\mathbf{q} = \overline{\mathrm{M}}$ with frequencies around $\omega_{\mathrm{A}}^{\overline{\mathrm{M}}} = 16$ meV and $\omega_{\mathrm{O}}^{\overline{\mathrm{M}}} = 46$ meV, respectively, as well as the momentum-resolved density maps of the $\lambda_{\mathbf{k}n}$ for each of the occupied spin-polarized bands definitely confirm that the electron-phonon interaction is dominated by these specific phonon-mediated spin-conserving electronic scattering processes. In particular, among all the possible inter-valley channels connecting the Fermi sheets, the phonon modes at momentum $\mathbf{q} = \overline{\mathrm{M}}$ connect the equivalent $\overline{\mathrm{Q}'}(\overline{\mathrm{Q}})$ with themselves and with the outer states of the $\overline{\mathrm{K}}(\overline{\mathrm{K}'})$ valleys for the spin-up (spin-down) polarization (green arrows in Figs. 4.15(a),(c) and (d)). Specially remarkable are the large values of the state-dependent electron-phonon coupling strengths, which are as large as $\lambda_{\mathbf{k}n} \sim 1.2$ near $\overline{\mathrm{K}}(\overline{\mathrm{K}'})$. Note that this coincides with the assertions given in the previous sections for the specific electron-doping level.

We come now to explain the origin of the multiple band-splittings of the electron spectral function. To this end, we illustrate the configuration of the electron spectral function in terms of the energy-dependent structure of the imaginary part of the electron self-energy. Figure 4.16(a) shows the *ab initio* calculated electron spectral function including the electron-phonon effects of the MoS_2 monolayer for the low-energy conduction-band structure and the electron-doping concentration $\rho = 0.075$ e/u.c.. The framed area delimited by the dashed black rectangle is displayed in Fig. 4.16(b) One immediately realizes that the electron spectral function exhibits two sharp band-splittings at binding energies coinciding with the $\omega_{\mathrm{A}}^{\overline{\mathrm{M}}}$ and $\omega_{\mathrm{O}}^{\overline{\mathrm{M}}}$ phonon frequencies. The calculated electron spectral function reproduces in great detail the recent ARPES measurements performed by Kang *et al.* [232]. The left panels of Figs. 4.16(c) and (d) represent the decomposition of the zoom of the electron spectral function in Fig. 4.16(b) into the outer (spin-up) and inner (spin-down) spin-split electron conduction-bands, respectively. The middle panels represent the corresponding dynamical structure of the imaginary part of the electron self-energy, evaluated at $\mathbf{k} = k_A$ close to $\overline{\mathrm{K}}$ (vertical dashed black lines in left panels). The right panels rationalize the imaginary part of the electron self-energy in terms of energy-conserving and spin-converving $\omega_{\mathrm{A}}^{\overline{\mathrm{M}}}$ and $\omega_{\mathrm{O}}^{\overline{\mathrm{M}}}$ phonon-mediated scattering processes connecting electrons from the DOS of occupied states at the equivalent $\overline{\mathrm{Q}'}$ valleys to the injected hole states at k_A.

First of all, we find that the outer spin-split valley shows outstandingly strong spectral electron-phonon signatures, while the inner spin-split valley shows much weaker spectral details. This is consistent with the above idea that the electron-phonon interaction is governed by $\mathbf{q} = \overline{\mathrm{M}}$ phonon-mediated spin-conserving electronic transitions. Indeed, the outer spin-split $\overline{\mathrm{K}}$ valley has the same spin-polarization as the lower spin-split $\overline{\mathrm{Q}'}$ valley, and hence, both valleys are effectively coupled. Conversely, the inner spin-split $\overline{\mathrm{K}}$ has

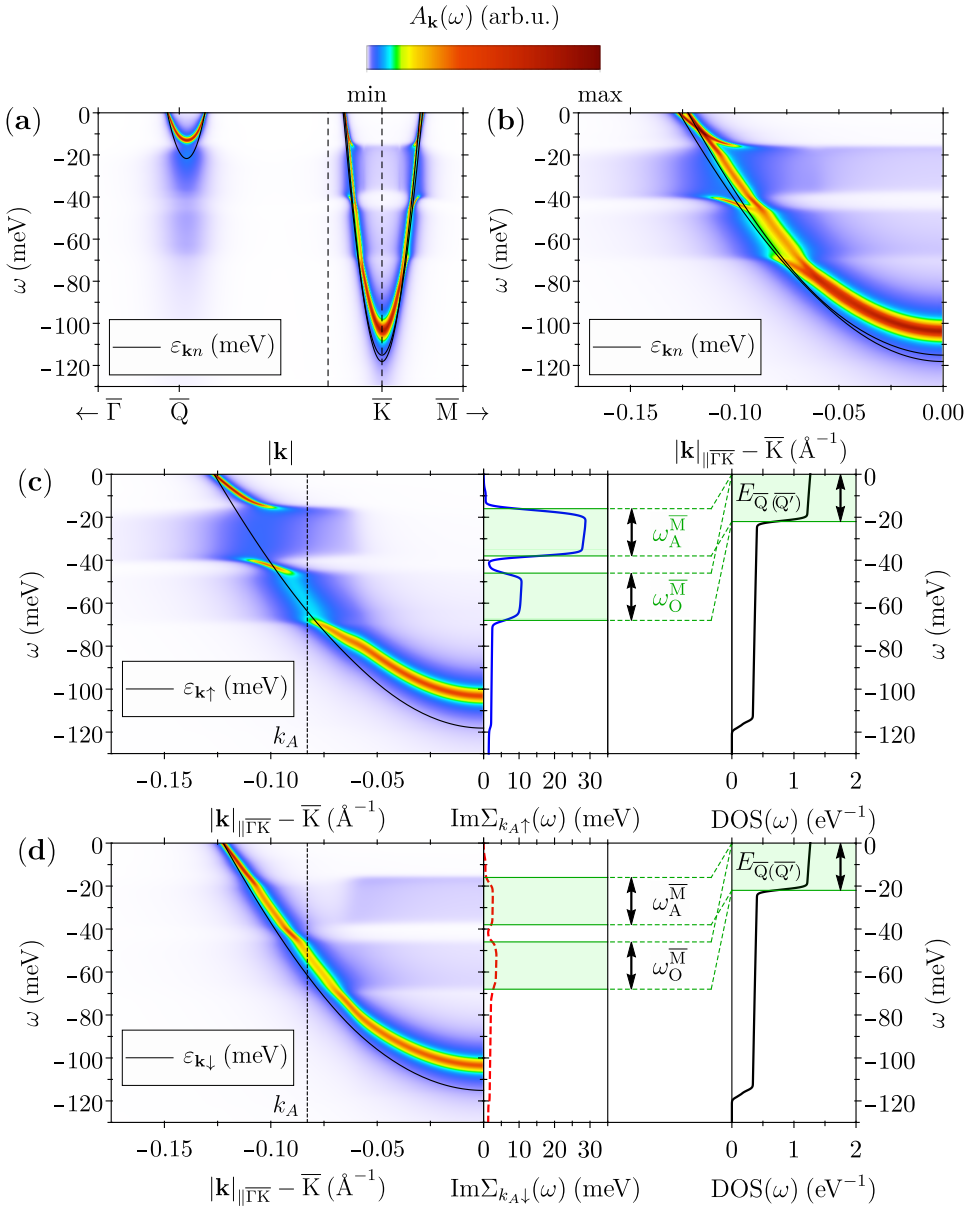

Figure 4.16. Electron spectral function of the MoS_2 monolayer conduction-band structure for the electron-doping concentration $\rho = 0.075$ e/u.c. calculated from first-principles and including electron-phonon interaction effects. The solid black lines represent the non-interacting bare electron conduction-bands. The color code scale represents the height of the spectral function. (a) Spectral function along the $\overline{\Gamma\mathrm{KM}}$ high-symmetry direction within the SBZ. (b) Zoom of the spectral function on the area highlighted in (a) by the dashed black rectangle. Zoom of the spectral function for the (c) outer and (d) inner spin-split states of the $\overline{\mathrm{K}}$ conduction-valley. In the middle panels, the corresponding imaginary part of the electron self-energy is evaluated for the electron state at $\mathbf{k} = k_A$. The onsets of the rectangular maxima are at $\omega_{\mathrm{A}}^{\overline{\mathrm{M}}}$ and $\omega_{\mathrm{O}}^{\overline{\mathrm{M}}}$, while their width is related to the enhanced DOS (right panel) of the occupied $\overline{\mathrm{Q}}'$ valleys (green shaded area).

the opposite spin-polarization, and thus, the coupling suppresses (Sec. 3.3.2). On the other hand, the imaginary part of the electron self-energy of the outer spin-split band exhibits a rather uncommon rectangular-shaped double structure of width $\sim |\varepsilon_{\overline{\mathrm{Q}}(\overline{\mathrm{Q}'})}| = 22$ meV (black double-arrows) with onsets precisely at binding energies corresponding to the $\omega_{\mathrm{A}}^{\overline{\mathrm{M}}}$ and $\omega_{\mathrm{O}}^{\overline{\mathrm{M}}}$ phonon frequencies. The low-energy rectangular shape in the imaginary part of the self-energy function with onset at $\omega_{\mathrm{A}}^{\overline{\mathrm{M}}}$ frequency has a maximum value of almost 28 meV, while the high-energy rectangular shape with onset at $\omega_{\mathrm{O}}^{\overline{\mathrm{M}}}$ has a maximum value of almost 10 meV. These two rectangular shapes are separated by a narrow window of almost 8 meV centered at the binding energy $\omega \sim 42$ meV with almost a vanishing value of ~ 1 meV. It is actually the large increase of the DOS at the occupied $\overline{\mathrm{Q}'}$ valleys that is the responsible of enhancing the available phase-space of the strongly-interacting $\overline{\mathrm{Q}'} \rightarrow \overline{\mathrm{K}}$ scattering process leading to the maximum values of $\mathrm{Im}\Sigma_{k_A\uparrow}(\omega)$ (green shaded areas in Fig. 4.16(e)).

It is also worth discussing the most uncommon spectral feature found in the ARPES experiment [232], found also in our calculated electron spectral at $\omega \sim 42$ meV. Indeed, this feature, if demonstrated to be a well-defined electron quasi-particle, would correspond to a very long-lived state despite being strongly interacting. This is a unique characteristic of the electron-doped MoS_2 monolayer, arising from the fact that the $\overline{\mathrm{K}}(\overline{\mathrm{K}'})$ and $\overline{\mathrm{Q}}(\overline{\mathrm{Q}'})$ conduction-valleys have different binding energies and that there are basically two relevant phonon modes which effectively connect those valleys. Following the previous energy conservation arguments, one notices that the rectangular-shaped double structure with the dip at $\omega \sim 42$ meV in the imaginary part of the electron self-energy will appear as long as electron states at the $\overline{\mathrm{Q}'}$ valleys are occupied and the condition $\omega_{\mathrm{O}}^{\overline{\mathrm{M}}} - \omega_{\mathrm{A}}^{\overline{\mathrm{M}}} > |\varepsilon_{\overline{\mathrm{Q}}(\overline{\mathrm{Q}'})}|$ holds. Thereby, no electron from the occupied $\overline{\mathrm{Q}'}$ valleys can scatter to fill the injected hole at $\mathbf{k} = k_A$ with energies between the two rectangular maxima. We therefore deduce that this electron state is very long-lived and that a double band-splitting structure at momenta near the $\overline{\mathrm{K}}$ valley is obtained as a consequence of the above observation (Figs. 4.14(e) and 4.16(c)). However, for higher doping concentrations, it is found that $|\varepsilon_{\overline{\mathrm{Q}}(\overline{\mathrm{Q}'})}| > \omega_{\mathrm{O}}^{\overline{\mathrm{M}}} - \omega_{\mathrm{A}}^{\overline{\mathrm{M}}}$. In this case, the sharp double band-splitting strucuture is replaced by more common features in the electron spectral function (Fig. 4.14(f)).

In ordinary metals, the imaginary part of the electron-phonon self-energy is a monotonically increasing function due to the practical constant DOS close to the Fermi level within an energy range equal to typical phonon frequencies (Appendix C). Therefore, this situation is radically different to what it is observed in the electron-doped MoS_2 monolayer, and probably in other doped semiconductors.

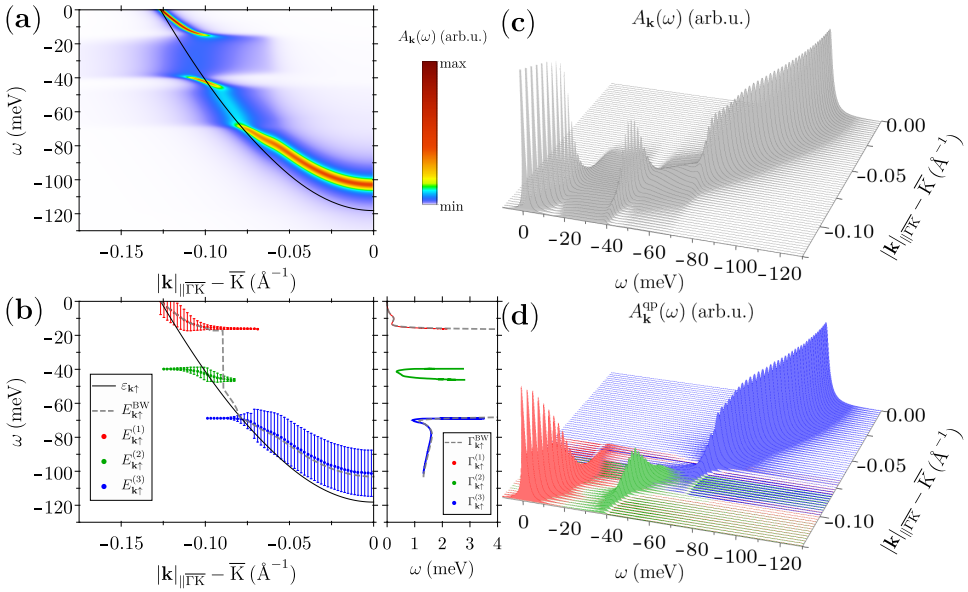

Figure 4.17. Comparison of (a) the electron spectral function and (b) the electron quasi-particle poles dispersion found for the outer spin-split conduction-band near the $\overline{\mathrm{K}}$ point. The solid black lines represent the non-interacting bare electron band. In (a), the color code scale represents the height of the spectral function. In (b), the dashed gray line represent the electron quasi-particle energy dispersion resulting from the Brillouin-Wigner perturbation theory approach (Eq. 2.29), while the red (1), green (2) and blue (3) dots represent the energy dispersion for the the multiple-electron quasi-particle picture found by solving properly the quasi-particle equation in Eq. 2.26 (left). The length of the bars represent the spectral weight of each pole. In the right panel, the electron quasi-particle linewdiths with respect to their energies are shown. (c) and (d) Comparison of the 3D-representation of the spectral function resulting directly from first-principles calculations (gray color) and the contributions from each complex quasi-particle pole, following the same color convention as in (b).

4.3.4 Multiple electron quasi-particle poles

In this section, we come now to rationalize the multiple band-splittings observed in the electron spectral structure in terms of electron quasi-particle poles (Sec. 2.3.1).

Figure 4.17 compares the electron spectral function (panel (a)) with the electron quasi-particle band structure (panel (b)) of the MoS_2 monolayer for the electron-doping concentration $\rho = 0.075$ e/u.c.. For the sake of clarity, we have focused on the same momentum region as in Fig.4.16(c) and only on the strongly interacting outer spin-split conduction-band of the $\overline{\mathrm{K}}$ valley. In Fig. 4.17(b), the dashed gray line represents the electron quasi-particle band structure resulting from the Brillouin-Wigner perturbation

theory approach ($j = \mathrm{BW}$) (Eq. 2.29), while the red ($j = 1$), green ($j = 2$) and blue ($j = 3$) dots represent the multiple-electron quasi-particle band structure found by properly solving the electron quasi-particle equation in the entire complex energy plane (Eq. 2.26). Close to the Fermi momentum, $|\mathbf{k}|_{\|\overline{\Gamma\mathrm{K}}} - \overline{\mathrm{K}} = -0.125$ Å^{-1}, and the Fermi level, $\omega = 0$, a polaron-like band ($j = 1$) [37] (Appendix C) appears with a strongly renormalized dispersion and a large lifetime, i.e a small linewidth $\Gamma^{(1)}_{\mathbf{k}n} \ll 1$ meV. As the electron momentum $\mathbf{k}$ approaches to the $\overline{\mathrm{K}}$ point, the electron quasi-particle band becomes dispersionless, saturating at the binding energy $\omega \sim -16$ meV and gradually losing its spectral weight in favor of deeperly bounded electron quasi-particle states. Far enough from the Fermi momentum at $\omega < -68$ meV, we find a damped ($\Gamma^{(3)}_{\mathbf{k}n} \geqslant 1$ meV) electron quasi-particle band ($j = 3$), following a similar dispersion to the one of the bare electron band structure. The most interesting result is that for intermediate values of the momentum, $|\mathbf{k}|_{\|\overline{\Gamma\mathrm{K}}} - \overline{\mathrm{K}} \in [-0.125; -0.075]$ Å^{-1}, and energy, $\omega \in [-38; -48]$ meV, an additional electron quasi-particle band ($j = 2$) is found, which exhibits a practically flat dispersion with an important spectral weight. This electron quasi-particle band appears long lived, since it lies just within the energy window where the imaginary part of the electron self-energy has almost a gap. It has a linewidth $\Gamma^{(2)}_{\mathbf{k}n} \sim 0.35$ meV, which almost negligible compared to the deep-energy damped quasi-particle band $j = 3$. Indeed, the $j = 2$ electron quasi-particle solutions constitute strongly-interacting and long lived states tending to localization. Said in pass, this result is not obtained by any means when only the real part of the self-energy is considered for calculating the dispersion of the quasi-particles, i.e. Brillouin-Wigner perturbation theory approach (dashed gray line).

Figures 4.17(c) and (d) compare the three-dimensional (3D) spectral representations of the interacting electron Green's function, $A_{\mathbf{k}\uparrow}(\omega)$ (Eq. 2.35), and the result obtained by considering the multiple-electron quasi-particle band structure, $A^{\mathrm{qp}}_{\mathbf{k}\uparrow}(\omega)$ (Eq. 2.38). The latter is explicitly broken into the spectral contributions of each electron quasi-particle band, with the red, green and blue colors associated to the $j = 1$, 2 and 3 electron quasi-particle bands, respectively. The agreement between the interacting electron and electron quasi-particle spectral functions is strikingly good. Moreover, the electron spectral weight condition (Eq. 2.36) is well fulfilled here as the integral of $A^{\mathrm{qp}}_{\mathbf{k}\uparrow}(\omega)$ turns out to be of the order but less than the unity for all the electron momenta analyzed. Indeed, this 3D spectral representation helps us to understand in which way the spectral weight is transferred from one electron quasi-particle band to the other ones as a function of the momentum $\mathbf{k}$, even when for some values of the momentum all the three many-body solutions coexist.

4.4 Conclusions

In this chapter, we have performed a comprehensive first principles analysis of the electron-phonon interaction in the electron-doped MoS_2 monolayer. In particular, we have focused on studying the non-adiabatic effects due to the electron-phonon coupling on the adiabatic phonon dispersion relations, as well as the effects due to the electron-phonon coupling on the bare electron band structures, as a function of doping.

In Sec. 4.1, we have presented the calculated ground-state electronic and lattice vibrational properties of the MoS_2 monolayer and studied their evolution from the undoped semiconductor to the increasingly doped metal phase. The electron-doping concentrations are divided in three different regimes, small, intermediate and large, depending on the level of occupation of the low-energy electron conduction bands. Significant doping-induced changes in the Fermi surface topology promote an enhancement of the Fermi surface nesting. This enhancement rationalized in terms of phonon-mediated and spin-conversing scattering processes is able to explain the strong dependence of the phonon dispersions on the electron-doping. Besides, the increasing electrostatic screening in response to phonon modes induce the development of lattice instabilities, precisely at the doping values at which all the multiple inequivalent spin-split conduction valleys start getting populated. This analysis already highlights the strong interaction between $\overline{\mathrm{K}}(\overline{\mathrm{K}'})$ and $\overline{\mathrm{Q}'}(\overline{\mathrm{Q}})$ valleys, which is mediated by in-plane acoustic and out-of-plane optical phonon modes at momentum $\mathbf{q} = \overline{\mathrm{M}}$.

In Sec. 4.2, we have analyzed the non-adiabatic electron-phonon effects on the phonon spectral function of the electron-doped MoS_2 monolayer. We separately focus on the large ($\mathbf{q} \gg \overline{\Gamma}$) and small ($\mathbf{q} \to \overline{\Gamma}$) momentum regimes. Within the large momentum regime, phonon modes are hardly renormalized and acquire finite lifetimes, exhibiting strong broadening of their linewidths upon doping and are satisfactorily described using the Rayleigh-Schrödinger perturbation theory. In particular, the in-plane polarized longitudinal acoustic (LA) phonon mode at $\mathbf{q} = \overline{\mathrm{M}}$ exhibits the most outstanding enhancement of its linewidth upon doping when passing from the small to the intermediate doping regime. This is followed by a similar strengthening of the electron-phonon coupling and the development of superconductivity, which has been experimentally measured [233]. All this makes it clear that the strong electron-phonon interaction is dominated by the LA phonon mode at $\mathbf{q} = \overline{\mathrm{M}}$ mediated electronic scattering of the equivalent $\overline{\mathrm{Q}'}(\overline{\mathrm{Q}})$ valleys with themselves and those involving the $\overline{\mathrm{K}}(\overline{\mathrm{K}'})$ valleys. Within the small momentum regime, the out-of-plane polarized optical mode (A_1') appears strongly renormalized upon doping, exhibiting large frequency hardenings, in agreement with Refs. [230, 231]. Furthermore, sharp dispersions close to the $\overline{\Gamma}$ point when approaching to the phase-space area corresponding to the electron-hole pair excitation continuum appear. This physical

phenomenon is rationalized in terms of virtual electron-hole pair excitations by means of an Einstein-like model for the MoS_2 monolayer. Likewise, we show that the intricate dynamical structure of the phonon spectral function is explained by the splitting of the adiabatic phonon branch into two physically different phonon quasi-particle branches. Though the MoS_2 monolayer represents a good example of strong electron-phonon interaction with a simple electron valley structure, it is evident that the physics described in this section is not unique to this system but of a quite general nature.

Finally, in Sec. 4.3, we have analyzed the electron-phonon effects on the electron spectral function of the electron-doped MoS_2 monolayer. While we find that within the small doping regime the renormalization effects are rather weak, a larger doping leads to an intricate electron spectra at the $\overline{\mathrm{K}}$ valley that are in good agreement with recent ARPES experiments [232]. We also find that the outer spin-split $\overline{\mathrm{K}}$ valley is strongly renormalized due to its effective coupling to the lower spin-split $\overline{\mathrm{Q}'}$ valleys by means of phonon modes at $\mathbf{q} = \overline{\mathrm{M}}$, while the inner spin-split band is weakly affected due to spin-conserving arguments. The genuine double band-splitting or "kink" structure of the outer spin-split valley is rationalized in terms of available electronic scattering phase-space from the lower spin-split $\overline{\mathrm{Q}'}$ occupied states to the injected hole in the $\overline{\mathrm{K}}$ valley, which under certain circumstances lead to narrow energy windows where electrons are highly renormalized and long lived due to virtual phonon processes. The singular spectral features are explained by a threefold spin-polarized electron quasi-particle band structure resulting from a single bare electron band, with the electron quasi-particle spectral function perfectly resembling the three-peak and double-gap structure observed in the simulated and ARPES measured spectra. These results rule out the original interpretation of Ref. [232] in terms of multi-phonon (higher order) excitations nor to side-bands or satellites without a clear physical meaning. It is worth noting here that one electron quasi-particle band appears long-lived and strongly renormalized, exhibiting a practically flat dispersion that indicates a sort of real space localization property, leaving the possibility of spin-polarized polaron-like states. We believe that these results may serve as a guidance to understand, explore and eventually take advantage of many-body interactions in future works.

Overview and final conclusions

The main goal of this thesis has been to investigate from first principles calculations the spin-dependence and the effects beyond the adiabatic approximation in connection with the electron-phonon interaction in solids. To this end, we have focused on nanostructures with strong relativistic corrections, which are preferential materials due to their strong spin-dependent electronic properties even when they are nominally non-magnetic. Besides, these low-dimensional materials show an enhancement of the electron-phonon interaction and they are experimentally accessible by means of several techniques.

The ground-state electronic and lattice vibrational properties have been studied from state-of-the-art *ab initio* calculations based on the DFT and DFPT theoretical formalisms which are described in Chapter 1. Based on the latter formalisms, the electron-phonon interaction has been described and a variety of well-known calculable expressions for the coupling related magnitudes has been derived in Chapter 2 using several approaches and in combination with many-body perturbation theory based on Green's functions. In this context, the converged computation of all these magnitudes requires a large number of **k**-points and **q**-points which is usually not accessible, or even prohibitive in many cases, by standard DFT and DFPT calculations. The systematic calculation of the wide variety of electron-phonon magnitudes has been possible through state-of-the-art techniques based on maximally localized Wannier functions for interpolating Kohn-Sham electron states and energies, as well as the electron-phonon matrix elements.

In Chapter 3, we have focused on the strongly relativistic Tl/Si(111) surface. In order to incorporate the electron spin degree of freedom together with relativistic effects up to the spin-orbit coupling into the theoretical formalism, we have turned to the quasi-relativistic limit of the Dirac equation. This leads to the generalization of DFT and DFPT to the non-collinear spin case in which Kohn-Sham wave functions are described by two-component spinors and the Kohn-Sham potential is described by a 2×2 matrix in the spin space including relativistic corrections. Apart from the relativis-

tic electron energy and phonon frequency corrections, the spin-orbit coupling determines the spin-polarization of spin-split low-dimensional electron states, governing the electron-phonon matrix elements. We have compared ground-state electronic and lattice vibrational properties of the narrow-gap semiconductor Tl/Si(111) surface with and without taking into account the non-collinear structure of the electron spin and the spin-orbit interaction. We have demonstrated that the unique crystal structure of this surface, combined with the inherent strong spin-orbit interaction due to the Tl heavy element, gives rise to spin-split surface states arising within the silicon bulk band gap in good agreement with ARPES experiments. While low-energy occupied surface states are rather spin-split and exhibit a Rashba-like spin-polarization, low-energy unoccupied surface states are strongly spin-split – the largest spin-splitting energy known in the literature – and exhibit a surface-perpendicular collinear spin-polarization. We have found that the electron spin and the spin-orbit interaction play a different role in the electron-phonon interaction of the Tl/Si(111) surface above and below the Fermi level. While the coupling is practically spin-suppressed for electron states at the bottom of the unoccupied surface bands, a strong and spin-dependent coupling remains for electron states in the top of the occupied surface bands. The former is a very attractive result for potential spintronic applications, since it ensures spin-polarized long-lived surface states, well-defined from bulk contributions, ensuring an ideal scenario for robust coupled spin-charge transport properties.

In Chapter 4, we have focused on the transition metal dichalcogenide MoS_2 monolayer. We have been interested in the low-energy electron conduction-band structure of the monolayer, which is composed of multiple and inequivalent spin-split valleys and very attractive for coupled spin-valley or valleytronics applications. We have seen that the increase of the electron-doping in the monolayer allows the tuning of the Fermi level, accompanied by quantitative shifts in the mutilvalley structure. This leads to deep changes in the shape of the Fermi surface of the system that promote the emergence of Kohn anomalies in the phonon dispersion relations, which even become lattice instabilities at highest dopings and point out a strengthening of the electron-phonon coupling. This enhancement goes hand in hand with the experimentally measured development of supercodunctivity upon doping in this material. We have also analyzed the importance of electron-phonon effects beyond the adiabatic approximation on bare electrons and adiabatic phonons. For the phonon modes in the large momentum regime ($\mathbf{q} \gg \overline{\Gamma}$), we have obtained large spectral broadenings that are linked to the strengthening of the electron-phonon coupling, and hence, to the onset of superconductivity. For the phonon modes in the small momentum regime ($\mathbf{q} \to \overline{\Gamma}$), we have discovered that optical modes are strongly renormalized in the long-wavelength limit as a result of virtual electron-hole pair excitations. Indeed, we have found that the electron-phonon interaction gives rise to two

non-adiabatic phonon quasi-particle modes from a single adiabatic phonon mode. We have been able to reproduce the effects by means of a simple but efficient Einstein model that collects all the physics and demonstrates the general character of the physical phenomenon. As for electron states, we have found a really outstanding spectra as a result of the strengthening of the electron-phonon coupling upon doping, which is in good agreement with recent ARPES experiments. We have rationalized these singular spectral features in terms of phonon-mediated and spin-conserving electronic transitions within the multi-valley structure. The conclusion is that this unique spectrum results from the strong interaction between equally spin-polarized inequivalent valleys mediated by more than one phonon mode. We have explained the intricate experimental electron spectrum in terms of a multiple electron quasi-particle band structure, which arises from a single bare electron band. Indeed, this study turns out to be essential in order to correctly interpret recent ARPES experiments in the electron-doped MoS_2 monolayer, which probably represents the first experiment in which a double band splitting in the electron spectrum has been observed unambiguously. Finally, we have highlighted the presence of a highly renormalized and long-lived spin-polarized quasi-particle flat band, which could favor the formation of spin-polarized polaron-like states.

To put an end to this thesis, we have demonstrated the importance of explicitly taking into account the non-collinear spin and the spin-orbit coupling in electron-phonon calculations at low dimensions. Likewise, we have deepened in the idea of a consistent solution of the Dyson's equation within the entire complex plane in order to describe the physically significant quasi-particle structures of materials. We finish this section by emphasizing that we have discovered a new physical mechanism in relation with the electron-phonon interaction which induces a many-body splitting that emerges for the optical phonon branches in the long-wavelength limit.

Appendices

Appendix A

Exchange-correlation functional approximations

As it has already been stated in Sec. 1.3.1, DFT is based on the Hohenberg-Kohn theorems [27] and the Kohn-Sham approximation [28]. While Kohn-Sham equations (Eq. 1.13-1.15) are derived in an exact form, their practical implementation depends on the ability of approximating as precisely and easily as possible the exchange-correlation energy functional, $E_{\mathrm{xc}}[n]$, whose exact form is unknown [29, 81]. In this appendix, we briefly review the two methods we have used throughout this thesis for approximating the exchange-correlation energy functional, which are the most commonly used approximations: the local density approximation (Sec. A.1) and the generalized gradient approximation (Sec. A.2).

A.1 Local density approximation

The simplest and most intuitive approximation to the exchange-correlation energy functional was already proposed in the original paper of Kohn and Sham in 1965 [28]. This approach consists in assuming that, in the limit of an infinitesimally small volume, the electron charge density of the real system is constant and equal to that of the homogeneous electron gas (HEG). As a consequence, the exchange-correlation energy per electron is assumed to behave locally as that of the HEG. This approach is known as the local density approximation (LDA). Within this approximation, the exchange-correlation energy reads as:

$$E_{\mathrm{xc}}^{\mathrm{LDA}}[n] = \int n(\mathbf{r})\epsilon_{\mathrm{xc}}^{\mathrm{HEG}}\big(n(\mathbf{r})\big)\mathrm{d}\mathbf{r}, \tag{A.1}$$

and the exchange-correlation potential, $V_{\mathrm{xc}}(\mathbf{r})$, reads as:

$$V_{\mathrm{xc}}^{\mathrm{LDA}}(\mathbf{r}) = \frac{\delta E_{\mathrm{xc}}^{\mathrm{LDA}}[n]}{\delta n(\mathbf{r})} = \left(\epsilon_{\mathrm{xc}}^{\mathrm{HEG}}\big(n(\mathbf{r})\big) + n(\mathbf{r})\frac{\mathrm{d}\epsilon_{\mathrm{xc}}^{\mathrm{HEG}}\big(n(\mathbf{r})\big)}{\mathrm{d}n(\mathbf{r})}\right), \tag{A.2}$$

with $\epsilon_{\mathrm{xc}}^{\mathrm{HEG}}\big(n(\mathbf{r})\big)$ the exchange-correlation energy per electron in a HEG with electron charge density $n(\mathbf{r})$.

This energy can be split into the exchange and correlation components, so that: $\epsilon_{\mathrm{xc}}^{\mathrm{HEG}}\big(n(\mathbf{r})\big) = \epsilon_{\mathrm{x}}^{\mathrm{HEG}}\big(n(\mathbf{r})\big) + \epsilon_{\mathrm{c}}^{\mathrm{HEG}}\big(n(\mathbf{r})\big)$. On the one hand, the exchange energy per electron for HEG has an exact analytical expression given by [6]:

$$\epsilon_{\mathrm{x}}^{\mathrm{HEG}}\big(n(\mathbf{r})\big) = -\frac{3}{4}\left(\frac{3}{\pi}\right)^{\frac{1}{3}}\big(n(\mathbf{r})\big)^{\frac{1}{3}}. \tag{A.3}$$

From this and by means of Eq. A.2, one can also derive the analytical expression of the exchange potential:

$$V_x^{\mathrm{LDA}}(\mathbf{r}) = -\frac{4}{3}\epsilon_{\mathrm{x}}^{\mathrm{HEG}}\big(n(\mathbf{r})\big) = -\left(\frac{3n(\mathbf{r})}{\pi}\right)^{1/3}, \tag{A.4}$$

and a simple form can also be obtained for the exchange energy functional in Eq. A.1:

$$E_{\mathrm{x}}^{\mathrm{LDA}}[n] = -\frac{3}{4}\left(\frac{3}{\pi}\right)^{\frac{1}{3}}\int\big(n(\mathbf{r})\big)^{\frac{4}{3}}\mathrm{d}\mathbf{r}. \tag{A.5}$$

On the other hand, the correlation term has not an analytical expression and various parametrizations based on different calculations exist in the literature [86, 261, 262]. The fitting used throughout this thesis corresponds to the simple analytical form parametrized by Perdew and Zunger (PZ) [88], based on the numerical calculations from nearly exact quantum Monte Carlo calculations for the HEG by Ceperley and Alder [87].

Although in principle LDA should only be satisfactory in the limit of the HEG, i.e. for large and slowly varying electron charge densities, experience has shown that this approximation works surprisingly well beyond its expected range of validity [29, 263]. However, LDA is prone to fail in the case of highly inhomogeneous and localized density distributions. It also works poorly in the case of strongly correlated systems, where the effects of the electron-electron interactions go far beyond the HEG model. In addition, LDA generally tends to overestimate binding energies, and consequently, underestimate bond lengths. Finally, it can be especially disastrous in semiconductors, since it systematically underestimates band gap energies [29, 81].

A.2 Generalized gradient approximation

The next natural step in approximating the exchange-correlation energy functional is to realize that realistic electron charge density distributions are not homogeneous. Therefore, the inclusion of information about their spatial variations can be a good strategy in order to create functionals that describe better real materials [29, 81]. This is practically done by allowing

the functional to depend on not just the local density but also on its gradient, $\boldsymbol{\nabla} n(\mathbf{r})$. This approach is known as the generalized gradient approximation (GGA). Within this approximation, the exchange-correlation energy reads as:

$$E_{\mathrm{xc}}^{\mathrm{GGA}}[n] = \int n(\mathbf{r})\epsilon_{\mathrm{xc}}\big(n(\mathbf{r}), |\boldsymbol{\nabla} n(\mathbf{r})|\big)\mathrm{d}\mathbf{r}. \tag{A.6}$$

There exist as many types of GGA functional as ways there are for including the correction of the density gradient in the exchange-correlation energy per electron. The two most widely used GGA functionals are the Perdew-Wang functional (PW91) [89] and the Perdew-Burke-Ernzerhof functional (PBE) [90]. In this thesis, calculations using the GGA approach to the exchange-correlation energy functionals are based on the latter approximation. Experience has demonstrated that GGA generally works better than LDA in predicting the geometry of the crystals as well as binding energies. Nevertheless, GGA is not a universal improvement over LDA, and also gives qualitatively wrong results for materials where electrons tend to be very localized and strongly correlated.

It is worth noting that there is no *a priori* rule to choose the best exchange-correlation functional approximation depending on the material under study. In fact, the best way to proceed is to test different functionals and observe which one gives the result that satisfies best our demands regarding the property we want to evaluate. Finally, it must also be said that there are many other types of exchange-correlation energy functionals, e.g. meta-GGA, which includes density gradient corrections of greater order than one, or hybrid-GGA, which describe exchange-correlation energies as a mixture of LDA and GGA exchange-correlation functionals including exact exchange energies [29, 81]. However, the analytical parametrization of this kind of approximations is far more complicated, and inevitably implies more calculations and more computing time.

Appendix B

The norm-conserving pseudopotential generation

As seen in Sec. 1.3.4, the pseudopotential approximation is an advantageous method for simplifying the description of atoms, and hence, that of solids. Within this approximation, the electron-nucleus potential of any given atom is replaced by an effective potential, i.e. the pseudopotential, which models the interaction between the valence electrons and the ion core. Thereby, one assumes the core electrons to be frozen together with the atomic nucleus as a single element. Likewise, the pseudopotential is constructed in such a way that the valence electron eigenstates are described by nodeless pseudo-wavefunctions. This approach has double computational benefits: it allows to deal with few delocalized valence electrons and the pseudo-wavefunctions of the latter can be expanded with far fewer plane waves, making plane wave basis sets of practical use. In this appendix, we describe the process for generating norm-conserving pseudopotentials [97], which are the ones we use in this thesis.

When constructing the pseudopotential of any given atom, the first thing to do is select a suitable set of valence electron states. This can be done by comparing the extension of the wave functions of the outermost electron eigenstates. The latter are obtained in the spherical atomic potential geometry through an all-electron DFT calculation of the atomic electronic structure subject to the choice of the exchange-correlation energy functional approximation (Appendix A). These all-electron (AE) wave functions are defined as: $\varphi^{\mathrm{AE}}_{nlm}(\mathbf{r}) = R^{\mathrm{AE}}_{nl}(r)Y_{lm}(\theta,\phi)$, where $R^{\mathrm{AE}}_{nl}(r)$ represents the radial part of the wave function, $Y_{lm}(\theta,\phi)$ are the spherical harmonic functions, and n and $\{l,m\}$ are the principal and orbital angular momentum quantum numbers, respectively. As an illustrative example, Fig. B.1 shows the radial parts of the all-electron wave functions for the outer electron eigenstates of the wolfram (W), also known as tungsten, atom ($Z = 74$) with the following electronic configuration: $[\mathrm{Xe}]4f^{14}5d^{4}6s^{2}6p^{0}$. In this case, $5d$, $6s$ and $6p$

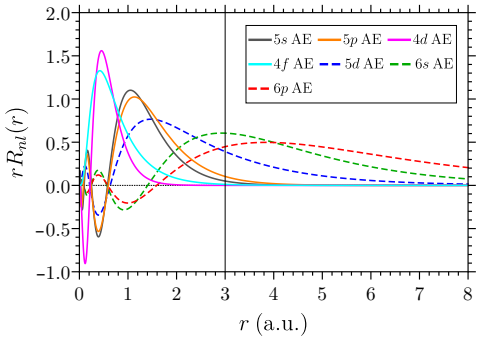

Figure B.1. Radial parts of the calculated all-electron wave functions for the outer electron eigenstates of the W atom. r denotes the radial distance from nucleus. $5d$, $6s$, and $6p$ are the selected valence states for constructing the pseudopotential, whose wave functions are represented by the dashed blue, green and red lines, respectively. $5s$, $5p$, $4d$ and $4f$ states are considered within the ion core, whose wave functions are represented by the solid gray, orange, magenta and cyan lines, respectively.

states, whose all-electron wave functions are represented by the dashed blue, red and green lines, respectively, are good valence electron candidates for building the W pseudopotential. Indeed, the latter exhibit larger amplitude distributions far from the nucleus ($r = 0$) than $5s$, $5p$, $4d$ and $4f$ states, whose all-electron wave functions are represented by the solid gray, orange, magenta and cyan lines, respectively, and almost meet the normalization condition at already $r = 4$ a.u..

Afterwards, one has to create the so-called pseudo-wavefunctions (PS) for each selected valence electron state $\{l, m\}$, which are also defined as: $\varphi_{lm}^{\mathrm{PS}}(\mathbf{r}) = R_l^{\mathrm{PS}}(r)Y_{lm}(\theta, \phi)$. Therefore, the question is reduced to construct the radial part of the pseudo-wavefunctions, $R_l^{\mathrm{PS}}(r)$. As a general rule, for each orbital angular momentum quantum number l, one must choose an arbitrary cutoff radius r_c^l, and then, construct the radial part of the pseudo-wavefunctions in such a way that $R_l^{\mathrm{PS}}(r) = R_{nl}^{\mathrm{AE}}(r)\ \forall\ r > r_c^l$ and $R_l^{\mathrm{PS}}(r)$ smoothly vanishes as $r \to 0\ \forall\ r < r_c^l$. This procedure allows to use far fewer plane waves for computationally describing pseudo-wavefunctions and is well justified because the binding properties of materials do not depend on the form of the wave functions close to the nucleus. Note that in order to retain as precisely as possible the electronic and scattering properties, one also has to make sure that the energy eigenvalues of the all-electron and the pseudo-wavefunctions are identical, as well as their logarithmic derivatives at $r = r_c^l$. Besides, the pseudopotentials used in this thesis have been generated respecting the norm-conserving condition [97], which requires the integrated probability distribution of the all-electron and pseudo-wavefunctions inside

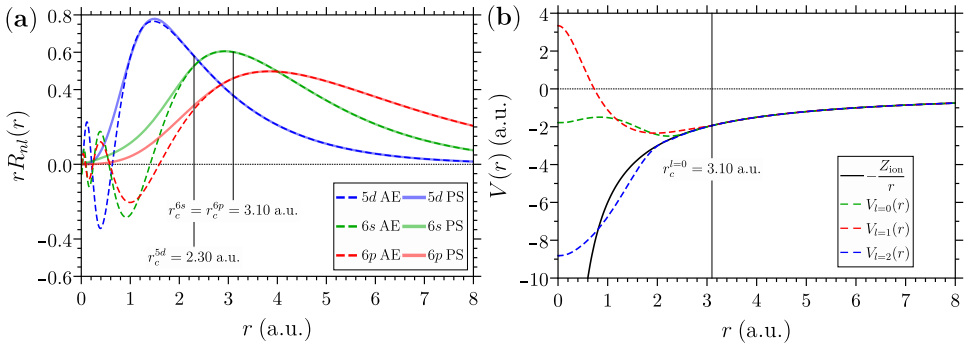

Figure B.2. (a) Comparison between the radial parts of the all-electron wave functions (dashed lines) and the pseudo-wavefunctions (solid lines) for the $5d$ (blue), $6s$ (green), and $6p$ (red) states of the W atom. The cutoff radius for each channel are $r_c^{5d} = 2.30$ a.u. and $r_c^{6s} = r_c^{6p} = 3.10$ a.u., respectively. (b) The corresponding ionic pseudopotentials $V_l(r)$ for orbital angular momentum quantum numbers $l = 0$, 1 and 2, represented by the dashed green, red and blue lines, respectively. $V_{l=0}(r)$ is the local channel. The ionic core potential $-Z_{\rm ion}/r$ is represented by the solid black line. It is clearly shown that $V_l(r) = V_{\rm loc}(r) = -Z_{\rm ion}/r \;\forall\; r > r_c^l$.

r_c^l to be the same:

$$\int_0^{r_c^l} r^2 \big(R_l^{\rm PS}(r)\big)^2 {\rm d}r = \int_0^{r_c^l} r^2 \big(R_{nl}^{\rm AE}(r)\big)^2 {\rm d}r. \tag{B.1}$$

The constructed radial parts of the pseudo-wavefunctions (solid lines) for the $5d$, $6s$ and $6p$ states of the W atom represented by the blue, red and green lines, respectively, are compared to their all-electron counterparts (dashed lines) in Fig. B.2(a). Once we make sure that the selected pseudo-wavefunctions fulfill all the previous requirements of transferability and norm-conservation, we can separately build the ionic pseudopotential $V_l(r)$ for each orbital angular momentum quantum number l by inverting the radial Schrödinger equation with the all-electron energy eigenvalue, $\varepsilon_{nl}^{\rm AE}$, yielding to:

$$V_l(r) = \varepsilon_{nl}^{\rm AE} - \frac{l(l+1)}{2r^2} + \frac{1}{2rR_l^{\rm PS}(r)} \frac{{\rm d}^2}{{\rm d}r^2} \Big(rR_l^{\rm PS}(r) \Big). \tag{B.2}$$

Note that $V_l(r)$ is not universally defined but depends on the arbitrarily chosen requirements of the valence configuration and the cutoff radius for generating the radial part of the corresponding pseudo-wavefunction. Thus, there is not one best pseudopotential for any given element, but many choices in fact, each one optimized for some particular use. For computational benefit, pseudopotentials are usually recast into the Kleinman-Bylander separable form [264], where the ionic pseudopotential operator, $\hat{V}$, is separated into a local (loc) l-independent part, $\hat{V}_{\rm loc}$, and a non-local (NL) l-dependent part,

$\hat{V}_{\rm NL}$, as:

$$\hat{V} = \hat{V}_{\rm loc} + \hat{V}_{\rm NL} = \hat{V}_{\rm loc} + \sum_{lm} \frac{|\delta V_l \varphi_{lm}^{\rm PS}\rangle \langle \delta V_l \varphi_{lm}^{\rm PS}|}{\langle \varphi_{lm}^{\rm PS}|\delta V_l|\varphi_{lm}^{\rm PS}\rangle}, \tag{B.3}$$

and $\delta V_l(r) = V_l(r) - V_{\rm loc}(r)$ is the non-local term for each angular momentum. One must define one of the angular momenta as the local channel in such a way that, for this precise angular momentum, $V_l(r) = V_{\rm loc}(r)\ \forall\ r$, and therefore, $\delta V_l(r) = 0\ \forall\ r$. Note that $V_{\rm loc}(r) = -Z_{\rm ion}/r\ \forall\ r > r_c^{\rm loc}$, where $Z_{\rm ion}$ is the number of chosen valence electrons. In addition, since $R_l^{\rm PS}(r) = R_{nl}^{\rm AE}(r)\ \forall\ r > r_c^l$ for each angular momentum, $V_l(r) = V_{\rm loc}(r)\ \forall\ r > r_c^l$. Therefore, by construction, $\delta V_l(r) = 0\ \forall\ r > r_c^l$, and hence, all the long-range Coulomb effects are included within $V_{\rm loc}(r)$. All these points are well illustrated in Fig. B.2(b), which displays the pseudopotentials $V_l(r)$ for $l = 0$ (s), 1 (p) and 2 (d) angular momenta represented by the dashed green, red and blue lines, respectively. In this case, the angular momentum $l = 0$ (s) is the local channel.

Fully relativistic pseudopotentials

As noted in Sec. 3.1.1, all relativistic effects originate deep in the ionic core, and therefore, can be directly included within pseudopotentials by generating them from atomic electronic structure calculations through the relativistic Dirac equation in the spherical atomic potential geometry. In this case, the spin $\mathbf{S}$ and the orbital $\mathbf{L}$ angular momenta of the electron are added and the total angular momentum reads $\mathbf{J} = \mathbf{L} + \mathbf{S}$, with allowed quantum numbers $j = l \pm \frac{1}{2}$ and $m_j = m \pm \frac{1}{2}$ for $l > 0$, and $j = \frac{1}{2}$ and $m_j = \frac{1}{2}$ for $l = 0$. The Dirac equation can be solved in the non-relativistic limit, $v/c \ll 1$, as an expansion in powers of $(v/c)^2$ and keeping the fully relativistic corrections (Appendix F). The corresponding eigenstates are defined by the set of two-component spinor wave functions as: $\varphi_{njlm_j}^{\rm AE}(\mathbf{r}) = R_{njl}^{\rm AE}(r)\mathcal{Y}_{jlm_j}(\theta,\phi)$, where $R_{njl}^{\rm AE}(r)$ represents the radial part of the wave function and $\mathcal{Y}_{jlm_j}(\theta,\phi)$ are the so-called spin-angular functions with the following two-component spinor form:

$$\mathcal{Y}_{jlm_j}^{j=l\pm\frac{1}{2},m_j=m\pm\frac{1}{2}}(\theta,\phi) = \frac{1}{\sqrt{2l+1}} \begin{pmatrix} \sqrt{l \pm m_j + \frac{1}{2}}\, Y_{lm_j-\frac{1}{2}}(\theta,\phi) \\ \pm\sqrt{l \mp m_j + \frac{1}{2}}\, Y_{lm_j+\frac{1}{2}}(\theta,\phi) \end{pmatrix}. \tag{B.4}$$

As in the non-relativistic case, one has to create the pseudo-wavefunctions defined as: $\varphi_{jlm_j}^{\rm PS}(\mathbf{r}) = R_{jl}^{\rm PS}(r)\mathcal{Y}_{jlm_j}(\theta,\phi)$. Once again, the question is reduced to construct the radial part of the pseudo-wavefunctions, $R_{jl}^{\rm PS}(r)$, but this time for each total angular momentum quantum number j for each orbital angular momentum quantum number l. Indeed, in the fully relativistic case, the functions $\varphi_{njlm_j}^{\rm AE}(\mathbf{r})$ are simultaneously eigenfunctions of the operators $\hat{\mathbf{L}}^2$, $\hat{\mathbf{S}}^2$, $\hat{\mathbf{J}}^2$ and $\hat{J}_z$, as well as of the operator

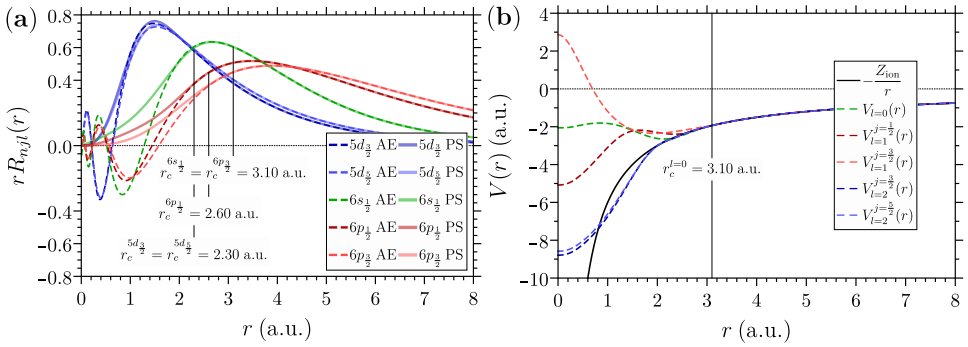

Figure B.3. (a) Comparison between the radial parts of the all-electron wave functions (dashed lines) and the pseudo-wavefunctions (solid lines) for the $5d_{3/2}$ (dark blue), $5d_{5/2}$ (light blue), $6s_{1/2}$ (green), $6p_{1/2}$ (dark red) and $6p_{3/2}$ (light red) fully relativistic states of the W atom. The cutoff radius for each channel are $r_c^{5d_j} = 2.30$ a.u., $r_c^{6p_{1/2}} = 2.60$ a.u. and $r_c^{6s_{1/2}} = r_c^{6p_{3/2}} = 3.10$ a.u., respectively. (b) The corresponding ionic pseudopotentials $V_{jl}(r)$ (dashed lines) for total and orbital angular momenta quantum numbers $j = \frac{1}{2}$ with $l = 0$ (green), $j = \frac{1}{2}$ (dark red) and $\frac{3}{2}$ (light red) with $l = 1$, and $j = \frac{3}{2}$ (dark blue) and $\frac{5}{2}$ (light blue) with $l = 2$. $V_{l=0}(r)$ is the local channel. The ionic core potential $-Z_{\rm ion}/r$ is displayed by the solid black line. It is clearly shown that $V_l(r) = V_{\rm loc}(r) = -Z_{\rm ion}/r \;\forall\; r > r_c^{l_j}$.

$\hat{\mathbf{L}} \cdot \hat{\mathbf{S}} = \frac{1}{2}(\hat{\mathbf{J}}^2 - \hat{\mathbf{L}}^2 - \hat{\mathbf{S}}^2)$, which is proportional to the spin-orbit interaction term. In fact, due to the spin-orbit coupling, eigenstates with $l \neq 0$ that are degenerated $2(2l+1)$ times in the non-relativistic case, are spin-split into two sets of eigenstates in the fully relativistic case: one with $j = l + \frac{1}{2}$ degenerated $2j + 1 = 2l + 2$ times and the other with $j = l - \frac{1}{2}$ degenerated $2j + 1 = 2l$ times. For eigenstates with $l = 0$ that are degenerated 2 times in the non-relativistic case, there is no spin-splitting and only one fully relativistic eigenstate is obtained with $j = \frac{1}{2}$. This can be seen for the W atom in Fig. B.3(a), where it is shown that the $5d$ states are spin-split into the $5d_{3/2}$ (dark blue line) and $5d_{5/2}$ (light blue lines) states, and the $6p$ states split into the $6p_{1/2}$ (dark red lines) and $6p_{3/2}$ (light red lines) states, compared to the non-relativistic case in Fig. B.2(a). The $6s$ (green lines) states are not spin-split, since they have $l = 0$. Note that all-electron and pseudo-wavefunctions are represented by the dashed and solid lines, respectively.

Once the relativistic pseudo-wavefunctions are satisfactorily constructed fulfilling the requirements of transferability and norm-conservation, we separately build the relativistic ionic pseudopotential $V_{jl}(r)$ for each total angular momentum quantum numbers $j = l \pm \frac{1}{2}$, by inverting the radial Dirac equation with the fixed all-electron eigenvalues $\epsilon_{njl}^{\rm AE}$. Within the Kleinman-Bylander separable form (Eq. B.3), it is straightforward to generalize the separated ionic pseudopotential operator $\hat{V} = \hat{V}_{\rm loc} + \hat{V}_{\rm NL}$ to the fully rela-

tivistic case, in such a way that the non-local part is defined as:

$$\hat{V}_{\mathrm{NL}} = \sum_{ljm_j} \frac{|\delta V_{jl}\varphi^{\mathrm{PS}}_{jlm_j}\rangle \langle \delta V_{jl}\varphi^{\mathrm{PS}}_{jlm_j}|}{\langle \varphi^{\mathrm{PS}}_{jlm_j}|\delta V_{jl}|\varphi^{\mathrm{PS}}_{jlm_j}\rangle}, \tag{B.5}$$

where $\delta V_{jl}(r) = V_{jl}(r) - V_{\mathrm{loc}}(r)$ for each total angular momentum quantum number j. Figure B.2(b) shows the ionic pseudopotentials $V_l^j(r)$ represented by the dashed lines for $j = \frac{1}{2}$ with $l = 0$ (green), $j = \frac{1}{2}$ (dark red) and $\frac{3}{2}$ (light red) with $l = 1$, and $j = \frac{3}{2}$ (dark blue) and $\frac{5}{2}$ (light blue) with $l = 2$ total and orbital angular momenta of the generated pseudopotential of the W atom, represented by the dashed blue, red and green lines, respectively. In this case, the angular momentum $l = 0$ is the local channel.

Appendix C

The Einstein model

In this appendix, we illustrate the renormalization effects due to the electron-phonon interaction on electrons by means of a simple coupled electron-phonon system based on the instructive Einstein model (EM). The Einstein model describes a single (non-interacting) electron band dispersing linearly with energy $\varepsilon_{\mathbf{k}} = v_{\mathrm{F}}|\mathbf{k}|$ interact with a single (non-interacting) dispersionless phonon branch with frequency ω_{o}, as seen in Fig. C.1. Electrons and phonons interact by means of a coupling strength λ_{o} at zero temperature, $T = 0$. The Einstein model is a highly idealized case but, as we will show in the following, it is very useful for understanding the physics behind the electron-phonon interaction, even in realistic materials.

From Eq. 2.18 and using the analytical expressions for both the electron band structure and the phonon dispersion relation, together with the integral definitions for infinite sums over momenta[1], we arrive to the analytical expression of the electron self-energy due to the electron-phonon interaction for the Einstein model, given by [2, 5, 37]:

$$\Sigma_{\mathrm{EM}}(\omega) = \lim_{\eta \to 0^+} \lambda_{\mathrm{o}}\omega_{\mathrm{o}} \left(-i\pi + \ln\left[\frac{\omega - \omega_{\mathrm{o}} + i\eta}{\omega + \omega_{\mathrm{o}} + i\eta}\right]\right). \tag{C.2}$$

Since the retarded electron self-energy satisfies causality (Sec. 2.2), its real and imaginary parts are related by Kramers-Kronig relations. The analytical expression of the real part of the electron self-energy is explicitly given by:

$$\mathrm{Re}\Sigma_{\mathrm{EM}}(\omega) = \lambda_{\mathrm{o}}\omega_{\mathrm{o}} \ln\left[\frac{\omega - \omega_{\mathrm{o}}}{\omega + \omega_{\mathrm{o}}}\right], \tag{C.3}$$

[1] In d spatial dimensions, we have that:

$$\lim_{N_{\mathbf{k}} \to \infty} \frac{1}{N_{\mathbf{k}}} \sum_{\mathbf{k}} = V^d \int \frac{\mathrm{d}\mathbf{k}}{(2\pi)^d}. \tag{C.1}$$

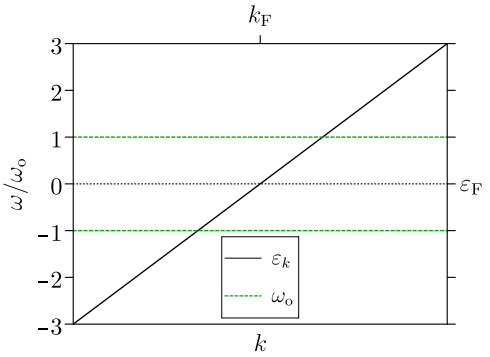

Figure C.1. The energy scales in the Einstein model. The black solid and green dashes lines represent the linear dispersing electron band with energy $\varepsilon_{\mathbf{k}} = v_{\mathrm{F}}|\mathbf{k}|$ and the dispersionless optical phonon branch with frequency ω_{o}. The horizontal black dotted line represents the Fermi level ε_{F}, set at $\omega = 0$.

and that of its imaginary part is explicitly expressed as:

$$\mathrm{Im}\Sigma_{\mathrm{EM}}(\omega) = -\pi\lambda_{\mathrm{o}}\omega_{\mathrm{o}}\Big(H(-\omega-\omega_{\mathrm{o}}) + H(\omega-\omega_{\mathrm{o}})\Big), \tag{C.4}$$

where $H(x)$ is the Heaviside step function. Note that the analytical expression of the electron self-energy is derived assuming that the non-interacting density of states is constant and equal to that of the Fermi level.

In Fig. C.2(a), we represent the real and the imaginary parts of the electron self-energy by the solid cyan and dashed orange lines, respectively, as a function of the excitation energy ω for a representative Einstein model with $\lambda_{\mathrm{o}} = 1/4$. The ω-dependent structure of the electron self-energy is better understood by looking at its imaginary part, which exhibits a step structure: $\mathrm{Im}\Sigma_{\mathrm{EM}}(\omega) = 0 \;\forall\; |\omega| < \omega_{\mathrm{o}}$ and $\pi\lambda_{\mathrm{o}}\omega_{\mathrm{o}} \;\forall\; |\omega| > \omega_{\mathrm{o}}$. This structure is simply explained when reasoning which phonon-mediated electronic scattering processes are allowed and forbidden depending on the energy of the excitation by many-body arguments and the Pauli exclusion principle [265], as schematically illustrated in Fig. C.2(b). On the one hand, for $|\omega| < \omega_{\mathrm{o}}$, excited electron states ($\omega > 0$) are forbidden to scatter, since they do not have enough excitation energy for decaying into any available unoccupied state by the emission of a phonon (panel (3)). Similarly, excited hole states ($\omega < 0$) are forbidden to scatter, since they do not have enough binding energy for being filled by any available occupied state by the emission of a phonon mode (panel (2)). Therefore, in this case, $\mathrm{Im}\Sigma_{\mathrm{EM}} = 0$. On the other hand, for $|\omega| > \omega_{\mathrm{o}}$, excited electron states are allowed to scatter, since they have enough excitation energy for decaying into any available unoccupied state by the emission of a phonon (panel (4)). Similarly, excited hole states are allowed to scatter, since they have enough binding energy for being filled by any available occupied state by the emission of a phonon (panel (1)). Since the value of the density of states is constant within the

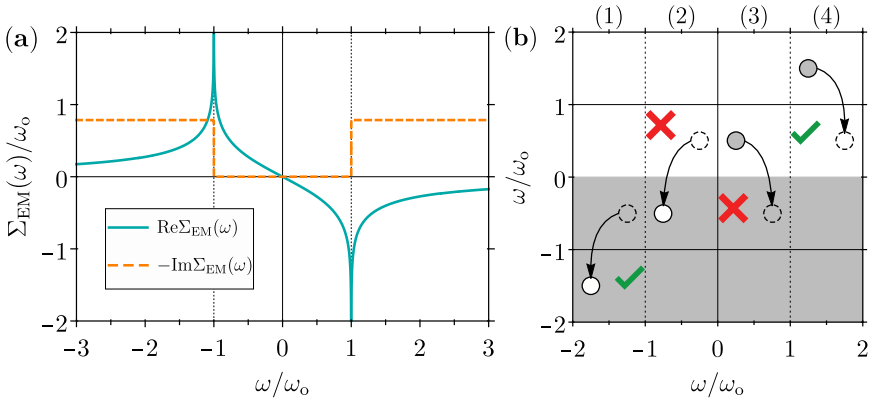

Figure C.2. (a) The real and the imaginary parts of the electron self-energy due to the electron-phonon coupling for an Einstein model with $\lambda_{\rm o} = 1/4$ are represented by the solid cyan and orange dashed lines. The excitation energy ω is measured from the Fermi level, set at $\omega = 0$. (b) Schematic explanation of the step structure of $\mathrm{Im}\Sigma_{\rm EM}(\omega)$. The shaded gray and white areas represent the occupied and unoccupied energy space, respectively. Excitations with $\omega < 0$ are injected hole states and excitations with $\omega > 0$ are injected electron states, represented by solid empty and solid gray-full circles, respectively. Occupied and unoccupied states are represented by dashed gray-full and dashed empty circles, respectively.

Einstein model, as well as the electron-phonon coupling strength, the imaginary part of the electron self-energy is finite. From Eq. 2.52, we obtain that $\mathrm{Im}\Sigma_{\rm EM}(\omega) = -\pi\lambda_{\rm o}\omega_{\rm o}$. This abrupt change in the imaginary part of the electron self-energy makes its real part exhibit maximum logarithmic peaks at precisely the phonon frequencies, $|\omega| = \omega_{\rm o}$, with a finite slope at $\omega \to 0$ with $-\partial\mathrm{Re}\Sigma_{\rm EM}(0)/\partial\omega = \lambda_{\rm o}$ (Eq. 2.34). For energies larger than the phonon frequency, $\mathrm{Re}\Sigma_{\rm EM}(\omega)$ vanishes. The sharp structure of the electron self-energy for the Einstein model appears because the model is designed for zero temperature. In more realistic systems, a finite temperature softens the step-like structure of the imaginary part of the electron self-energy and flattens the logarithmic-like peaks of its real part.

Let us now analyze the renormalization effects of the electron-phonon coupling on the non-interacting electron band structure within the Einstein model. In Fig. C.3(a), we represent with a color code the dressed electron spectral function $A_{\mathbf{k}}(\omega)$ (Eq. 2.35). The non-interacting energy dispersion is represented by the dotted black line. To complete this analysis, we also also describe the dressed electron band structure induced by the electron-phonon interaction in terms of electron quasi-particles. To this end, we solve the electron Dyson's equation by using the analytic continuation of the electron self-energy for the Einstein model from the upper to the lower complex half plane [35–37, 126], which is given by:

$$\Sigma_{\rm EM}(z) = \lambda_{\rm o}\omega_{\rm o}\Big(-i\pi + \ln\big[i(\omega_{\rm o} - z)\big] - \ln\big[-i(z - \omega_{\rm o})\big]\Big). \qquad \text{(C.5)}$$

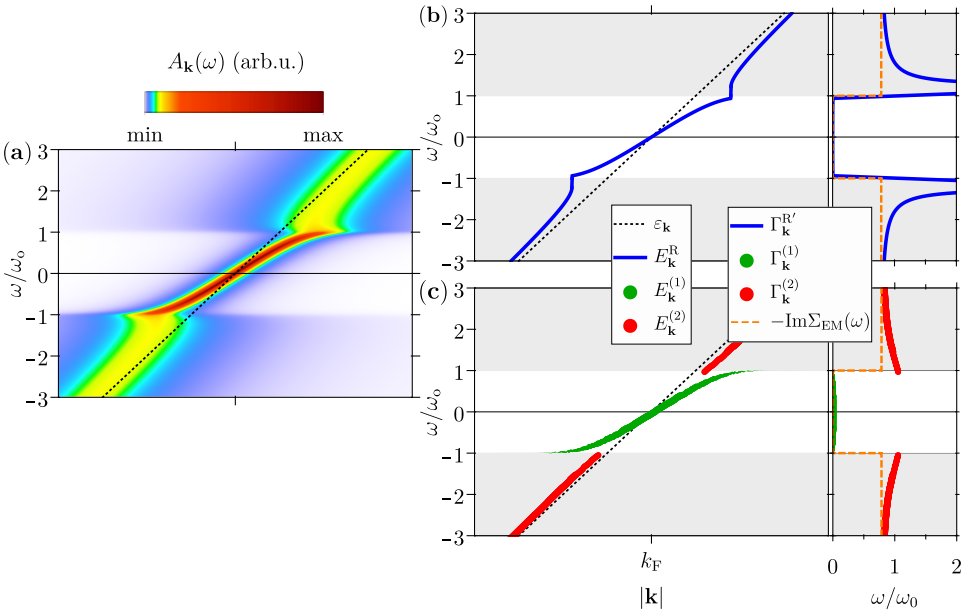

Figure C.3. (a) The dressed electron spectral function for the Einstein model with $\lambda_o = 1/4$. The color code scale represents the height of the spectral line. A non-zero value of $\omega_o/20$ is chosen in order to discern electron spectral peaks when $\mathrm{Im}\Sigma_{\mathrm{EM}}(\omega) = 0$. (b) The solid blue line represents the electron quasi-particle band structure (left) and the quasi-particle linewidth as a function of the energy (right) obtained by solving the approximate electron Dyson's equation within the Brillouin-Wigner perturbation theory approach (Eq. 2.29). (c) The filled green and red circle markers represent the multiple-electron quasi-particle band structure resulting from properly solving the complex electron Dyson's equation (Eq. 2.26). The size of the markers indicates the spectral weight of each quasi-particle. The white and gray areas represent the energy space in which $\mathrm{Im}\Sigma_{\mathrm{EM}}(\omega) = 0$ and $\mathrm{Im}\Sigma_{\mathrm{EM}}(\omega) = \pi\lambda_o\omega_o$, respectively. The dashed black line represent the bare linear dispersion $\varepsilon_{\mathbf{k}}$.

In Fig. C.3(b), we represent the electron quasi-particle structure resulting from solving the approximate electron Dyson's equation only along the real axis within the Brillouin-Wigner (BW) perturbation theory approach as in Eq. 2.29 (solid blue line), while in Fig. C.3(c) we show the multiple-electron quasi-particle structure resulting from solving the proper complex electron Dyson's equation as in Eq. 2.26 (green and red circle markers). The left panels of Figs. C.3(b) and (c) represent the corresponding electron quasi-particle band structure together with that of the non-interacting band (dotted black line), while the right panels represent the electron quasi-particle linewidth as a function of its energy together with the imaginary part of the electron self-energy (dashed orange line). Looking at the height of $A_{\mathbf{k}}(\omega)$ in Fig. C.3(a), it is evident that the electron-phonon interaction divides the spectrum of both electrons ($\omega > 0$) and holes ($\omega < 0$) in two regions, one for excitation energies close to the Fermi level in the range of the phonon

frequency, i.e. $|\omega| < \omega_{\mathrm{o}}$, and the other one for higher excitation energies beyond the phonon frequency, i.e. $|\omega| > \omega_{\mathrm{o}}$.

On the one hand, for $|\omega| < \omega_{\mathrm{o}}$, the spectral line appears as a sharp peak, since the scattering of charge carriers by the emission of a phonon is forbidden at these energies, i.e. $\mathrm{Im}\Sigma_{\mathrm{EM}}(\omega) = 0$. The imaginary part of the electron self-energy does not play any role at these energies, and therefore, the approximate electron quasi-particle band $E_{\mathbf{k}}^{\mathrm{BW}}$ and the proper quasi-particle band $E_{\mathbf{k}}^{(1)}$ in the left panels of Figs. C.3(b) and (c), respectively, are equal. In addition, these quasi-particle states are seen as infinitely long-lived with null linewidths, i.e. $\Gamma_{\mathbf{k}}^{(1)} = \Gamma_{\mathbf{k}}^{\mathrm{BW}} = 0$ in the right panels of Figs. C.3(b) and (c). Compared to the non-interacting linear electron band, the dispersions of $A_{\mathbf{k}}(\omega)$, $E_{\mathbf{k}}^{\mathrm{BW}}$ and $E_{\mathbf{k}}^{(1)}$ are highly renormalized close to the Fermi level. The flattening of the electron quasi-particle band with respect to the non-interacting case puts in evidence both the reduction of the band velocity (Eq. 2.32) and the enhancement of the effective band mass (Eq. 2.33) close to the Fermi level, due to the electron-phonon interaction. In fact, from a quantum many-body point of view electrons and holes are allowed to emit and reabsorb phonons by means of virtual processes, despite of the absence of available energy for real phonon-emission. This leads to the formation of a heavy cloud of phonons that dresses the charge carriers and makes their effective mass to increase, explaining the behavior described above. As we move away from the Fermi level towards the phonon frequency, i.e. $|\omega| \lesssim \omega_{\mathrm{o}}$, the largest spectral renormalizations are found, induced by the logarithmic peaked structure of the real part of the electron self-energy at $|\omega| = \omega_{\mathrm{o}}$ (Fig. C.2(a)). While the approximate electron quasi-particle states track the maxima of $A_{\mathbf{k}}(\omega)$ exhibiting a "kink" structure at $E_{\mathbf{k}}^{\mathrm{BW}} \approx \pm\omega_{\mathrm{o}}$, the electron quasi-particle band $E_{\mathbf{k}}^{(1)}$ approaches $\pm\omega_{\mathrm{o}}$ asymptotically as $\mathbf{k}$ moves away from k_{F}, losing increasingly its spectral weight (marker size in the right panel of Fig. C.3(c)). This can be interpreted as an increasingly localized state due to the dressing of the heavy cloud of phonons originating from the virtual processes, analogous to a polaron state in insulators.

On the other hand, for $|\omega| > \omega_{\mathrm{o}}$, the electron-phonon interaction promotes the splitting of the non-interacting band structure with the appearance of an additional electron quasi-particle band $E_{\mathbf{k}}^{(2)}$ for both injected electrons and holes, along with the dispersionless renormalized band $E_{\mathbf{k}}^{(1)}$. In this energy range, the scattering of charge carriers by the emission of a phonon is allowed, i.e. $\mathrm{Im}\Sigma_{\mathrm{EM}}(\omega) \neq 0$, and hence, the electron-phonon interaction leads to the broadening of the electron spectral line. Thus, the electron quasi-particle band $E_{\mathbf{k}}^{(2)}$ represents a dressed electron damped state which has acquired a finite linewidth, i.e. $\Gamma_{\mathbf{k}}^{(2)} \neq 0$, and hence, a finite lifetime. $\Gamma_{\mathbf{k}}^{(2)}$ follows the constant value of the imaginary part of the electron self-energy for $|\omega| \gg \omega_{\mathrm{o}}$. This behavior is also exhibited by

the approximate electron quasi-particle linewidth, $\Gamma_{\mathbf{k}}^{\mathrm{BW}}$. At these energies, the electronic scattering involving the real emission of phonons are much more probable than the virtual processes, leading to a reduction of the energy renormalizations with respect to the non-interacting band structure, i.e. $\mathrm{Re}\Sigma_{\mathrm{EM}}(\omega) \to 0$ (Fig. C.2(a)). Consequently, both $\Gamma_{\mathbf{k}}^{(2)}$ and $\Gamma_{\mathbf{k}}^{\mathrm{BW}}$ tend to $-\mathrm{Im}\Sigma_{\mathrm{EM}}(\varepsilon_{\mathbf{k}}) = \pi\lambda_{\mathrm{o}}\omega_{\mathrm{o}}$, which is the value that one obtains from the Fermi's golden rule or the Rayleigh-Schrödinger perturbation theory approach. When approaching the phonon frequency, i.e. $|\omega| \gtrsim \omega_{\mathrm{o}}$, $\Gamma_{\mathbf{k}}^{(2)}$ is slightly enhanced with respect to $\mathrm{Im}\Sigma_{\mathrm{EM}}(\omega)$. On the contrary, $\Gamma_{\mathbf{k}}^{\mathrm{BW}}$ exhibits an unphysical enhancement, originating from the divergence of $\mathbb{Z}_{\mathbf{k}}^{\mathrm{BW}}$ at these energies, since $\mathrm{Re}\Sigma'_{\mathrm{EM}}(\omega) \to \infty$ (Eq. 2.31).

The examination of the electron quasi-particle structure for the Einstein model reveals that the standard approximation of neglecting the imaginary part of the quasi-particle poles for solving the electron Dyson's equation (Eq. 2.29) is inappropriate even for this simple model. Indeed, at excitation energies close to the the phonon frequency from the Fermi level, the spectral function is well represented by a multiple-electron quasi-particle picture, resulting from solving the electron Dyson's equation within the whole complex plane. Note that the Einstein model allows to visualize that the electron-phonon interaction governs the actual low-energy carrier quasi-particle dynamics that in turn has a profound impact on the transport and thermodynamical properties of metals.

Appendix D

Fermi's golden rule for electron and phonon self-energies

Fermi's golden rule states that the scattering rate, i.e. the probability of scattering per unit time, for an initial state $|i\rangle$ with energy ε_i into all the possible final states $|f\rangle$ with energy ε_f by an excitation with energy ω_0 resulting from the perturbation $\Delta\hat{H}$ is given by:

$$\frac{1}{\tau_i} = 2\pi \sum_f |\langle f|\Delta\hat{H}|i\rangle|^2 \delta(\varepsilon_i - \varepsilon_f + \omega_0). \tag{D.1}$$

The decay rate of any particle is related to the imaginary part of its self-energy due to many-body interactions, and evaluated at the unperturbed energy within standard perturbation theory. Regarding the electron-phonon interaction, we have that $1/\tau_{\mathbf{k}n} = 2|\mathrm{Im}\Sigma_{\mathbf{k}n}(\varepsilon_{\mathbf{k}n})|$ for electrons and $1/\tau_{\mathbf{q}\nu} = 2|\mathrm{Im}\tilde{\Pi}_{\mathbf{q}\nu}(\omega_{\mathbf{q}\nu})|$ for phonons. From Eq. D.1 and using many-body arguments based on the Pauli exclusion principle [265], one finds that the decay rate of a Kohn-Sham single-electron state with momentum $\mathbf{k}$ and band index n is given by:

$$\begin{aligned}\frac{1}{\tau_{\mathbf{k}n}} = 2\big|\mathrm{Im}\Sigma_{\mathbf{k}n}(\varepsilon_{\mathbf{k}n})\big| = \frac{2\pi}{N_{\mathbf{q}}} \sum_{\mathbf{q}}^{1\mathrm{BZ}} \sum_{m\nu} \big|g^{\nu}_{mn}(\mathbf{k},\mathbf{q})\big|^2 \times \\ \Big(\big[1 - f(\varepsilon_{\mathbf{k}+\mathbf{q}m})\big]\big[1 + n_{\mathrm{B}}(\omega_{\mathbf{q}\nu})\big]\delta(\varepsilon_{\mathbf{k}n} - \varepsilon_{\mathbf{k}+\mathbf{q}m} - \omega_{\mathbf{q}\nu}) + \\ f(\varepsilon_{\mathbf{k}+\mathbf{q}m})\, n_{\mathrm{B}}(\omega_{\mathbf{q}\nu})\, \delta(\varepsilon_{\mathbf{k}n} - \varepsilon_{\mathbf{k}+\mathbf{q}m} - \omega_{\mathbf{q}\nu}) + \\ \big[1 - f(\varepsilon_{\mathbf{k}+\mathbf{q}m})\big] n_{\mathrm{B}}(\omega_{\mathbf{q}\nu})\, \delta(\varepsilon_{\mathbf{k}n} - \varepsilon_{\mathbf{k}+\mathbf{q}m} + \omega_{\mathbf{q}\nu}) + \\ f(\varepsilon_{\mathbf{k}+\mathbf{q}m})\big[1 + n_{\mathrm{B}}(\omega_{\mathbf{q}\nu})\big]\delta(\varepsilon_{\mathbf{k}n} - \varepsilon_{\mathbf{k}+\mathbf{q}m} + \omega_{\mathbf{q}\nu})\Big).\end{aligned} \tag{D.2}$$

The first term on the right-hand side of Eq. D.2 refers to the electronic scattering from the state $|\psi_{\mathbf{k}n}\rangle$ to the state $|\psi_{\mathbf{k}+\mathbf{q}m}\rangle$, which has the probability

$1-f(\varepsilon_{\mathbf{k}+\mathbf{q}m})$ of not being occupied, by the emission of a phonon mode $|\mathbf{q}\nu\rangle$, with $1+n_{\mathrm{B}}(\omega_{\mathbf{q}\nu})$ its corresponding temperature factor. The second term is of a many-body character. It appears because one must include by the Pauli exclusion principle the possibility for electronic scattering from the state $|\psi_{\mathbf{k}+\mathbf{q}m}\rangle$, which has the probability $f(\varepsilon_{\mathbf{k}+\mathbf{q}m})$ of being occupied, to the state $|\psi_{\mathbf{k}n}\rangle$ by the absorption of a phonon mode $|\mathbf{q}\nu\rangle$, with $n_{\mathrm{B}}(\omega_{\mathbf{q}\nu})$ its corresponding temperature factor. The third and fourth terms have an analogous interpretation as the first and second terms, respectively, but this time related to the respective absorption and emission of a phonon mode $|\mathbf{q},\nu\rangle$. In the same way, from Eq. D.1 and using many-body arguments based on the Pauli exclusion principle, one finds that the decay rate of an adiabatic phonon mode with momentum $\mathbf{q}$ and branch index ν is given by:

$$\begin{aligned}\frac{1}{\tau_{\mathbf{q}\nu}} = 2\big|\mathrm{Im}\tilde{\Pi}_{\mathbf{q}\nu}(\omega_{\mathbf{q}\nu})\big| = \frac{2\pi}{N_{\mathbf{k}}}\sum_{\mathbf{k}}^{1\mathrm{BZ}}\sum_{mn}\big|g^{\nu}_{mn}(\mathbf{k},\mathbf{q})\big|^2\times \\ \Big(f(\varepsilon_{\mathbf{k}n})\big[1-f(\varepsilon_{\mathbf{k}+\mathbf{q}m})\big]\delta(\varepsilon_{\mathbf{k}n}-\varepsilon_{\mathbf{k}+\mathbf{q}m}+\omega_{\mathbf{q}\nu})- \\ f(\varepsilon_{\mathbf{k}+\mathbf{q}m})\big[1-f(\varepsilon_{\mathbf{k}n})\big]\delta(\varepsilon_{\mathbf{k}n}-\varepsilon_{\mathbf{k}+\mathbf{q}m}+\omega_{\mathbf{q}\nu})\Big).\end{aligned} \tag{D.3}$$

The first term on the right-hand side of Eq. D.3 refers to the decay of a phonon mode $|\mathbf{q},\nu\rangle$ into an electron-hole pair excitation, composed of the occupied state $\psi_{\mathbf{k}n}$ and the unoccupied state $\psi_{\mathbf{k}+\mathbf{q}m}$, with probabilities $f(\varepsilon_{\mathbf{k}n})$ and $1-f(\varepsilon_{\mathbf{k}+\mathbf{q}m})$, respectively. The second term is of a many-body character. Because of the Pauli exclusion principle, one must exclude the possibility of creating a phonon mode $|\mathbf{q},\nu\rangle$ induced by the relaxation of an electron-hole pair, composed of the unoccupied state $\psi_{\mathbf{k}n}$ and the occupied state $\psi_{\mathbf{k}+\mathbf{q}m}$, with probabilities $1-f(\varepsilon_{\mathbf{k}n})$ and $f(\varepsilon_{\mathbf{k}+\mathbf{q}m})$, respectively. If now one simplifies Eqs. D.2 and D.3 and makes the dynamical replacement $\varepsilon_{\mathbf{k}n}\to\omega$ and $\omega_{\mathbf{q}\nu}\to\omega$, respectively, the absolute value of the imaginary part of Eqs. 2.52 and 2.61 are easily obtained. Finally, one recovers the latter complete expressions of the retarded electron and phonon self-energies by applying a Kramers-Kronig relation to electrons:

$$\Sigma_{\mathbf{k}n}(\omega) = \lim_{\eta\to 0^+}\frac{1}{\pi}\int_{-\infty}^{\infty}\frac{\big|\mathrm{Im}\Sigma_{\mathbf{k}n}(\omega')\big|}{\omega-\omega'+i\eta}\mathrm{d}\omega', \tag{D.4}$$

and to phonons:

$$\Pi_{\mathbf{q}\nu}(\omega) = \lim_{\eta\to 0^+}\frac{1}{\pi}\int_{-\infty}^{\infty}\frac{\big|\mathrm{Im}\Pi_{\mathbf{q}\nu}(\omega')\big|}{\omega-\omega'+i\eta}\mathrm{d}\omega'. \tag{D.5}$$

Appendix E

The Rashba model

In this appendix, we review the basic aspects of the Rashba model [148], which is broadly considered as the standard model for analyzing the properties of surface electron states under a strong spin-orbit interaction. The inversion asymmetry at surfaces directly enters in the spin-orbit coupling term in Eq. 3.9 through the gradient of the potential. Within the Rashba model, the surface potential gradient is assumed as a constant electric field completely oriented along the surface-perpendicular direction, $\hat{\mathbf{z}}$, leading to the simplified spin-orbit interaction term:

$$H_{\mathrm{R}} = \alpha_{\mathrm{R}}(\boldsymbol{\sigma} \times \mathbf{p}) \cdot \hat{\mathbf{z}} = \alpha_{\mathrm{R}}(\sigma_x p_y - \sigma_y p_x), \tag{E.1}$$

where $\alpha_{\mathrm{R}} = \epsilon/(4c^2)$ is the so-called Rashba parameter that controls the strength of the spin-orbit coupling, with ϵ the electric field determined by the out-of-plane potential gradient, and (x, y) is the surface plane. The Rashba model considers that the simplified spin-orbit coupling in Eq. E.1 acts on a 2D free electron gas constrained to the surface plane, which has analytic solutions. For an in-plane momentum $\mathbf{k}_\parallel = (k_x, k_y, 0) = k_\parallel(\cos\varphi_{\mathbf{k}_\parallel}, \sin\varphi_{\mathbf{k}_\parallel}, 0)$, the electron spinor wave functions and energies are:

$$\psi_{\mathbf{k}_\parallel,\pm}(\mathbf{r}_\parallel) = \frac{e^{i\mathbf{k}_\parallel\cdot\mathbf{r}_\parallel}}{\sqrt{2}} \begin{pmatrix} ie^{-i\varphi_{\mathbf{k}_\parallel}/2} \\ \pm e^{i\varphi_{\mathbf{k}_\parallel}/2} \end{pmatrix} \quad \text{and} \quad \varepsilon_{\mathbf{k}_\parallel,\pm} = \frac{k_\parallel^2}{2m^*} \pm \alpha_{\mathrm{R}} k_\parallel, \tag{E.2}$$

respectively, with m^* the electron effective band mass. The corresponding spin-polarization vectors, which are defined as the expectation value of the Pauli spin-operator, are given by

$$\mathbf{m}_{\mathbf{k}_\parallel,\pm} = \langle\psi_{\mathbf{k}_\parallel,\pm}|\boldsymbol{\sigma}|\psi_{\mathbf{k}_\parallel,\pm}\rangle = \pm \begin{pmatrix} \sin\varphi_{\mathbf{k}_\parallel} \\ -\cos\varphi_{\mathbf{k}_\parallel} \\ 0 \end{pmatrix} \perp \mathbf{k}_\parallel. \tag{E.3}$$

From Eqs. E.2 and E.3, it is clear that the effect of the simplified spin-orbit coupling in Eq. E.1 within the Rashba model is to split the original spin-degenerate 2D parabolic band into two isotropic spin-split parabola with

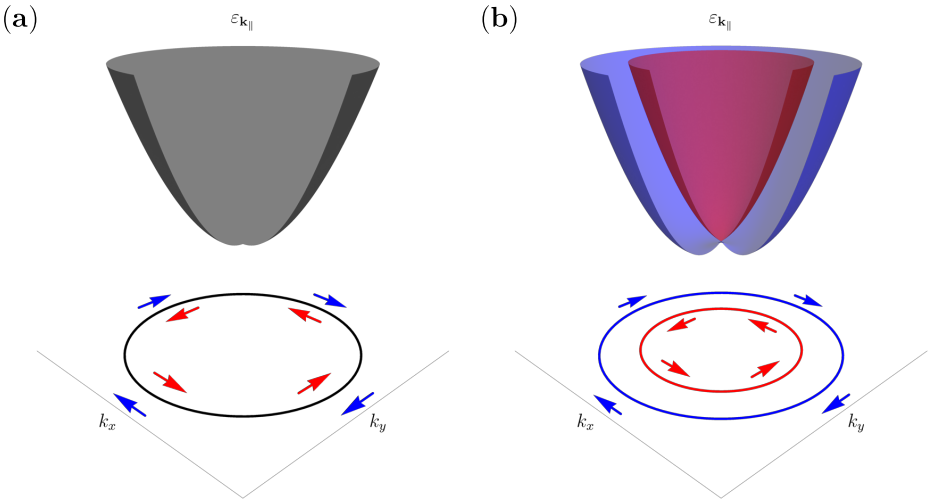

Figure E.1. Schematic representation of the spin-orbit interaction induced energy splitting within the Rashba model. (a) The original spin-degenerated 2D free electron parabolic band is split into (b) two isotropic parabola with opposite spin-polarizations, lying within the surface plane and perpendicular to the electron momentum $\mathbf{k}_\parallel$.

opposite chiral in-plane spin-polarizations, perpendicular to the corresponding electron momentum $\mathbf{k}_\parallel$. The general features of the Rashba model are displayed schematically in Fig. E.1.

Let imagine now an external perturbation of momentum $\mathbf{q}_\parallel$ that involves an effective change $\Delta V_{\mathbf{q}_\parallel}$ in the potential. Without the spin-orbit interaction, the matrix element describing this perturbation between two electron states at momenta $\mathbf{k}_\parallel + \mathbf{q}_\parallel$ and $\mathbf{k}_\parallel$ is equal to $g(\mathbf{k}_\parallel, \mathbf{q}_\parallel) = \langle \psi_{\mathbf{k}_\parallel+\mathbf{q}_\parallel} | \Delta V_{\mathbf{q}_\parallel} | \psi_{\mathbf{k}_\parallel} \rangle$, where $\psi_{\mathbf{k}_\parallel}(\mathbf{r}_\parallel) = e^{i\mathbf{k}_\parallel \cdot \mathbf{r}_\parallel}$. When the spin-orbit interaction is taken into account, the matrix element will be governed by the overlap between the spin states. Thereby, the matrix element between two electron spinor states within the same spin-split band reads as:

$$\begin{aligned} g_{\pm\pm}(\mathbf{k}_\parallel, \mathbf{q}_\parallel) &= \langle \psi^{\pm}_{\mathbf{k}_\parallel+\mathbf{q}_\parallel} | \Delta V_{\mathbf{q}_\parallel} | \psi^{\pm}_{\mathbf{k}_\parallel} \rangle \\ &= \frac{g(\mathbf{k}_\parallel, \mathbf{q}_\parallel)}{2} \begin{pmatrix} -ie^{i\varphi_{\mathbf{k}_\parallel}/2} & \pm e^{-i\varphi_{\mathbf{k}_\parallel}/2} \end{pmatrix} \begin{pmatrix} ie^{-i\varphi_{\mathbf{k}_\parallel+\mathbf{q}_\parallel}/2} \\ \pm e^{i\varphi_{\mathbf{k}_\parallel+\mathbf{q}_\parallel}/2} \end{pmatrix} \\ &= g(\mathbf{k}_\parallel, \mathbf{q}_\parallel) \cos\left(\frac{\theta}{2}\right), \end{aligned} \tag{E.4}$$

where $\theta = \varphi_{\mathbf{k}_\parallel+\mathbf{q}_\parallel} - \varphi_{\mathbf{k}_\parallel}$. The corresponding scattering probability is given by the squared module of the matrix elements, and hence, reads as:

$$|g_{\pm\pm}(\mathbf{k}_\parallel, \mathbf{q}_\parallel)|^2 = |g(\mathbf{k}_\parallel, \mathbf{q}_\parallel)|^2 \cos^2\left(\frac{\theta}{2}\right) = |g(\mathbf{k}_\parallel, \mathbf{q}_\parallel)|^2 \frac{1+\cos\theta}{2}. \tag{E.5}$$

Similarly, the matrix element between two electron spinor states in different spin-split bands reads as:

$$\begin{aligned} g_{\pm\mp}(\mathbf{k}_\parallel, \mathbf{q}_\parallel) &= \langle \psi^{\pm}_{\mathbf{k}_\parallel+\mathbf{q}_\parallel} | \Delta V_{\mathbf{q}_\parallel} | \psi^{\mp}_{\mathbf{k}_\parallel} \rangle \\ &= \frac{g(\mathbf{k}_\parallel, \mathbf{q}_\parallel)}{2} \Big(-ie^{i\varphi_{\mathbf{k}_\parallel}/2} \pm e^{-i\varphi_{\mathbf{k}_\parallel}/2} \Big) \begin{pmatrix} ie^{-i\varphi_{\mathbf{k}_\parallel+\mathbf{q}_\parallel}/2} \\ \mp e^{i\varphi_{\mathbf{k}_\parallel+\mathbf{q}_\parallel}/2} \end{pmatrix} \\ &= g(\mathbf{k}_\parallel, \mathbf{q}_\parallel) i \sin\left(\frac{\theta}{2}\right), \end{aligned} \tag{E.6}$$

and in the same way we find that $g_{\mp\pm}(\mathbf{k}_\parallel, \mathbf{q}_\parallel) = g_{\pm\mp}(\mathbf{k}_\parallel, \mathbf{q}_\parallel)$. The corresponding scattering probability is given by the squared module of the matrix elements, and hence, reads as:

$$\begin{aligned} |g_{\pm\mp}(\mathbf{k}_\parallel, \mathbf{q}_\parallel)|^2 = |g_{\mp\pm}(\mathbf{k}_\parallel, \mathbf{q}_\parallel)|^2 &= |g(\mathbf{k}_\parallel, \mathbf{q}_\parallel)|^2 \sin^2\left(\frac{\theta}{2}\right) \\ &= |g(\mathbf{k}_\parallel, \mathbf{q}_\parallel)|^2 \frac{1-\cos\theta}{2}. \end{aligned} \tag{E.7}$$

Therefore, it is easy to see that the spin-split intra-band and inter-band electronic scattering are modulated by the geometrical factors $(1+\cos\theta)/2$ and $(1-\cos\theta)/2$, respectively.

Appendix F

From the Dirac equation to the Schrödinger-Pauli equation

In this appendix, we illustrate how to incorporate the electron spin degree of freedom and the relativistic interactions in non-relativistic quantum mechanics on which the DFT formalism is based.

In the framework of relativistic quantum mechanics, the proper way to describe any system of spin-$\frac{1}{2}$ massive particles as electrons is the Dirac equation [179, 180], which generalizes the Schrödinger equation in a relativistically covariant form. For an electron moving in the external electric scalar potential ϕ and magnetic vector potential $\mathbf{A}$, which are recast into the electromagnetic four-potential defined as: $A_\mu = \big(\phi/c, -\mathbf{A}\big)$, the Dirac equation can be write in the form of two coupled equations for the large (L) and small (S) two-component spinors, ψ_L and ψ_S, respectively [172]:

$$\begin{aligned} \sum_{\sigma'} c\big[\boldsymbol{\sigma}_{\sigma\sigma'} \cdot (\mathbf{p} - \mathbf{A})\big]\psi_S^{\sigma'} &= (\varepsilon' - c^2 - \phi)\psi_L^{\sigma} \\ \sum_{\sigma'} c\big[\boldsymbol{\sigma}_{\sigma\sigma'} \cdot (\mathbf{p} - \mathbf{A})\big]\psi_L^{\sigma'} &= (\varepsilon' + c^2 - \phi)\psi_S^{\sigma} \end{aligned}, \tag{F.1}$$

where ε' is the relativistic energy of the particle and $\boldsymbol{\sigma} = \{\sigma_x, \sigma_y, \sigma_z\}$ are the 2×2 Pauli matrices, which are related to the spin angular momentum operator as $\hat{\mathbf{S}} = \frac{1}{2}\hat{\boldsymbol{\sigma}}$ and are defined as:

$$\sigma_x = \begin{pmatrix} 0 & 1 \\ 1 & 0 \end{pmatrix}, \quad \sigma_y = \begin{pmatrix} 0 & -i \\ i & 0 \end{pmatrix}, \quad \sigma_z = \begin{pmatrix} 1 & 0 \\ 0 & -1 \end{pmatrix}. \tag{F.2}$$

In addition, in Eq. F.1 the large and small two-component spinors form the four-component Dirac spinor. Nevertheless, the Dirac spinor is rather "uncomfortable" to deal with. In this sense, using the second equation in

Eq. F.1 in order to get rid of the small spinor in the first equation, one obtains that:

$$\big[\boldsymbol{\sigma}\cdot(\mathbf{p}-\mathbf{A})\big]\left[\frac{c^2}{\varepsilon'+c^2-\phi}\right]\big[\boldsymbol{\sigma}\cdot(\mathbf{p}-\mathbf{A})\big]\psi_L=(\varepsilon'-c^2-\phi)\psi_L, \tag{F.3}$$

At this point, one can approximate the relativistic Dirac equation in Eq. F.3 adopting the quasi-relativistic limit, i.e. $v/c \ll 1$, with v the electron velocity [172]. Within this limit, one can assume that the non-relativistic energy of the electron ε is related to the relativistic one as: $\varepsilon = \varepsilon' - c^2$. Thus, we can make the following expansion up to order $(v/c)^2$:

$$\frac{c^2}{\varepsilon+2c^2-\phi}=\frac{1}{2}\left(1-\frac{\varepsilon-\phi}{2c^2}+\mathcal{O}\big((v/c)^4\big)\right). \tag{F.4}$$

Plugging this relation into Eq. F.3, one arrives to a Schrödinger-Pauli-like equation of the form:

$$\hat{H}_L\psi_L=\varepsilon\psi_L, \tag{F.5}$$

where $\hat{H}_L$ is a 2×2 matrix Hamiltonian:

$$\hat{H}_L=\frac{1}{2}\big[\hat{\boldsymbol{\sigma}}\cdot(\hat{\mathbf{p}}-\hat{\mathbf{A}})\big]\left[1-\frac{\varepsilon-\hat{\phi}}{2c^2}\right]\big[\hat{\boldsymbol{\sigma}}\cdot(\hat{\mathbf{p}}-\hat{\mathbf{A}})\big]+\hat{\phi} \tag{F.6}$$

Note that in the non-relativistic limit of the Dirac equation, i.e. $v/c \to 0$, Eq. F.5 becomes the Schrödinger-Pauli equation [178]:

$$\left[\frac{1}{2}(\hat{\mathbf{p}}-\hat{\mathbf{A}})^2-\frac{1}{2}\hat{\boldsymbol{\sigma}}\cdot\hat{\mathbf{B}}+\hat{\phi}\right]\psi_L=\varepsilon\psi_L, \tag{F.7}$$

which corresponds to the formulation of the Schrödinger equation for spin-$\frac{1}{2}$ particles taking into account the Stern-Gerlach or Zeeman interaction that describes the coupling between the magnetic moment of the electron spin and the external magnetic field $\mathbf{B}=\boldsymbol{\nabla}\times\mathbf{A}$ (second term on the left-hand side of Eq. F.6).

Nevertheless, this last equation completely neglects relativistic interactions. In order to maintain them within the quasi-relativistic limit, one must keep the second term on the right-hand side of Eq. F.4. In the following, for simplicity we treat the non-magnetic case, i.e. $\mathbf{A}=0$, and hence $\mathbf{B}=0$, in Eq. F.6. Yet, there are some drawbacks with the interpretation of Eq. F.5. First, the large two-component spinor ψ_L does not satisfy the normalization requirement because the probabilistic interpretation of the Dirac equation requires that:

$$\int\Big(\big(\psi_L(\mathbf{r})\big)^\dagger\psi_L(\mathbf{r})+\big(\psi_S(\mathbf{r})\big)^\dagger\psi_S(\mathbf{r})\Big)\mathrm{d}\mathbf{r}=1. \tag{F.8}$$

From the second equation in Eq. F.1, one can adopt the following approximation for the small two-component spinor:

$$\psi_S \approx \frac{\boldsymbol{\sigma}\cdot\mathbf{p}}{2c}\psi_L. \tag{F.9}$$

This suggests that in the quasi-relativistic approach we should work with a new two-component wave function defined as: $\psi = \Omega\psi_L$ with $\Omega = 1 + \frac{\mathbf{p}^2}{8c^2}$, where the normalization requirement is fulfilled up to order $(v/c)^2$ as:

$$\int \big(\psi(\mathbf{r})\big)^\dagger\psi(\mathbf{r})\mathrm{d}\mathbf{r} \approx \int \big(\psi_L(\mathbf{r})\big)^\dagger\left(1+\frac{\mathbf{p}^2}{4c^2}\right)\psi_L(\mathbf{r})\mathrm{d}\mathbf{r} \approx 1, \tag{F.10}$$

Using this new definition, one must modify Eq. F.5 and multiply it from the left by $\Omega^{-1} = 1 - \frac{\mathbf{p}^2}{8c^2}$. Thereby, one obtains:

$$\Omega^{-1}\hat{H}_L\Omega^{-1}\psi = \varepsilon\Omega^{-2}\psi. \tag{F.11}$$

Explicitly, keeping terms up to order $(v/c)^2$, we have:

$$\left[\frac{\hat{\mathbf{p}}^2}{2} + \hat{\phi} + \frac{1}{8c^2}\left[\{\hat{\mathbf{p}}^2, \varepsilon-\hat{\phi}\} - 2(\hat{\boldsymbol{\sigma}}\cdot\hat{\mathbf{p}})(\varepsilon-\hat{\phi})(\hat{\boldsymbol{\sigma}}\cdot\hat{\mathbf{p}})\right] - \frac{\hat{\mathbf{p}}^4}{8c^2}\right]\psi = \varepsilon\psi. \tag{F.12}$$

The third term of the Hamiltonian on the left-hand side of Eq. F.12 depends on the energy ε, which is the solution of the eigenvalue problem. For overcoming this incongruity, we use the useful property for any pair of operators $\{\hat{A}^2, \hat{B}\} - 2\hat{A}\hat{B}\hat{A} = \big[\hat{A}, [\hat{A}, \hat{B}]\big]$. We make $\hat{\boldsymbol{\sigma}}\cdot\hat{\mathbf{p}} = \hat{A}$, and $\varepsilon - \hat{\phi} = \hat{B}$. The following equality is derived[1]:

$$\big[\hat{\boldsymbol{\sigma}}\cdot\hat{\mathbf{p}}, [\hat{\boldsymbol{\sigma}}\cdot\hat{\mathbf{p}}, \varepsilon-\hat{\phi}]\big] = \hat{\boldsymbol{\nabla}}\cdot\hat{\boldsymbol{\nabla}}\hat{\phi} + 2\boldsymbol{\sigma}\cdot(\hat{\boldsymbol{\nabla}}\hat{\phi}\times\hat{\mathbf{p}}). \tag{F.13}$$

Then, plugging Eq. F.13 into Eq. F.12, one recovers an equation free of the aforementioned difficulties that can be regarded as the Schrödinger-Pauli equation for spin-$\frac{1}{2}$ electrons which additionally includes relativistic interactions up to order[2] $(v/c)^2$:

$$\sum_{\sigma'}\left[\left(\frac{\mathbf{p}^2}{2} + \phi - \frac{\mathbf{p}^4}{8c^2} + \frac{\boldsymbol{\nabla}\cdot\boldsymbol{\nabla}\phi}{8c^2}\right)\delta_{\sigma\sigma'} + \frac{\boldsymbol{\sigma}_{\sigma\sigma'}\cdot\big(\boldsymbol{\nabla}\phi\times\mathbf{p}\big)}{4c^2}\right]\psi_{\sigma'} = \varepsilon\psi_\sigma. \tag{F.14}$$

In Eq. F.14, the first two terms do not need any explanation, as they are already presented in non-relativistic quantum mechanics. The third and fourth terms are the so-called scalar-relativistic (SR) corrections and are, respectively, known as the mass-velocity and the Darwin terms. The fifth term is associated with the fully relativistic (FR) correction of the spin-orbit (SO) interaction, i.e. the coupling between the spin and the orbital angular momenta of the electron.

[1] The following equalities are used: $(\boldsymbol{\sigma}\cdot\mathbf{A})(\boldsymbol{\sigma}\cdot\mathbf{B}) = \mathbf{A}\cdot\mathbf{B} + i\boldsymbol{\sigma}(\mathbf{A}\times\mathbf{B})$ and $\boldsymbol{\nabla}\times\boldsymbol{\nabla}\phi = 0$

[2] Note that Eq. F.14 has been derived in the absence of any external magnetic potential, i.e. $\mathbf{A} = 0$ and hence, the external magnetic field is $\mathbf{B} = \boldsymbol{\nabla}\times\mathbf{A} = 0$. If one wanted to include such a magnetic field or potential, one would have to substitute $\mathbf{p} \to \mathbf{p} - \mathbf{A}$ and take into account the Stern-Gerlach or Zeeman interaction term $\frac{1}{2}\hat{\boldsymbol{\sigma}}\cdot\hat{\mathbf{B}}$.

Publications

The work presented here has been published in the following references:

1. *Coupled spin and electron-phonon interaction at the Tl/Si(111) surface from relativistic first principles calculations*,
   Peio Garcia-Goiricelaya, Idoia G. Gurtubay and Asier Eiguren,
   Physical Review B 97, 125435(R) (2018)

2. *Long-living carriers in a strong electron-phonon interacting two-dimensional doped semiconductor*,
   Peio Garcia-Goiricelaya, Jon Lafuente-Bartolome Idoia G. Gurtubay and Asier Eiguren,
   Communications Physics 2, 81 (2019)

3. *Emergence of large non-adiabatic effects induced by the electron-phonon interaction on the complex vibrational quasi-particle spectrum of the doped monolayer MoS_2*,
   Peio Garcia-Goiricelaya, Jon Lafuente-Bartolome Idoia G. Gurtubay and Asier Eiguren,
   Physical Review B 101, 054304 (2020)

Resumen

Esta tesis se centra en el acoplamiento entre electrones y fonones. Los fonones se definen como las excitaciones elementales de baja energía correspondientes a los cuantos asociados a las vibraciones colectivas de la red atómica en sólidos cristalinos. De hecho, el estudio de la interacción electrón-fonón es contemporáneo al concepto mismo de los fonones, que data de hace casi un siglo a la vez que el nacimiento de la teoría cuántica de los sólidos. Por lo tanto, el acoplamiento entre electrones y fonones representa uno de los capítulos más estudiados de la Física del Estado Sólido y está considerablemente documentado en una gran cantidad de libros y revistas [1–4].

A pesar de ser un tema muy estudiado, la interacción electrón-fonón continúa atrayendo un gran interés, ya que está presente en una gran variedad de fenómenos físicos. De esta manera, tiene gran influencia en la dependencia con la temperatura de la capacidad calorífica electrónica y de la movilidad, la conductividad y la resistencia eléctrica en los metales y en los semiconductores, así como en la termalización de portadores de carga "calientes" y en el efecto termoeléctrico. También influye en las propiedades ópticas de los semiconductores y aislantes, ya que participa activamente en la dependencia con la temperatura de la banda prohibida (en inglés *gap*) y en la absorción óptica asistida por fonones en los materiales con un *gap* indirecto. Además, la interacción electrón-fonón da lugar a desdoblamientos característicos de las bandas de los electrones, llamadas estructuras de pliegues (en inglés *kinks*), en los espectros de fotoemisión y a fuertes disminuciones en las frecuencias de los fonones, llamadas anomalías de Kohn, en los espectros de dispersión inelástica de luz o de neutrones. Del mismo modo, desempea un papel fundamental en la superconductividad convencional o mediada por fonones, ya que proporciona el mecanismo para atraer electrones y emparejarlos en superconductores convencionales.

La velocidad efectiva, equivalente a la masa efectiva, la energía real y el tiempo de vida de los estados de electrón, así como la frecuencia y el tiempo de vida de los modos de fonón, están determinados por las interacciones de muchos cuerpos [5]. Estos incluyen la interacción tanto de los electrones como de los fonones con otras excitaciones de partículas individuales – electrones o huecos excitados – así como con excitaciones de pares electrón-hueco y con otras excitaciones colectivas – fonones, plasmones, magnones o

excitones – y defectos de los sólidos. Para ilustrar la importancia de la interacción electrón-fonón, es importante destacar que a temperaturas realistas del orden de unos pocos cientos de Kelvin, el espacio de fases para la dispersión electrónica se reduce a una ventana estrecha de energía del orden de 10 meV cerca del nivel de Fermi en metales. Este rango de energías coincide con las frecuencias típicas de los fonones, mientras que las energías típicas de transición electrónica son del orden de 10 meV [6]. De esta manera, la dinámica de baja energía de los portadores de carga, es decir, electrones y huecos excitados, está generalmente dominada por la dispersión electrónica mediada por fonones, la cual, por lo tanto, gobierna las propiedades termodinámicas y de transporte de los sólidos [7].

Los primeros estudios sobre la interacción electrón-fonón se realizaron entre las décadas de 1930 y 1950 [8–13]. Estos fueron motivados por la necesidad de establecer una teoría cuántica para el transporte en sólidos, basada en Hamiltonianos semiempíricos de Frhlich [14] y de Holstein [15] junto con el uso del modelo de gas de Fermi para los electrones [16] y los modelos de Einstein [17] y de Debye [18] para los fonones. Estos trabajos iniciales fueron esenciales para comprender la estructura matemática de los elementos de matriz de la interacción electrón-fonón y el papel desempeado por el apantallamiento eléctrico en el cambio del potencial inducido por los desplazamientos de la red. Sin embargo, fue a finales de la década de 1950 y a principios de la década de 1960 que comenzó a formularse la teoría de la interacción electrón-fonón tal y como se conoce actualmente. Para ello, se utilizó un enfoque basado en la teoría cuántica de campos, como resultado del advenimiento de la teoría del líquido de Landau-Fermi [19] – junto con el concepto de cuasi-partícula – y el desarrollo de la teoría de perturbaciones basado en las funciones de Green de muchos cuerpos [5] – junto con el concepto de autoenergía, que relaciona los propagadores sin perturbar y perturbados a través de la ecuación de Dyson. La formulación general, y todavía hoy la más completa, de la teoría de la interacción electrón-fonón se estableció durante los aos 1960 y 1970 [20, 21].

Esta tesis se basa en cálculos *ab initio* de la interacción electrón-fonón, cuyos primeros cálculos no se realizaron hasta finales de la década de 1990 [22–26]. La razón de esta demora es que la formulación y la implementación práctica de la teoría del funcional de la densidad (de sus siglas en inglés DFT) [27–29] tardó desde mediados de la década de 1960 hasta la década de 1980, mientras que el desarrollo de la teoría de la perturbación del funcional de la densidad (de sus siglas en inglés DFPT) [30–33] no llegó hasta los últimos aos de la década de 1980 y principios de la década de 1990. De hecho, hoy por hoy, los cálculos de primeros principios de la interacción electrón-fonón se basan en expresiones aproximadas pero útiles de la interacción [2] que tienen como punto de partida las propiedades electrónicas y vibracionales resultantes de las teorías de DFT y de DFPT, respectivamente [4]. Estos formalismos teóricos se basan en la aproximación

adiabática [34], la cual supone que los electrones responden instantáneamente al movimiento de la red. Este enfoque conduce a una imagen física simplificada de los electrones moviéndose en una red rígida, y de los fonones incluyendo sólo el apantallamiento electrostático en las vibraciones de la red. Sin embargo, se espera que la interacción electrón-fonón afecte tanto a los estados de electrón como a los modos de fonón definidos dentro de la aproximación adiabática, dando lugar a una renormalización de sus propiedades y una disminución de sus tiempos de vida.

Uno de los objetivos principales de esta tesis es analizar el impacto de la interacción electrón-fonón más allá de la aproximación adiabática, es decir, los efectos no adiabáticos. De hecho, las correcciones no adiabáticas debidas a la interacción electrón-fonón se han detectado generalmente comparando estructuras de banda de electrones sin perturbar y relaciones de dispersión de fonones adiabáticos con funciones espectrales de electrones y fonones, respectivamente, calculadas teóricamente o medidas experimentalmente. Las funciones espectrales son magnitudes de gran interés físico, ya que su estructura dependiente del momento y de la energía describe la densidad de probabilidad de los estados de electrón o de los modos de fonón, conteniendo información valiosa sobre las propiedades de las cuasi-partículas, así como de las interacciones de muchos cuerpos [2, 5]. Es importante sealar que, si bien los efectos no adiabáticos de la interacción electrón-fonón se han estudiado ampliamente en electrones sin perturbar, estos efectos se han limitado principalmente al centro de la zona de Brillouin en el caso de los fonones adiabáticos [4]. Por otro lado, las estructuras de banda de electrones renormalizados y las relaciones de dispersión de fonones renormalizados se han calculado generalmente utilizando las teorías de perturbaciones de Brillouin-Wigner y de Rayleigh-Schrdinger [5]. Aunque estos cálculos han sido muy útiles para estimar cuantitativamente varios fenómenos físicos, también conducen a resultados divergentes y sin significado físico. En este sentido, investigaciones recientes han racionalizado con éxito las esctructuras de *kinks* en los experimentos de fotoemisión en términos de múltiples bandas de electrones renormalizados con diferente significado físico y que surgen de una sola banda sin perturbar debido a la interacción electrón-fonón [35, 36]. Estos trabajos combinan cálculos de primeros principios con las propiedades analíticas de las funciones de Green [37] para resolver de manera autoconsistente la ecuación de Dyson en todo el plano complejo de energía, dando lugar a una evaluación sistemática de las cuasi-partículas a partir de técnicas *ab initio*. Vale la pena destacar que no se tiene constancia de ningún estudio en estos términos sobre la renormalización de los fonones adiabáticos debido a la interacción electrón-fonón.

En el lado experimental, la espectroscopía de fotoemisión con resolución angular [38] y la dispersión inelástica de neutrones y de rayos X, así como la dispersión de Raman, [39, 40] son las técnicas más comunes para sondear las funciones espectrales de electrones y de fonones, respectivamente.

La mayoría de estas técnicas analizan la componente del momento paralela a la superficie y, por lo tanto, son sólo adecuadas para estudiar materiales bidimensionales (2D) o cuasi-2D, donde la interacción electrón-fonón es generalmente más fuerte [41–46]. Así pues, las superficies de baja dimensión y las monocapas representan un entorno privilegiado para estudiar, tanto experimental como teóricamente, los efectos no adiabáticos de la interacción electrón-fonón en electrones y en fonones y, de este modo, comprobar la idoneidad de las teorías de muchos cuerpos. En este sentido, los sistemas 2D compuestos de elementos pesados han resultado tener un valor aadido muy interesante. En estos materiales, la falta de la simetría de inversión inherente a la superficie y el fuerte acoplamiento espín-órbita inherente al elemento pesado dan lugar a la generación de estados de superficie de electrón desdoblados y polarizados en el espín, incluso en materiales no magnéticos [47–61]. Por lo tanto, comprender la dinámica acoplada de la carga y del espín a bajas energías en sistemas 2D con un fuerte acoplamiento espín-órbita es de capital importancia debido a sus atractivas aplicaciones en el campo de la espintrónica [62–67] y se ha convertido en una línea de investigación muy activa en la actualidad [68–70]. Sin embargo, la coexistencia de las interacciones espín-órbita y electrón-fonón sólo se ha investigado considerando modelos teóricos instructivos basados en los Hamiltonianos de Frhlich y de Holstein [71–74]. No ha sido hasta hace muy poco, y simultáneamente con esta tesis, que el papel del acoplamiento espín-órbita en la interacción electrón-fonón se ha tratado más allá de simples correcciones relativistas [75–78].

El objetivo principal de esta tesis es dar un paso más en el campo de la investigación de la interacción electrón-fonón. Por un lado, se estudia el papel que desempean el espín del electrón y el acoplamiento espín-órbita en la interacción electrón-fonón en superficies con fuertes interacciones relativistas a partir de cálculos de primeros principios. Por otro lado, se analiza la renormalización no adiabática debido a la interacción electrón-fonón no sólo en electrones sin perturbar sino también en fonones adiabáticos, yendo más allá de las aproximaciones teóricas estándar, en materiales que representan un desafío para las teorías de muchos cuerpos.

Esta tesis se organiza de la siguiente manera. El Capítulo 1 está dedicado a describir los formalismos teóricos de DFT y de DFPT utilizados para calcular a partir de primeros principios las propiedades electrónicas del estado fundamental y las propiedades vibracionales de la red en los sólidos. Estas propiedades son esenciales en el Capítulo 2 para formular el Hamiltoniano de la interacción electrón-fonón, así como para derivar expresiones prácticas para una gran variedad de magnitudes relacionadas con la interacción, donde se utilizan varias aproximaciones en combinación con la teoría de perturbaciones de muchos cuerpos basada en las funciones de Green. En este capítulo, se presta especial atención al marco teórico adecuado para calcular las propiedades de cuasi-partícula del electrón y del fonón. Se presentan también las técnicas vanguardistas basadas en funciones de Wannier máxi-

mamente localizadas [135–137] para interpolar los estados y las energías de electrón, así como los elementos de matriz de la interacción electrón-fonón [4, 138–140]. El uso de esta metodología permite realizar cálculos de primeros principios que requieren de una gran cantidad de puntos para converger y que no son generalmente accesibles, siendo incluso prohibitivos en muchos casos, mediante cálculos estándar de DFT y de DFPT.

En el Capítulo 3, se considera una monocapa de talio (Tl) sobre una superficie de silicio en la dirección (111), es decir la superficie de Tl/Si(111). El grado de libertad del espín del electrón junto con las interacciones relativistas, incluyendo el acoplamiento espín-órbita, se incorporan dentro de la teoría de DFT recurriendo al límite cuasi-relativista de la ecuación de Dirac. Esto lleva a la generalización del formalismo teórico al caso de espín no colineal, en el que las funciones de onda del electrón se describen mediante un vector de dos componentes y el potencial que sufren los electrones se describe mediante una matriz 2×2, el cual ya incorpora las interacciones relativistas. La superficie de Tl/Si(111), que es un semiconductor con un *gap* de energía estrecho, exhibe dos regímenes completamente diferentes con respecto de la polarización de espín para los estados de superficie desdoblados. Esto se debe al fuerte acoplo espín-órbita asociado al elemento pesado Tl en combinación con la estructura cristalina específica de este material, en buena concordancia con los experimentos de fotoemisión [161–166]. Mientras que los estados de superficie ocupados de baja energía aparecen moderadamente desdoblados y exhiben una polarización de espín similar a la de Rashba [148], los estados de superficie no ocupados de baja energía están fuertemente desdoblados – con la energía de desdoblamiento del espín más grande recogida en la literatura – y exhiben una polarización de espín colineal y perpendicular a la superficie. De esta manera, se encuentra que el espín del electrón y la interacción espín-órbita entran de una manera decisiva modulando e incluso suprimiendo la interacción electrón-fonón debajo y encima del nivel de Fermi en la superficie de Tl/Si(111). Este último aspecto resulta muy atractivo para posibles aplicaciones en el campo de la espintrónica, ya que garantiza estados de superficie bien separados de las contribuciones del volumen y con largos tiempos de vida, así como con polarizaciones de espín bien definidas, todo ello asegurando un escenario ideal para un transporte robusto y acoplado de carga y de espín.

En el Capítulo 4, se considera la monocapa del dicalcogenuro de metal de transición MoS_2. A bajas energías, este material presenta una estructura de bandas de conducción de electrón compuesta de varios valles desiguales, que están desdoblados y polarizados de manera colineal en el espín. Una vez dopada, esta estructura resulta muy atractiva para aplicaciones en el campo de la valletrónica, es decir, la electrónica que asocia las bandas de electrones con forma de valles con el grado de libertad del espín del electrón. El aumento del dopaje electrónico en la monocapa permite el ajuste del nivel de Fermi, conduciendo a cambios significativos en la forma de la superficie de

Fermi y, a su vez, promoviendo la aparición de anomalías de Kohn. Para los dopajes más altos, estas anomalías se convierten incluso en inestabilidades de la red, siendo evidente el aumento de la interacción electrón-fonón. Este fortalecimiento del acoplamiento va de la mano con la superconductividad medida experimentalmente en el material dopado [233–236]. Se estudia la importancia de los efectos no adiabáticos relacionados con la interacción electrón-fonón y regulados por la polarización del espín electrónico tanto para electrones como para fonones en función del dopaje electrónico. Con respecto de los fonones, para los modos con longitudes de onda cortas se observan grandes ensanchamientos de la función espectral, vinculados al aumento de la interacción electrón-fonón. Para los modos con longitudes de onda largas se observa que los modos ópticos se renormalizan dramáticamente como resultado de excitaciones virtuales de pares electrón-hueco. De hecho, la interacción electrón-fonón da lugar a la aparición de dos modos no adiabáticos de cuasi-partícula de fonón bien definidos en el plano complejo de frecuencia a partir de un solo modo adiabático, y cuya naturaleza física es capaz de entenderse de manera general por medio de un sencillo modelo de Einstein. En cuanto a los electrones, se encuentra un espectro realmente sobresaliente como resultado del aumento de la interacción electrón-fonón con el dopaje y en excepcional acuerdo con experimentos de espectroscopía de fotoemisión recientemente medidos [232]. Este experimento representa probablemente el primero en el que se ha observado inequívocamente un doble *kink* en las bandas del espectro del electrón. Estas singularidades espectrales se racionalizan en términos de transiciones electrónicas mediadas por fonones y conservando el espín dentro de la estructura de varios valles. La conclusión es que este espectro único es el resultado de la fuerte interacción entre valles desiguales e igualmente polarizados, mediada por más de un modo de fonón de frecuencia distinta. Asimismo, se explica el complicado espectro experimental de electrones en términos de una estructura de múltiples bandas de cuasi-partícula, que surge a partir de una sola banda de electrones sin perturbar. Finalmente, se incide en la presencia de una banda de cuasi-partícula altamente renormalizada y casi plana, con una polarización de espín bien definida y un largo tiempo de vida, que podría favorecer la formación de estados de tipo polarón polarizados en el espín.

Bibliography

[1] J. Ziman, *Electrons and Phonons: The Theory of Transport Phenomena in Solids.* Oxford University Press, Oxford, 1960.

[2] G. Grimvall, *The Electron-Phonon Interaction in Metals, Selected Topics in Solid State Physics.* North-Holland, New York, 1981.

[3] E. G. Maksimov, D. Y. Savrasov, and S. Y. Savrasov, *"The electron-phonon interaction and the physical properties of metals",* Physics-Uspekhi **40**, 337–358 (1997).

[4] F. Giustino, *"Electron-phonon interactions from first principles",* Rev. Mod. Phys. **89**, 015003 (2017).

[5] G. Mahan, *Many-Particle Physics.* Physics of Solids and Liquids. Springer US, 2000.

[6] N. Ashcroft and N. Mermin, *Solid State Physics.* Saunders College, Philadelphia, 1976.

[7] R. E. Prange and L. P. Kadanoff, *"Transport Theory for Electron-Phonon Interactions in Metals",* Phys. Rev. **134**, A566–A580 (1964).

[8] L. Nordheim, *"Zur Elektronentheorie der Metalle. I",* Annalen der Physik **401**, 607-640 (1931).

[9] N. F. Mott and H. Jones, *The Theory of the Properties of Metals and Alloys.* Oxford University Press, 1936.

[10] J. Bardeen, *"Conductivity of Monovalent Metals",* Phys. Rev. **52**, 688–697 (1937).

[11] H. Frhlich and N. F. Mott, *"Theory of electrical breakdown in ionic crystals",* Proceedings of the Royal Society of London. Series A - Mathematical and Physical Sciences **160**, 230-241 (1937).

[12] H. Frhlich and N. F. Mott, *"The mean free path of electrons in polar crystals",* Proceedings of the Royal Society of London. Series A. Mathematical and Physical Sciences **171**, 496-504 (1939).

[13] J. Bardeen and D. Pines, *"Electron-Phonon Interaction in Metals",* Phys. Rev. **99**, 1140–1150 (1955).

[14] H. Frhlich, *"Electrons in lattice fields",* Advances in Physics **3**, 325-361 (1954).

[15] T. Holstein, *"Studies of polaron motion: Part I. The molecular-crystal model",* Annals of Physics **8**, 325 - 342 (1959).

[16] E. Fermi, *"Zur Quantelung des idealen einatomigen Gases",* Zeitschrift für Physik **36**, 902–912 (1926).

[17] A. Einstein, *"Die Plancksche Theorie der Strahlung und die Theorie der spezifischen Wrme",* Annalen der Physik **327**, 180-190 (1907).

[18] P. Debye, *"Zur Theorie der spezifischen Wrmen",* Annalen der Physik **344**, 789-839 (1912).

[19] L. D. Landau, *"The Theory of a Fermi Liquid",* Sov. Phys. - JETP Lett. **30**, 1058–1064 (1956).

[20] G. Baym, *"Field-theoretic approach to the properties of the solid state",* Annals of Physics **14**, 1 - 42 (1961).

[21] L. Hedin and S. Lundqvist, *"Effects of Electron-Electron and Electron-Phonon Interactions on the One-Electron States of Solids",* volume 23 of *Solid State Physics*, pp. 1 – 181. Academic Press, 1970.

[22] S. Y. Savrasov, D. Y. Savrasov, and O. K. Andersen, *"Linear-response calculations of electron-phonon interactions",* Phys. Rev. Lett. **72**, 372–375 (1994).

[23] F. Mauri, O. Zakharov, S. de Gironcoli, S. G. Louie, and M. L. Cohen, *"Phonon Softening and Superconductivity in Tellurium under Pressure",* Phys. Rev. Lett. **77**, 1151–1154 (1996).

[24] A. Y. Liu and A. A. Quong, *"Linear-response calculation of electron-phonon coupling parameters",* Phys. Rev. B **53**, R7575–R7579 (1996).

[25] S. Y. Savrasov and D. Y. Savrasov, *"Electron-phonon interactions and related physical properties of metals from linear-response theory",* Phys. Rev. B **54**, 16487–16501 (1996).

[26] R. Bauer, A. Schmid, P. Pavone, and D. Strauch, *"Electron-phonon coupling in the metallic elements Al, Au, Na, and Nb: A first-principles study",* Phys. Rev. B **57**, 11276–11282 (1998).

[27] P. Hohenberg and W. Kohn, *"Inhomogeneous Electron Gas",* Phys. Rev. **136**, B864–B871 (1964).

[28] W. Kohn and L. J. Sham, *"Self-Consistent Equations Including Exchange and Correlation Effects",* Phys. Rev. **140**, A1133–A1138 (1965).

[29] W. Kohn, *"Nobel Lecture: Electronic structure of matter—wave functions and density functionals",* Rev. Mod. Phys. **71**, 1253–1266 (1999).

[30] S. Baroni, P. Giannozzi, and A. Testa, *"Green's-function approach to linear response in solids",* Phys. Rev. Lett. **58**, 1861–1864 (1987).

[31] X. Gonze, *"Adiabatic density-functional perturbation theory",* Phys. Rev. A **52**, 1096–1114 (1995).

[32] X. Gonze, *"Erratum: Adiabatic density-functional perturbation theory",* Phys. Rev. A **54**, 4591–4591 (1996).

[33] S. Baroni, S. de Gironcoli, A. Dal Corso, and P. Giannozzi, *"Phonons and related crystal properties from density-functional perturbation theory",* Rev. Mod. Phys. **73**, 515–562 (2001).

[34] M. Born and R. Oppenheimer, *"Zur Quantentheorie der Molekeln",* Annalen der Physik **389**, 457-484 (1927).

[35] A. Eiguren and C. Ambrosch-Draxl, *"Complex Quasiparticle Band Structure Induced by Electron-Phonon Interaction: Band Splitting in the* 1×1H/W(110) *Surface",* Phys. Rev. Lett. **101**, 036402 (2008).

[36] A. Eiguren, C. Ambrosch-Draxl, and P. M. Echenique, *"Self-consistently renormalized quasiparticles under the electron-phonon interaction",* Phys. Rev. B **79**, 245103 (2009).

[37] S. Engelsberg and J. R. Schrieffer, *"Coupled Electron-Phonon System",* Phys. Rev. **131**, 993–1008 (1963).

[38] A. Damascelli, Z. Hussain, and Z.-X. Shen, *"Angle-resolved photoemission studies of the cuprate superconductors",* Rev. Mod. Phys. **75**, 473–541 (2003).

[39] T. P. Devereaux and R. Hackl, *"Inelastic light scattering from correlated electrons",* Rev. Mod. Phys. **79**, 175–233 (2007).

[40] *"Bosonic Spectral Function and the Electron-Phonon Interaction in HTSC Cuprates",* J Advances in Condensed Matter Physics **2010**, 423725 (2010).

[41] A. Eiguren, B. Hellsing, F. Reinert, G. Nicolay, E. V. Chulkov, V. M. Silkin, S. Hüfner, and P. M. Echenique, *"Role of Bulk and Surface Phonons in the Decay of Metal Surface States",* Phys. Rev. Lett. **88**, 066805 (2002).

[42] B. Hellsing, A. Eiguren, and E. V. Chulkov, *"Electron-phonon coupling at metal surfaces",* Journal of Physics: Condensed Matter **14**, 5959–5977 (2002).

[43] A. Eiguren, B. Hellsing, E. V. Chulkov, and P. M. Echenique, *"Phonon-mediated decay of metal surface states",* Phys. Rev. B **67**, 235423 (2003).

[44] E. Plummer, J. Shi, S.-J. Tang, E. Rotenberg, and S. Kevan, *"Enhanced electronphonon coupling at metal surfaces",* Progress in Surface Science **74**, 251 - 268 (2003). Maria Steslicka Memorial Volume.

[45] J. Krger, *"Electron–phonon coupling at metal surfaces",* Reports on Progress in Physics **69**, 899–969 (2006).

[46] P. Hofmann, I. Y. Sklyadneva, E. D. L. Rienks, and E. V. Chulkov, *"Electron-phonon coupling at surfaces and interfaces",* New Journal of Physics **11**, 125005 (2009).

[47] E. Rotenberg, J. W. Chung, and S. D. Kevan, *"Spin-Orbit Coupling Induced Surface Band Splitting in Li/W(110) and Li/Mo(110)",* Phys. Rev. Lett. **82**, 4066–4069 (1999).

[48] M. Hochstrasser, J. G. Tobin, E. Rotenberg, and S. D. Kevan, *"Spin-Resolved Photoemission of Surface States of* W(110)$-(1 \times 1)$H*",* Phys. Rev. Lett. **89**, 216802 (2002).

[49] G. Bihlmayer, S. Blügel, and E. V. Chulkov, *"Enhanced Rashba spin-orbit splitting in* BiAg(111) *and* PbAg(111) *surface alloys from first principles",* Phys. Rev. B **75**, 195414 (2007).

[50] S. Mathias, A. Ruffing, F. Deicke, M. Wiesenmayer, I. Sakar, G. Bihlmayer, E. V. Chulkov, Y. M. Koroteev, P. M. Echenique, M. Bauer, and M. Aeschlimann, *"Quantum-Well-Induced Giant Spin-Orbit Splitting",* Phys. Rev. Lett. **104**, 066802 (2010).

[51] A. Eiguren and C. Ambrosch-Draxl, *"Spin polarization and relativistic electronic structure of the* 1×1 *H/W(110) surface",* New Journal of Physics **11**, 013056 (2009).

[52] I. Barke, F. Zheng, T. K. Rügheimer, and F. J. Himpsel, *"Experimental Evidence for Spin-Split Bands in a One-Dimensional Chain Structure",* Phys. Rev. Lett. **97**, 226405 (2006).

[53] I. Gierz, T. Suzuki, E. Frantzeskakis, S. Pons, S. Ostanin, A. Ernst, J. Henk, M. Grioni, K. Kern, and C. R. Ast, *"Silicon Surface with Giant Spin Splitting",* Phys. Rev. Lett. **103**, 046803 (2009).

[54] S. Hatta, T. Aruga, Y. Ohtsubo, and H. Okuyama, *"Large Rashba spin splitting of surface resonance bands on semiconductor surface",* Phys. Rev. B **80**, 113309 (2009).

[55] K. Yaji, Y. Ohtsubo, S. Hatta, H. Okuyama, K. Miyamoto, T. Okuda, A. Kimura, H. Namatame, M. Taniguchi, and T. Aruga, *"Large Rashba spin splitting of a metallic surface-state band on a semiconductor surface",* Nature Communications **1**, 17 (2010).

[56] T. Okuda, K. Miyamoto, Y. Takeichi, H. Miyahara, M. Ogawa, A. Harasawa, A. Kimura, I. Matsuda, A. Kakizaki, T. Shishidou, and T. Oguchi, *"Large out-of-plane spin polarization in a spin-splitting one-dimensional metallic surface state on Si(557)-Au",* Phys. Rev. B **82**, 161410 (2010).

[57] Y. Ohtsubo, S. Hatta, H. Okuyama, and T. Aruga, *"A metallic surface state with uniaxial spin polarization on Tl/Ge(111)-(*1×1*)",* Journal of Physics: Condensed Matter **24**, 092001 (2012).

[58] P. Höpfner, J. Schäfer, A. Fleszar, J. H. Dil, B. Slomski, F. Meier, C. Loho, C. Blumenstein, L. Patthey, W. Hanke, and R. Claessen, *"Three-Dimensional Spin Rotations at the Fermi Surface of a Strongly Spin-Orbit Coupled Surface System",* Phys. Rev. Lett. **108**, 186801 (2012).

[59] J. Ibañez Azpiroz, A. Eiguren, E. Y. Sherman, and A. Bergara, *"Spin-Flip Transitions Induced by Time-Dependent Electric Fields in Surfaces with Strong Spin-Orbit Interaction",* Phys. Rev. Lett. **109**, 156401 (2012).

[60] D. V. Gruznev, L. V. Bondarenko, A. V. Matetskiy, A. Y. Tupchaya, A. A. Alekseev, C. R. Hsing, C. M. Wei, S. V. Eremeev, A. V. Zotov, and A. A. Saranin, *"Electronic band structure of a Tl/Sn atomic sandwich on Si(111)",* Phys. Rev. B **91**, 035421 (2015).

[61] A. V. Matetskiy, S. Ichinokura, L. V. Bondarenko, A. Y. Tupchaya, D. V. Gruznev, A. V. Zotov, A. A. Saranin, R. Hobara, A. Takayama, and S. Hasegawa, *"Two-Dimensional Superconductor with a Giant Rashba Effect: One-Atom-Layer Tl-Pb Compound on Si(111)",* Phys. Rev. Lett. **115**, 147003 (2015).

[62] S. Datta and B. Das, *"Electronic analog of the electro–optic modulator",* Applied Physics Letters **56**, 665-667 (1990).

[63] J. Nitta, T. Akazaki, H. Takayanagi, and T. Enoki, *"Gate Control of Spin-Orbit Interaction in an Inverted $In_{0.53}Ga_{0.47}As/In_{0.52}Al_{0.48}As$ Heterostructure",* Phys. Rev. Lett. **78**, 1335–1338 (1997).

[64] S. A. Wolf, D. D. Awschalom, R. A. Buhrman, J. M. Daughton, S. von Molnár, M. L. Roukes, A. Y. Chtchelkanova, and D. M. Treger, *"Spintronics: A Spin-Based Electronics Vision for the Future",* Science **294**, 1488–1495 (2001).

[65] I. Žutić, J. Fabian, and S. Das Sarma, *"Spintronics: Fundamentals and applications",* Rev. Mod. Phys. **76**, 323–410 (2004).

[66] J. Sinova, D. Culcer, Q. Niu, N. A. Sinitsyn, T. Jungwirth, and A. H. MacDonald, *"Universal Intrinsic Spin Hall Effect",* Phys. Rev. Lett. **92**, 126603 (2004).

[67] A. Soumyanarayanan, N. Reyren, A. Fert, and C. Panagopoulos, *"Emergent phenomena induced by spin-orbit coupling at surfaces and interfaces",* Nature **539**, 509 (2016). Review Article.

[68] G. Bihlmayer, O. Rader, and R. Winkler, *"Focus on the Rashba effect",* New Journal of Physics **17**, 050202 (2015).

[69] A. Manchon, H. C. Koo, J. Nitta, S. M. Frolov, and R. A. Duine, *"New perspectives for Rashba spin-orbit coupling",* Nature Materials **14**, 871 EP - (2015). Review Article.

[70] E. I. Rashba, *"Spin-orbit coupling goes global",* Journal of Physics: Condensed Matter **28**, 421004 (2016).

[71] Z. Liu, M. O. Nestoklon, J. L. Cheng, E. L. Ivchenko, and M. W. Wu, *"Spin-dependent intravalley and intervalley electron-phonon scatterings in germanium",* Physics of the Solid State **55**, 1619–1634 (2013).

[72] E. Cappelluti, C. Grimaldi, and F. Marsiglio, *"Electron-phonon effects on spin-orbit split bands of two-dimensional systems",* Phys. Rev. B **76**, 085334 (2007).

[73] E. Cappelluti, C. Grimaldi, and F. Marsiglio, *"Topological Change of the Fermi Surface in Low-Density Rashba Gases: Application to Superconductivity",* Phys. Rev. Lett. **98**, 167002 (2007).

[74] L. Covaci and M. Berciu, *"Polaron Formation in the Presence of Rashba Spin-Orbit Coupling: Implications for Spintronics",* Phys. Rev. Lett. **102**, 186403 (2009).

[75] M. J. Verstraete, *"Ab initio calculation of spin-dependent electron–phonon coupling in iron and cobalt",* Journal of Physics: Condensed Matter **25**, 136001 (2013).

[76] N. F. Hinsche, A. S. Ngankeu, K. Guilloy, S. K. Mahatha, A. Grubišić Čabo, M. Bianchi, M. Dendzik, C. E. Sanders, J. A. Miwa, H. Bana, E. Travaglia, P. Lacovig, L. Bignardi, R. Larciprete, A. Baraldi, S. Lizzit, K. S. Thygesen, and P. Hofmann, *"Spin-dependent electron-phonon coupling in the valence band of single-layer WS_2",* Phys. Rev. B **96**, 121402 (2017).

[77] S. K. Mahatha, A. S. Ngankeu, N. F. Hinsche, I. Mertig, K. Guilloy, P. L. Matzen, M. Bianchi, C. E. Sanders, J. A. Miwa, H. Bana, E. Travaglia, P. Lacovig, L. Bignardi, D. Lizzit, R. Larciprete, A. Baraldi, S. Lizzit, and P. Hofmann, *"Electronphonon coupling in single-layer MoS_2",* Surface Science **681**, 64 - 69 (2019).

[78] R. Heid, I. Y. Sklyadneva, and E. V. Chulkov, *"Electron-phonon coupling in topological surface states: The role of polar optical modes",* Scientific Reports **7**, 1095 (2017).

[79] E. Schrödinger, *"Quantisierung als Eigenwertproblem",* Annalen der Physik **384**, 361-376 (1926).

[80] E. Brovman and Y. Kagan, *"The Phonon Spectrum of Metals",* Soviet Journal of Experimental and Theoretical Physics **25**, 365 (1967).

[81] R. M. Martin, *Electronic Structure: Basic Theory and Practical Methods.* Cambridge University Press, 2004.

[82] E. Fermi, *"Un Metodo Statistico per la Determinazione di alcune Priopriet dell'Atomo",* Rend. Accad. Naz. Lincei. **6**, 602–607 (1927).

[83] D. R. Hartree, *"The Wave Mechanics of an Atom with a Non-Coulomb Central Field. Part I. Theory and Methods",* Mathematical Proceedings of the Cambridge Philosophical Society **24**, 89110 (1928).

[84] V. Fock, *"Näherungsmethode zur Lösung des quantenmechanischen Mehrkörperproblems",* Zeitschrift für Physik **61**, 126–148 (1930).

[85] J. C. Slater, *"The Theory of Complex Spectra",* Phys. Rev. **34**, 1293–1322 (1929).

[86] E. Wigner, *"On the Interaction of Electrons in Metals",* Phys. Rev. **46**, 1002–1011 (1934).

[87] D. M. Ceperley and B. J. Alder, *"Ground State of the Electron Gas by a Stochastic Method",* Phys. Rev. Lett. **45**, 566–569 (1980).

[88] J. P. Perdew and A. Zunger, *"Self-interaction correction to density-functional approximations for many-electron systems",* Phys. Rev. B **23**, 5048–5079 (1981).

[89] J. P. Perdew and Y. Wang, *"Accurate and simple analytic representation of the electron-gas correlation energy",* Phys. Rev. B **45**, 13244–13249 (1992).

[90] J. P. Perdew, K. Burke, and M. Ernzerhof, *"Generalized Gradient Approximation Made Simple",* Phys. Rev. Lett. **77**, 3865–3868 (1996).

[91] M. C. Payne, M. P. Teter, D. C. Allan, T. A. Arias, and J. D. Joannopoulos, *"Iterative minimization techniques for ab initio total-energy calculations: molecular dynamics and conjugate gradients",* Rev. Mod. Phys. **64**, 1045–1097 (1992).

[92] F. Bloch, *"Über die Quantenmechanik der Elektronen in Kristallgittern",* Zeitschrift für Physik **52**, 555–600 (1929).

[93] P. Giannozzi, S. Baroni, N. Bonini, M. Calandra, R. Car, C. Cavazzoni, D. Ceresoli, G. L. Chiarotti, M. Cococcioni, I. Dabo, A. Dal Corso, S. de Gironcoli, S. Fabris, G. Fratesi, R. Gebauer, U. Gerstmann, C. Gougoussis, A. Kokalj, M. Lazzeri, L. Martin-Samos, N. Marzari, F. Mauri, R. Mazzarello, S. Paolini, A. Pasquarello, L. Paulatto, C. Sbraccia, S. Scandolo, G. Sclauzero, A. P. Seitsonen, A. Smogunov, P. Umari, and R. M. Wentzcovitch, *"QUANTUM ESPRESSO: a modular and open-source software project for quantum simulations of materials",* Journal of Physics: Condensed Matter **21**, 395502 (19pp) (2009).

[94] P. Giannozzi, O. Andreussi, T. Brumme, O. Bunau, M. B. Nardelli, M. Calandra, R. Car, C. Cavazzoni, D. Ceresoli, M. Cococcioni, N. Colonna, I. Carnimeo, A. D. Corso, S. de Gironcoli, P. Delugas, R. A. D. Jr, A. Ferretti, A. Floris, G. Fratesi, G. Fugallo, R. Gebauer, U. Gerstmann, F. Giustino, T. Gorni, J. Jia, M. Kawamura, H.-Y. Ko, A. Kokalj, E. Kkbenli, M. Lazzeri, M. Marsili, N. Marzari, F. Mauri, N. L. Nguyen, H.-V. Nguyen, A. O. de-la Roza, L. Paulatto, S. Ponc, D. Rocca, R. Sabatini, B. Santra, M. Schlipf, A. P. Seitsonen, A. Smogunov, I. Timrov, T. Thonhauser, P. Umari, N. Vast, X. Wu, and S. Baroni, *"Advanced capabilities for materials modelling with QUANTUM ESPRESSO",* Journal of Physics: Condensed Matter **29**, 465901 (2017).

[95] H. J. Monkhorst and J. D. Pack, *"Special points for Brillouin-zone integrations",* Phys. Rev. B **13**, 5188–5192 (1976).

[96] E. Anderson, Z. Bai, C. Bischof, S. Blackford, J. D. J. Dongarra, J. D. Croz, A. Greenbaum, S. Hammarling, A. McKenney, and D. Sorensen, *LAPACK Users' Guide.* SIAM, Philadelphia, Pennsylvania, USA, third ed., 1999.

[97] D. R. Hamann, *"Generalized norm-conserving pseudopotentials",* Phys. Rev. B **40**, 2980–2987 (1989).

[98] M. Born and K. Huang, *Dynamical Theory of Crystal Lattices.* Oxford University Press, Oxford, 1954.

[99] P. D. DeCicco, F. A. Johnson, and R. A. Smith, *"The quantum theory of lattice dynamics. IV",* Proceedings of the Royal Society of London. A. Mathematical and Physical Sciences **310**, 111-119 (1969).

[100] R. M. Pick, M. H. Cohen, and R. M. Martin, *"Microscopic Theory of Force Constants in the Adiabatic Approximation",* Phys. Rev. B **1**, 910–920 (1970).

[101] H. Hellmann, *"Zur Rolle der kinetischen Elektronenenergie für die zwischenatomaren Kräfte",* Zeitschrift für Physik **85**, 180–190 (1933).

[102] R. P. Feynman, *"Forces in Molecules",* Phys. Rev. **56**, 340–343 (1939).

[103] R. Fletcher, *Practical Methods of Optimization.* Wiley, 2013.

[104] M. Calandra, G. Profeta, and F. Mauri, *"Adiabatic and nonadiabatic phonon dispersion in a Wannier function approach",* Phys. Rev. B **82**, 165111 (2010).

[105] P. B. Allen, *Phonons and the superconducting transition temperature*, volume 3 of *Dynamical Properties of Solids*, ch. 1, pp. 95–196. North-Holland, New York, 1980.

[106] J. J. Sakurai, *Modern quantum mechanics; rev. ed.* Addison-Wesley, Reading, MA, 1994.

[107] K. M. Ho, C. L. Fu, B. N. Harmon, W. Weber, and D. R. Hamann, *"Vibrational Frequencies and Structural Properties of Transition Metals via Total-Energy Calculations",* Phys. Rev. Lett. **49**, 673–676 (1982).

[108] M. T. Yin and M. L. Cohen, *"Theory of lattice-dynamical properties of solids: Application to Si and Ge",* Phys. Rev. B **26**, 3259–3272 (1982).

[109] S. Wei and M. Y. Chou, *"Ab initio calculation of force constants and full phonon dispersions",* Phys. Rev. Lett. **69**, 2799–2802 (1992).

[110] S. Wei and M. Y. Chou, *"Phonon dispersions of silicon and germanium from first-principles calculations",* Phys. Rev. B **50**, 2221–2226 (1994).

[111] W. Frank, C. Elsässer, and M. Fähnle, *"Ab initio Force-Constant Method for Phonon Dispersions in Alkali Metals",* Phys. Rev. Lett. **74**, 1791–1794 (1995).

[112] G. J. Ackland, M. C. Warren, and S. J. Clark, *"Practical methods in ab initio lattice dynamics",* Journal of Physics: Condensed Matter **9**, 7861–7872 (1997).

[113] K. Parlinski, Z. Q. Li, and Y. Kawazoe, *"Ab initio calculations of phonons in* $LiNbO_3$*",* Phys. Rev. B **61**, 272–278 (2000).

[114] D. Pines and P. Nozières, *The Theory of Quantum Liquids: Normal Fermi liquids.* The Theory of Quantum Liquids. W.A. Benjamin, 1966.

[115] S. K. Sinha, *Phonons in transition metals*, volume 3 of *Dynamical Properties of Solids*, ch. 1, pp. 1–94. North-Holland, New York, 1980.

[116] A. G. Eguiluz and A. A. Quong, *Electronic screening in metals: from phonons to plasmons*, volume 3 of *Dynamical Properties of Solids*, ch. 1, pp. 95–196. North-Holland, New York, 1980.

[117] R. M. Martin, *"Dielectric Screening Model for Lattice Vibrations of Diamond-Structure Crystals",* Phys. Rev. **186**, 871–884 (1969).

[118] A. A. Quong, A. A. Maradudin, R. F. Wallis, J. A. Gaspar, A. G. Eguiluz, and G. P. Alldredge, *"First-principles screening calculation of the surface-phonon dispersion curves at the (001) surface of sodium",* Phys. Rev. Lett. **66**, 743–746 (1991).

[119] A. A. Quong and B. M. Klein, *"Self-consistent-screening calculation of interatomic force constants and phonon dispersion curves from first principles",* Phys. Rev. B **46**, 10734–10737 (1992).

[120] R. F. Wallis, A. A. Maradudin, V. Bortolani, A. G. Eguiluz, A. A. Quong, A. Franchini, and G. Santoro, *"Comparison between phenomenological and pseudopotential force constants for the lattice dynamics of Al",* Phys. Rev. B **48**, 6043–6053 (1993).

[121] A. A. Quong, *"First-principles determination of the interatomic-force-constant tensor of Au",* Phys. Rev. B **49**, 3226–3229 (1994).

[122] R. M. Sternheimer, *"Electronic Polarizabilities of Ions from the Hartree-Fock Wave Functions",* Phys. Rev. **96**, 951–968 (1954).

[123] G. D. Mahan, *"Modified Sternheimer equation for polarizability",* Phys. Rev. A **22**, 1780–1785 (1980).

[124] I. Štich, R. Car, M. Parrinello, and S. Baroni, *"Conjugate gradient minimization of the energy functional: A new method for electronic structure calculation",* Phys. Rev. B **39**, 4997–5004 (1989).

[125] A. B. Migdal, *"Interaction between Electrons and Lattice Vibrations in a Normal Metal",* Sov. Phys. - JETP Lett. **34**, 996–1001 (1958).

[126] B. Farid, *Ground and Low-Lying Excited States of Interacting Electron Systems. A Survey and Some Critical Analyses*, pp. 103–261. 1999.

[127] P. Garcia-Goiricelaya, J. Lafuente-Bartolome, I. G. Gurtubay, and A. Eiguren, *"Emergence of large nonadiabatic effects induced by the electron-phonon interaction on the complex vibrational quasiparticle spectrum of doped monolayer* MoS_2*",* Phys. Rev. B **101**, 054304 (2020).

[128] P. B. Allen, *"Neutron Spectroscopy of Superconductors",* Phys. Rev. B **6**, 2577–2579 (1972).

[129] J. Bardeen, L. N. Cooper, and J. R. Schrieffer, *"Microscopic Theory of Superconductivity",* Phys. Rev. **106**, 162–164 (1957).

[130] J. Bardeen, L. N. Cooper, and J. R. Schrieffer, *"Theory of Superconductivity",* Phys. Rev. **108**, 1175–1204 (1957).

[131] G. Eliashberg, *"Interactions between Electrons and Lattice Vibrations in a Superconductor",* Sov. Phys. - JETP Lett. **38**, 966–976 (1960).

[132] J. P. Carbotte, *"Properties of boson-exchange superconductors",* Rev. Mod. Phys. **62**, 1027–1157 (1990).

[133] W. L. McMillan, *"Transition Temperature of Strong-Coupled Superconductors",* Phys. Rev. **167**, 331–344 (1968).

[134] P. B. Allen and R. C. Dynes, *"Transition temperature of strong-coupled superconductors reanalyzed",* Phys. Rev. B **12**, 905–922 (1975).

[135] N. Marzari and D. Vanderbilt, *"Maximally localized generalized Wannier functions for composite energy bands",* Phys. Rev. B **56**, 12847–12865 (1997).

[136] I. Souza, N. Marzari, and D. Vanderbilt, *"Maximally localized Wannier functions for entangled energy bands",* Phys. Rev. B **65**, 035109 (2001).

[137] N. Marzari, A. A. Mostofi, J. R. Yates, I. Souza, and D. Vanderbilt, *"Maximally localized Wannier functions: Theory and applications",* Rev. Mod. Phys. **84**, 1419–1475 (2012).

[138] F. Giustino, M. L. Cohen, and S. G. Louie, *"Electron-phonon interaction using Wannier functions",* Phys. Rev. B **76**, 165108 (2007).

[139] F. Giustino, J. R. Yates, I. Souza, M. L. Cohen, and S. G. Louie, *"Electron-Phonon Interaction via Electronic and Lattice Wannier Functions: Superconductivity in Boron-Doped Diamond Reexamined",* Phys. Rev. Lett. **98**, 047005 (2007).

[140] A. Eiguren and C. Ambrosch-Draxl, *"Wannier interpolation scheme for phonon-induced potentials: Application to bulk MgB_2, W, and the* (1×1) *H-covered W(110) surface",* Phys. Rev. B **78**, 045124 (2008).

[141] J. Ibañez Azpiroz, *Applications of maximally localized Wannier functions: spin-flip excitations, plasmon dispersion and tight binding models for optical lattices.* PhD thesis, University of the Basque Country, 2013.

[142] G. H. Wannier, *"The Structure of Electronic Excitation Levels in Insulating Crystals",* Phys. Rev. **52**, 191–197 (1937).

[143] A. A. Mostofi, J. R. Yates, Y.-S. Lee, I. Souza, D. Vanderbilt, and N. Marzari, *"wannier90: A tool for obtaining maximally-localised Wannier functions",* Computer Physics Communications **178**, 685 - 699 (2008).

[144] I. Tamm, *"Über eine mögliche Art der Elektronenbindung an Kristalloberflächen",* Zeitschrift für Physik **76**, 849–850 (1932).

[145] W. Shockley, *"On the Surface States Associated with a Periodic Potential",* Phys. Rev. **56**, 317–323 (1939).

[146] J. Black, F. Shanes, and R. Wallis, *"Surface vibrations on face centered cubic metal surfaces: the (111) surfaces",* Surface Science **133**, 199 - 215 (1983).

[147] J. Black, *"The lattice dynamical behavior of a plateau of atoms",* Surface Science **278**, 229 - 236 (1992).

[148] Y. A. Bychkov and E. I. Rashba, *"Properties of a 2D electron gas with a lifted spectrum degeneracy",* Sov. Phys. - JETP Lett. **39**, 78–81 (1984).

[149] S. LaShell, B. A. McDougall, and E. Jensen, *"Spin Splitting of an Au(111) Surface State Band Observed with Angle Resolved Photoelectron Spectroscopy",* Phys. Rev. Lett. **77**, 3419–3422 (1996).

[150] M. Hoesch, M. Muntwiler, V. N. Petrov, M. Hengsberger, L. Patthey, M. Shi, M. Falub, T. Greber, and J. Osterwalder, *"Spin structure of the Shockley surface state on* Au(111)*",* Phys. Rev. B **69**, 241401 (2004).

[151] J. Henk, A. Ernst, and P. Bruno, *"Spin polarization of the L-gap surface states on Au(111)",* Phys. Rev. B **68**, 165416 (2003).

[152] G. Nicolay, F. Reinert, S. Hüfner, and P. Blaha, *"Spin-orbit splitting of the L-gap surface state on Au(111) and Ag(111)",* Phys. Rev. B **65**, 033407 (2001).

[153] Y. M. Koroteev, G. Bihlmayer, J. E. Gayone, E. V. Chulkov, S. Blügel, P. M. Echenique, and P. Hofmann, *"Strong Spin-Orbit Splitting on Bi Surfaces",* Phys. Rev. Lett. **93**, 046403 (2004).

[154] J. I. Pascual, G. Bihlmayer, Y. M. Koroteev, H.-P. Rust, G. Ceballos, M. Hansmann, K. Horn, E. V. Chulkov, S. Blügel, P. M. Echenique, and P. Hofmann, *"Role of Spin in Quasiparticle Interference",* Phys. Rev. Lett. **93**, 196802 (2004).

[155] P. Hofmann, J. E. Gayone, G. Bihlmayer, Y. M. Koroteev, and E. V. Chulkov, *"Electronic structure and Fermi surface of Bi(100)",* Phys. Rev. B **71**, 195413 (2005).

[156] K. Sugawara, T. Sato, S. Souma, T. Takahashi, M. Arai, and T. Sasaki, *"Fermi Surface and Anisotropic Spin-Orbit Coupling of Sb(111) Studied by Angle-Resolved Photoemission Spectroscopy",* Phys. Rev. Lett. **96**, 046411 (2006).

[157] T. Hirahara, T. Nagao, I. Matsuda, G. Bihlmayer, E. V. Chulkov, Y. M. Koroteev, P. M. Echenique, M. Saito, and S. Hasegawa, *"Role of Spin-Orbit Coupling and Hybridization Effects in the Electronic Structure of Ultrathin Bi Films",* Phys. Rev. Lett. **97**, 146803 (2006).

[158] J. H. Dil, *"Spin and angle resolved photoemission on non-magnetic low-dimensional systems",* Journal of Physics: Condensed Matter **21**, 403001 (2009).

[159] E. E. Krasovskii, *"Spin-orbit coupling at surfaces and 2D materials",* Journal of Physics: Condensed Matter **27**, 493001 (2015).

[160] C. R. Ast, J. Henk, A. Ernst, L. Moreschini, M. C. Falub, D. Pacilé, P. Bruno, K. Kern, and M. Grioni, *"Giant Spin Splitting through Surface Alloying",* Phys. Rev. Lett. **98**, 186807 (2007).

[161] K. Sakamoto, T. Oda, A. Kimura, K. Miyamoto, M. Tsujikawa, A. Imai, N. Ueno, H. Namatame, M. Taniguchi, P. E. J. Eriksson, and R. I. G. Uhrberg, *"Abrupt Rotation of the Rashba Spin to the Direction Perpendicular to the Surface",* Phys. Rev. Lett. **102**, 096805 (2009).

[162] S. D. Stolwijk, A. B. Schmidt, M. Donath, K. Sakamoto, and P. Krüger, *"Rotating Spin and Giant Splitting: Unoccupied Surface Electronic Structure of* Tl/Si(111)*",* Phys. Rev. Lett. **111**, 176402 (2013).

[163] K. Sakamoto, T.-H. Kim, T. Kuzumaki, B. Müller, Y. Yamamoto, M. Ohtaka, J. R. Osiecki, K. Miyamoto, Y. Takeichi, A. Harasawa, S. D. Stolwijk, A. B. Schmidt, J. Fujii, R. I. G. Uhrberg, M. Donath, H. W. Yeom, and T. Oda, *"Valley spin polarization by using the extraordinary Rashba effect on silicon",* Nature Communications **4**, 2073 (2013).

[164] S. D. Stolwijk, K. Sakamoto, A. B. Schmidt, P. Krüger, and M. Donath, *"Spin texture with a twist in momentum space for Tl/Si(111)",* Phys. Rev. B **91**, 245420 (2015).

[165] J. Ibañez Azpiroz, A. Eiguren, and A. Bergara, *"Relativistic effects and fully spin-polarized Fermi surface at the Tl/Si(111) surface",* Phys. Rev. B **84**, 125435 (2011).

[166] J. Lafuente-Bartolome, I. G. Gurtubay, and A. Eiguren, *"Relativistic response and novel spin-charge plasmon at the Tl/Si(111) surface",* Phys. Rev. B **96**, 035416 (2017).

[167] V. Chis, G. Benedek, P. M. Echenique, and E. V. Chulkov, *"Phonons in ultrathin Bi(111) films: Role of spin-orbit coupling in electron-phonon interaction",* Phys. Rev. B **87**, 075412 (2013).

[168] I. Y. Sklyadneva, R. Heid, K.-P. Bohnen, P. M. Echenique, G. Benedek, and E. V. Chulkov, *"The Effect of Spin-Orbit Coupling on the Surface Dynamical Properties and Electron-Phonon Interaction of Tl(0001)",* The Journal of Physical Chemistry A **115**, 7352-7355 (2011).

[169] A. Einstein, *"Zur Elektrodynamik bewegter Krper",* Annalen der Physik **322**, 891-921 (1905).

[170] S. Blundell, *Magnetism in Condensed Matter*. Oxford Master Series in Condensed Matter Physics. Oxford University Press, Oxford, 2001.

[171] S. Wilson, I. Grant, and B. Györffy, *The Effects of Relativity in Atoms, Molecules, and the Solid State*. Springer, 1991.

[172] J. Sakurai, *Advanced Quantum Mechanics*. Always learning. Pearson Education, Incorporated, 1967.

[173] U. Kaldor and S. Wilson, *Theoretical Chemistry and Physics of Heavy and Superheavy Elements*. Progress in Theoretical Chemistry and Physics. Springer Netherlands, 2003.

[174] U. von Barth and L. Hedin, *"A local exchange-correlation potential for the spin polarized case. I",* Journal of Physics C: Solid State Physics **5**, 1629–1642 (1972).

[175] A. K. Rajagopal and J. Callaway, *"Inhomogeneous Electron Gas",* Phys. Rev. B **7**, 1912–1919 (1973).

[176] A. K. Rajagopal, *"Inhomogeneous relativistic electron gas",* Journal of Physics C: Solid State Physics **11**, L943–L948 (1978).

[177] A. H. MacDonald and S. H. Vosko, *"A relativistic density functional formalism",* Journal of Physics C: Solid State Physics **12**, 2977–2990 (1979).

[178] W. Pauli, *"Zur Quantenmechanik des magnetischen Elektrons",* Zeitschrift für Physik **43**, 601–623 (1927).

[179] P. A. M. Dirac and R. H. Fowler, *"The quantum theory of the electron",* Proceedings of the Royal Society of London. Series A, Containing Papers of a Mathematical and Physical Character **117**, 610-624 (1928).

[180] P. A. M. Dirac and R. H. Fowler, *"A theory of electrons and protons",* Proceedings of the Royal Society of London. Series A, Containing Papers of a Mathematical and Physical Character **126**, 360-365 (1930).

[181] H. Kroemer, *"The Thomas precession factor in spinorbit interaction",* American Journal of Physics **72**, 51-52 (2004).

[182] J. Kubler, K. H. Hock, J. Sticht, and A. R. Williams, *"Density functional theory of non-collinear magnetism",* Journal of Physics F: Metal Physics **18**, 469–483 (1988).

[183] P. Kurz, F. Förster, L. Nordström, G. Bihlmayer, and S. Blügel, *"Ab initio treatment of noncollinear magnets with the full-potential linearized augmented plane wave method",* Phys. Rev. B **69**, 024415 (2004).

[184] J. E. Peralta, G. E. Scuseria, and M. J. Frisch, *"Noncollinear magnetism in density functional calculations",* Phys. Rev. B **75**, 125119 (2007).

[185] E. Engel, S. Keller, and R. M. Dreizler, *"Generalized gradient approximation for the relativistic exchange-only energy functional",* Phys. Rev. A **53**, 1367–1374 (1996).

[186] E. Engel, T. Auth, and R. M. Dreizler, *"Relativistic spin-density-functional theory: Robust solution of single-particle equations for open-subshell atoms",* Phys. Rev. B **64**, 235126 (2001).

[187] V. Theileis and H. Bross, *"Relativistic modified augmented plane wave method and its application to the electronic structure of gold and platinum",* Phys. Rev. B **62**, 13338–13346 (2000).

[188] A. D. Corso and A. M. Conte, *"Spin-orbit coupling with ultrasoft pseudopotentials: Application to Au and Pt",* Phys. Rev. B **71**, 115106 (2005).

[189] J. Fabian and S. Das Sarma, *"Phonon-Induced Spin Relaxation of Conduction Electrons in Aluminum",* Phys. Rev. Lett. **83**, 1211–1214 (1999).

[190] T. Noda, S. Mizuno, J. Chung, and H. Tochihara, *"T4Site Adsorption of Tl Atoms in a Si(111)-(*1×1*)-Tl Structure, Determined by Low-Energy Electron Diffraction Analysis",* Japanese Journal of Applied Physics **42**, L319–L321 (2003).

[191] N. D. Kim, C. G. Hwang, J. W. Chung, T. C. Kim, H. J. Kim, and D. Y. Noh, *"Structural properties of a thallium-induced Si(111)-*1×1 *surface",* Phys. Rev. B **69**, 195311 (2004).

[192] S. S. Lee, H. J. Song, N. D. Kim, J. W. Chung, K. Kong, D. Ahn, H. Yi, B. D. Yu, and H. Tochihara, *"Structural and electronic properties of thallium overlayers on the Si(111)-*7×7 *surface",* Phys. Rev. B **66**, 233312 (2002).

[193] M.-H. Liu and C.-R. Chang, *"Upstanding Rashba spin in honeycomb lattices: Electrically reversible surface spin polarization",* Phys. Rev. B **80**, 241304 (2009).

[194] S. D. Stolwijk, K. Sakamoto, A. B. Schmidt, P. Krüger, and M. Donath, *"Thin line of a Rashba-type spin texture: Unoccupied surface resonance of Tl/Si(111) along $\overline{\Gamma M}$",* Phys. Rev. B **90**, 161109 (2014).

[195] H. Zhu, J. Yi, M.-Y. Li, J. Xiao, L. Zhang, C.-W. Yang, R. A. Kaindl, L.-J. Li, Y. Wang, and X. Zhang, *"Observation of chiral phonons",* Science **359**, 579–582 (2018).

[196] M. Hengsberger, D. Purdie, P. Segovia, M. Garnier, and Y. Baer, *"Photoemission Study of a Strongly Coupled Electron-Phonon System",* Phys. Rev. Lett. **83**, 592–595 (1999).

[197] T. Valla, A. V. Fedorov, P. D. Johnson, and S. L. Hulbert, *"Many-Body Effects in Angle-Resolved Photoemission: Quasiparticle Energy and Lifetime of a Mo(110) Surface State",* Phys. Rev. Lett. **83**, 2085–2088 (1999).

[198] S. LaShell, E. Jensen, and T. Balasubramanian, *"Nonquasiparticle structure in the photoemission spectra from the Be(0001) surface and determination of the electron self energy",* Phys. Rev. B **61**, 2371–2374 (2000).

[199] E. Rotenberg, J. Schaefer, and S. D. Kevan, *"Coupling Between Adsorbate Vibrations and an Electronic Surface State",* Phys. Rev. Lett. **84**, 2925–2928 (2000).

[200] A. Lanzara, P. V. Bogdanov, X. J. Zhou, S. A. Kellar, D. L. Feng, E. D. Lu, T. Yoshida, H. Eisaki, A. Fujimori, K. Kishio, J.-I. Shimoyama, T. Noda, S. Uchida, Z. Hussain, and Z.-X. Shen, *"Evidence for ubiquitous strong electron-phonon coupling in high-temperature superconductors",* Nature **412**, 510-514 (2001).

[201] X. J. Zhou, J. Shi, T. Yoshida, T. Cuk, W. L. Yang, V. Brouet, J. Nakamura, N. Mannella, S. Komiya, Y. Ando, F. Zhou, W. X. Ti, J. W. Xiong, Z. X. Zhao, T. Sasagawa, T. Kakeshita, H. Eisaki, S. Uchida, A. Fujimori, Z. Zhang, E. W. Plummer, R. B. Laughlin, Z. Hussain, and Z.-X. Shen, *"Multiple Bosonic Mode Coupling in the Electron Self-Energy of* $(La_{2-x}Sr_x)CuO_4$*",* Phys. Rev. Lett. **95**, 117001 (2005).

[202] K. Sugawara, T. Sato, S. Souma, T. Takahashi, and H. Suematsu, *"Anomalous Quasiparticle Lifetime and Strong Electron-Phonon Coupling in Graphite",* Phys. Rev. Lett. **98**, 036801 (2007).

[203] A. Eiguren, S. de Gironcoli, E. V. Chulkov, P. M. Echenique, and E. Tosatti, *"Electron-Phonon Interaction at the Be(0001) Surface",* Phys. Rev. Lett. **91**, 166803 (2003).

[204] F. Giustino, M. L. Cohen, and S. G. Louie, *"Small phonon contribution to the photoemission kink in the copper oxide superconductors",* Nature **452**, 975-978 (2008).

[205] C. Verdi, F. Caruso, and F. Giustino, *"Origin of the crossover from polarons to Fermi liquids in transition metal oxides",* Nature Communications **8**, 15769 (2017).

[206] W. Kohn, *"Image of the Fermi Surface in the Vibration Spectrum of a Metal",* Phys. Rev. Lett. **2**, 393–394 (1959).

[207] A. Q. R. Baron, H. Uchiyama, Y. Tanaka, S. Tsutsui, D. Ishikawa, S. Lee, R. Heid, K.-P. Bohnen, S. Tajima, and T. Ishikawa, *"Kohn Anomaly in* MgB_2 *by Inelastic X-Ray Scattering",* Phys. Rev. Lett. **92**, 197004 (2004).

[208] S. Piscanec, M. Lazzeri, F. Mauri, A. C. Ferrari, and J. Robertson, *"Kohn Anomalies and Electron-Phonon Interactions in Graphite",* Phys. Rev. Lett. **93**, 185503 (2004).

[209] P. Aynajian, T. Keller, L. Boeri, S. M. Shapiro, K. Habicht, and B. Keimer, *"Energy Gaps and Kohn Anomalies in Elemental Superconductors",* Science **319**, 1509–1512 (2008).

[210] D. A. Stewart, *"Ab initio investigation of phonon dispersion and anomalies in palladium",* New Journal of Physics **10**, 043025 (2008).

[211] I. P. Ipatova and A. V. Subashiev, *"Long-wave optical-phonon spectrum in metals and heavily doped semiconductors",* Sov. Phys. - JETP Lett. **39**, 349–354 (1974).

[212] E. Maksimov and S. Shulga, *"Nonadiabatic effects in optical phonon self-energy",* Solid State Communications **97**, 553 - 560 (1996).

[213] A. I. Morosov, *"Nonadiabatic effects in the phonon spectrum of metal compounds",* Journal of Experimental and Theoretical Physics Letters **73**, 79-81 (2001).

[214] E. G. Maksimov and A. Karakozov Physics-Uspekhi **51**, 535 (2008).

[215] Y. S. Ponosov, G. A. Bolotin, C. Thomsen, and M. Cardona, *"Raman Scattering in Os: Nonadiabatic Renormalization of the Optical Phonon Self-Energies",* Physica Status Solidi (B) **208**, 257-269 (1998).

[216] M. Calandra and F. Mauri, *"Electron-phonon coupling and phonon self-energy in* MgB_2*: Interpretation of* MgB_2 *Raman spectra",* Phys. Rev. B **71**, 064501 (2005).

[217] E. Cappelluti, *"Electron-phonon effects on the Raman spectrum in* MgB_2*"*, Phys. Rev. B **73**, 140505 (2006).

[218] M. Lazzeri and F. Mauri, *"Nonadiabatic Kohn Anomaly in a Doped Graphene Monolayer"*, Phys. Rev. Lett. **97**, 266407 (2006).

[219] S. Pisana, M. Lazzeri, C. Casiraghi, K. S. Novoselov, A. K. Geim, A. C. Ferrari, and F. Mauri, *"Breakdown of the adiabatic Born-Oppenheimer approximation in graphene"*, Nature Materials **6**, 198-201 (2007).

[220] S. Piscanec, M. Lazzeri, J. Robertson, A. C. Ferrari, and F. Mauri, *"Optical phonons in carbon nanotubes: Kohn anomalies, Peierls distortions, and dynamic effects"*, Phys. Rev. B **75**, 035427 (2007).

[221] A. M. Saitta, M. Lazzeri, M. Calandra, and F. Mauri, *"Giant Nonadiabatic Effects in Layer Metals: Raman Spectra of Intercalated Graphite Explained"*, Phys. Rev. Lett. **100**, 226401 (2008).

[222] M. P. M. Dean, C. A. Howard, S. S. Saxena, and M. Ellerby, *"Nonadiabatic phonons within the doped graphene layers of* XC_6 *compounds"*, Phys. Rev. B **81**, 045405 (2010).

[223] Y. S. Ponosov and S. V. Streltsov, *"Raman evidence for nonadiabatic effects in optical phonon self-energies of transition metals"*, Phys. Rev. B **94**, 214302 (2016).

[224] M. d'Astuto, R. Heid, B. Renker, F. Weber, H. Schober, O. De la Peña Seaman, J. Karpinski, N. D. Zhigadlo, A. Bossak, and M. Krisch, *"Nonadiabatic effects in the phonon dispersion of* $Mg_{1-x}Al_xB_2$*"*, Phys. Rev. B **93**, 180508 (2016).

[225] F. Caruso, M. Hoesch, P. Achatz, J. Serrano, M. Krisch, E. Bustarret, and F. Giustino, *"Nonadiabatic Kohn Anomaly in Heavily Boron-Doped Diamond"*, Phys. Rev. Lett. **119**, 017001 (2017).

[226] D. Novko, *"Nonadiabatic coupling effects in* MgB_2 *reexamined"*, Phys. Rev. B **98**, 041112 (2018).

[227] L. J. Li, E. C. T. O'Farrell, K. P. Loh, G. Eda, B. Özyilmaz, and A. H. Castro Neto, *"Controlling many-body states by the electric-field effect in a two-dimensional material"*, Nature **529**, 185-189 (2016).

[228] Z. Wang, S. McKeown Walker, A. Tamai, Y. Wang, Z. Ristic, F. Y. Bruno, A. de la Torre, S. Riccò, N. C. Plumb, M. Shi, P. Hlawenka, J. Sánchez-Barriga, A. Varykhalov, T. K. Kim, M. Hoesch, P. D. C. King, W. Meevasana, U. Diebold, J. Mesot, B. Moritz, T. P.

Devereaux, M. Radovic, and F. Baumberger, *"Tailoring the nature and strength of electron-phonon interactions in the $SrTiO_3$(001) 2D electron liquid",* Nature Materials **15**, 835-839 (2016).

[229] B. Chakraborty, A. Bera, D. V. S. Muthu, S. Bhowmick, U. V. Waghmare, and A. K. Sood, *"Symmetry-dependent phonon renormalization in monolayer MoS_2 transistor",* Phys. Rev. B **85**, 161403 (2012).

[230] T. Sohier, E. Ponomarev, M. Gibertini, H. Berger, N. Marzari, N. Ubrig, and A. F. Morpurgo, *"Enhanced Electron-Phonon Interaction in Multivalley Materials",* Phys. Rev. X **9**, 031019 (2019).

[231] D. Novko, *"Broken adiabaticity induced by Lifshitz transition in MoS2 and WS2 single layers",* Communications Physics **3**, 30 (2020).

[232] M. Kang, S. W. Jung, W. J. Shin, Y. Sohn, S. H. Ryu, T. K. Kim, M. Hoesch, and K. S. Kim, *"Holstein polaron in a valley-degenerate two-dimensional semiconductor",* Nature Materials **17**, 676-680 (2018).

[233] J. T. Ye, Y. J. Zhang, R. Akashi, M. S. Bahramy, R. Arita, and Y. Iwasa, *"Superconducting Dome in a Gate-Tuned Band Insulator",* Science **338**, 1193–1196 (2012).

[234] Y. Saito, Y. Nakamura, M. S. Bahramy, Y. Kohama, J. Ye, Y. Kasahara, Y. Nakagawa, M. Onga, M. Tokunaga, T. Nojima, Y. Yanase, and Y. Iwasa, *"Superconductivity protected by spin-valley locking in ion-gated MoS2",* Nature Physics **12**, 144 (2015).

[235] J. M. Lu, O. Zheliuk, I. Leermakers, N. F. Q. Yuan, U. Zeitler, K. T. Law, and J. T. Ye, *"Evidence for two-dimensional Ising superconductivity in gated MoS_2",* Science **350**, 1353–1357 (2015).

[236] D. Costanzo, S. Jo, H. Berger, and A. F. Morpurgo, *"Gate-induced superconductivity in atomically thin MoS_2 crystals",* Nature Nanotechnology **11**, 339 (2016). Article.

[237] Y. Ge and A. Y. Liu, *"Phonon-mediated superconductivity in electron-doped single-layer MoS_2: A first-principles prediction",* Phys. Rev. B **87**, 241408 (2013).

[238] M. Rösner, S. Haas, and T. O. Wehling, *"Phase diagram of electron-doped dichalcogenides",* Phys. Rev. B **90**, 245105 (2014).

[239] Y. Fu, E. Liu, H. Yuan, P. Tang, B. Lian, G. Xu, J. Zeng, Z. Chen, Y. Wang, W. Zhou, K. Xu, A. Gao, C. Pan, M. Wang, B. Wang, S.-C. Zhang, Y. Cui, H. Y. Hwang, and F. Miao, *"Gated tuned*

superconductivity and phonon softening in monolayer and bilayer MoS_2", npj Quantum Materials **2**, 52 (2017).

[240] E. Piatti, D. De Fazio, D. Daghero, S. R. Tamalampudi, D. Yoon, A. C. Ferrari, and R. S. Gonnelli, *"Multi-Valley Superconductivity in Ion-Gated MoS2 Layers",* Nano Letters **18**, 4821-4830 (2018).

[241] A. Molina-Sánchez and L. Wirtz, *"Phonons in single-layer and few-layer MoS_2 and WS_2",* Phys. Rev. B **84**, 155413 (2011).

[242] P. A. Young, *"Lattice parameter measurements on molybdenum disulphide",* Journal of Physics D: Applied Physics **1**, 936–938 (1968).

[243] L. Kleinman, *"Relativistic norm-conserving pseudopotential",* Phys. Rev. B **21**, 2630–2631 (1980).

[244] S. Lebègue and O. Eriksson, *"Electronic structure of two-dimensional crystals from ab initio theory",* Phys. Rev. B **79**, 115409 (2009).

[245] K. F. Mak, C. Lee, J. Hone, J. Shan, and T. F. Heinz, *"Atomically Thin* MoS_2*: A New Direct-Gap Semiconductor",* Phys. Rev. Lett. **105**, 136805 (2010).

[246] A. Kuc, N. Zibouche, and T. Heine, *"Influence of quantum confinement on the electronic structure of the transition metal sulfide TS_2",* Phys. Rev. B **83**, 245213 (2011).

[247] E. S. Kadantsev and P. Hawrylak, *"Electronic structure of a single MoS_2 monolayer",* Solid State Communications **152**, 909 - 913 (2012).

[248] X. Li, J. T. Mullen, Z. Jin, K. M. Borysenko, M. Buongiorno Nardelli, and K. W. Kim, *"Intrinsic electrical transport properties of monolayer silicene and MoS_2 from first principles",* Phys. Rev. B **87**, 115418 (2013).

[249] R. Roldn, J. A. Silva-Guilln, M. P. Lpez-Sancho, F. Guinea, E. Cappelluti, and P. Ordejn, *"Electronic properties of single-layer and multilayer transition metal dichalcogenides MX_2 (M = Mo, W and X = S, Se)",* Annalen der Physik **526**, 347-357 (2014).

[250] H.-M. Dong, S.-D. Guo, Y.-F. Duan, F. Huang, W. Xu, and J. Zhang, *"Electronic and optical properties of single-layer MoS_2",* Frontiers of Physics **13**, 137307 (2018).

[251] Z. Y. Zhu, Y. C. Cheng, and U. Schwingenschlögl, *"Giant spin-orbit-induced spin splitting in two-dimensional transition-metal dichalcogenide semiconductors",* Phys. Rev. B **84**, 153402 (2011).

[252] H. Zabel, *"Phonons in layered compounds"*, Journal of Physics: Condensed Matter **13**, 7679–7690 (2001).

[253] T. Brumme, M. Calandra, and F. Mauri, *"First-principles theory of field-effect doping in transition-metal dichalcogenides: Structural properties, electronic structure, Hall coefficient, and electrical conductivity"*, Phys. Rev. B **91**, 155436 (2015).

[254] M. D. Johannes and I. I. Mazin, *"Fermi surface nesting and the origin of charge density waves in metals"*, Phys. Rev. B **77**, 165135 (2008).

[255] K. Kaasbjerg, K. S. Thygesen, and K. W. Jacobsen, *"Phonon-limited mobility in n-type single-layer MoS_2 from first principles"*, Phys. Rev. B **85**, 115317 (2012).

[256] F. Stern, *"Polarizability of a Two-Dimensional Electron Gas"*, Phys. Rev. Lett. **18**, 546–548 (1967).

[257] P. Coleman, *Introduction to Many-Body Physics*. Cambridge University Press, 2015.

[258] S. Moser, L. Moreschini, J. Jaćimović, O. S. Barišić, H. Berger, A. Magrez, Y. J. Chang, K. S. Kim, A. Bostwick, E. Rotenberg, L. Forró, and M. Grioni, *"Tunable Polaronic Conduction in Anatase TiO_2"*, Phys. Rev. Lett. **110**, 196403 (2013).

[259] C. Chen, J. Avila, E. Frantzeskakis, A. Levy, and M. C. Asensio, *"Observation of a two-dimensional liquid of Fröhlich polarons at the bare $SrTiO_3$ surface"*, Nature Communications **6**, 8585 (2015).

[260] C. Cancellieri, A. S. Mishchenko, U. Aschauer, A. Filippetti, C. Faber, O. S. Barisic, V. A. Rogalev, T. Schmitt, N. Nagaosa, and V. N. Strocov, *"Polaronic metal state at the $LaAlO_3/SrTiO_3$ interface"*, Nature Communications **7**, 10386 (2016).

[261] M. Gell-Mann and K. A. Brueckner, *"Correlation Energy of an Electron Gas at High Density"*, Phys. Rev. **106**, 364–368 (1957).

[262] L. Hedin and B. I. Lundqvist, *"Explicit local exchange-correlation potentials"*, Journal of Physics C: Solid State Physics **4**, 2064–2083 (1971).

[263] R. O. Jones and O. Gunnarsson, *"The density functional formalism, its applications and prospects"*, Rev. Mod. Phys. **61**, 689–746 (1989).

[264] L. Kleinman and D. M. Bylander, *"Efficacious Form for Model Pseudopotentials"*, Phys. Rev. Lett. **48**, 1425–1428 (1982).

[265] W. Pauli, *"Über den Zusammenhang des Abschlusses der Elektronengruppen im Atom mit der Komplexstruktur der Spektren"*, Zeitschrift für Physik **31**, 765–783 (1925).

Acknowledgements

"Gratus animus est una virtus non solum maxima, sed etiam mater virtutum omnium reliquarum."

Marcus Tullius Cicero

At the end of a journey, it is worth looking back and admire the road traveled. I remember very well when I started this adventure. It was at the end of 2012 and the beginning of 2013, after an exhausting year studying the Master in Physics and Technology of Materials from the University of the Basque Country and working for an industrial company that, to be honest, did not met my expectations. At that time I was – and probably still – that boy who greatly enjoyed studying the Degree in Physics from the University of the Basque Country, always encouraged by the desire to understand everything. It was during the master that I met Asier and Idoia, supervisors of this PhD thesis. Both quickly convinced me to work with them in the exciting world of solid state physics, a subject that I loved during the degree and the master, showing me a great passion and a wide knowledge that actually made me decide to embark on this project.

Still, this journey has not been an easy one. Outside of workplace, I had to face cancer twice and undergo surgery, together with the brutality of the chemotherapy treatments, in order to overcome the disease. This kept me out of play for a long time and caused me metabolism deficiencies that I will have to drag for the rest of my life. I had to work with the torment that creates the fear of falling back on the disease and the unanswered question of "Why me?" when I was a healthy young man in his early twenties. Regarding work, the lack of progress and results during many stages of the thesis led me to a desert journey and a depression that made me doubt my knowledge, my capacity and myself. I admit that many times continuing with the thesis became so hard that in more than one occasion I seriously considered leaving the ship. Nevertheless, I never gave up. Finally, I have managed to finish this PhD thesis in the most honorable way that I have been able to do, and for which I must thank many people.

First of all, I would like to acknowledge my supervisors, Asier and Idoia, for giving me the opportunity and the honor to be part of the "Computational theory in Condensed Matter Physics" research group, for which I foresee great successes in the future. You make a great team and I wish you all the luck in the world. You took a student coming from the experimental "dark" side, totally unfamiliar with first principles theories of many-body physics, and you have managed to turn him into a fervent lover of the theory. Despite all the troubles I have given you with reading and correcting countless times my heavyweight drafts, I deeply thank you all your help, tolerance and confidence, as well as all your teachings. I would be really happy if you have learned with me at least a small portion of all that I have learned with you. I want also to thank you how well you have always treated me and your patience at a time that PhD thesis is intended to last four years, instead of the seven I have spent. Last, I want to thank you for always having understood my delicate health situation. *Bihotzez, eskerrik asko denagatik.*

I would like to acknowledge financial support from the University of the Basque Country UPV/EHU (Grant No. PIF/UPV/12/279) and the Donostia International Physics Center (DIPC), which also provided the computer facilities for performing calculations. Thank you for having allowed research to be my way to make a living during these seven years. In particular, I would like to thank the DIPC for financing me some months before and especially these final years after the period of the four-year grant, when they had no duty to do it, giving me an essential economic tranquility to work and finish my PhD thesis.

I would like to acknowledge my scientific older "brother" and "sister", Julen and Ainhoa, as well as middle and younger "brothers", Aitzol, Jon and Haritz. I would like to make special mention to Julen, Jon and Haritz. *Julen: Eskerrik asko beti pantailaren beste aldean egoteagatik, Alemanian zein Donostian, eta nire kezkak eta frustrazioak entzuteagatik... Tl/Si(111) gainazal madarikatua! Jon: Niretzako benetako sostengua izan zarelako Leioan, eskerrik asko bihotzez. Kriston pertsona ona zara eta biziki miresten dizut. Animo asko geratzen zaizkizun azken hilabete hauetan! Haritz: Eutsi gogor eta ez eman amorerik igoera luze eta gogor honetan, laster gauzak ateratzen hasiko direlako eta helmuga gertuago izango delako!*

Next, I would like to acknowledge a special group of people that has been crucial during these long years, the *Gose Naiz Taldea (GNT)*, composed of *Joanes (Zer dozo?), Asier (Aupa Isuntza!), Iraultza (Ez gitxi laun!), Iagoba (Ttak!), Julen (Deabruaren abokatua!), Iigo (Barru xauk!), Mattin (Posterman!), Lafu (Aupa Laranga!), Haritz (Zeamako "maillot jaune"!), Xabimen (Gora Foruak!), Telmo (Beste Deustuarra!) eta Oskar (Gaztela euskaldunok sortu genuen!). Eskerrik asko eguneroko bazkaria alaitzeagatik, batez ere unerik txarrenetan. Pertsona oso garrantzitsuak izan zarete niretzat urte*

luze hauetan. Maite zaituztet zuek guztiak eta beti eramango zaituztet bihotzean. Gora GNT!

I would also like to acknowledge the Department of Condensed Matter Physics and the Department of Applied Physics II of the University of the Basque Country, as well as all the people compose them. Thank you for your closeness and your affection. At this point, and together with the people from the Department of Theoretical Physics, I would to acknowledge all the people has taught me during first the degree and then the master. Thank you for teaching me the beauty of physics.

I would also like to acknowledge all the young researchers with whom I have coincided in the "Becdromos" and that I have not yet cited. Iaki, Unai, Urko, Jos Fernando, Bea, Gemma, Sofa, Patri, Leire, Brahim, Paul, Iigo Setin and Iigo Gonzlez de Arrieta, Balma, Mikel and many others I am sure I am unintentionally forgetting. Thank you, eskerrik asko, muchas gracias, merci beaucoup, for creating an outstandingly good atmosphere for working. *Me gustara tener un especial agradecimiento para mi maico del alma, Gerardito, y mi chico del tiempo, Santitos. Gerardo: Muchas gracias por los buenos momentos, un beso para la Llop y para t. Espero veros pronto. Santos Jos: Muchas gracias por todo, Aitziber y t habis sido muy especiales para m, sobre todo en los ltimos momentos. Os quiero mucho.*

Outside research, I would like to acknowledge all the doctors and the nurses that make up the Departments of Urology and Oncology of the Igualatorio Mdico Quirrgico (IMQ), especially the doctor Ricardo Fernndez, the doctor Ander Astobieta and the nurse Bea. *Dobles infinitas gracias por curarme y permitirme seguir viviendo mi vida dignamente.*

I would also like to acknowledge all my *kuadrillas. En primer lugar, a mi cuadrilla de siempre, a los txabatars: Jon I., Jon G., Bruno, Mateo, Javi, Ispizua, Kano, Iciar et Elsouille, y cada vez ms Markel, Paula y Gil. Muchas gracias por vuestros nimos! Merci beaucoup pour vos clins! Aupa Athletic! Bigarrenik, eskerrik asko marruskiei: Altuna, Bertix, Deierro, Edrigi, Gontzal, Jintxaur, Lukentzio eta Santiago y cierra Espaa. Eskerrik asko nirekin Foruen alde eta Karlismoaren alde topa egiteagatik. Azkenik, eskerrik asko Wolframio Kopon! kuadrillari: Aiala, Ander, Aritz, Arratinson, Dodxo, Iratuki, Naroita, la Repe, Noetxu, Olaita, Pablito, Pattinson, Unaitxo eta Xabitxu. Eskerrik asko eskumaldeko mutiko hau bertokoa izango balitz bezela hartzeagatik zuekin. Gora Ezkerralde euskalduna! Aipu berezi bat Ainizeri eta Kaskanteri ere bai, eskerrik asko, maite zaituztet.*

I would also like to acknowledge my family. *Muchas gracias, eskerrik asko, Amama, tos y tas, primos y primas. Os quiero mucho, asko maite zaituztet. Hemen aipu oso berezi bat eman nahi diot nire izeko Lolari. Faltan botatzen zaitugu eta asko maite zaitugu. Egun handira arte. Eskerrak eman nahi dizkiot ere nire Santurtziko familiari, Fran eta Marijo, eskerrik asko beti bikainki tratatzeagatik. Maite zaituztet.*

Finally, I would like to acknowledge especially my closest ones.

Sardinera: Eskerrik asko denagatik. Zure pazientzia, zure maitasuna, zure kariua, zure laztanak... zure ordainezin "dena" ezinbestekoa izan da azken urte hauetan tesi hau porturatzeko. Eskerrik asko ni salbatzeagatik, zentzu guztietan. Maite zaitut, ene sardinera.

Aita, Ama y Begotxu: Muchas gracias por todo, por la vida que me habis dado, por haberme criado, por haberme enseado, por no dejarme caer, y cuando he caido por ayudarme a ponerme en pie, por quererme,... en definitiva por haberme hecho quien soy. Siempre habis sido y seris una fuente de motivacin inagotable. Siempre os tengo presentes y os llevo en el corazn. Os quiero, maite zaituztet.

Natural sentitzen dut, egiten dudana
eta natural egin, sentitzen dudana.
Doktore egin naiz, horixe da dana
ahaztu gabe guztioi, muxu handi bana.

Azote Kaldz!